UNIVERSITY OF SOUTHAMPTON

FACULTY OF NATURAL AND ENVIRONMENTAL SCIENCES

Ocean and Earth Science

The Continent-Ocean Transition at the Deep Galicia Margin: Insights from wide-angle seismic data

by

Richard Gareth Davy

A thesis submitted to the University of Southampton in accordance with the requirements for the degree of Doctor of Philosophy

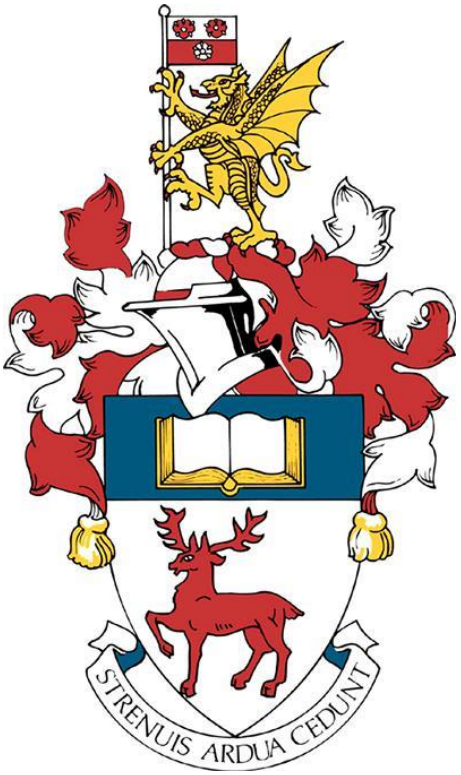

May 2017

Dedicated to my amazing parents,

Lynley Davidson and Bryan Davy

UNIVERSITY OF SOUTHAMPTON

ABSTRACT

FACULTY OF NATURAL AND ENVIRONMENTAL SCIENCES
SCHOOL OF OCEAN AND EARTH SCIENCE

Doctor of Philosophy

THE CONTINENT-OCEAN TRANSITION AT THE DEEP GALICIA MARGIN: INSIGHTS FROM WIDE-ANGLE SEISMIC DATA

by Richard Gareth Davy

Magma-poor rift margins provide the ideal environment in which to study the processes responsible for continental breakup and the transition to seafloor spreading. The Iberia-Newfoundland rifted margin in the North Atlantic Ocean has long been an archetype of such rifted margins, with previous studies of this margin having shaped the current understanding of how rifted margins evolve. The Deep Galicia margin is situated on the Iberia margin and is characterised by continental hyperextension, observed as a complex pattern of faulting, thin continental fault blocks, and the serpentinisation, with local exhumation of mantle peridotites along an interpreted detachment surface known as the S reflector. West of these features, the enigmatic Peridotite Ridge has previously been inferred to delimit the western extent of this continent-ocean transition. This thesis presents a variety of analyses applied to new wide-angle seismic data collected at the Deep Galicia margin in 2013.

Travel-time tomography modelling of a 160-km-long wide-angle seismic profile provides new insights into the transition from continental thinning to the onset of oceanic crust. West of the Peridotite Ridge, mantle exhumation is seen to continue over a short distance (< 25 km), before shallow and sparse Moho reflections indicate the earliest formation (< 122 Ma) of an anomalously thin (0.5 – 1.5 km) oceanic crustal layer. This thin oceanic crust is inferred to be underlain by serpentinised mantle peridotite, indicated by low velocity gradients and a smooth transition to mantle velocities. East of the Peridotite Ridge, a combination of travel-time tomography and time-domain full-waveform inversion were used to produce a high resolution P-wave velocity model of the hyperextended continental crust and the underlying mantle, separated by the S reflector. This model is used to interpret previously unidentified faults and crustal blocks in seismic reflection imaging, giving an increased understanding of the fine-scale patterns of deformation. Velocities below the S reflector are shown to vary between 5.5 and 8.0 km s^{-1}, corresponding to peridotite serpentinisation of 70% to 0% (unaltered), respectively. Lower seismic velocities and higher degrees of serpentinisation are coincident with the terminus of normal faulting, and is interpreted to be the result of preferential mantle hydration along such faults. Additionally, analysis of ambient noise recorded during this seismic experiment has been used to determine the phase velocity dispersion of fundamental Rayleigh waves, which were inverted to give estimates of the shear velocity within the hyperextended domain. Shear wave velocities are seen to be 0.94 ± 0.12 km s^{-1} in the sediments, 2.21 ± 0.36 km s^{-1} in the upper crust, 3.48 ± 0.36 km s^{-1} in the lower crust, and 4.25 ± 0.35 km s^{-1} in the uppermost mantle.

Table of Contents

List of Tables

List of Figures

DECLARATION OF AUTHORSHIP

I, Richard Gareth Davy, declare that this thesis and the work presented in it are my own and has been generated by me as the result of my own original research.

The Continent-Ocean transition at the Deep Galicia margin: Insights from wide-angle seismic data.

I confirm that:

1. This work was done wholly or mainly while in candidature for a research degree at this University;
2. Where any part of this thesis has previously been submitted for a degree or any other qualification at this University or any other institution, this has been clearly stated;
3. Where I have consulted the published work of others, this is always clearly attributed;
4. Where I have quoted from the work of others, the source is always given. With the exception of such quotations, this thesis is entirely my own work;
5. I have acknowledged all main sources of help;
6. Where the thesis is based on work done by myself jointly with others, I have made clear exactly what was done by others and what I have contributed myself;
7. Parts of this work has or will be published in peer-reviewed scientific journals:

    - **Chapter 3** has been published as: Davy, R., Minshull, T., Bayrakci, G., Bull, J., Klaeschen, D., Papenberg, C., Reston, T.J., Sawyer, D., and Zelt, C. (2016), Continental hyperextension, mantle exhumation, and thin oceanic crust at the continent-ocean transition, West Iberia: New insights from wide-angle seismic, *Journal of Geophysical Research: Solid Earth*. DOI: 10.1002/2016JB012825
    - **Chapter 4** has been submitted for publication in *Geophysical Journal International* with the title "Resolving the fine-scale velocity structure of continental hyperextension at the Deep Galicia margin using full-waveform inversion", and authors: Davy, R., Morgan, J., Minshull, T., Bayrakci, G., Bull, J., Klaeschen, D., Reston, T.J., Sawyer, D., Lymer, G., and Cresswell, D.
    - **Chapter 5** is to submitted for publication in the *Bulletin of the Seismological Society of America*

Signed: .....

Date: .....

Acknowledgements

I would like to start by first thanking my excellent supervisors Tim Minshull and Jon Bull, both of whom were incredibly generous with their time and expertise during my time at Southampton University. Tim, as my primary supervisor, ensured that I maintained a strong focus throughout my PhD, and provided me with an invaluable range of experiences, including the opportunity to work at Imperial College London, participate in research cruises, and present at international conferences. Jon readily provided me with feedback on my research ideas and writing, and also gave me the opportunity to teach exploration geophysics to undergraduate students. I also thank Tim and Jon for sourcing an additional four months of funding for my scholarship.

Gaye Bayrakci was integral to my research and time at Southampton University, acting as both a mentor and colleague working on the Galicia-3D project. Gaye was generous with both her time and knowledge throughout my PhD programme.

I also express great gratitude to both Joanna Morgan and Nick Harmon, who acted as quasi-supervisors for my second and third science chapters. Joanna hosted me at Imperial College London for many weeks, showing me through the application of full-waveform inversion, and provided valuable feedback on my manuscript. Nick provided me with his expertise in passive seismic techniques, and showed me a different view on seismology, guiding me through the methods of ambient noise cross-correlation and beamforming.

Galicia-3D is a large research collaboration and I give thanks to everyone involved, especially those who provided useful information and feedback on my particular research focus. In particular I would like to acknowledge Tim Reston, Dale Sawyer, Dirk Klaeschen, Cord Papenberg, and all of the MSc students, PhD students and Postdocs who have also worked on this dataset.

I would like to thank my all friends and family for their support and encouragement during this period and made this a truly enjoyable experience. In particular I'd like to thank Sam, Sam and Chris for all the sports, games and hilarious times we had while avoiding reality. And last, but not least, I would like to thank Lissette for the loving support and patience toward the end of my PhD.

Definitions and Abbreviations

2D	Two-dimensional
3D	Three-dimensional
COT	Continent-Ocean Transition
DGM	Deep Galicia margin
EGF	Empirical Green's Function
FAA	Free Air Anomaly
FWI	Full-waveform Inversion
FTAN	Frequency Time Analysis
G3D	Galicia-3D seismic experiment
IAM	Iberia Atlantic Margins group
IODP	International Ocean Drilling Programme
ISE	Iberia Seismic Experiment
MCS	Multi-Channel Seismic
mGal	Milligal
Moho	Mohorovičić discontinuity
NCF	Noise Correlation Function
OBC	Ocean Bottom Cable
OBH	Ocean Bottom Hydrophone
OBIF	Ocean Bottom Instrumentation Facility
OBS	Ocean Bottom Seismometer
OCB	Ocean-Continent Boundary
OCC	Oceanic Core Complex
OCT	Ocean-Continent Transition
Pg	Refracted seismic arrivals from the crust
PmP	Seismic reflections from the Moho
Pn	Refracted seismic arrivals from the mantle
PR	Peridotite Ridge
RMS	Root Mean square
SEGY	Society of Exploration Geophysicists digital recording standard Y
SIAP	Southern Iberia Abyssal Plain
TWT	Two Way travel-Time
WE-1	Western Extension 1
V_p	Compressional velocity
V_s	Shear velocity
ZECM	Zone of Exhumed Continental Mantle

Chapter 1: Introduction and tectonic setting

1.1 Introduction

Continental rifting leading to the onset of seafloor spreading is a fundamental process in the plate tectonic cycle and has been the focus of a geophysical studies for over four decades. Yet many questions still remain around the processes of rift initiation and magmatic style, lithospheric thinning and deformation, and the eventual onset of seafloor spreading and accretion of ocean crust.

Early models of rifting suggested that the continental lithosphere responded to far-field extensional forces by stretching and thinning via mechanisms of pure, simple shear, or a combination of both (Figure 1-1) [*McKenzie*, 1978; *Le Pichon and Sibuet*, 1981; *Wernicke*, 1981; *Lister et al.*, 1986]. The initial pure shear model, proposed by *McKenzie* [1978], assumes a constant stretching throughout the continental lithosphere (Figure 1-1A). In the brittle upper lithosphere this stretching is accommodated by normal faulting, forming large rotated continental blocks and graben structures, while the ductile lower lithosphere stretches and thins. Pure shear models were used to explain lithospheric thinning and subsidence, but are inconsistent with the observations of asymmetric rift systems and the presence of major low angle faulting (e.g. the Basin and Range Province). Models of rifting via simple shear were suggested in order to account for these observations [e.g., *Wernicke*, 1981; 1985]. These models proposed that large low angle (< 30^{o}) shear zones or detachment faults cut through the entire lithosphere, with continuing extension focused onto these surfaces (Figure 1-1B). While simple shear models produce asymmetric rift systems, they conflict with some studies of active faulting which show that movement along such faults does not occur below ~30^{o} [*Anderson*, 1951; *Jackson*, 1987]. Composite rift models postulated that rifting occurred with components of both pure and simple shear. In these models the brittle upper crust deforms through processes of simple shear, while the ductile lower crust stretches by pure shear [*Lister et al.*, 1986; *Lister and Davis*, 1989].

These classic rift models were primarily based on observations of terrestrial continental rifts or rift basins within the proximal margin. Extending these models to the point of continental breakup resulted in simplistic patterns of deformation and the direct

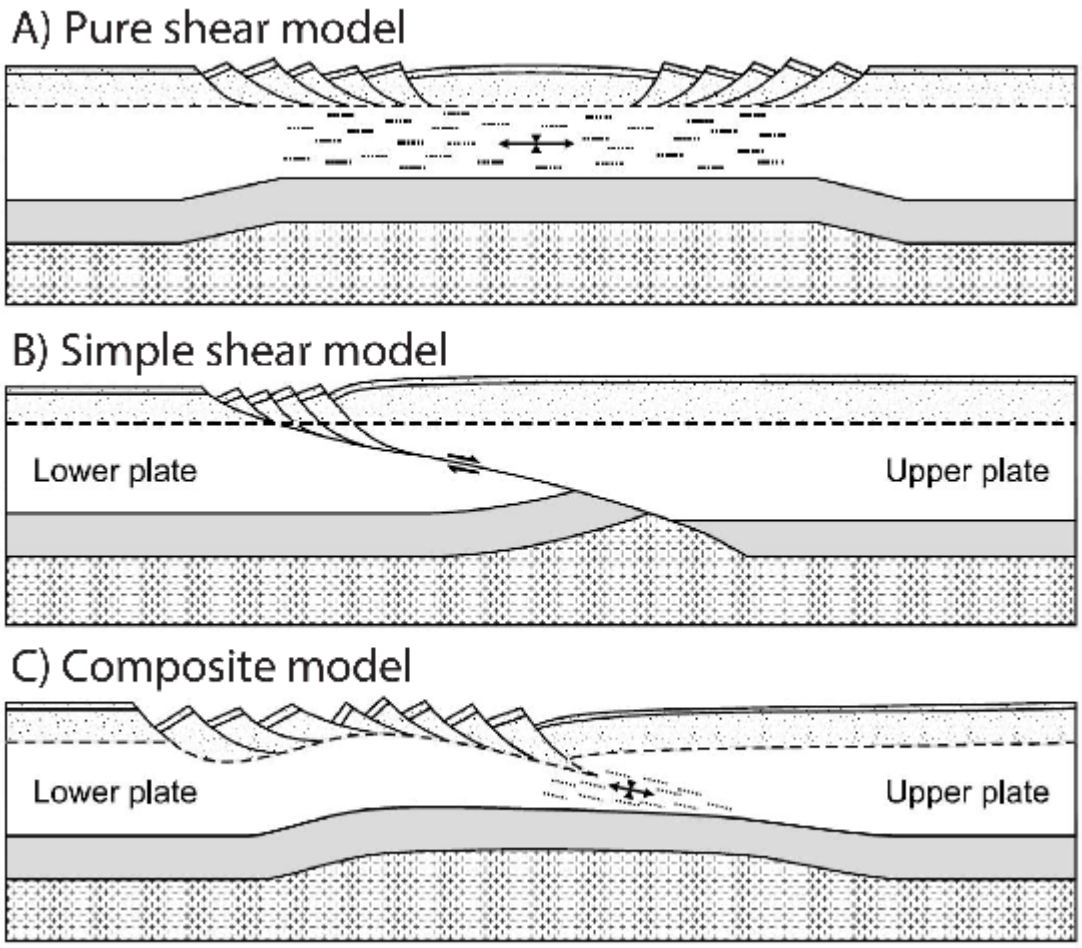

Figure 1-1: Classic rift models were based on mechanisms of A) pure shear, B) simple shear, or C) a combination of both. From Dean [1999], after Lister et al. [1986] and Lister and Davis [1989].

juxtaposition of continental and oceanic crust. Such results are incompatible with modern observations within the distal zones of continental rift margins, where there often exists wide transition zones between the continental and oceanic crust, containing complex deformation patterns and lithologies.

1.2 Rift structure

The rifted transition between continental crust of full thickness and unambiguous oceanic crust has several domains with distinct structural characteristics. All rifted continental margins share first order structural similarities within these distinct domains [*Peron-Pinvidic et al.*, 2013]. The proximal domain lies oceanward of unextended continental crust, and has been stretched by low degrees of extension. This extension is accommodated by high-angle normal faulting, which form graben and half graben basins, filled with syn-tectonic sedimentary wedges. Normal faulting within the proximal domain terminates at mid-crustal depths, as the brittle upper crust is decoupled from the ductile lower crust

[*Weinberg et al.*, 2007; *Sutra and Manatschal*, 2012]. Seaward of the proximal domain the continental crust transitions to what is termed the necking domain, which is usually characterised by a rapid decrease in the crustal thickness from ~30 km to less than 10 km [*Péron-Pinvidic and Manatschal*, 2009; *Mohn et al.*, 2010]. This is seen as the convergence of the top of basement and the seismic Moho. At the seaward limit of the necking domain the continental crust becomes fully brittle, coupling the upper and lower crust and enabling normal faults to cut through to the underlying mantle [*Pérez-Gussinyé and Reston*, 2001]. This leads into the domain commonly referred to as the continent-ocean transition (COT), or alternatively the ocean-continent transition (OCT), a zone separating unequivocal continental crust and unambiguous oceanic crust [*Whitmarsh and Miles*, 1995; *Minshull*, 2009]. It is also commonly referred to as the hyperextended domain, or distal domain, where continental crust is thinned to less than 10 km, is fully brittle and completely cut by faulting [*Pérez-Gussinyé and Reston*, 2001]. Depending on the rift setting and lithospheric composition, the COT can contain blocks of upper and lower continental crust, detachment faults, exhumed and serpentinised continental mantle, and intrusive and/or extrusive magmatic materials [e.g., *Mutter*, 1985; *Beslier et al.*, 1993; *Dean et al.*, 2000]. The boundary between the COT and the onset of oceanic crust is often termed the continent-ocean boundary (COB). However, this boundary can often be difficult to define as the onset of oceanic crustal accretion can be a diffuse phenomenon.

Despite the similarities shared by all continental rift margins, there is also significant variability within their structure and the processes responsible for their formation. These differences have broadly been categorised into two distinct end members; magma-rich and magma-poor margins [*Mutter*, 1993; *Sawyer et al.*, 2007; *Reston*, 2009b].

1.2.1 Magma-rich margins

Magma-rich margins comprise the majority of the rifted continental margins globally, with some authors suggesting they make up to 90% of all rifted margins (Figure 1-2) [*Skogseid*, 2001; *Menzies et al.*, 2002]. Magma-rich rift margins are typically characterised by two distinct features, the first of which is the presence of thick wedges of layered subaerial lava/basalt flows, which are seen in seismic reflection imaging as seaward dipping reflectors (SDRs) (Figure 1-3) [*Hinz*, 1981; *Mutter et al.*, 1982]. Crustal thinning at magma-rich margins occurs over relatively short distances (< 100 km) and produces an abrupt COT

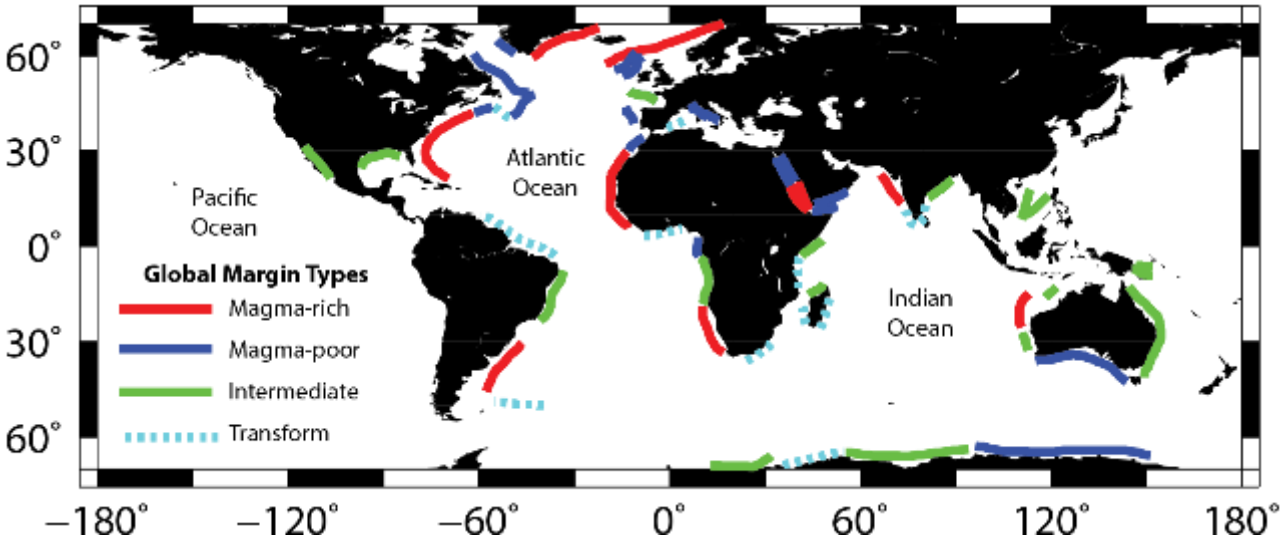

Figure 1-2: Map of global continental rift margins and their magmatic mode. Margins are classified as either magma-rich (red), magma-poor (blue) or intermediate (green). Modified from Reston [2009b].

which is marked by such SDR packages, which can extend up to 200 km in width. Various models and interpretations place the COT at the landward edge, the centre of, or the seaward edge of these SDRs [*Franke*, 2013]. The second primary characteristic of magma-rich rift margins is the presence of high-velocity bodies (V_p > 7.3 km s^{-1}) in the lower crust, confined to a narrow zone (~50 km) seaward of the rifted continent [*White et al.*, 2008]. The origin of these high-velocity bodies is still debated, with authors suggesting that these could be mafic intrusions, magmatic underplating, or in some cases partially serpentinised mantle peridotites [*Skogseid et al.*, 2000; *Ebinger and Casey*, 2001; *Lundin and Doré*, 2011]. At magma-rich rift margins continental breakup occurs with the rupture of the lithospheric mantle before, or at the same time as, the rupture of the continental crust [*Franke*, 2013].

Magma-rich rift margins produce large amounts of magma in relatively short periods of time (e.g., 10 million km^3 in 2-3 m.y. in the northern North Atlantic Ocean) [*White et al.*, 1992]. The exact processes responsible for the generation of these magmas is still a focus of research, however it is generally accepted that extension of the continental lithosphere leads to the passive upwelling of asthenospheric mantle, which undergoes adiabatic decompression melting to produce voluminous magma [*White and McKenzie*, 1989]. Localisation of the lithospheric thinning leads to the focusing of these melt materials into the region of continental breakup [*Armitage et al.*, 2010]. Numerical models have shown that anomalously hot mantle temperatures will result in larger amounts of magma being produced, with some suggesting that mantle plumes have provided these elevated

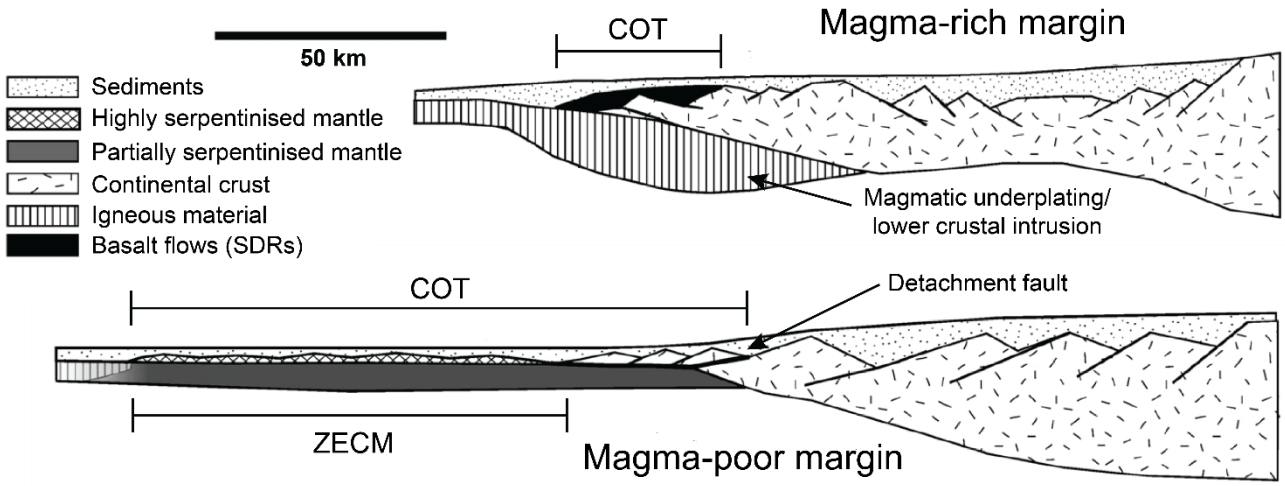

Figure 1-3: Schematic diagrams of magma-rich and magma poor continental rift margins. These two continental margin end members exhibit clear structural differences. Modified from Reston [2009b].

temperatures in certain regions [*White and McKenzie*, 1989; *Holbrook et al.*, 2001]. It is also evident that the duration of rifting plays a role in the production of magmatic material. Longer duration allows the mantle to conductively cool, which results in lower levels of decompression melting [*Pedersen and Ro*, 1992]. Initial mantle composition and temperature, inherited structure and the rate of lithosphere extension all play a crucial role in the magma generation, and ultimately controls the whether a margin is magma-rich or magma-poor [*Bassi*, 1995].

1.2.2 Magma-poor margins

All magma-poor margins are primarily characterised by the relative absence of magmatism during the rifting leading to continental breakup. These margins also express other common characteristics including the presence of highly thinned continental crust, asymmetry in the rift structure between the conjugate margins, detachment faulting, the exhumation and serpentinisation of the subcontinental mantle, and the onset of thin oceanic crust [*Reston et al.*, 1996; *Dean et al.*, 2000; *Whitmarsh et al.*, 2001a]. While these features are typical of magma-poor margins, they are not necessarily found at all such margins.

Extreme thinning of the continental crust from its initial thickness to only a few kilometres, or less, typically occurs over large distances, often in excess of 100-200 km [*Dean et al.*, 2000; *Reston*, 2009b]. Through the necking domain the continental crust thins to less than 10 km, becoming hyperextended, coupling the upper and lower crust. Without the presence of significant magmatic processes to catalyse continental breakup, the

continental crust continues to extend and thin. Normal faulting cuts through the thinned continental crust to the upper mantle, enabling the hydration of the upper mantle [*Pérez-Gussinyé and Reston*, 2001]. Hydration of mantle peridotite results in the formation of serpentinite, which is an inherently weak material, with a low coefficient of friction and high pore pressures [*Pérez-Gussinyé and Reston*, 2001]. Continued extension within this hyperextended domain is accommodated in this layer of serpentinite, forming a detachment surface, which can be active to low angles (< 20^{o}) (e.g., the S reflector at the Deep Galicia margin) [*Reston et al.*, 1996]. Such detachment faults result in first order asymmetry between the conjugate margins, with one margin exhibiting an abrupt end to continental thinning while the other possesses the domain of hyperextended continental crust [e.g., *Wernicke*, 1985; *Hopper et al.*, 2004]. Without the sufficient generation of magmatic melts for the onset of seafloor spreading, continued extension leads to the breakup of the continental crust, unroofing the continental mantle, and forming transition zones of exhumed continental mantle (ZECMs) [*Brun and Beslier*, 1996; *Pickup et al.*, 1996]. Within these zones, mantle peridotite is serpentinised in a gradational fashion, decreasing with depth. This is seen in velocity analysis as an increase in P-wave velocities from ~4.5-5.0 km s^{-1} at the top of reflective basement, to > 7.0 km s^{-1} 2-4 km below, reaching mantle velocities (> 7.8 km s^{-1}) 5-6 km below top basement [*Minshull*, 2009]. This gradational increase in seismic velocity results in an absence of Moho reflections within this transitional domain. ZECMs greatly range in width, with some only 10's of km wide, while others exceed 100 km; some authors suggest that magma-poor margins with wider regions of thinned continental crust possess narrower ZECMs and vice versa [*Dean et al.*, 2000]. These transition zones give way to the onset of oceanic crust, which is often atypically thin [e.g., *Whitmarsh et al.*, 1996; *Funck et al.*, 2003]. This thin crust is the result of conductive cooling of the mantle during the long pre-break-up stretching phase, resulting in lower melt generation [*Whitmarsh et al.*, 2001b].

While these two end members of passive continental rifting have been described, it should be noted that it is unlikely that either end member is completely devoid of the characteristics of the other. For example some magma-poor margins exhibit evidence of magmatic intrusion within the COT (e.g., the southern Iberia Abyssal Plain), while evidence of highly thinned continental crust and mantle serpentinisation have been observed at magma-rich margins (e.g., the Møre margin) [*Russell and Whitmarsh*, 2003; *Osmundsen and Ebbing*, 2008; *Lundin and Doré*, 2011]. The range of rifted margins which exist can be

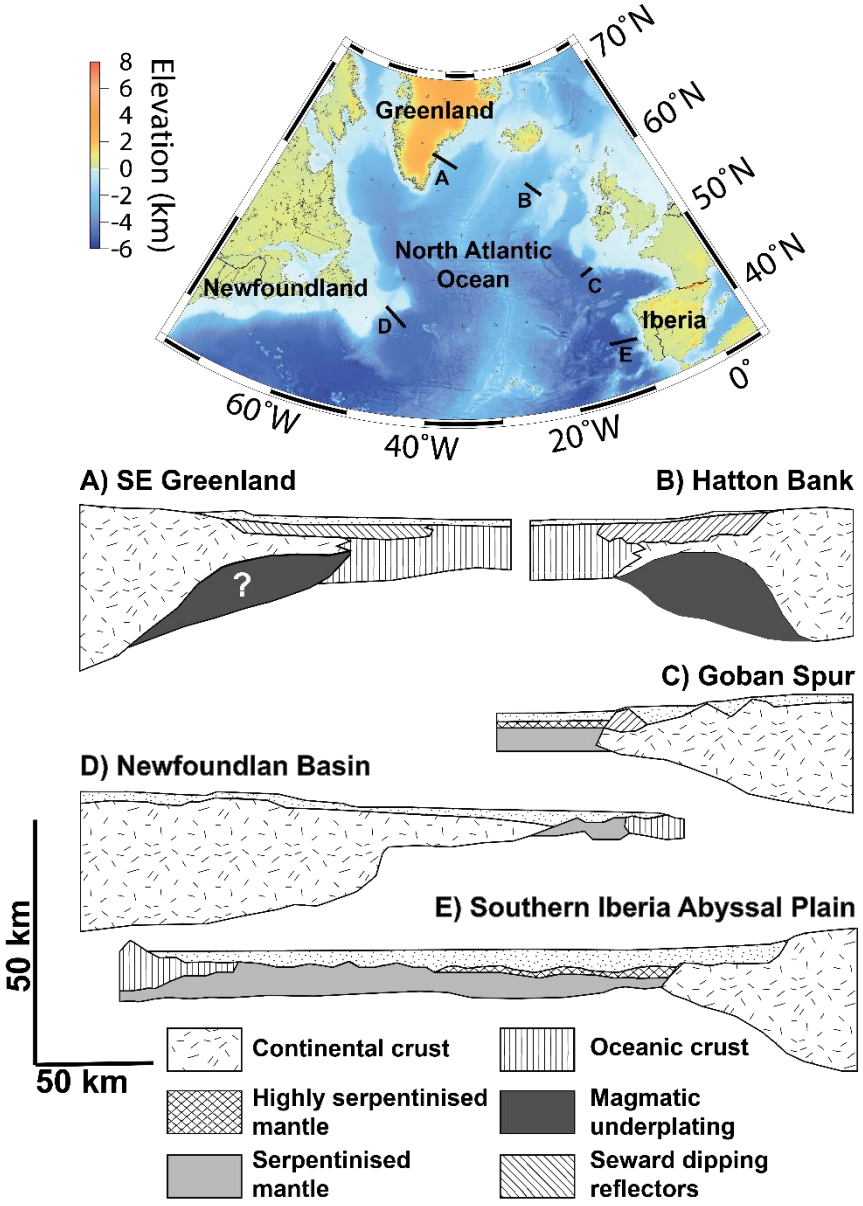

Figure 1-4: North Atlantic Ocean rift margins. Schematic diagrams of rift margins at A) SE Greenland [Hopper et al., 2003], B) Hatton Bank [White and Smith, 2009], C) Goban Spur [Bullock and Minshull, 2005], D) Newfoundland Basin [Dean et al., 2000; Van Avendonk et al., 2006], E) Southern Iberia Abyssal Plain [Dean et al., 2000].

considered a continuum between these two end members, with some margins displaying characteristics of both end members of rifting (e.g., the Woodlark Basin) and can be termed intermediate margins (Figure 1-2) [*Reston*, 2009b].

1.3 North Atlantic Rifting

Rifted continental margins surrounding the North Atlantic Ocean cover the full spectrum of magmatic types. The opening of the North Atlantic Ocean progressed from south to north, beginning with magma-poor rifting between the Iberia and Newfoundland margin in

the late Triassic–early Jurassic period (~200 Ma), culminating in continental lithosphere breakup in the late Aptian-early Albian (~113 Ma) (ages use timescale of *Gradstein et al.* [2012], unless stated otherwise) [*Tucholke et al.*, 2007]. The southern margins of the North Atlantic are characterised by asymmetric rift geometries, extreme thinning of the continental crust, crustal detachment faults, the exhumation and serpentinisation of mantle peridotites over large areas, and the eventual onset of anomalously thin oceanic crust (e.g., the Newfoundland and Iberia conjugate margin, Figure 1-4D and E) [*Dean et al.*, 2000; *Van Avendonk et al.*, 2006; *Reston*, 2009b]. As rifting progressed northward it was occasionally accompanied by low levels of syn-rift magmatism, which typically manifested as subaerial basalt flows at the oceanward extent of thinned continental crust (e.g., the Goban Spur, Figure 1-4C) [*Bullock and Minshull*, 2005]. These intermediate margins still possess COTs with regions of exhumed and serpentinised mantle, before the onset of thin oceanic crust. Rifting at high latitudes in the NE North Atlantic is believed to have been driven by the influence of the Icelandic Plume, resulting in voluminous melt generation and magma-rich rifting beginning around 70 Ma [*Mjelde et al.*, 2008]. Magma-rich margins in the NE North Atlantic are characterised by a relative symmetry between conjugate margins, abrupt thinning of the continental crust with the oceanward juxtaposition of thick oceanic crust, large regions of subaerial basalts flows (SDRs), and high-velocity zones below the thinned continental crust, believed to be magmatic underplating (e.g., the SE Greenland and Hatton Bank conjugate margin, Figure 1-4A and B) [*Hopper et al.*, 2003; *White and Smith*, 2009].

1.4 Iberia-Newfoundland rift system

Numerous geophysical studies and International Ocean Drilling Project (IODP) missions at the Iberia rift margin, and the conjugate Newfoundland margin, have made it the most studied magma-poor margin in the world, and an archetype for understanding similar systems globally. The Iberia margin can be divided into three distinct segments from north to south: the Deep Galicia margin (DGM), the Southern Iberia Abyssal Plain (SIAP), and the Tagus Abyssal Plain (TAP) (Figure 1-5). This thesis focusses on the structure and processes at the DGM, however there will often be comparisons to the SIAP, and the conjugate Flemish Cap margin, the direct conjugate to the DGM on the Newfoundland margin.

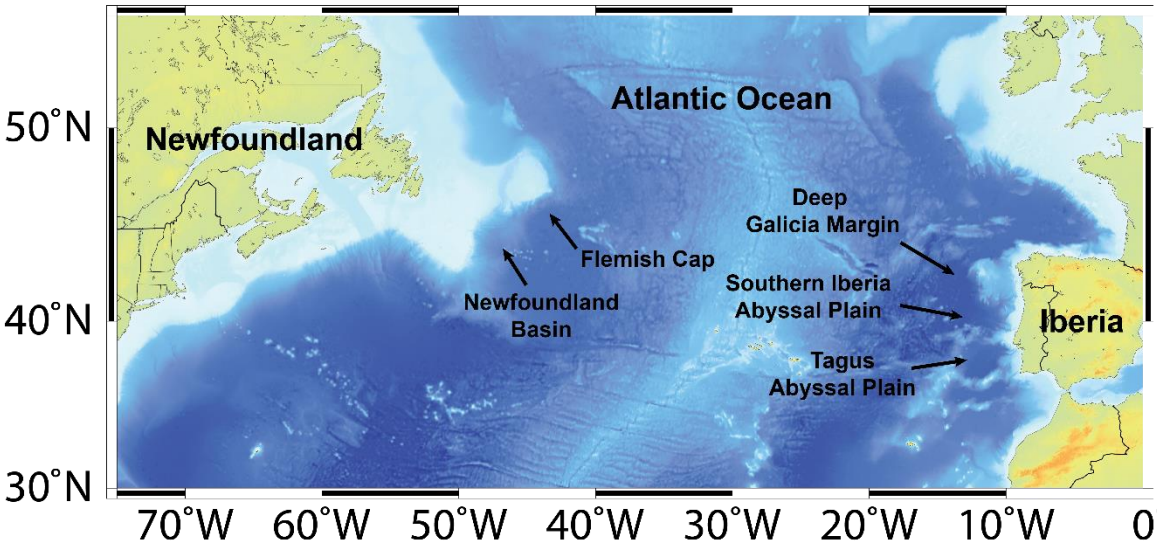

Figure 1-5: Map of the Iberia-Newfoundland rift margin and regions of interest. This study focuses on the Deep Galicia margin (DGM), on the Iberia margin.

1.4.1 Formation and present day architecture

The Iberia – Newfoundland ultra-slow rift system was active during the early stages of the opening of the North Atlantic Ocean. The first significant phase of rifting at this margin initiated during the Late Triassic - Early Jurassic (~200 Ma) [*Pérez-Gussinyé et al.*, 2003; *Tucholke et al.*, 2007; *Mohn et al.*, 2015]. This initial period of rifting saw the formation of fault-bound continental rift basins on the proximal margins of the rift system (e.g. Lusitanian, Porto and Galicia Interior basins) [*Murillas et al.*, 1990; *Péron-Pinvidic et al.*, 2007; *Tucholke et al.*, 2007]. The second phase of significant rifting initiated in the Late Jurassic - Early Cretaceous (~145 Ma), and saw the continued extension and thinning of the continental lithosphere. This deformation shifted from a broad region, and became focused in the distal margins, where the continental crust eventually thinned to < 10 km in thickness and ruptured in the Early-Mid Cretaceous (> 122 Ma), subsequently followed by breakup of the continental lithosphere (~113 Ma) [*Tucholke et al.*, 2007; *Reston*, 2009b; *Mohn et al.*, 2015].

Rifting at the Deep Galicia margin (Figure 1-5) has resulted in the extreme thinning of the continental crust over distances of 100 – 200km. Unaltered crust landward of the proximal rift margin is ~30 km thick and has been thinned through a complex pattern of faulting to only a few km at the distal limits of the margin [*Zelt et al.*, 2003; *Reston*, 2009b]. Initial extensional deformation is inferred to have occurred as high-angle normal faulting, which formed large fault-bound blocks between 10 and 20 km wide, thinning the crust to between

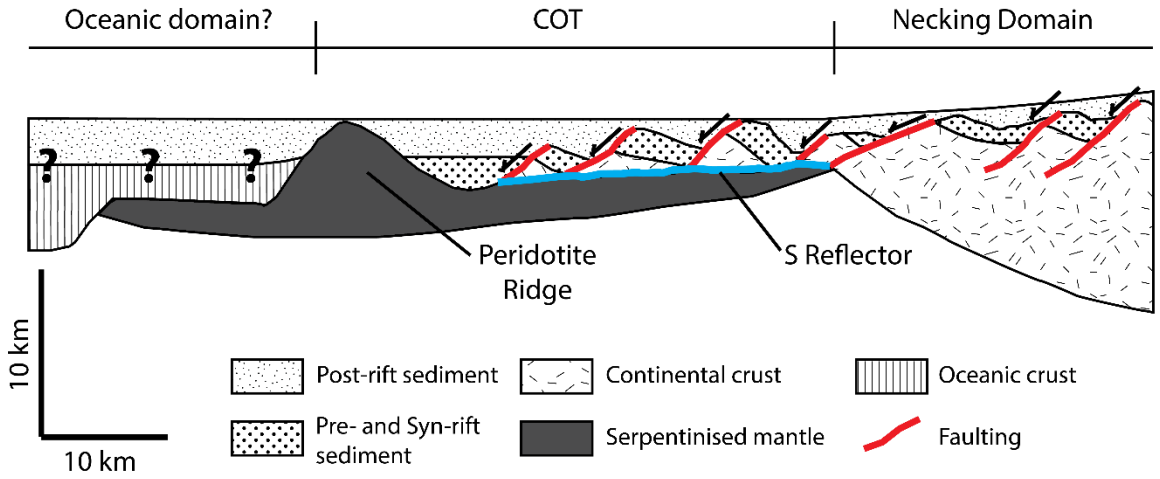

Figure 1-6: Schematic diagram of the Deep Galicia margin. Schematic based on the velocity model of Whitmarsh et al. [1996] and Zelt et al. [2003], and seismic reflection images of Reston et al. [2007].

20 and 30 km thick [*Ranero and Pérez-Gussinyé*, 2010]. With continued extension of the margin, these continental fault blocks rotated to low-angles, at which point their bounding faults locked up [*Ranero and Pérez-Gussinyé*, 2010]. The faulting mechanism responsible for how continued extension was accommodated still remains controversial, and is discussed in more detail in **1.4.4**.

As the margin extended and thinned at an ultra-slow rate (< 10 mm/yr half spreading rate), it allowed time for the entire crust to cool conductively, resulting in the normally ductile mid and lower crust becoming progressively embrittled [*Srivastava et al.*, 2000; *Pérez-Gussinyé and Reston*, 2001; *Pérez-Gussinyé et al.*, 2003]. Once the crustal thicknesses reached < 10 km, the entire crust became brittle and coupled (hyperextended). This process enabled listric normal faults to form through the entire crust, from the seafloor to the underlying mantle (Figure 1-6) [*Pérez-Gussinyé and Reston*, 2001; *Pérez-Gussinyé et al.*, 2003; *Pérez-Gussinyé*, 2013]. These faults acted as conduits, delivering seawater to the upper mantle and forming a layer of serpentinised mantle [*Pérez-Gussinyé and Reston*, 2001; *Reston et al.*, 2007; *Bayrakci et al.*, 2016]. With continued extension these faults soled out into this structurally weak layer, forming a large and low angle (< 20^{o}) detachment fault, known as the S reflector (Figure 1-6), which also corresponds to the crust-mantle boundary in the distal margin [*Reston et al.*, 2007]. It has been shown recently that these faults, which sole into the S reflector, preferentially hydrate the upper mantle which results in varying degrees of mantle serpentinisation, observed as a pattern of high and low P-wave velocities [*Bayrakci et al.*, 2016].

In the final stages of rifting serpentinised mantle was exhumed to the seafloor along the S reflector, and was also emplaced west of this hyperextended domain, forming a structure known as the Peridotite Ridge (Figure 1-6) [*Beslier et al.*, 1993]. Continental breakup occurred somewhere west of the Peridotite Ridge, leaving it and the hyperextended domain on the Galicia margin, and a more abrupt structure of continental thinning on the conjugate Flemish Cap margin [*Funck et al.*, 2003; *Hopper et al.*, 2006]. The basement structure west of the Peridotite Ridge remains unclear, with early studies suggesting the immediate onset of thin oceanic crust (2-3 km), underlain by serpentinised mantle, before transitioning to oceanic crust of normal thickness (7 km) some 20 km oceanward [*Whitmarsh et al.*, 1996]. However, recent studies have suggested that this basement may be comprised of exhumed mantle, similar to the ZECM and peridotite ridge province seen in the SIAP [*Dean et al.*, 2015]

1.4.2 Previous seismic studies and basement sampling

Much of what we currently understand about the structure and tectonic processes at the Deep Galicia margin has been observed from seismic studies conducted over the past four decades (Figure 1-7). Early studies included multichannel seismic profiles by the Institut Francais du Petrole (IFP) in 1975 and 1980 (GP profiles), which revealed tilted and thinned continental fault blocks, syn- and post-rift sedimentary units, and a prominent reflector, which we now know as the S reflector, which represents a west dipping detachment fault within the hyperextended domain [*De Charpal*, 1978; *Mauffret and Montadert*, 1987; *Boillot and Winterer*, 1988; *Reston et al.*, 1996]. These studies also revealed the presence of the north-south trending ridge of serpentinised mantle peridotite, known as the Peridotite Ridge, which was confirmed by seafloor dredging and ODP drilling (ODP site 637) [*Boillot et al.*, 1980; *Boillot et al.*, 1987; *Shipboard Scientific Party*, 1987]. Early seismic reflection interpretations proposed that this ridge marked the oceanward extent of the COT, with oceanic crust emplaced directly westward [*Sibuet et al.*, 1987].

Seismic refraction surveying, coincident with these GP profiles, enabled the modelling of the seismic velocities of features within the COT [*Whitmarsh et al.*, 1996]. It was shown that over a distance of 100 km the continental crust thinned from 17 km at the continental slope, to 2 km at the termination of continental crust. Modelled compressional velocities within this continental crust steadily increase from 2.0 - 7 km s^{-1}, typical of similar rifted

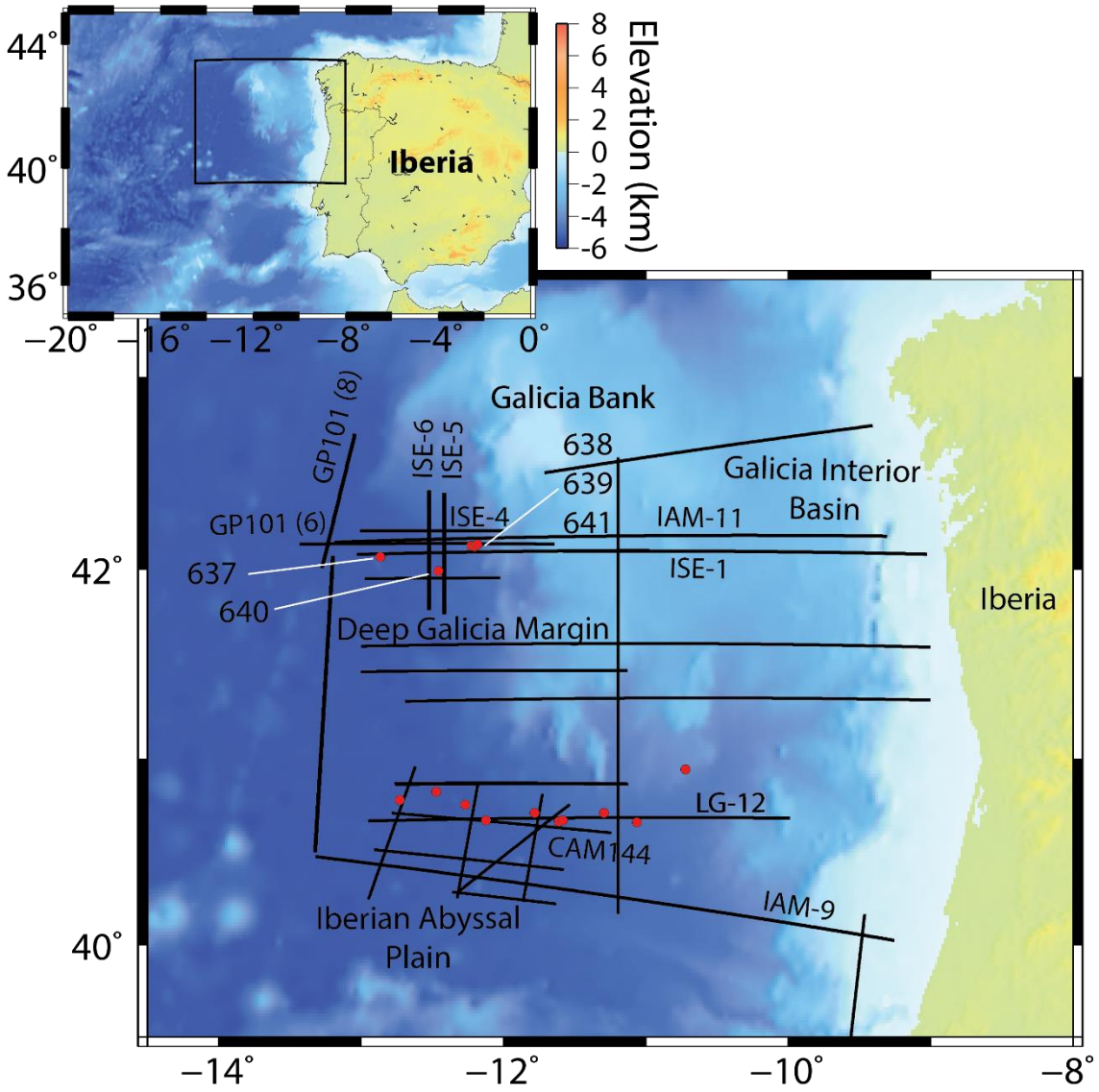

Figure 1-7: Existing seismic reflection studies of the West Iberia margin. Subsets of previous seismic experiments are displayed as black lines in order to illustrate the existing coverage. GP [Beslier et al., 1993], ISE [Sawyer et al., 1997], CAM [Minshull et al., 1998], LG [Beslier et al., 1993], and IAM [Pickup et al., 1996; Dean et al., 2000].ODP Leg 103, 149 and 173 drill sites are indicated by red circles.

margins. Seismic velocities of 7.0 km s^{-1} were also modelled directly below the S reflector, with no jump in seismic velocities across this boundary. Below the S reflector velocities gradually increase to normal mantle velocities (~8.0 km s^{-1}) approximately 5 km below the detachment surface, which we know now to be consistent with decreasing serpentinisation. Velocities within the Peridotite Ridge increase from 3.5 km s^{-1} at the top to 6.9 km s^{-1} 4 km below, again consistent with decreasing levels of serpentinisation. Thin oceanic crust (2.5-3.5 km thick) was modelled directly west of the Peridotite Ridge (GP101 velocity profile, Figure 1-8), increasing to full thickness oceanic crust 20 km further west [*Whitmarsh et al.*, 1996]. We note that the velocity model in this interpreted oceanic

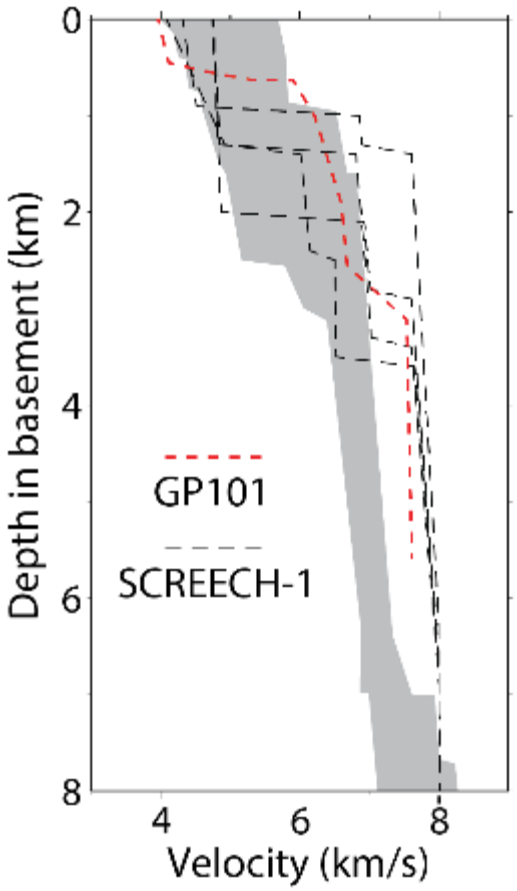

Figure 1-8: Seismic velocity profiles through thin oceanic cruston conjugate DGM and Flemish Cap margins, compared with the enveloped for Atlantic oceanic crust aged 59-170 Ma (grey shading) [White et al., 1992]. GP101 velocities on DGM margin are from Whitmarsh et al. [1996]; SCREECH-1 velocities are from Funck et al. [2003].

domain is constrained only by three ocean bottom seismometers, in a margin parallel configuration, with only one instrument exhibiting PmP arrivals.

More recently, the Iberia Seismic Experiment (ISE) provided a suite of margin normal and parallel seismic reflection and refraction profiles, covering the central and southern Galicia Bank and deep margin [*Sawyer et al.*, 1997]. Seismic pre-stack depth migration images and subsidence modelling of the margin normal lines revealed that the region of exhumed and serpentinised mantle within the COT increases in width, south of the Deep Galicia margin [*Henning et al.*, 2004]. Higher fidelity seismic reflection imaging allowed detailed investigations of the S reflector (Figure 1-9). Analysis of syn-rift sedimentary units, above the thinned rotated continental fault blocks, indicate that the S reflector is a rooted detachment fault active at low angles (< 20^{o}) [*Reston et al.*, 2007]. Of particular interest is the ISE-1 seismic profile, which provides the most complete coverage of Galicia rift margin, documenting the bulk thinning of the continental crustal from the proximal margin to just west of the Peridotite Ridge [*Zelt et al.*, 2003]. Unfortunately the ISE-1 profile did not

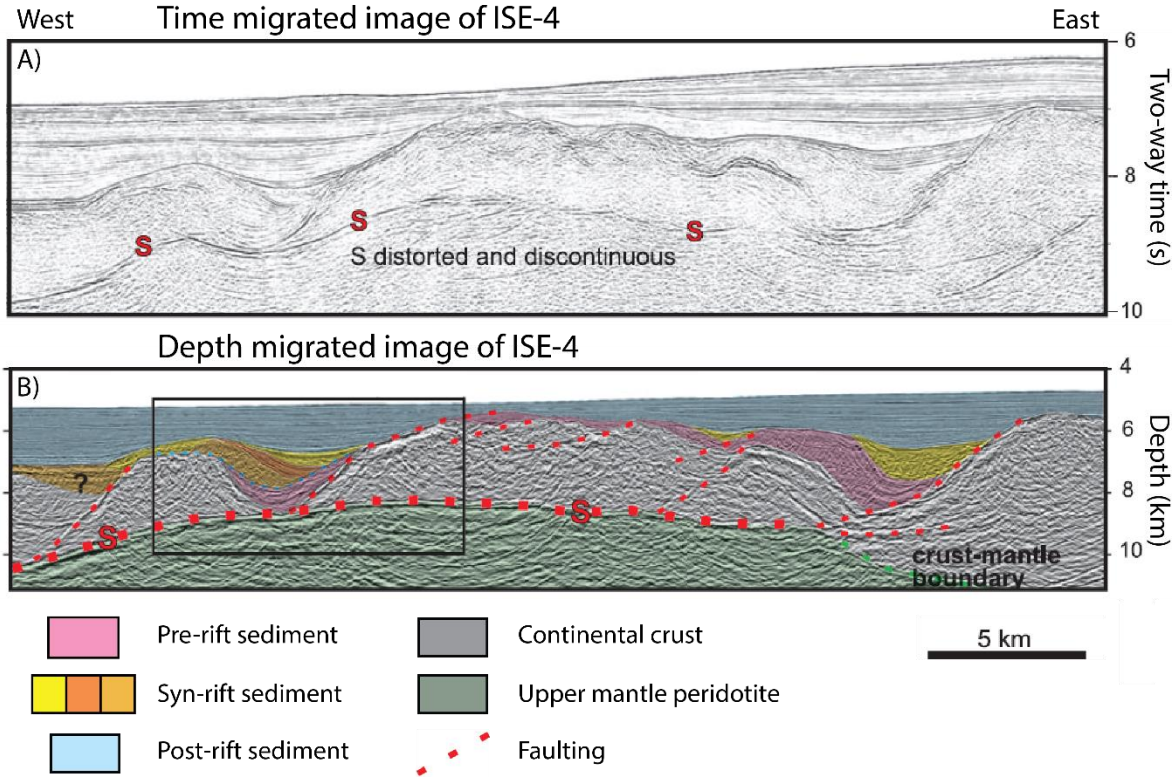

Figure 1-9: S reflector along ISE-4 at the Deep Galicia margin.A) Time migrated seismic image with S reflector indicated by red S characters. B) Interpreted depth migrated seismic image showing pre-, syn- and post-rifting sedimentary deposits. Modified from Reston et al. [2007].

extend far enough oceanward to identify oceanic crust of full thickness, leaving the western extent of the COT undetermined. This thesis will look to resolve the nature of basement at the oceanward extent of the DGM. Seismic travel-time velocity models and full-waveform inversion of the ISE seismic data reveal lower crustal velocities of ~5.5 km s^{-1} above the S reflector, with a marked increase to ~6.5-7.0 km s^{-1} directly below the S reflector, gradually increasing to mantle velocities [*Zelt et al.*, 2003; *Leythaeuser et al.*, 2005]. These velocity results confirm the suggestions that the S reflector represents the juxtaposition of lower continental crust and serpentinised upper mantle.

Other notable seismic surveys of the West Iberia margin include the Lusigal survey (LG) [*Beslier et al.*, 1993], Iberian Atlantic Margins (IAM) [*Banda and Torne*, 1995], and the CAM seismic profiles [*Minshull et al.*, 1998; *Péron-Pinvidic et al.*, 2007]. IAM-9, in the SIAP south of the DGM, is the only profile along which the velocity structure of typical, full thickness oceanic crust has unambiguously been identified, making this the only seismic transect on the West Iberia margin which encompasses the full breadth of the COT [*Dean et al.*, 2000]. A ~170 km wide ZECM is observed along IAM-9, which possesses an upper layer which is 2 – 4 km thick with velocities between 4.5 – 7.0 km/s and a high-velocity-gradient (1 s^{-1}),

and a lower layer up to 4 km thick with velocities increasing to 7.6 km/s and has a low-velocity-gradient [*Dean et al.*, 2000; *Minshull et al.*, 2014]. Several overlapping peridotite ridges are identified within the ZECM, similar to that seen at the DGM, and have been sampled by submersible and drilling at ODP site 897 and 1070, returning peridotite and serpentinised peridotite [*Whitmarsh et al.*, 2001a; *Minshull et al.*, 2014]. These ridges roughly bound the oceanward limit of the COT, with oceanic crust 6.5 – 7.0 km thick observed 10 – 20 km westward.

The conjugate Newfoundland margin has been well characterised by the Study of Continental Rifting and Extension on Eastern Canadian Shelf (SCREECH) survey, which comprises three margin normal seismic reflection and refraction profiles at the South and North Newfoundland Basin, and the Flemish Cap [*Funck et al.*, 2003; *Hopper et al.*, 2004; *Van Avendonk et al.*, 2006]. The structure of the Flemish Cap margin, the direct conjugate to the DGM, has been documented by SCREECH-1. At this margin there is an abrupt thinning of the continental crust, from 30 km to 3 km over a distance of 80 km, which starkly contrasts the wide zone of continental thinning at the DGM [*Hopper et al.*, 2006]. Original interpretations of the seismic profile placed thin oceanic crust (3-4 km) directly oceanward of the continental crust, underlain by serpentinised mantle, before becoming even thinner (< 1.3 km) further oceanward, with little evidence of a wide ZECM (SCREECH-1 velocity profiles, Figure 1-8) [*Funck et al.*, 2003; *Hopper et al.*, 2004]. This thin oceanic crust extends 55 km before the onset of full thickness oceanic crust. However, this thin oceanic crust has recently been reinterpreted as tectonised serpentinised mantle, with the previously interpreted mantle reflections argued to have originated from a serpentinisation front [*Gillard et al.*, 2016]. The latter interpretation implies that there is an 80 km wide ZECM preceding the onset of normal oceanic crust.

The basement of the DGM has been sampled by ODP leg 103 (Figure 1-7) [*Boillot et al.*, 1987; *Boillot and Winterer*, 1988]. Sites 638, 639 and 641 were drilled into a well-defined tilted block within the necking domain and recovered pre-rift / early rift onset Upper Jurassic and Lower Cretaceous limestone, deposited in shallow marine environments [*Sibuet*, 1992]. Above this, Valanginian–Hauterivian deep water syn-rift sandstones were recovered, covered by a syn-rift Aptian–Barremian sediment unit [*Boillot and Winterer*, 1988]. These syn-rift units are covered by Tertiary-Aptian post-rift sediments. This stratigraphic record indicates that the duration of rifting was ~25 M.y [*Reston*, 2005].

Site 637, drilled on the Peridotite Ridge, returned peridotite and serpentinised mantle peridotite, and was the first time serpentinised mantle was sampled by drilling within a rift COT.

The SIAP and Newfoundland margins have also been sampled by ODP legs 149, 173 and 210, at positions determined to be conjugate to one another, and both documented by seismic reflection and refraction surveying [*Shipboard Scientific Party ODP Leg 149*, 1993; *Shipboard Scientific Party ODP Leg 173*, 1998; *Tucholke and Sibuet*, 2007]. Drilling within the COT at both margins recovered serpentinised peridotite and minor amounts of basalt, indicating that the exhumation of subcontinental mantle occurs on both margins preceding lithospheric breakup [*Dean et al.*, 2000; *Shillington et al.*, 2006; *Van Avendonk et al.*, 2006].

1.4.3 Magnetic anomalies and timing of continental breakup

Magnetic field reversals (isochrons) recorded in newly formed oceanic crust are often used to identify the timing of continental breakup and the onset and rate of seafloor spreading. However, there are two prominent issues in using this method at the Iberia-Newfoundland margin. The first issue is that the continental breakup and first onset of oceanic crust may have occurred during the Cretaceous constant polarity interval (121 – 83 Ma), resulting in a lack of strong magnetic reversals which would enable the clear identification of oceanic crust [*Sibuet et al.*, 1995]. The second issue comes from the fact that the onset of oceanic crust is preceded by the exhumation of serpentinised mantle peridotites, which have been suggested to also record magnetic reversals, creating debate over the nature of magnetic isochrons at magma-poor margins [*Russell and Whitmarsh*, 2003; *Sibuet et al.*, 2007; *Bronner et al.*, 2011]. It would appear that magnetic anomalies recorded in exhumed and serpentinised continental mantle might enable the determination of the timing in which basement is emplaced, but does not allow for the differentiation between oceanic crust and serpentinised mantle [*Bronner et al.*, 2011].

The first clear and undisputed oceanic isochron oceanward of both the Iberia and Newfoundland margins is C34, which is approximately 280 km west of the Peridotite Ridge at the DGM, and has an age of 84 Ma (Figure 1-10) [*Bronner et al.*, 2011; *Gradstein et al.*, 2012]. However, there is a prominent magnetic anomaly present within the COT on both margins, referred to as the J anomaly (Figure 1-10). In the past this anomaly has been

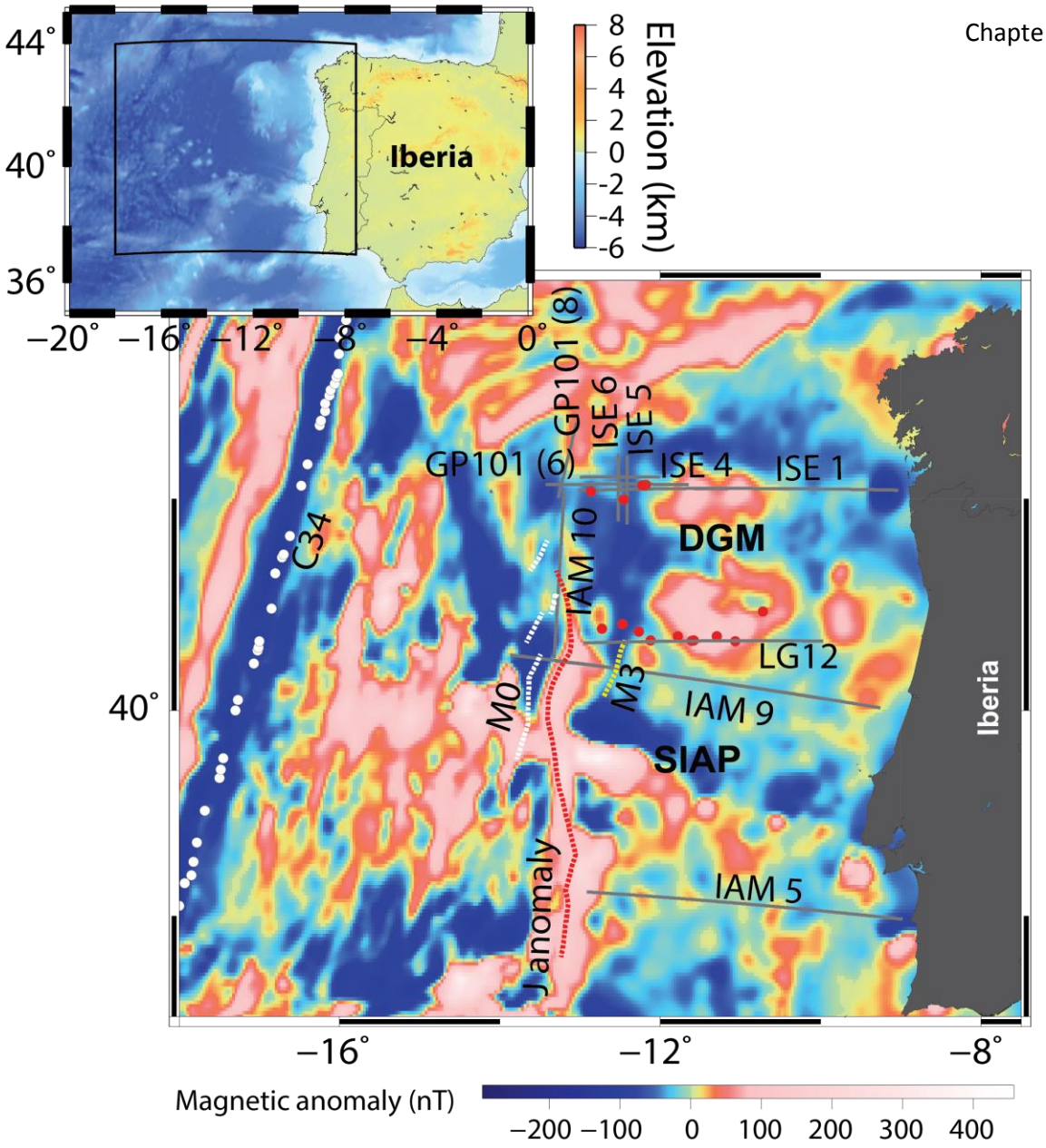

Figure 1-10: Magnetic anomaly map of the West Iberia rift margin [Maus et al., 2009]. Previous seismic experiments are illustrated by grey lines, GP [Beslier et al., 1993], ISE [Sawyer et al., 1997], LG [Beslier et al., 1993], and IAM [Pickup et al., 1996; Dean et al., 2000]. Picks of isochron C34 are shown as white circles [Klitgord and Schouten, 1986]. White dashed line represents the interpreted location of magnetic anomaly M0 [Srivastava et al., 2000], and yellow dashed line represents the interpreted location of magnetic anomaly M3 [Whitmarsh and Miles, 1995]. Red dashed lines represent the location of the interpreted J anomaly [Beslier et al., 1993]. ODP Leg 103, 149 and 173 drill sites are indicated by red circles.

interpreted as either the beginning of the M sequence of seafloor spreading anomalies (M0–M3) or alternatively as the result of a pulse of magmatism that led to continental breakup before seafloor spreading [*Sibuet et al.*, 2007; *Bronner et al.*, 2011]. The J anomaly is well defined in the southern Iberia Abyssal Plain, but rapidly decreases in amplitude north of IAM-9, and is not observed at the Deep Galicia margin. Many kinematic plate reconstructions have been performed using the magnetic anomalies of the M series or the

J anomaly itself [*Srivastava et al.*, 2000; *Bronner et al.*, 2011]. However, it has recently been shown that kinematic plate reconstructions using the J anomaly as a seafloor spreading isochron are problematic, suggesting that the anomaly was diachronus in its formation, while others have questioned whether the M series of magnetic anomalies are truly present [*Tucholke and Sibuet*, 2012; *Nirrengarten et al.*, 2017].

Srivastava et al. [2000] interprets a magnetic anomaly west of the Peridotite Ridge to be that of the M0 sea-floor spreading anomaly (126 Ma, [*Gradstein et al.*, 2012]). However, *Sibuet et al.* [1995] fit a model to the same magnetic data, showing that the topography of a highly magnetized (5 A/m), and thin oceanic crust (~1 km), recording no magnetic field reversals, can also explain the observed magnetic anomaly. *Sibuet et al.* [1995] also state that no magnetic field reversals were expected, as oceanic crust in this region formed during the Cretaceous constant polarity interval, later than the M series of seafloor spreading magnetic anomalies

At the SIAP, interpreted magnetic seafloor spreading anomalies M2 and M3 (128 – 130 Ma) are situated within the ZECM along IAM-9, while anomaly M1 (125 – 128 Ma) is recorded by the first oceanic crust (Figure 1-10) [*Gradstein et al.*, 2012; *Minshull et al.*, 2014]. At the Flemish Cap, it is proposed that M0 is recorded at the oceanward extent of exhumed serpentinised mantle / thin oceanic crust [*Srivastava et al.*, 2000; *Hopper et al.*, 2006; *Gillard et al.*, 2016]

1.4.4 Extension discrepancy and proposed mechanisms

At the Galicia margin, and many other magma-poor margins, there is a discrepancy between the total observed crustal thinning and measured brittle extension [*Sibuet*, 1992; *Davis and Kusznir*, 2004]. While pure shear models are able fit the lithospheric thinning and subsidence observed within rift basins, they predict more upper crustal extension than measured along faults imaged in seismic reflection data [*Marrett and Allmendinger*, 1992; *Kusznir and Karner*, 2007]. Estimates of crustal thinning are often derived from observations of subsidence or from wide-angle seismic models [e.g., *Sibuet*, 1992; *Zelt et al.*, 2003; *Reston and McDermott*, 2014]. Extensional deformation in the crust can be determined from the measurement of fault heaves, palinspastic restorations, or the simple geometry of faulting relative to top basement [e.g., *Davis and Kusznir*, 2004; *Reston*, 2005; *Egan and Meredith*, 2007].

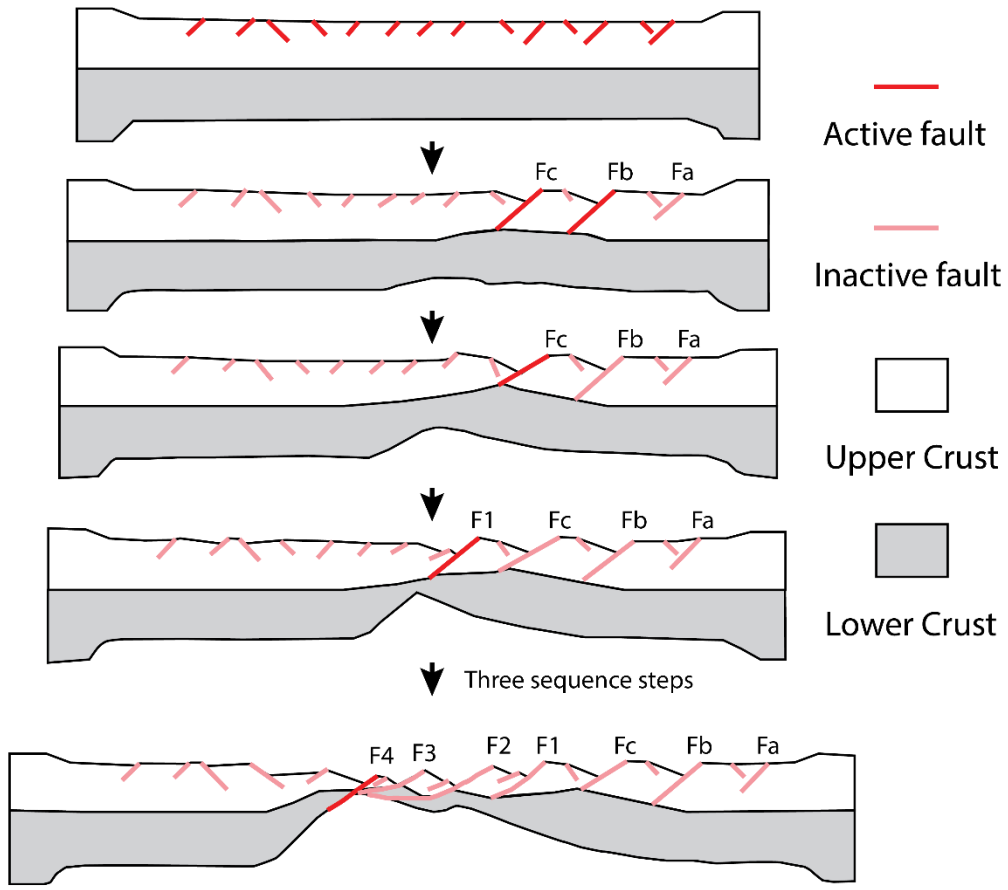

Figure 1-11: Schematic diagram illustrating sequential faulting mechanism. Model based on the structure observed along IAM-11 (Figure 1-7). Fault naming convention is used later in this thesis. Modified from Ranero and Pérez-Gussinyé [2010].

From the edge of the continental shelf to the termination of continental crust at the Galicia margin, the average crustal stretching factor, measured from fault heaves, is β_f ~1.37 (where $\beta = t_{initial}/t_{final}$, t is thickness). Over the same area the crustal stretching factor, determined from wide-angle seismic velocity models, is β_c ~1.98 [*Reston and McDermott*, 2014]. From these observations, the observed faulting only accounts for 38% of the total crustal thinning. However, this discrepancy becomes even more significant when looking at the hyperextended domain, above the S reflector, in isolation. Here, the observed β_f is ~1.35, while conservative calculations of β_c are 11.50. There have been several processes proposed to explain this extension discrepancy, yet it remains a debated research question at magma-poor margins.

A simple explanation for some of the extension discrepancy is that smaller faults are unresolved in reflection seismic imaging, referred to as subseismic faulting, and therefore go unaccounted for in the estimates of crustal thinning [*Marrett and Allmendinger*, 1992]. However, the distribution of fault size and displacement follows a fractal distribution,

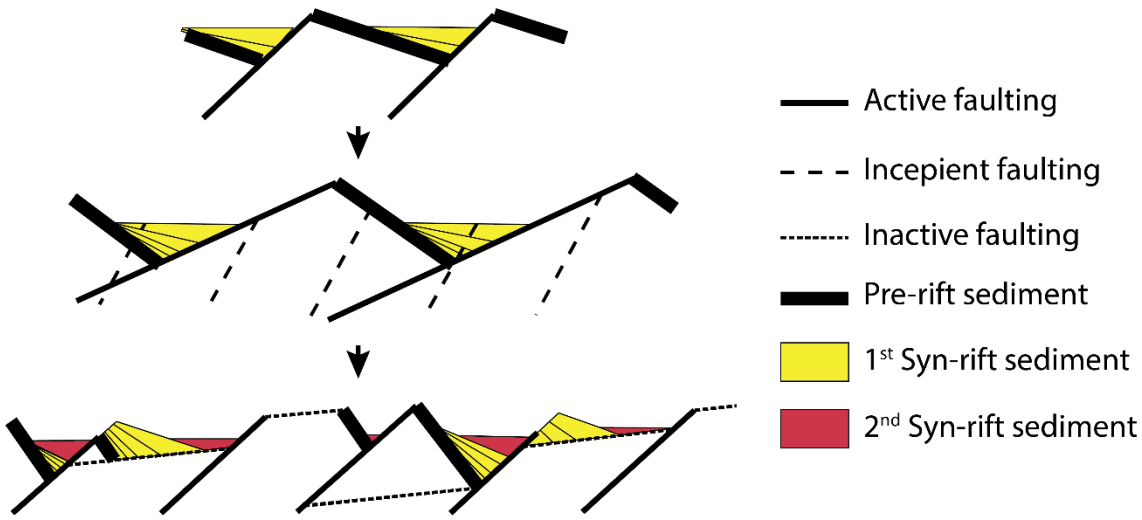

Figure 1-12: Schematic diagram illustrating the polyphase faulting mechanism. Modified from Reston [2009a].

which means that the contribution of subseismic faulting can be estimated [*Walsh and Watterson*, 1992]. Using these fractal relationships the total subseismic extension at the DGM has been calculated to be anywhere between 13 – 47 % of the total crustal extension, which although significant, is not enough to explain the total extension discrepancy [*Reston and McDermott*, 2014].

Several authors have argued that the extension discrepancy can be explained by different faulting mechanisms, with the two primary suggestions being sequential and polyphase faulting [*Reston*, 2007a; *Ranero and Pérez-Gussinyé*, 2010; *Reston and McDermott*, 2014]. In the sequential faulting mechanism, continued extension either reactivated existing faults, rotating them to lower angles, or formed new preferentially oriented faults through the thinned crust [*Ranero and Pérez-Gussinyé*, 2010]. Deformation at any one time is focused on a single fault, with successive faults cutting through the crust thinned by the preceding fault, resulting in a migrating rift center and the formation of hyperextended crust, giving rise to an asymmetric rift system (Figure 1-11) [*Ranero and Pérez-Gussinyé*, 2010; *Pérez-Gussinyé*, 2013]. *Ranero and Pérez-Gussinyé* [2010] argue that faults forming in this sequential manner resolve the extension discrepancy as the faults cut the hanging wall of the previous fault, adding localized further extension, such that $\beta_f = \beta_c$. However, other authors argue that the sequential faulting model does not predict an extension discrepancy, and therefore cannot explain one [*Reston and McDermott*, 2014]. These authors propose that the deformation instead occurred by polyphase faulting, where blocks of continental crust, bound by normal faults, were rotated to low angles to a point where the faults locked up. New, preferentially oriented, faults formed simultaneously

through the existing faults and fault blocks, overprinting the existing faulting and fault blocks [*Reston*, 2007a; *McDermott and Reston*, 2015]. This polyphase faulting results in a much more complicated pattern of deformation (Figure 1-12) [*Reston*, 2009a]. These complex fault patterns prove to be much more difficult to identify in seismic imaging and hinder the ability to produce palinspastic restorations of the rift margins. This results in an underestimation of brittle thinning, and hence could explain the extension discrepancy [*Reston and McDermott*, 2014].

If it is assumed that all the deformation in the brittle crust is accounted for, then the extension discrepancy must occur due to unaccounted thinning in the ductile middle and lower crust. Some authors have proposed that upwelling and diverging lithosphere and asthenosphere flow has resulted in depth-dependent thinning of the continental lithosphere [*Davis and Kusznir*, 2004; *Kusznir and Karner*, 2007]. Significant lithospheric thinning in the ductile middle and lower crust, relative to the brittle upper crust, has been shown to occur in numerical fluid flow models, and can explain the observed lithospheric thinning, with low levels of upper crustal deformation [*Kusznir and Karner*, 2007]. The key issue with depth-dependent thinning is how this thinning is balanced horizontally; if viscous lower crust and upper mantle is displaced, it would either be have been pushed oceanward, or landward, resulting in a thickening away from the divergent fluid flow [*Reston and McDermott*, 2014].

1.5 Research questions

- What is the nature of the continent-ocean transition west of the Peridotite Ridge at the DGM? Recent studies have suggested that there is potentially continued mantle exhumation, while classical interpretations have inferred the direct onset of oceanic crust. Any findings at the DGM will have implications for the interpretations made at the conjugate Flemish Cap margin, which has also had the same differing interpretations made of its transitional domain. Resolving the nature of the basement could demonstrate that despite an asymmetric thinning of the continental crust at magma-poor margins, the transitional domains at each conjugate margin exhibit a symmetry in their structure.
- How is the upper mantle below detachment faults, such as the S reflector, hydrated? It has been well established that detachment faulting within the COT at

magma-poor margins represents the contact between lower crustal lithologies and the serpentinised upper mantle, but the exact nature by which this hydration occurs has not been well defined. To what degree can the velocity structure of this serpentinisation phenomenon be resolved using classic tomographic methods and more novel techniques?

- To what degree can we resolve the fine-scale deformation structure observed within the hyperextended domain of magma-poor margins? Existing seismic studies at the DGM fail to identify many of the fault structures and crustal units present. Resolving to a greater degree the patterns of faulting within these domains could assist us in the understanding of the extension discrepancy and the mechanisms of rift extension leading to continental breakup. How are these deformation patterns related to detachment faulting and the production of the Peridotite Ridge? Can the interpretation of high resolution seismic reflection images be assisted by greater resolution in seismic modelling?
- Can we determine the shear velocity structure within the COT, and what can it tell us about the nature of magma-poor continental breakup? Shear-wave velocities are often difficult to determine at deep water margins, given the presence of thick sedimentary deposits and a lack of strong velocity contrasts to promote the conversion of compressional waves to shear waves. Can surface waves be utilised in order to generate shallow shear-wave velocity models of the thinned continental crust and upper mantle?

1.6 Thesis outline

In this thesis we look to contribute to the understanding of several of the questions which remain about the DGM and magma-poor margins, using a newly collected seismic reflection and refraction data. We have applied a variety of wide-angle seismic modelling methods, in order to resolve the velocity structure of the COT, including the hyperextended domain and the transition to oceanic crust. Some of the methods we apply have rarely been used in such deep water settings, and we explore their applicability to future studies.

Chapter 2 details the acquisition of seismic reflection and refraction data, and gravity data during the Galicia-3D cruise. Modelling methods are described which are applied to this

data set, including travel-time tomography, full-waveform inversion, ambient noise cross-correlation and beamforming, and gravity modelling.

Chapter 3 presents the results of the travel-time tomography applied to a long seismic reflection and refraction profile which crosses from the necking domain of the DGM, to the basement west of the Peridotite Ridge in order to determine the oceanward extent of the COT and the nature of the oceanward basement. Gravity modelling is used to verify the travel-time tomography models.

Chapter 4 explores the application of 2D full-waveform inversion to the deep and sparse dataset collected over the hyperextended domain of the DGM. Full-waveform inversion utilises the travel-time tomography model determined in Chapter 3, returning a greater resolution of velocity structure at the DGM, and aides in the interpretation of the high-fidelity seismic reflection data.

Chapter 5 describes the application of ambient noise cross-correlation and beamforming to continuous data collected by the entire 3D OBS/H array. Three different methods are used to determine the phase velocity of fundamental Rayleigh waves, and produce a 1D shear velocity structure of the sediments, upper and lower crust, and mantle below the hyperextended domain of the DGM.

Chapter 6 concludes the thesis with a summary of the main findings from Chapter 3 – 5, and provides suggestions for future work.

Appendix A contains tables detailing the relocation of OBS/H and the correction of instrument timing.

Appendix B contains figures of OBS/H receiver gathers with travel-time picks and modelled synthetic travel times, complementing the results of Chapter 3.

Appendix C contains figures of real and synthetic OBS/H receiver gathers from the FWI, complementing the results of Chapter 4.

Authors note: Chapters 3 – 5 are written as stand-alone research papers, with each chapter providing a short review of the tectonic setting and seismic methods. Accordingly there may be some degree of repetition between Chapters 1-2 and Chapters 3-5.

Chapter 2: Data and modelling methods

2.1 Galicia-3D survey

The Galicia-3D survey was a seismic experiment conducted between May and September of 2013, with the aim of gaining a greater understanding of the processes responsible for continental rifting and lithospheric breakup at the Deep Galicia margin. Rifting leading to continental breakup is an inherently 3D process and the Galicia-3D seismic experiment looked to expand upon previous 2D seismic experiments at the DGM, by resolving the 3D structure of the S reflector and the associated seismic velocities. Galcia-3D was a combined multichannel and wide-angle seismic experiment undertaken as a collaboration between UK, US, German and Spanish research institutes. Two research vessels were utilised in this seismic experiment. The *R/V Marcus G. Langseth*, operated by Lamont-Doherty Earth Observatory's Office of Marine Operations, recorded 3D multichannel seismic reflection, gravity, magnetic and bathymetric data. The *F. S. Poseidon*, operated by GEOMAR Helmholtz Centre for Ocean Research, deployed and recovered an array of ocean bottom seismometers and hydrophones (OBS/H), which recorded wide-angle seismic reflection and refraction data from the concurrent seismic reflection experiment.

2.1.1 Multichannel reflection seismic acquisition

The primary acquisition of the Galicia-3D survey was a high-resolution 3D seismic reflection survey at the DGM, covering an area of 65 km (east-west) by 20 km (north-south), and is here referred to as the 3D Box (Figure 2-1B). The survey covers the oceanward extent of continental crustal necking, the S reflector detachment fault and the overlying hyperextended crust, and the oceanward Peridotite Ridge. Additional 2D seismic profiles were acquired west of the primary 3D array, with the intention of imaging and modelling the basement west of the Peridotite Ridge, in order to identify the onset of unambiguous oceanic crust. These two profiles are referred to as Western Extension 1 and 2 (WE-1 and WE-2, respectively), with WE-1 extending and additional 90 km west of the primary 3D seismic experiment (Figure 2-1B).

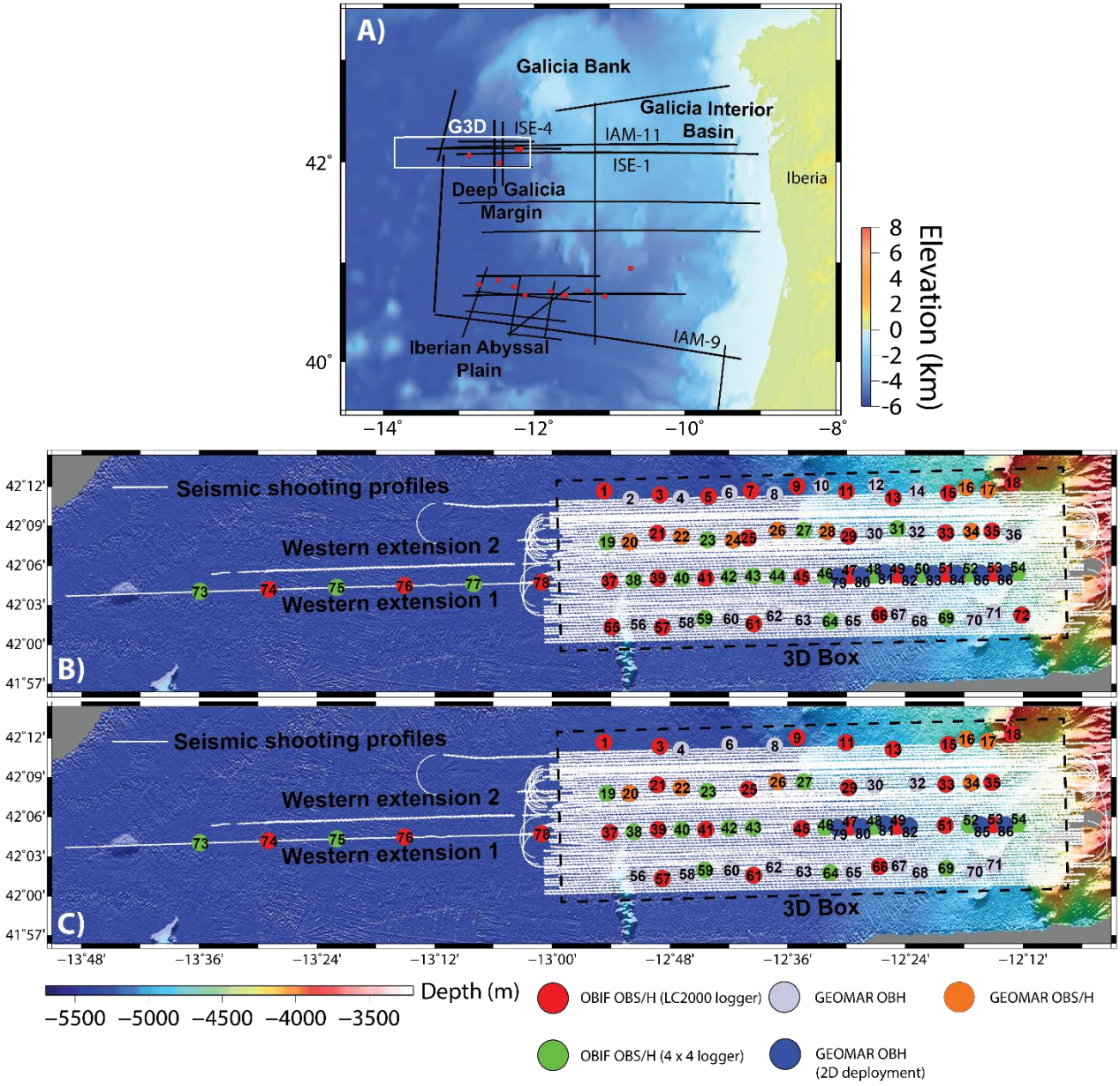

Figure 2-1: Galicia-3D seismic experiment map. A) Galicia-3D in context of previous seismic experiments, white box is shows area illustrated in B) and C). B) Seismic reflection sail lines (white) and OBS/H recording coincident wide-angle reflection and refractions (red, green, dark and light blue circles). C) Same as B), but only including OBS/H which were recovered and returned usable data.

Three-dimensional seismic reflection data were collected within the 3D Box (Figure 2-1B) with a seismic acquisition configuration comprised of four 6 km long hydrophone streamers, towed 200 m apart (Figure 2-2). Each streamer contained 468 hydrophone channels spaced 12.5 m apart, and were towed at a constant depth of 15 m. The seismic source consisted of two airgun arrays, towed 100 m apart and at a depth of 9 m, each of which contained two airgun strings. Each airgun array contained 20 airguns with capacities between 40 cu. in. and 360 cu. in. and a total individual array volume of

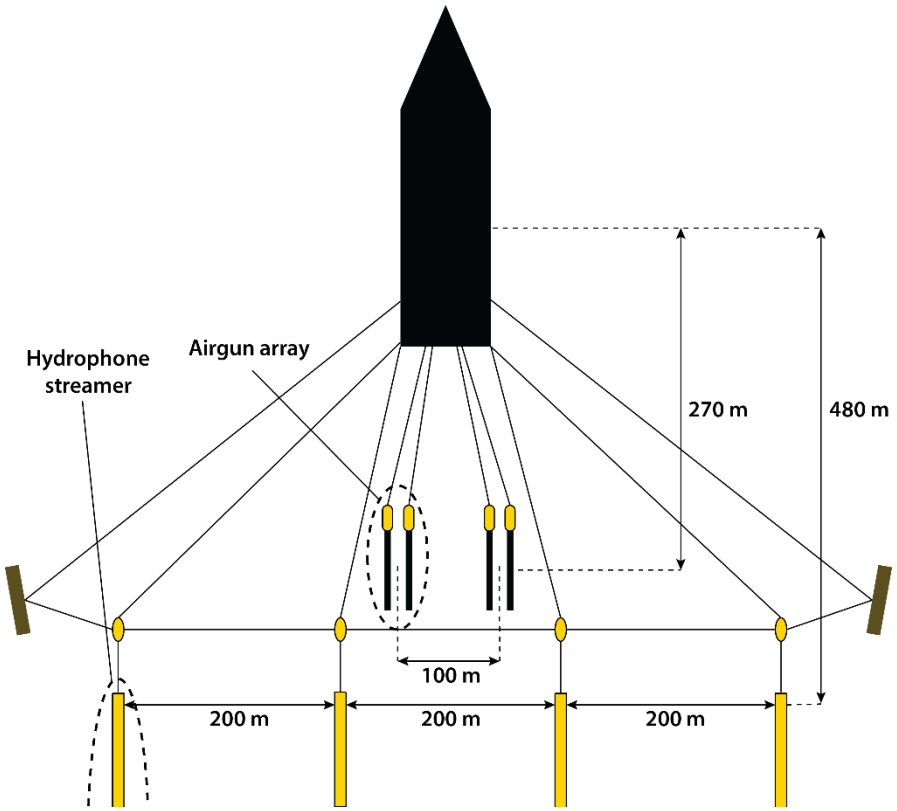

Figure 2-2 Schematic diagram of the 3D reflection seismic acquisition configuration used in the Galicia-3D seismic experiment.

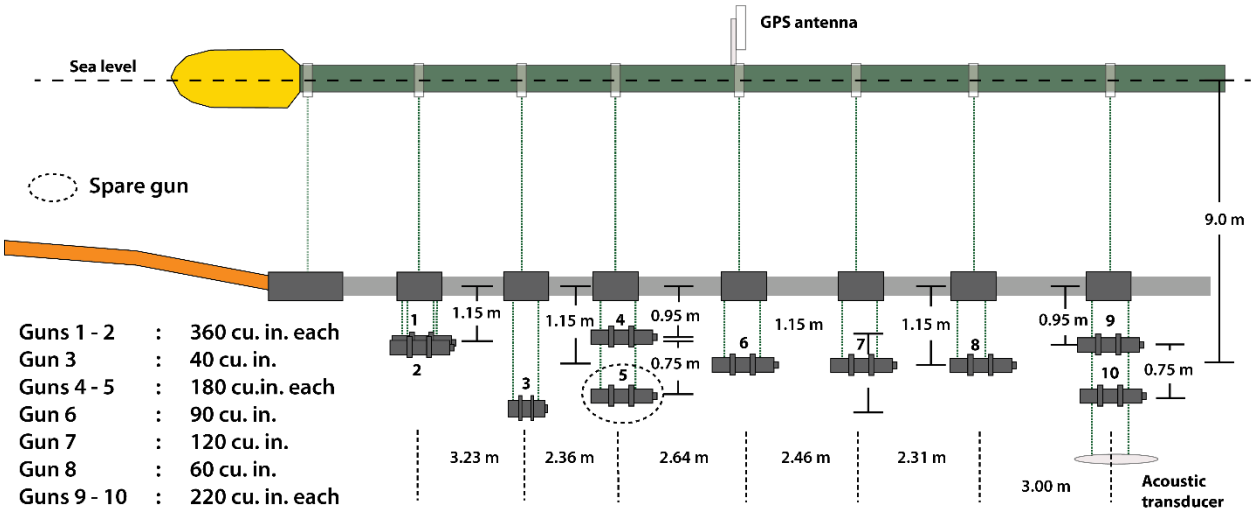

Figure 2-3: Schematic diagram of the airgun strings used during the Galicia-3D seismic experiment.

3,3300 cu. in. (Figure 2-3). The airgun arrays were tuned for the purpose of seismic reflection imaging, and produced a source signature with peak energy between 35 and 55 Hz (Figure 2-4). The two source arrays were fired alternately every 37.5 m (a shot interval of approximately 16 s), as determined by the shipboard GPS. The full 3D acquisition enabled 8 adjacent CMP profiles, spaced 50 m apart, to be recorded along a

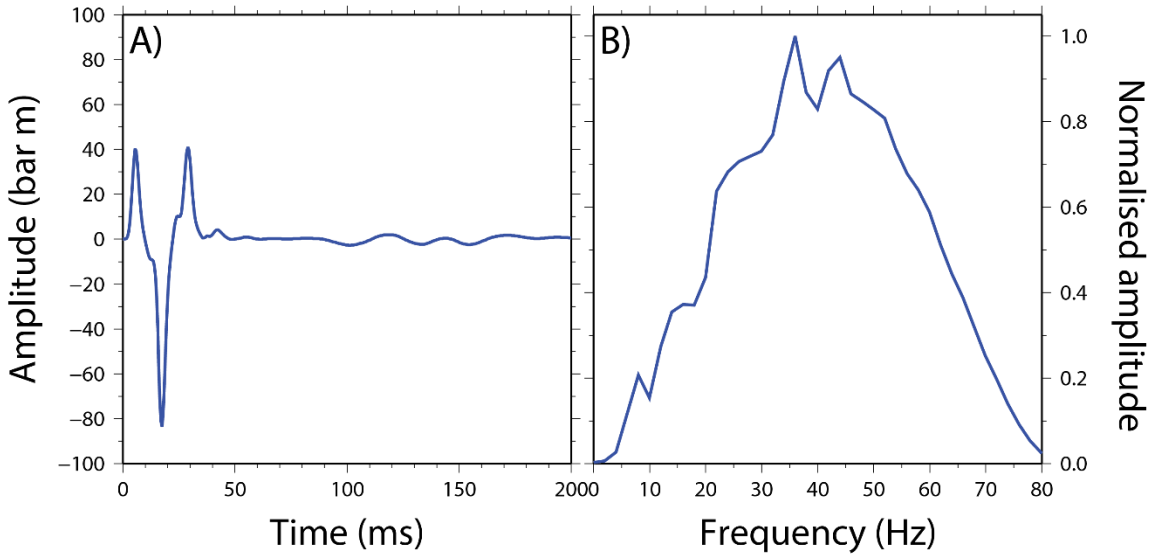

Figure 2-4: Modelled source signature and associated spectrum. A) Source signature. B) Source frequency spectrum. Modelled by Lamont-Doherty Earth Observatory.

single sail line. Within the 3D Box a total of 50 east-west sail lines were recorded, resulting in the 3D seismic reflection volume comprising approximately 400 CMP lines (Figure 2-1B).

WE-1 extends west of the 3D Box (Figure 2-1B), and was primarily recorded for the purpose of identifying the transition to oceanic crust. The landward extent of WE-1, within the 3D Box, is coincident with the oceanward extent of the existing ISE-1 seismic profile [*Sawyer et al.*, 1997]. Without a specific need for high-resolution 3D seismic reflection images of the basement west of the Peridotite Ridge, seismic shots were fired every 150 m (a shooting period of approximately 64 s). This shooting rate is more optimal for the purpose of wide-angle seismic refraction surveying, allowing more time for the energy of the previous shot to dissipate. The result is a higher signal-to-noise ratio in the recorded OBS/H data, but a lower fold in the MCS reflection imaging.

2.1.2 Wide-angle reflection and refraction acquisition and processing

OBS/H were deployed prior to the seismic reflection experiment, and recorded the wide-angle reflections and refractions produced during the active source shooting. The UK Ocean Bottom Instrumentation Facility (OBIF) provided 50 OBS/H, each of which had a three-component Sercel L-28 4.5Hz geophone (two horizontal and a vertical channel), and a High Tech HTI-90-U hydrophone [*Minshull et al.*, 2005]. These instruments utilised either an LC2000 or an LC4x4 digital logger, which were developed by the Scripps Institute of Oceanography, and recorded seismic data at a rate of 250 Hz. GEOMAR provided 7 OBS/H,

each of which had three-component KUM 4.5 Hz geophone and a High Tech HTI-01-PCA hydrophone, as well as 21 OBH consisting of a single High Tech HTI-01-PCA hydrophone. GEOMAR instruments utilised MLS digital loggers developed by SEND GmbH, and recorded at a rate of 200 Hz.

As with the seismic reflection experiment, there were two different experiment configurations, with the primary array configuration focused on resolving the 3D seismic velocity structure within the 3D Box. In this configuration, four profiles of 18 OBS/H were deployed east-west within the 3D box (Figure 2-1B). These profiles were separated by ~6 km in the north-south direction, with the instruments along each profile separated by ~3.2 km in the east-west direction. Each instrument was deployed for an average of 79 days, and recorded 32 days of active source seismic shooting.

The second configuration of OBS/H was deployed along the 2D WE-1 profile, extending from the eastern limits of the 3D Box, and continued westward of the Peridotite Ridge. This profile was recorded prior to the 3D experiment, and incorporated the instruments along the third most northern OBS/H profile of the 3D Box refraction array. Eight GEOMAR OBH were temporarily deployed (3 days) between the easternmost OBS/H of the 3D Box experiment, giving a higher density of instruments over the S reflector, for the purpose of full-waveform inversion (Figure 2-1B). Oceanward of the Peridotite Ridge a further 6 OBIF OBS/H were deployed for the purpose of modelling the seismic velocity structure of undetermined basement (Figure 2-1B). A total of 32 instruments were deployed to record active source seismic shooting along the WE-1 profile. Instrument spacing along this profile saw the eastern 17 instruments spaced at ~1.7 km intervals, the central section comprised 9 instruments spaced at distances of ~3.4 km, and west of the Peridotite Ridge the 6 instruments had an average spacing of ~9.7 km (Figure 2-1B).

During the recovery of the OBS/H a total of 8 instruments were unable to be recovered, while another 9 instruments were recovered with issues which included dead batteries, flooded loggers, or channels which did not return usable data. All instruments which were successfully incorporated into this study can be seen in Figure 2-1C.

2.1.2.1 Timing and drift correction

In order to produce accurate seismic velocity models, it is critical to determine accurate timings for the airgun shots, both when they are fired at the surface and when the resulting seismic arrivals are recorded by the seafloor instrumentation.

The timing and location of seismic shots are recorded accurately by the *R/V Marcus G. Langseth's* on-board Global Positioning System (GPS), as well as GPS connected to the seismic source arrays. At the time of deployment, the internal clock of each OBS/H is synchronised with the same on-board GPS. Upon instrument recovery, the time is read from the OBS/H's internal clock ($t_{recovered}$) and compared with the actual time from the ships onboard GPS (t_{GPS}). The total drift (T_{drift}) of each instruments internal clock during the deployment is simply:

$$T_{drift} = t_{recovered} - t_{GPS} \qquad \text{(Equation 2.1)}$$

The simplest assumption is that the internal clocks drift linearly over time at a constant rate. Therefore the drift rate (D_{rate}) of each instrument is calculated as:

$$D_{rate} = \frac{T_{drift}}{T_{deployment}} \qquad \text{(Equation 2.2)}$$

where $T_{deployment}$ is the total time of the OBS/H deployment, between the initial clock synchronisation and final clock reading.

Data samples are recorded by each OBS/H and are associated with a time code supplied by the instrument's internal clock. Timing corrections to account for clock drift can be made for each recorded sample using the calculated drift rates for each instrument. This gives the correct sample times relative to the shipboard GPS, and therefore are corrected to be consistent with the seismic source arrays. The calculated drift rates for all recovered instruments can be found in Appendix A.

2.1.2.2 Instrument relocation

OBS/H are deployed by placing the instruments into the ocean and allowing them to sink to seafloor. The instruments deployment location is accurately recorded using the ship's GPS. However, the instruments descend through the water column, which in some areas exceeds 5,000 m, before settling on the ocean bottom. As the OBS/H sink they unavoidably move laterally in the water column, a result of ocean currents and hydrodynamic

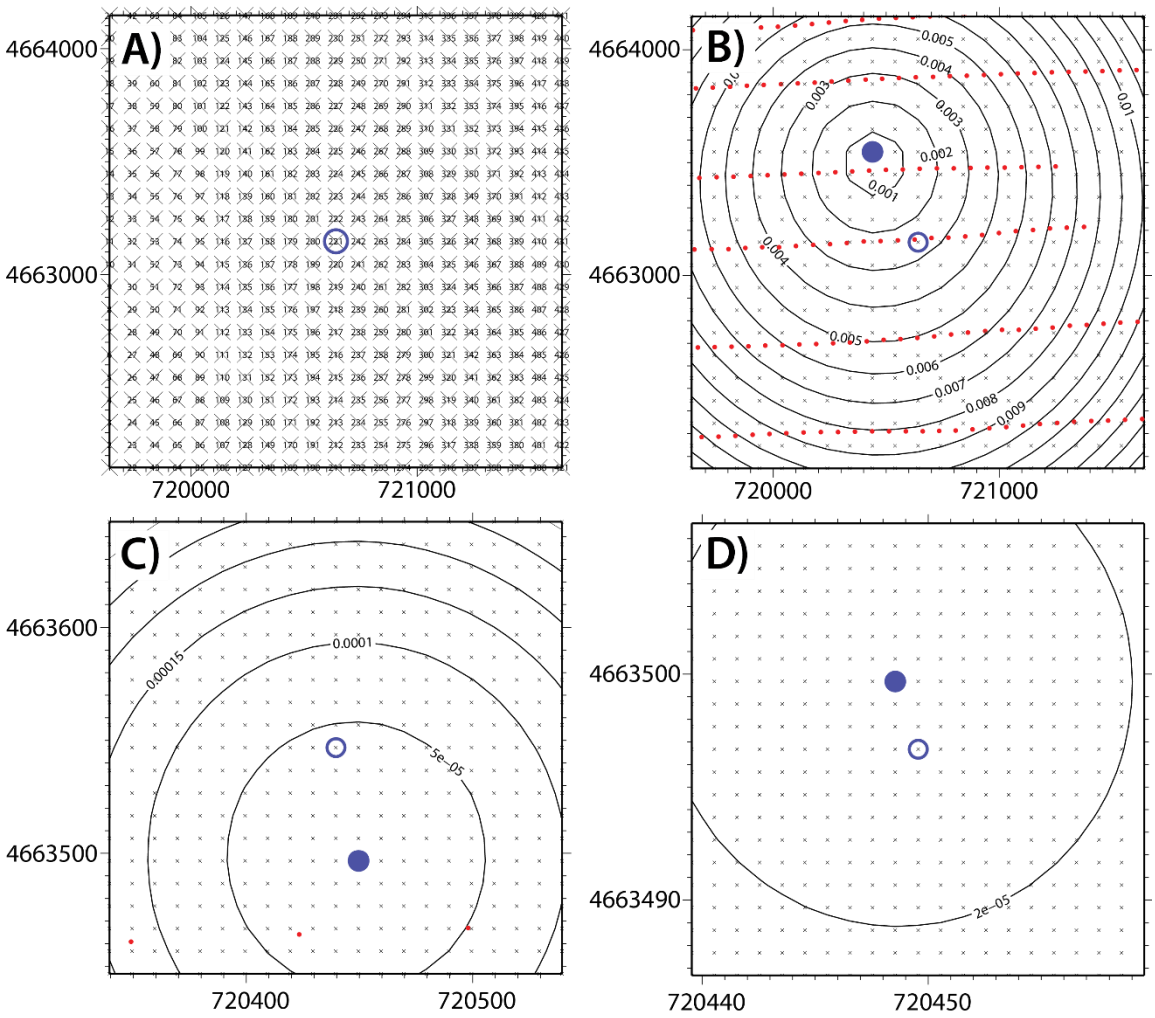

Figure 2-5: 3D relocation of OBS/H. A) Initial 21 x 21 grid with 100 m spacing. Open blue circle indicates the initial location of the instrument for each step. B) Instrument relocation on initial grid. Red dots indicate shot locations, closed blue circle indicates new instrument location, and contours indicate RMS misfit residuals of equal value. C) Instrument relocation on 10 m grid spacing. D) Instrument relocation on 1 m grid spacing.

instabilities created by the instrument. Uncorrected instrument locations will result in apparent timing errors in the recorded seismic phases, leading to models with appreciable error.

Instruments were relocated using the direct seismic arrival through the water column and the depth of instrument, which was determined from the recorded bathymetry data. Sound velocity profiles, used for the generation of the bathymetric data, were used to extract an average water column velocity of 1.52 km s^{-1}.

Within the 3D Box, each instrument recorded a large number of seismic shots with an excellent azimuthal coverage around each instrument, thus enabling an accurate instrument relocation. In order to relocate the OBS/H within the 3D Box a least-squares

travel-time misfit code was written, utilising the dense coverage of seismic shots and bathymetric depths surrounding each instrument. The code relocates each instrument based on the following steps:

1. The direct water-wave arrival was picked on the seven nearest seismic profiles, using receiver gathers from the OBS/H to be relocated.
2. A grid, centred on the original OBS/H deployment position, was established with dimensions of 21 x 21 nodes and 100 m spacing (100 m spacing is used for the first iteration of the code), see Figure 2-5A.
3. The depth of each grid node is determined from the bathymetry data acquired during seismic surveying.
4. At each grid node the direct distance to each shot is calculated using the equation:

$$d = \sqrt{\left(\sqrt{(n_x - s_x)^2 + \left(n_y - s_y\right)^2}\right)^2 + z^2} \qquad \text{(Equation 2.3)}$$

   Where d is the direct distance, n_x and n_y are the UTM longitude and latitude of the grid node, s_x and s_y are the UTM longitude and latitude of the shot location, and z is the depth of the grid node.
5. Travel-times through the water column, from the picked seismic shots to the grid nodes, were calculated using the constant water velocity of 1.52 km/s. Residual travel-times were calculated by subtracting the observed travel-times observed at each shot point from the calculated travel-times.
6. At each grid node the root mean square (RMS) value of the residual travel-times was calculated. The grid node which has the smallest RMS travel-time residual value was set as the relocated OBS/H position, see Figure 2-5B.
7. Steps 3 – 6 are repeated with decreasing node spacing of 10 m and 1 m (see Figure 2-5C and D), with the final position representing the OBS/H relocation.

Instruments along the 2D WE-1 seismic profile did not benefit from a full azimuthal coverage of seismic shots for their relocation. Most of these instruments recorded shots along WE-1 as well as the parallel WE-2 (Figure 2-1). These instruments are relocated using a simplified method:

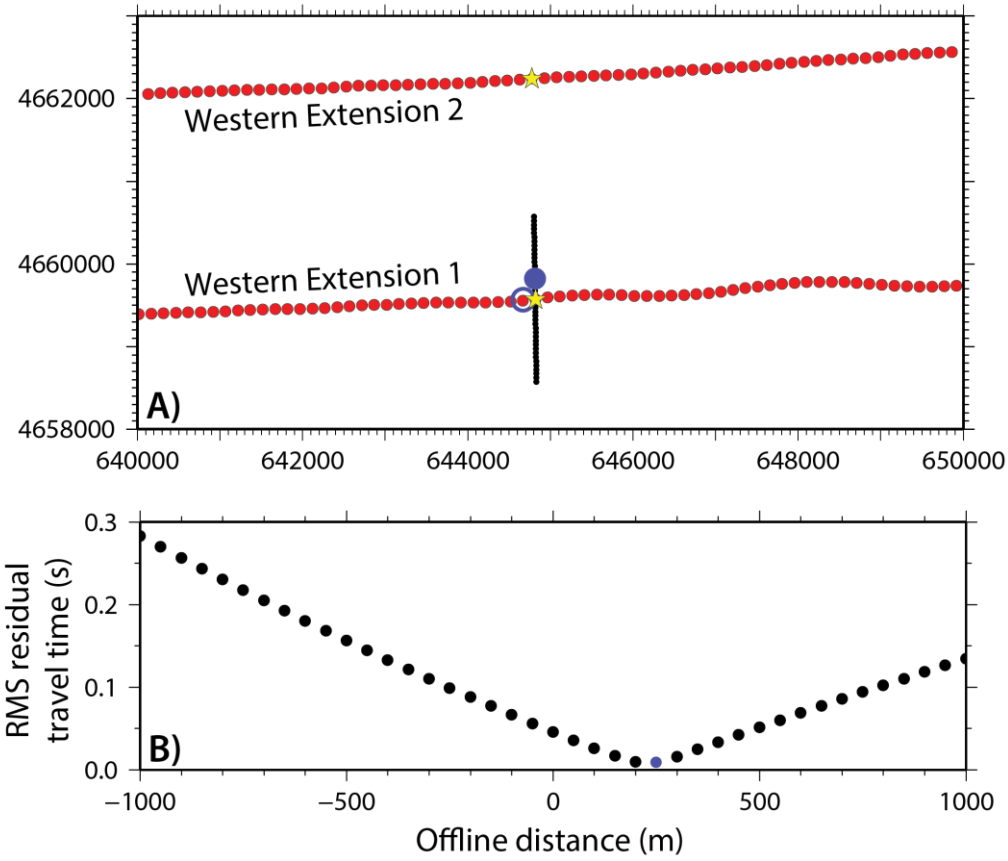

Figure 2-6: 2D relocation of OBS/H. A) Red circles represent the two shooting profiles, the stars are the closest shots to the instrument along each line, black dots indicate tested relocation positions, blue open circle indicates deployment position, solid blue circle indicates relocation position. B) Plot of RMS travel-time misfit residuals at tested locations, blue dot indicates minimum RMS travel-time.

1. The direct water-wave arrival from shots along profiles WE-1 and WE-2 (where possible) were picked in the receiver gather data of the OBS/H to be relocated.
2. The instrument is first relocated to the inline position, along WE-1, of the shot with the smallest travel-time. From there it is assumed that the instrument lies along the line connecting the nearest shots recorded from WE-1 and WE-2 (Figure 2-6A).
3. Node locations along this line are determined every 50 m, 1,000 m either side of WE-1. The direct distance between these nodes and the shot locations are calculated according to Equation 2.3.
4. Travel-times through the water column, from the picked seismic shots to each node, were calculated using a constant water velocity of 1.52 km/s. Residual travel-times were calculated by subtracting the observed travel-times from the calculated travel-times.
5. The RMS residual travel-times were calculated at each node location (Figure 2-6B). The node with the smallest RMS travel-time residual value was set as the relocated OBS/H position, see Figure 2-6A.

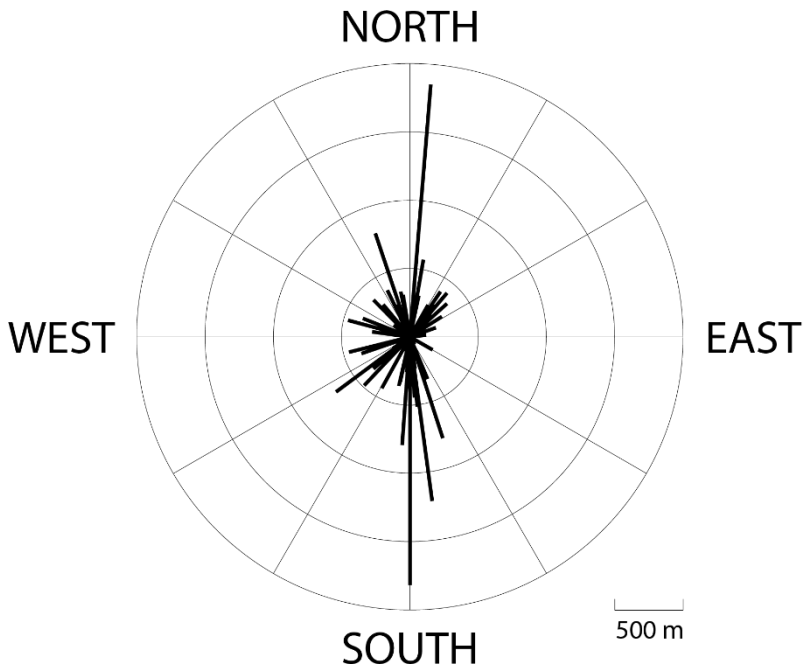

Figure 2-7: Instrument relocation rose plot indicating the distance and azimuth of relocated instruments relative to their deployment positions.

Where an instrument only recorded a single 2D shooting profile, the same steps are followed, except that it is assumed that the instrument lies along a line perpendicular to the recorded 2D shooting profile. Which side of the shooting profile such an instrument lies is considered to be insignificant.

Instruments relocated using the 3D method move laterally from their deployment positions by a mean distance of 367 m. We suspect that there are at least three anomalous relocation distances (> 1,000 m), which could be errors in the recording of the deployment positions (Figure 2-7). Those relocated using the 2D method, move laterally from their deployment position by mean distance of 237 m. There appears to be no obvious correlation in the direction of the lateral movement occurring during an instruments descent, indicating that movement in the water column is dominated by hydrodynamic instabilities (Figure 2-7).

2.2 Gravity data and processing

Gravity data were collected throughout the seismic experiment using a Bell BGM-3 Gravimeter. The shipborne gravimeter was tied to a known gravity station at Muelle de Guixar in Vigo, Spain, on the 8th of June and 12th of July, 2013, using a Lacoste and Romberg portable gravimeter.

In order to convert the raw gravity measurements to useable relative free-air anomalies (FAA) the data is reduced using the following equation:

$$FAA = g_{raw} - g_{\theta} + E \qquad \text{(Equation 2.4)}$$

Where g_{raw} is the recorded gravity measurement after applying the instrument conversion factor (5.0962178), g_{θ} is the expected gravity with latitude (θ), and E is the Eötvös correction, all in values of mGal. The latitude correction, g_{θ}, accounts for the expected changes in Earth's gravity with latitude and is calculated using the World Geodetic System 1984 Ellipsoidal Gravity formula:

$$g_{\theta} = \frac{1 \pm 0.0019318513 \cdot sin^{2}(\theta)}{\sqrt{1 - 0.00669437999013 \cdot sin^{2}(\theta)}} \qquad \text{(Equation 2.5)}$$

Where θ is the latitude of the observed gravity measurement, in the WGS 84 datum. The Eötvös correction amends the measured gravitational force for the contribution of centrifugal acceleration experienced by the vessel when it is headed east or west. This correction is given by:

$$E = 7.503 \cdot v \cdot \sin(\emptyset)\cos(\theta) + 0.004154 \cdot v^{2} \qquad \text{(Equation 2.6)}$$

Where Ø is the ship's bearing in degrees, v is the ship velocity in knots, and θ is the ship's latitude.

2.3 Seismic modelling methods

Within this thesis we have applied several different seismic modelling techniques to extract velocity information from the wide-angle seismic dataset. Chapter 3 looks at the use of wide angle seismic travel-times to produce 2D forward and inverse travel-time tomography velocity models of the continent-ocean transition. In Chapter 4, we build on these compressional velocity models by implementing full-waveform inversion, in order to gain a higher resolution 2D compressional velocity model of the hyperextended domain. In Chapter 5, we employ cross-correlation of continuous wide-angle seismic data in order to observe the dispersion of Rayleigh waves, and determine a one-dimensional shear velocity structure of the hyperextended domain.

This section provides a brief description of the methods and codes used to achieve these results.

2.3.1 Forward ray tracing

Forward ray tracing methods enable the calculation of seismic ray paths through a pre-defined velocity model using physical principles (e.g. Huygen's principle, Fermat's principle and Snell's law). These methods rely on trial and error modifications of the velocity model in order to match the travel-times of synthetic rays to those which are observed.

In Chapter 3 of this study we utilise the forward ray-tracing algorithm of RAYINVR, developed by *Zelt and Smith* [1992]. Here, we follow the description of RAYINVR as presented in *Zelt and Smith* [1992] and *Zelt and Ellis* [1988].

RAYINVR velocity models are parameterised by node-defined layers, forming trapezoids with isotropic velocities (Figure 2-8). Velocities within the layers are defined by an upper and lower velocity, for each straight line segment between nodes. Linear interpolation of velocity between the upper and lower boundaries of a trapezoid is such that the velocity v_0 at some point (x_0, z_0), is defined as:

$$v_0 = \frac{(v_1 m_2 - v_1 m_2)x_0 + (v_2 - v_1)z_0 + (v_1 b_2 - v_2 b_1)}{(m_2 - m_1)x_0 + (b_2 - b_1)} \qquad \text{(Equation 2.7)}$$

Where v_1 and v_2 are the velocities of the upper and lower boundaries, respectively, m_1, b_1 and m_2, b_2 come from the equations of the upper and lower line segments, respectively (Figure 2-8).

Once the model has been parameterised, ray paths are calculated by numerically solving the ray tracing equations [see *Červený et al.*, 1977]. For a ray travelling near-horizontally:

$$\frac{\partial z}{\partial x} = cotan\,\theta, \frac{\partial \theta}{\partial x} = \frac{v_z - v_x\, cotan\,\theta}{v} \qquad \text{(Equation 2.8)}$$

for a ray travelling near-vertically:

$$\frac{\partial x}{\partial z} = tan\,\theta, \frac{\partial \theta}{\partial z} = \frac{v_z\, tan\,\theta - v_x}{v} \qquad \text{(Equation 2.9)}$$

with initial conditions of $x = x_o, z = z_0, \theta = \theta_0$.

Where θ is the angle between the tangent of the ray and the z-axis, v is the seismic wave velocity, and v_z and v_x are the partial derivatives of the seismic wave velocity with respect to the x and z coordinates, respectively. θ_0 is defined as the initial ray take-off angle, and the initial x and z coordinates correspond to the source location. Snell's law is applied to rays passing through layer boundaries, where velocities abruptly change.

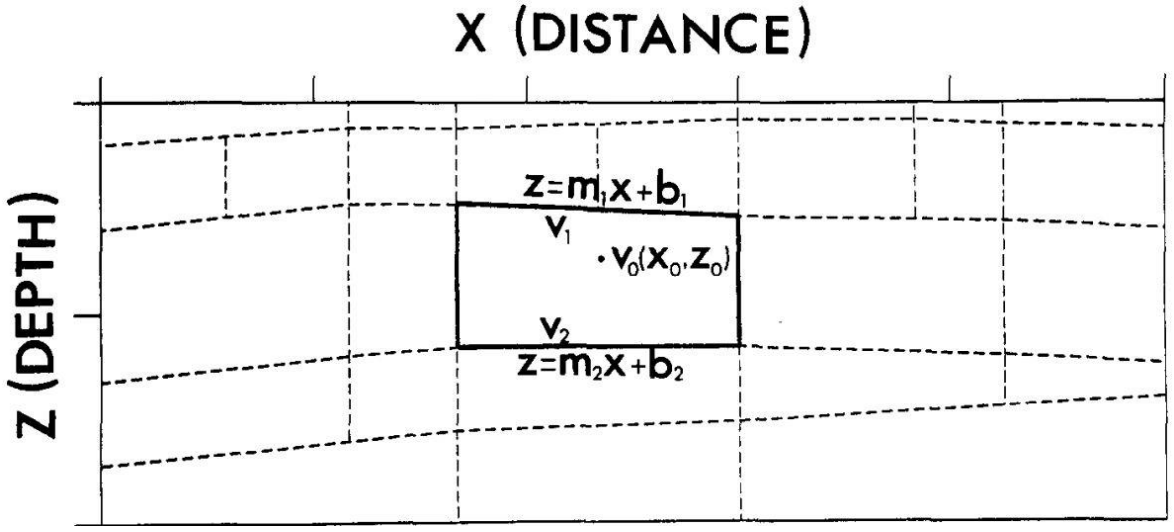

Figure 2-8: RAYINVR model parameterisation. From Zelt and Ellis [1988].

The increment in the x or z direction for equations 2.8 and 2.9 is referred to as the step length, Δ. The step length is adjusted along the ray path throughout the ray tracing procedure by the following equation:

$$\Delta = \frac{\alpha v}{|v_x| + |v_z|} \qquad \text{(Equation 2.10)}$$

Where α is a constant defined by the user. The application of a variable step length through the ray tracing procedure avoids the inaccuracy of using large increments in the local partial derivatives when the ray bending is large, and the use of unnecessarily small step lengths when the ray bending smaller.

After the ray tracing procedure is complete the code returns a RMS travel-time misfit between the travel-times along the calculated ray paths and those which are observed. Models are modified by trial and error with the aim of reducing this RMS travel-time misfit.

2.3.2 Travel-time inversion

Travel-time inversion of seismic data goes a step beyond the forward ray tracing method, removing the trial and error component of velocity structure determination. In travel-time inversion the travel-time residuals between calculated ray paths through an initial model, and those which are observed, are used to invert and update the initial model.

In Chapter 3 of this study, we use the travel-time inversion code TOMO2D of *Korenaga et al.* [2000]. TOMO2D allows for the joint inversion of both reflection and refraction data, in

order to resolve subsurface velocities and the depth to a given boundary reflector. Here, we follow the description of TOMO2D as presented in *Korenaga et al.* [2000].

TOMO2D models are parameterised by a hanging sheared mesh, which in our study is hung from the bathymetry of the sea-floor. Node spacing of the mesh can vary both horizontally and vertically. It is common practise to employ a finer vertical node spacing in the shallow sections of the model, where there is greater ray coverage and often higher degrees or geological variation. Larger node spacing is used at greater depths, as these areas of the subsurface are typically sampled by fewer ray paths and are not as well constrained. Additionally, a floating reflection surface is defined as a series of linear segments whose node spacing is independent of the sheared mesh. This reflection surface has a single degree of freedom, allowing only its depth to be modified. The reflector depth is controlled by seismic reflections, but does not introduce a velocity discontinuity into the velocity model.

2.3.2.1 Forward problem

TOMO2D utilises a hybrid approach to the forward ray tracing method; a combination of the graph method (shortest path method) (Figure 2-9A) and the ray bending method. The graph method calculates the shortest connection between an origin node, and all other nodes in a network [e.g. *Dijkstra*, 1959; *Gallo and Pallottino*, 1986]. Treating the seismic travel-times between nodes as the nodal distance allows this global optimisation scheme to calculate ray paths and their travel-times [*Nakanishi and Yamaguchi*, 1986; *Moser*, 1991]. However, the graph method is restricted by the forward-star, which defines the possible node connections, resulting in the ray path zig-zagging (e.g. Figure 5A), and giving an over estimate of the travel-times.

To overcome this issue, the graph method solution is improved upon by applying ray-bending theory [*Um and Thurber*, 1987; *Prothero et al.*, 1988; *Moser et al.*, 1992]. The ray-bending method of *Moser et al.* [1992] is used, which minimises the travel-time along a ray path, first determined by the graph method, using the conjugate gradient method. Rays through the model are defined by beta-splines, which express a variety of curves given a limited number of control points, aiding the conjugate gradient method in converging to

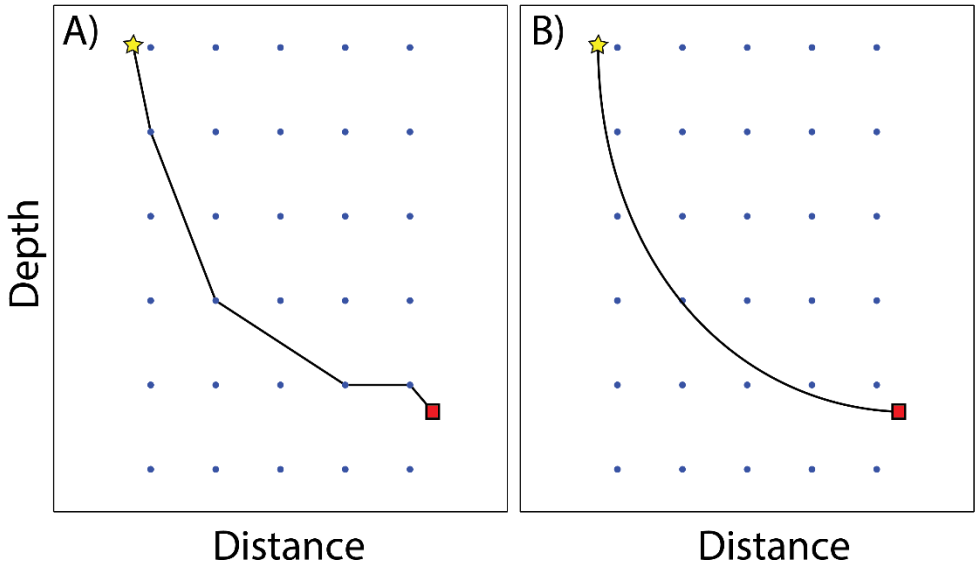

Figure 2-9: Schematic diagram of hybrid ray bending. A) Ray-path determined using the graph method. B) Ray-path determined using the hybrid ray-tracing method. Yellow star indicates shot location, red square indicates receiver location, blue dots indicate model nodes.

a minimum travel-time ray path. A visual comparison between the ray paths determined by the graph method and the hybrid approach of *Korenaga et al.* [2000] is seen in Figure 2-9.

2.3.2.2 Inverse problem

The inversion process requires an initial velocity model in order to calculate synthetic ray paths and travel-times. Initial models are often just geologically sensible velocity gradients, varying only with depth. Subtracting the calculated travel-times through the starting model from the observed travel-times gives a suite of travel-time residuals, δT_j. These travel-time residuals along a ray path through the starting model can be described by:

$$\delta T_j = \int_{\Gamma_j} \delta u d\Gamma \qquad \text{(Equation 2.11)}$$

where δu are slowness perturbations along the ray paths, Γ_j. Reflection residual travel-times are similarly described:

$$\delta T_j = \int_{\Gamma_j} \delta u d\Gamma + \left.\frac{\partial T}{\partial z}\right|_{x=x_j} \delta z(x_j) \qquad \text{(Equation 2.12)}$$

where $x_j$is the location where the j-th ray reflects off the floating reflector. Equations 2.11 and 2.12 can be expressed as:

$$\mathbf{d} = \mathbf{G}\delta\mathbf{m} \qquad \text{(Equation 2.13)}$$

where $\mathbf{d}$ is a vector comprised of the travel-time residuals, $\mathbf{G}$ is a Fréchet derivative matrix, and $\delta\mathbf{m}$ is an unknown model perturbation vector, which is the model update to minimise travel-time residuals. Equation 2.13 forms the integral matrix equation of the travel-time inversion scheme. The Fréchet matrix contains information on the velocity and depth sensitivity of the inversion. Velocity sensitivity is the ray-path length distribution relative to the models velocity nodes, while the depth sensitivity is described by the incident angle of reflection, angle of the reflector, and velocity at the reflector [Bishop et al., 1985]. The convergence of Equation 2.13 to an appropriate velocity model is dependent on the accuracy of the starting model. A starting model close to the true velocity structure will require fewer iterations of the above linearised inversion, than a significantly inaccurate starting model. Equation 2.13 can be rewritten as a regularised linear system:

$$\begin{bmatrix} \mathbf{d} \\ 0 \\ 0 \\ 0 \end{bmatrix} = \begin{bmatrix} \mathbf{G_v} & w\mathbf{G_d} \\ \lambda_v \mathbf{L_{Hv}} & 0 \\ \lambda_v \mathbf{L_{Vv}} & 0 \\ 0 & w\lambda_d \mathbf{L_d} \end{bmatrix} \begin{bmatrix} \delta\mathbf{m_v} \\ \frac{1}{\mathrm{w}}\delta\mathbf{m_d} \end{bmatrix} \qquad \text{(Equation 2.14)}$$

where the subscripts v and d represent the velocity and depth components of matrices, respectively. $\mathbf{L_{Hv}}$ and $\mathbf{L_{Vv}}$ are the horizontal and vertical smoothing matrices for slowness perturbations, respectively, while $\mathbf{L_d}$ is a smoothing matrix for the depth of the floating reflector. λ_v and λ_d determine on the relative importance of smoothing constraints. W is the depth-kernel weighting parameter which controls the depth sensitivity. Equation 2.14 is a sparse matrix equation, which can be solved using the LSQR algorithm of Paige and Saunders [1982]. Issues can arise when the starting model is far from the true model, creating significant model updates and leading to instabilities in the subsequent inversion iterations. In order to eliminate these instabilities a damping factor for both the velocity and depth nodes is added to Equation 2.14:

$$\begin{bmatrix} \mathbf{d} \\ 0 \\ 0 \\ 0 \\ 0 \\ 0 \end{bmatrix} = \begin{bmatrix} \mathbf{G_v} & w\mathbf{G_d} \\ \lambda_v \mathbf{L_{Hv}} & 0 \\ \lambda_v \mathbf{L_{Vv}} & 0 \\ 0 & w\lambda_d \mathbf{L_d} \\ \alpha_v \mathbf{D_v} & 0 \\ 0 & w\alpha_d \mathbf{D_d} \end{bmatrix} \begin{bmatrix} \delta\mathbf{m_v} \\ \frac{1}{w}\delta\mathbf{m_d} \end{bmatrix} \qquad \text{(Equation 2.15)}$$

where $\mathbf{D_v}$ and $\mathbf{D_d}$ are damping matrices whose influence is controlled by α_v and α_d, for velocity and depth nodes, respectively. This gives a total of two smoothing parameters and

two damping parameters for the travel-time inversion described by Equation 2.15. This gives the user a limitless number of parameter permutations for the inversion process. *Korenaga et al.* [2000] recommend a trial and error approach for the testing of these parameters by first testing parameters on a single inversion iteration, before fixing the preferred parameters for larger numbers of iterations.

2.3.3 Full-waveform inversion

Full-waveform inversion (FWI) is similar to travel-time tomography in the sense that it is an iterative inversion process. However, unlike travel-time tomography, where the inversion process looks to minimise the misfit between picked travel-times and travel-times through a velocity model, FWI looks to minimise the misfit between the observed wavefield and the calculated/synthetic wavefield generated through a velocity model.

In Chapter 4 of this study, we utilise the FWI code Full-Wavefield 3D of *Warner et al.* [2013] in order to perform a 2D, isotropic, acoustic, time-domain FWI along the eastern section of WE-1. Here we describe the how this code handles forward and inverse FWI problem, following *Warner et al.* [2013] and *Warner* [2012]. Comprehensive reviews of FWI are also provided by *Pratt et al.* [1998] and *Virieux and Operto* [2009]

2.3.3.1 Forward problem

The forward problem in FWI involves modelling seismic wave propagation through a velocity model, $\mathbf{m}$. This is achieved by solving the numerical wave equation. In this study we utilise a simple form of the wave equation, which is a second order partial differential equation, assuming the wave propagation is through an acoustic, isotropic, inhomogeneous medium, given by the equation:

$$\frac{1}{{V_p}^2}\frac{\partial^2 p}{\partial t^2} - \rho\nabla.\left(\frac{1}{\rho}\nabla p\right) = \mathrm{s} \qquad \text{(Equation 2.16)}$$

where V_p is the acoustic wave velocity, t is time, ρ is density, p is the acoustic wavefield and s is the wavefield source. The wavefield and source vary as a function of both space and time, while wave velocity and density vary only in space. This wave equation represents a linear relationship between the wavefield and the source, and can be solved by discretising

the wavefield propagation into time steps and solving through a method of finite differences. Rewriting equation 2.16 as a matrix equation gives:

$$\mathbf{Ap} = \mathbf{s} \qquad \text{(Equation 2.17)}$$

where the matrix $\mathbf{A}$ relies upon the model parameters V_p and ρ, and represents the discrete numerical implementation of the forward modelling operator:

$$\frac{1}{\mathrm{V_p}^2}\frac{\partial^2}{\partial \mathrm{t}^2} - \rho\nabla.\left(\frac{1}{\rho}\nabla\right) \qquad \text{(Equation 2.18)}$$

The wave equation can also be written as a non-linear relationship between the model, $\mathbf{m}$, and the predicted data, $\mathbf{d}$:

$$\mathbf{B}(\mathbf{m}) = \mathbf{d} \qquad \text{(Equation 2.19)}$$

where $\mathbf{B}$ is a non-linear function describing how to calculate the wavefield for a given model and source. The model, m, contains the model parameters throughout the model, which in our study is the acoustic velocity, V_p.

2.3.3.2 Inverse problem

The inverse problem looks to determine a model, $\mathbf{m}$, contained in a dataset, $\mathbf{d}$, by using a mapping operator, $\mathbf{B}$, such that:

$$\mathbf{m} = \mathbf{B}^{-1}(\mathbf{d}) \qquad \text{(Equation 2.20)}$$

This inverse problem relies on the minimisation of data residuals between the observed wavefield, $\mathbf{d_o}$, and the synthetic/calculated wavefield, $\mathbf{d_c}$. The measure of misfit between these two datasets is known as the objective function, or the L2-norm, and is the sum of squares difference between the datasets over all sources and receivers, over all times. The objective function, f, is given by:

$$f(\mathbf{m}) = \frac{1}{2}\left|\left|\delta\mathbf{d}\right|\right|^2 = \frac{1}{2}\delta\mathbf{d}^{\mathrm{T}}\delta\mathbf{d} = \sum^{n_s}\sum^{n_r}\sum^{n_t}|\mathbf{d_o} - \mathbf{d_c}|^2 \qquad \text{(Equation 2.21)}$$

where n_s, n_r and n_t are the number of sources, receivers and time samples, respectively. Minimisation of the objective function relies on the iterative perturbation of a velocity model toward the true subsurface velocities. This is achieved when the differential of the objective function, with respect to the model parameters, is zero:

$$\frac{\partial f}{\partial \mathbf{m}} = \nabla_{\mathbf{m}} f = 0 \qquad \text{(Equation 2.22)}$$

FWI starts with an estimate of the subsurface velocity, $\mathbf{m_0}$, which is typically derived from travel-time tomography modelling. The new model is defined as:

$$\mathbf{m} = \mathbf{m_0} + \delta\mathbf{m} \qquad \text{(Equation 2.23)}$$

where δm is the model update. For each iteration in the inversion scheme, the objective function of the starting model, $f(\mathbf{m_0})$, and the updated model, $f(\mathbf{m_0} + \delta\mathbf{m})$, must be considered. The objective function is assumed to be a quadratic when close to its' minimum, and can therefore be approximated as a first-order Taylor series:

$$f(\mathbf{m_0} + \delta\mathbf{m}) \approx f(\mathbf{m_0}) + \left(\frac{\partial f(\mathbf{m_0})}{\partial \mathbf{m}}\right)\delta\mathbf{m} \qquad \text{(Equation 2.24)}$$

At the minimum of the objective function the first derivative of equation 2.24 will be zero:

$$\frac{\partial f}{\partial \mathbf{m}} + \frac{\partial^2 f}{\partial \mathbf{m}^2}\delta\mathbf{m} = 0 \qquad \text{(Equation 2.25)}$$

Rearranging enables determination of the model update:

$$\delta\mathbf{m} = -\left(\frac{\partial^2 f}{\partial \mathbf{m}^2}\right)^{-1}\frac{\partial f}{\partial \mathbf{m}} = -\mathbf{H}^{-1}\nabla_{\mathbf{m}} f \qquad \text{(Equation 2.26)}$$

where $\mathbf{H}$ is a Hessian matrix of second order derivatives, and $\nabla_{\mathbf{m}} f$ is the gradient of the objective function. The Hessian matrix is a symmetric matrix of size M x M, where M is the total number of model parameters, and describes how the objective function changes with respect to changes in pairs of model parameters. The gradient ($\nabla_{\mathbf{m}} f$) is a vector of the same size as the model, **m**, and informs us of what direction to change the model.

The model update according to equation 2.26 can be calculated using direct solvers known as Newton methods, however, where models are large it becomes computationally expensive to calculate and store the inverse of the Hessian matrix. Explicit calculations of the Hessian matrix are avoided by using approximations, commonly known as Gauss-Newton or quasi-Newton methods. The code of Warner et al. [2013] uses the steepest descent method, which replaces the inverse Hessian with a scalar step length calculation, such that equation 2.26 becomes:

$$\delta\mathbf{m} \approx -\alpha\nabla_{\mathbf{m}} f \qquad \text{(Equation 2.27)}$$

where α is the step length.

There are now two terms which need to be calculated, the gradient of the objective function, $\nabla_{\mathbf{m}} f$, which indicates the direction of the model perturbation for minimisation, and the step length, α, which tells by how much to change the model in each inversion iteration.

Gradient calculation

The gradient could be determined by perturbing each of the model parameters in order to see the change in the objective function, however, this would require M + 1 forward model calculations. Instead the adjoint method of Tarantola [1984] is used. The gradient can be expressed by re-writing 2.21 as:

$$\nabla_{\mathbf{m}} f = \frac{\partial f}{\partial \mathbf{m}} = \frac{\partial}{\partial \mathbf{m}}\left(\frac{1}{2}\delta \mathbf{d}^{\mathrm{T}}\delta \mathbf{d}\right) = \left(\frac{\partial \mathbf{d}}{\partial \mathbf{m}}\right)^{\mathrm{T}} \delta \mathbf{d} = \mathbf{G}^{\mathrm{T}}\delta \mathbf{d} \qquad \text{(Equation 2.28)}$$

where $\mathbf{G}$ is a Fréchet derivative matrix, that is, the differential of the data with respect to the model parameters. We now differentiate the wavefield equation (2.17) with respect to the model parameters, **m**:

$$\frac{\partial \mathbf{A}}{\partial \mathbf{m}}\mathbf{p} + \mathbf{A}\frac{\partial \mathbf{p}}{\partial \mathbf{m}} = \frac{\partial \mathbf{s}}{\partial \mathbf{m}} = 0 \qquad \text{(Equation 2.29)}$$

As the source has no dependence on the model, this equation is equal to zero. Then, if we consider a subset $\mathbf{d}$ of the wavefield:

$$\mathbf{d} = \mathbf{D}\mathbf{p} \qquad \text{(Equation 2.30)}$$

where $\mathbf{D}$ is a diagonal matrix with non-zero values only where there are observed data, the equation 2.29 can be rearranged and multiplied by $\mathbf{D}$ to extract the wavefield only where there is data:

$$\mathbf{D}\frac{\partial \mathbf{p}}{\partial \mathbf{m}} = -\mathbf{D}\mathbf{A}^{-1}\frac{\partial \mathbf{A}}{\partial \mathbf{m}}\mathbf{p} \qquad \text{(Equation 2.31)}$$

This allows for the Fréchet derivative matrix expression (equation 2.28), in combination with equation 2.30, to be rewritten as:

$$\mathbf{G} = \frac{\partial \mathbf{d}}{\partial \mathbf{m}} = \mathbf{D}\frac{\partial \mathbf{p}}{\partial \mathbf{m}} = -\mathbf{D}\mathbf{A}^{-1}\frac{\partial \mathbf{A}}{\partial \mathbf{m}}\mathbf{p} \qquad \text{(Equation 2.32)}$$

Substituting back into equation 2.28 gives the gradient of the objective function as:

$$\nabla_{\mathbf{m}} f = \mathbf{G}^{\mathrm{T}} \delta \mathbf{d} = -\mathbf{p}^{\mathrm{T}} \left(\frac{\partial \mathbf{A}}{\partial \mathbf{m}} \right)^{\mathrm{T}} (\mathbf{A}^{-1})^{\mathrm{T}} \delta \mathbf{d} \qquad \text{(Equation 2.33)}$$

The first term in this equation, $\mathbf{p}^{\mathrm{T}} \left(\frac{\partial \mathbf{A}}{\partial \mathbf{m}} \right)^{\mathrm{T}}$, represents a forward modelling process of the wavefield, while the second term, $(\boldsymbol{A}^{-1})^{\mathrm{T}} \delta \mathbf{d}$, represents the backward propagation of the residual wavefield. This second term can be rewritten as:

$$(\mathbf{A}^{-1})^{\mathrm{T}} \delta \mathbf{d} = \delta \mathbf{p} \qquad \text{(Equation 2.34)}$$

which when rearranged gives:

$$\delta \mathbf{d} = \mathbf{A}^{\mathrm{T}} \delta \mathbf{p} \qquad \text{(Equation 2.35)}$$

where $\delta \mathbf{p}$ is the wavefield generated by a virtual source, $\delta \mathbf{d}$, and propagated by the operator $\mathbf{A}^{\mathrm{T}}$, the adjoint of the original operator in equation 2.17. This means that, finally, the gradient can be expressed as:

$$\nabla_{\mathbf{m}} f = -\mathbf{p}^{\mathrm{T}} \left(\frac{\partial \mathbf{A}}{\partial \mathbf{m}} \right)^{\mathrm{T}} \delta \mathbf{p} \qquad \text{(Equation 2.36)}$$

In order to determine the gradient, one must determine the forward wavefield, $\mathbf{p}$, the differential of the numerical operator, $\mathbf{A}$, and the back propagation of the residual wavefield, $\delta \mathbf{p}$. In simpler terms, the gradient represents the weighted zero lag cross-correlation between the forward wavefield, $\mathbf{p}$, for a certain source, with the back-propagated residual wavefield, $\delta \mathbf{p}$, for all receivers with the same source.

Step length calculation

While the gradient determines the direction of the model update toward the objective function minimum, the step-length determines by how much to perturb the model. This is done by first perturbing the model slightly in the opposite direction to the gradient. The forward wavefield is subsequently calculated through this new model, $\mathbf{m_n}$, giving a new set of data residuals, $\delta \boldsymbol{d}_{\mathbf{n}}$. If the change between the models and the change in the residuals is assumed to be linearly related, then the data residuals for the optimal step length, $\delta \mathbf{d}_{\boldsymbol{\alpha}}$, can be expressed as:

$$\delta \mathbf{d}_{\boldsymbol{\alpha}} = \delta \mathbf{d_0} + \alpha(\mathbf{d_n} - \mathbf{d_0}) = \delta \mathbf{d_0} + \alpha(\delta \mathbf{d_n} - \delta \mathbf{d_0}) \qquad \text{(Equation 2.37)}$$

where $\delta\mathbf{d_0}$ and $\mathbf{d_0}$ are calculated from the starting model and $\delta\mathbf{d_n}$ and $\mathbf{d_n}$ are calculated from the slightly perturbed model. The objective function of this equation can be written as (from equation 2.21):

$$f = \frac{1}{2}(\delta\mathbf{d_0} - \alpha(\delta\mathbf{d_0} - \delta\mathbf{d_n}))^{\mathrm{T}}(\delta\mathbf{d_0} - \alpha(\delta\mathbf{d}_0 - \delta\mathbf{d_n})) \quad \text{(Equation 2.38)}$$

Differentiating this equation with respect to α, and setting equal to zero (for minimum), gives the step-length:

$$\alpha = \frac{\delta\mathbf{d_0}^{\mathrm{T}}(\delta\mathbf{d_0} - \delta\mathbf{d_n})}{(\delta\mathbf{d_0} - \delta\mathbf{d_n})^{\mathrm{T}}(\delta\mathbf{d_0} - \delta\mathbf{d_n})} \quad \text{(Equation 2.39)}$$

With both the gradient and step length calculated, the optimal model update, leading to the minimisation of the objective function, can be determined using the equation:

$$\mathbf{m} = \mathbf{m_0} - \alpha\nabla_{\mathbf{m}} f \quad \text{(Equation 2.40)}$$

2.3.3.3 Cycle-skipping

FWI requires an accurate starting model capable of reproducing the majority of the observed wavefield to within half a seismic cycle at the lowest inversion frequency, observed seismic data, and the derivation of a source wavelet [*Virieux and Operto*, 2009]. As FWI is a localised inversion method it runs the risk of converging to a local minimum, commonly referred to as cycle-skipping [*Bunks et al.*, 1995; *Sirgue*, 2006]. Cycle-skipping occurs when seismic arrivals in the synthetic wavefield are more than 180° out of phase with that of the observed wavefield. This phenomenon results in the inversion process attempting to force a match between the observed and synthetic wavefield which is one or more cycles from the true match (Figure 2-10). In an effort to mitigate against cycle-skipping, it is common practice to start FWI at long wavelengths (low frequencies), which are easier to match within half a cycle, and systematically incorporate shorter wavelengths (higher frequencies) into the modelling, commonly referred to as multiscale FWI [*Bunks et al.*, 1995; *Sirgue*, 2006].

2.3.4 Noise cross-correlation, frequency time analysis and beamforming

Both theoretical and practical studies have shown that empirical Green's function (EGF) can be derived from the cross-correlation of seismic ambient noise recorded at two seismic receivers [e.g. *Lobkis and Weaver*, 2001; *Shapiro and Campillo*, 2004; *Roux et al.*, 2005;

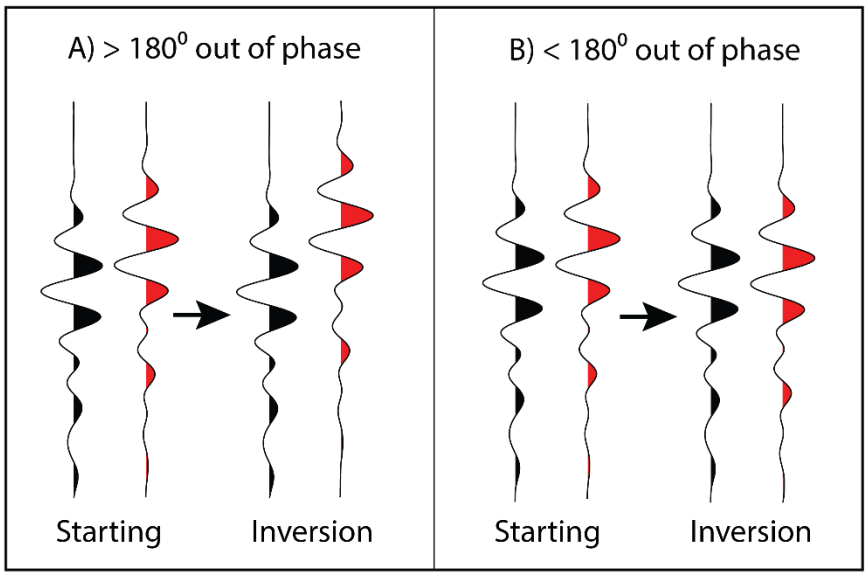

Figure 2-10: Schematic demonstration of cycle-skipping. A) When the synthetic trace through the starting model is more than 180^o out of phase with the observed trace (black), it results in cycle-skipping in the inversion. B) When the synthetic trace through the starting model is less than 180^o out of phase, the inversion converges to the correct minima, reproducing an accurate match to the observed wavefield.

Sabra et al., 2005b]. Estimates of the Green's function from ambient noise cross-correlation can be used to extract information on the shear structure of the medium separating two or more point receivers.

In Chapter 5 of this study we perform ambient noise cross-correlation to determine the group and phase velocities of fundamental Rayleigh waves. We also perform 1D and 2D beamforming in order to identify the source of ambient noise and provide and provide an alternative estimate of the phase velocity. Here we describe the methods applied, which are implemented using MATLAB based codes.

2.3.4.1 Noise cross-correlation functions and empirical Green's functions

The noise cross-correlation function (NCF) of seismic ambient noise recorded at two recording stations can used to estimate the empirical Green's function (EGF) of surface waves travelling between these two locations [*Lobkis and Weaver*, 2001; *Roux et al.*, 2005; *Sabra et al.*, 2005a; *Sánchez-Sesma and Campillo*, 2006]. The EGF determined in such manner differs only from the real Green's function by frequency dependent amplitude factor [*Lobkis and Weaver*, 2001; *Shapiro and Campillo*, 2004; *Sabra et al.*, 2005a; *Sánchez-Sesma and Campillo*, 2006]. Following *Sánchez-Sesma and Campillo* [2006], for two receivers A and B, separated by a distance d, recording the ground motion of an isotropic and diffuse wavefield, then the cross-correlation between these stations is:

$$C_{AB}(\omega) = \langle v_A(\omega) v_B^*(\omega) \rangle = |F(\omega)|^2 J_0(kd) \qquad \text{(Equation 2.41)}$$

where v_A and v_B are the recorded wavefields at A and B, ω is angular frequency, k is the wave number, $|F(\omega)|^2$ is the average spectral density of the field, J_0 is a Bessel function of the first kind, $\langle . \rangle$ represents the ensemble average, and $*$ indicates the complex conjugate. In the time domain, the NCF of the same two stations in the time-domain is:

$$C_{AB}(t) \approx \int_0^{t_c} v_A(\tau) v_B(t+\tau)\, \delta\tau \qquad \text{(Equation 2.42)}$$

where t_c is the total time of the cross-correlated data, and τ is the time-shift in signal between the two stations. The Green's function in the frequency domain for Rayleigh waves has the form:

$$G_{AB}(\omega) = \frac{1}{4}\, \mu [Y_0(kd) + i J_0(kd)] \qquad \text{(Equation 2.43)}$$

where Y_0 is a Neumann function of zero order (Y_0 and J_0 are Hilbert transform pairs), and μ is the shear modulus. Equations 2.41 and 2.43 shows that the cross-correlation of the ground motion recorded at the two stations is proportional to the imaginary part of the surface wave Green's function:

$$C_{AB}(\omega) \propto Im[G_{AB}(\omega)] \qquad \text{(Equation 2.43)}$$

where Im denotes the imaginary part of the function.

The cross-correlation of ambient noise between two receivers returns both a time positive and time negative impulse response. The NCF, $C_{AB}(t)$, represents the cross-correlation at receiver B for a theoretical point source at A, and the time-reversed NCF, $C_{BA}(-t)$, represents the cross-correlation at receiver A for a theoretical point source at B. Viewed as a time series, these impulse responses are seen at $t > 0$ response (causal signal), and as a $t < 0$ (acausal signal) (Figure 2-11) [Yao et al., 2006]. In a purely homogeneous ambient noise field these components should be symmetric in time, and are often summed together to give only the positive time component (casual signal).

Determination of either the NCF or EGF for a number of point receiver pairs, with varying separation, reveals the dispersion characteristics of surface waves [e.g. Shapiro and Campillo, 2004; Sabra et al., 2005b; Shapiro et al., 2005]. Both the group and phase velocities of surface waves can be determined from the dispersion of either the NCF or EFG,

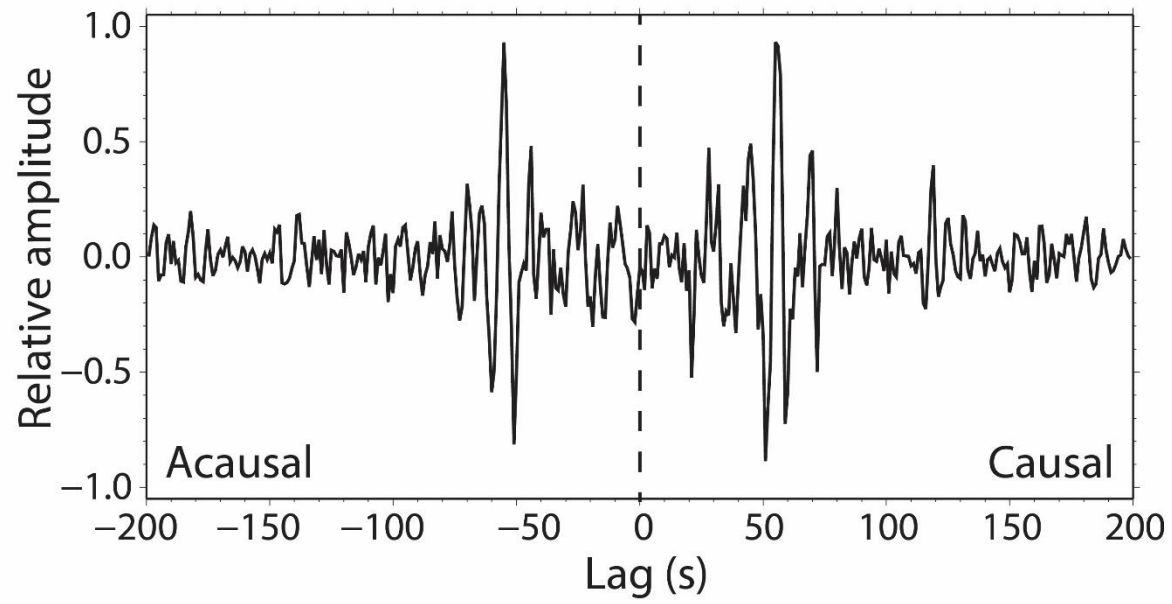

Figure 2-11: Example noise correlation function. The time positive component of the signal is referred to as the causal signal, while the negative time component is known as the acausal signal.

however, it has to be noted that the there is a $\frac{\pi}{4}$ phase shift between the NCF and EGF, which must be accounted for when determining phase velocities [Roux et al., 2005].

In this study we determine the group and phase velocities of fundamental Rayleigh waves using the NCF calculated between OBS/H within our study area.

2.3.4.2 Frequency time analysis

Group and phase velocities of fundamental Rayleigh waves can be extracted from the calculated NCF or estimated Green's function, using frequency-time analysis (FTAN) [Dziewonski et al., 1969; Levshin et al., 1989; Levshin and Ritzwoller, 2001]. In this study we use the automated frequency-time analysis algorithm (AFTAN) of Bensen et al. [2007], described here. NCF are input into the AFTAN algorithm, which constructs 2D diagrams of signal power as a function of group velocity and the central frequency/period of a suite of successive narrow-band Gaussian filters. An example of such an FTAN power diagram is seen in Figure 2-12. At each filter period the group velocity is determined by picking the peak energy of the resulting envelope of signal amplitude.

Phase velocities can subsequently be determined from these group velocities using the following equation:

$$S_c = S_u + (\omega d)^{-1}(\phi(t_u) + 2\pi N - \frac{\pi}{4}) \qquad \text{(Equation 2.44)}$$

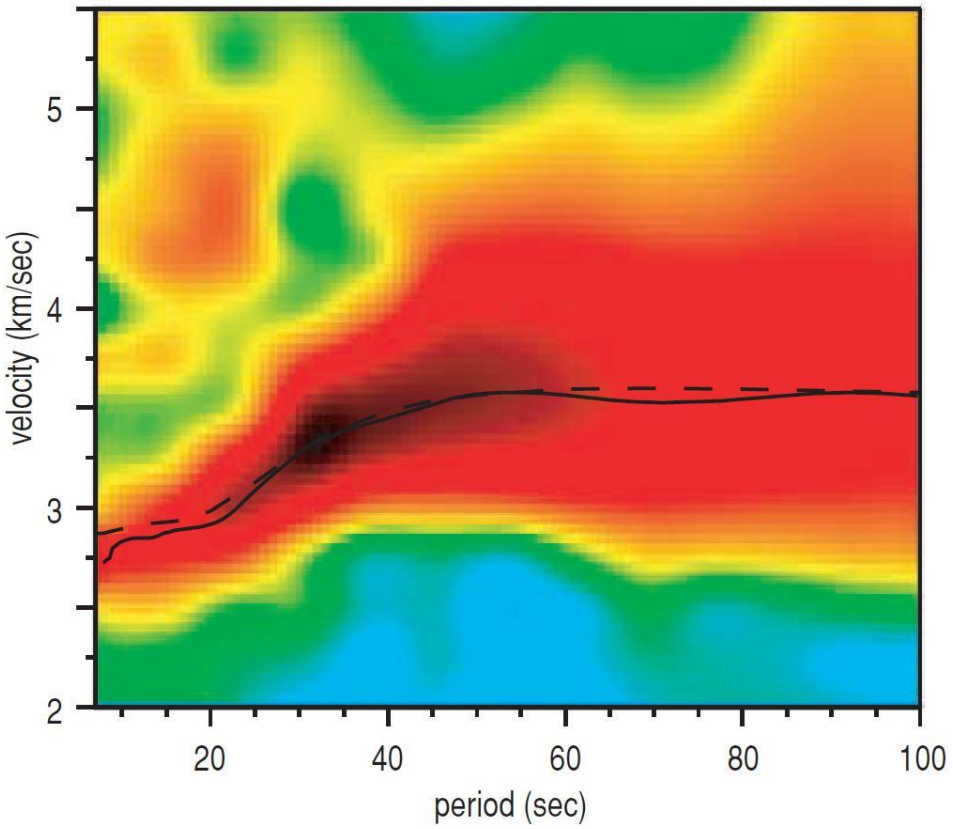

Figure 2-12: FTAN signal power plot for group velocity versus signal period. Group velocity is determined from the maximum signal power at each period, seen as the black line. After Bensen et al. [2007].

where S_c and S_u are the phase and group slowness, respectively, ω is angular frequency, d is interstation distance, $\phi(t_u)$ is the phase of the observed group arrival time, N = 0, ± 1, ± 2 … etc, $t_u = d/U$, and U is the phase velocity ($U = \frac{1}{S_u}$).

2.3.4.3 Beamforming

Beamforming is the process of recovering coherent signal between receivers in an array, assuming that such a signal is coincident with the array in the form of a plane wave [Rost and Thomas, 2002]. For ambient noise beamforming this requires the assumption that the noise sources are sufficiently far from the array, such that a surface wave arriving at the array can be approximated as a plane wave. Differential travel-times of a plane wave arriving at individual receivers within the array are a function of the slowness of the medium in which the wave is travelling, and the back azimuth of that wave. Receivers within the array which record the same wave can be time shifted based on slowness and back azimuth, which will result in the signal summing constructively when time shifted using the correct parameters [Rost and Thomas, 2002]. In our study the application of

beamforming enables the determination of Rayleigh wave phase velocities and their source direction.

2.3.4.3.1 1D Beamforming

Rayleigh wave phase velocities may be estimated from what can be described as a 1-D beamforming method, which has no dependence on azimuth. Following the methods of Harmon et al. [2010] and Harmon and Rychert [2016], the frequency domain NCF for two receivers, A and B, can be determined by integrating the phase delay of a plane wave between these receivers for all possible angles of incidence, θ , weighted by the normalised amplitude density function, $A(\theta)$

$$C_{AB}\left(\omega,\frac{d}{c(\omega)},\Theta\right)=\frac{1}{2\pi}\int_{0}^{2\pi}A(\theta)exp\left(i\frac{\omega d}{c(\omega)}cos(\theta-\Theta)\right)\delta\theta \qquad \text{(Equation 2.45)}$$

where ω is angular frequency, *d* is interstation distance, *c* is the phase velocity at a given angular frequency, and *Θ* is the interstation azimuth. The integral is reformulated as an infinite series by expansion of $A(\theta)$ in a Fourier series [Cox, 1973]:

$$\begin{aligned}C_{AB}=\ & a_0J_0\left(\frac{\omega d}{c(\omega)}\right)\\ & +2\sum_{m=1}^{\infty}i^mJ_m\left(\frac{\omega d}{c(\omega)}\right)[a_m(\omega)\,cos(m\Theta)\\ & +b_m(\omega)sin(m\Theta)]\end{aligned} \qquad \text{(Equation 2.46)}$$

where a_m and b_m are Fourier coefficients of $A(\theta)$, and J_m is a Bessel function of the first kind. For a uniform amplitude density, $C_{AB}(\omega)\approx a_0J_0\left(\frac{\omega d}{c(\omega)}\right)$, leaving no dependence on the interstation azimuth. Using the assumption that we record a homogeneous distribution of noise sources of equal amplitude, Bessel functions of the first kind (of the form $a_0J_0\left(\frac{\omega d}{c(\omega)}\right)$) can be fit to the real Fourier component of all station to station NCF, for given periods of interest ($\frac{2\pi}{\omega}$). This is achieved by calculating Bessel functions for a range of phase velocities. For each period of investigation we select the phase velocity which minimises the misfit between the calculated Bessel function and the real Fourier components of the NCF. The amplitude component, $a_{0,}$ does not influence this fitting method, as the phase velocity which best matches the Bessel functions zero crossing will yield the minimal misfit [Harmon and Rychert, 2016].

This method provides a quick estimation of the average phase velocity through the array for a range of periods. However, the result must be treated with caution as the method has no dependence on the incidence angle of plane waves, and makes the assumption that the ambient noise source is homogenous in all possible azimuths.

2.3.4.3.2 2D Beamforming

In this study we follow the methods of Gerstoft and Tanimoto [2007] in order to perform 2D ambient noise beamforming, which reveals the phase velocity and the direction of origin for ambient noise surface waves detected by our array.

Ambient noise data recorded at each receiver in the array is cut into short time series, and are Fourier transformed into the frequency domain. This results in a complex-valued vector $\mathbf{v}(\omega, t_i)$ for each frequency, where t_i is the time of the Fourier transform. This vector contains the response of all the receivers in our array. The cross-spectral density matrix is then calculated by ensemble averaging:

$$\mathbf{C}(\omega, t) = \frac{1}{N}\sum_{n=1}^{N} \mathbf{v}(\omega, t + t_n)\mathbf{v}^{\dagger}\mathbf{v}(\omega, t + t_n) \qquad \text{(Equation 2.47)}$$

where the † is the transpose complex conjugate. The cross-spectral density matrix, $\mathbf{C}(\omega, t)$, contains the phase delay between all receiver pairs, for the angular frequency ω.

The plane wave response of the receiver array is given by:

$$\mathbf{p}(\omega, s, \theta, \mathbf{r}) = \exp(i\omega s(\mathbf{r}\ \mathbf{e})) \qquad \text{(Equation 2.48)}$$

Where s is slowness, **r** is the coordinates of the receivers relative to their mean, and $\mathbf{e} = (sin\,\theta\,, cos\,\theta)^{\mathrm{T}}$. The subsequent beamformer output is given by:

$$b(\omega, s, \theta, t) = \mathbf{p}^{\dagger}(\omega, s, \theta)\mathbf{C}(\omega, t)\,\mathbf{p}(\omega, s, \theta) \qquad \text{(Equation 2.49)}$$

which can be plotted in polar coordinates in order to illustrate the coherent energy of surface waves recorded by the array at a range of slownesses and azimuths, for different wave periods.

2.4 Gravity modelling method

Seismic velocity and rock density are intrinsically related, enabling the use of gravity data and modelling to constrain and independently test the validity of seismic velocity models.

Many relationships between seismic velocity and density exist, which enable models of P-wave velocity to be converted to density. The expected gravity signature associated with derived velocity models can be calculated and compared with the observed gravity data. Coherence or mismatch between the observed and calculated gravity anomaly can highlight strengths or weaknesses in the velocity/density models of the subsurface.

In this study we write a C shell script, based on the description of Fortran code developed by Scott [2009], in order to calculate the gravity anomaly of the velocity model developed in Chapter 3. The script first converts the input compressional velocity model to density. This is achieved using is the Nafe-Drake curve, a fourth-order polynomial fit to the dataset of [Ludwig et al., 1970], which describes the relationship between P-wave velocity and density of water saturated sediment and sedimentary rocks. The fourth-order polynomial fit to the Nafe-Drake curve is described as:

$$\rho = -0.6997 + 2.2302v_p - 0.598{v_p}^2 + 0.07036{v_p}^3 - 0.0028311{v_p}^4 \quad \text{(Equation 2.50)}$$

Where ρ is the density in kg m^{-3} and v_p is the P-wave velocity in m s^{-1}.

This relationship is most accurate when converting the compressional velocities of water-saturated sediment to density but also provides a good first-order approximation of non-mantle rock densities [Brocher, 2005].

The script then calculates the contribution to the free-air gravity anomaly from all cells within the density model, at discrete observation points along the model profile, according to:

$$g_m = \sum_{n=1}^{N} \rho_n \psi_{mn} \quad \text{(Equation 2.51)}$$

Where g_m is the vertical component of gravity at observation point *m*, ρ_n is the density at grid cell *n*, and ψ_{mn} is gravitational attraction per unit density at point *m* due to cell *n*. In order to calculate the approximate gravity anomalies, it is assumed that each grid cell (*n*) in the xz plane extends to ±∞ in the y direction, forming cuboids of homogeneous density (see Figure 2-13).

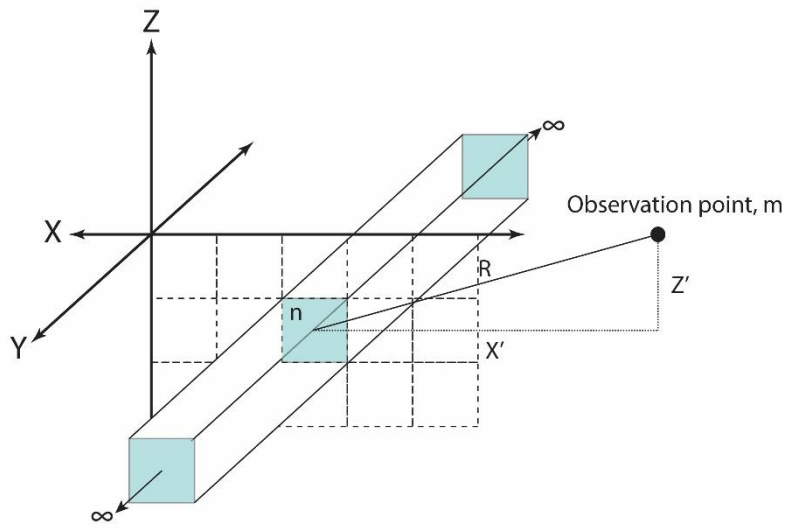

Figure 2-13: Schematic diagram of gravity model cells. Figure demonstrates the assumption that gravity can be approximated by calculating the contribution to gravity of nodes which extend infinitely in the y-direction.

The vertical contribution of such a cuboid to the gravity anomaly, observed at point m, is given by:

$$\overrightarrow{g_z} = \frac{2Ga^2\Delta\rho z}{x^2 + z^2}\hat{r} \qquad \text{(Equation 2.52)}$$

Where G is the universal gravitational constant equal to $6.67 \times 10^{-11}\,\mathrm{m^3 kg^{-1} s^{-2}}$, a is the surface area of the cell, $\Delta\rho$ is the density contrast between the cuboids density and a set background density, z and x are the depth and horizontal distance to centre of the cell from the observation point, respectively, and $\hat{r}$ is a directional vector with positive downwards.

Chapter 3: Continental hyperextension, mantle exhumation and thin oceanic crust at the continent-ocean transition, West Iberia: new insights from wide-angle seismic

Author contributions. This chapter has been published in the peer-reviewed journal *Journal of Geophysical Research: Solid Earth.* The full reference is: Davy, R., Minshull, T., Bayrakci, G., Bull, J., Klaeschen, D., Papenberg, C., Reston, T.J., Sawyer, D., and Zelt, C. (2016), Continental hyperextension, mantle exhumation, and thin oceanic crust at the continent-ocean transition, West Iberia: New insights from wide-angle seismic, *Journal of Geophysical Research: Solid Earth*, **121**(5), 3177-3199, doi: 10.1002/2016JB012825. TM, DK, CP, TR, DS and others designed the seismic experiment. CZ provided supplementary ISE-1 data. RD performed the seismic tomography and gravity modelling, with guidance from TM and GB. All authors contributed feedback on the text.

Abstract

Hyperextension of continental crust at the Deep Galicia rifted margin in the North Atlantic has been accommodated by the rotation of continental fault blocks, which are underlain by the S reflector, an interpreted detachment fault, along which exhumed and serpentinised mantle peridotite is observed. West of these features, the enigmatic Peridotite Ridge has been inferred to delimit the western extent of the continent-ocean transition. An outstanding question at this margin is where oceanic crust begins, with little existing data to constrain this boundary and a lack of clear seafloor spreading magnetic anomalies. Here we present results from a 160-km-long wide-angle seismic profile (WE-1). Travel-time tomography models of the crustal compressional velocity structure reveal highly thinned and rotated crustal blocks separated from the underlying mantle by the S reflector. The S reflector correlates with the 6.0 – 7.0 km s^{-1} velocity contours, corresponding to peridotite serpentinisation of 60 – 30 %, respectively. West of the Peridotite Ridge, shallow and sparse Moho reflections indicate the earliest formation of an anomalously thin oceanic crustal layer, which increases in thickness from ~0.5 km at ~20 km west of the Peridotite Ridge to ~1.5 km, 35 km further west. P wave velocities increase smoothly and rapidly below top basement, to a depth of 2.8 – 3.5 km, with an average velocity gradient of 1.0 s^{-1}. Below this, velocities slowly increase toward typical mantle velocities. Such a downward increase into mantle velocities is interpreted as decreasing serpentinisation of mantle rock with depth.

3.1 Introduction

Rifted continental margins are delimited by the continent-ocean transition (COT), a zone separating unequivocal thin continental crust and unambiguous oceanic crust. The present day morphology of the crust and mantle in these areas gives insight into the extensional processes which lead to the failure of continental crust and the onset of seafloor spreading [*Buck*, 1991]. To understand these processes, it is critical to image structural deformation within COT and define both its inner and outer extents. Many studies of late-stage rift processes and deformation structures have been conducted at ultra-slow extending margins, where geophysical imaging is not impeded by voluminous magmatic processes [*Whitmarsh et al.*, 1996; e.g. *Dean et al.*, 2000; *Zelt et al.*, 2003; *Van Avendonk et al.*, 2006]. However, ultra-slow extension margins pose a challenge, with low magma supply resulting

in wide transitional zones suggested to be comprised of either exhumed and serpentinised upper mantle materials, or anomalously thin oceanic crust underlain by serpentinised mantle, which can be difficult to discriminate without physical sampling [*Van Avendonk et al.*, 2006]. Wide-angle seismic studies of zones of exhumed continental mantle have shown that seismic velocities rapidly increase to ~7.6 km s^{-1} within a few kilometers of top basement [*Minshull*, 2009]. These velocities are too high to be explained by magmatic underplating at such shallow depths, and is better explained by seawater penetrating and serpentinising the unroofed mantle peridotite [*Christensen*, 2004]. However, velocities also increase rapidly to > 7.6 km s^{-1}, within a few kilometers of top basement, in areas of anomalously thin oceanic crust [*Mutter and Mutter*, 1993; *Funck et al.*, 2003]. These two basement types are sometimes distinguished from one another by the presence of, frequently weak, Moho reflections and seafloor spreading magnetic anomalies, which are attributed to the presence of oceanic crust [*Sibuet et al.*, 1995; *Pickup et al.*, 1996].

Where mantle exhumation is observed before the onset of normal seafloor spreading, the process responsible for the switch from mantle exhumation to seafloor spreading is currently poorly understood. However, observations and numerical modelling of magma-poor rift margins have shown that the extension rate may have an influence on the generation of magmatic melt and/or the exhumation of mantle materials [e.g. *Bown and White*, 1995; *Minshull et al.*, 2001; *Pérez-Gussinyé*, 2013]. Exhumation of mantle occurs at ultra-slow extension rates of < 10 mm/yr (< ~6.4 mm/yr in most observed data), while extension/spreading half-rates of > 10 mm/yr promote the generation of magmatic melt, which may be sufficient to accrete oceanic crust [*Pérez-Gussinyé et al.*, 2006; *Sibuet et al.*, 2007; *Pérez-Gussinyé*, 2013].

The Iberia-Newfoundland conjugate rifted margin is considered the archetype of magma-poor rift margins; the COT at the Iberia margin is characterized by extreme thinning of the crust (continental hyperextension), detachment faulting and the exhumation of continental mantle materials over wide areas [*Whitmarsh et al.*, 2001a; *Pérez-Gussinyé*, 2013; *Peron-Pinvidic et al.*, 2013; *Minshull et al.*, 2014]. At the conjugate Newfoundland margin the COT is much narrower [e.g. *Hopper et al.*, 2004; *Shillington et al.*, 2006; *Van Avendonk et al.*, 2006; *Van Avendonk et al.*, 2009]. Zones of mantle exhumation are observed within COT on both conjugate margins, landward of unequivocal oceanic crust [e.g. *Dean et al.*, 2000; *Van Avendonk et al.*, 2006].

Geophysical studies at the Deep Galicia margin have documented comprehensively the progressive extension, deformation and thinning of the continental crust, but no survey has extended far enough oceanward to positively identify unequivocal oceanic crust, leaving the oceanward extent of the COT undetermined. *Sibuet et al.* [1995] inferred the presence of thin oceanic crust west of the Peridotite Ridge from magnetic modelling that implied the presence of high magnetizations (5 A/m). *Whitmarsh et al.* [1996] used sparsely sampled reflection and refraction data to infer the presence of an anomalously thin oceanic crust (2.5 – 3.5 km thick), underlain by a serpentinised peridotite body, directly west of the Peridotite Ridge, and oceanic crust of normal thickness (7 km) around 20 km oceanward. Recently *Dean et al.* [2015] interpreted new multichannel seismic data west of the Peridotite Ridge. Based on basement morphology, these authors identified five ridge-like structures and propose that these structures formed through a combination of processes, starting with the continued exhumation of mantle material, transitioning to episodic volcanism which produced thin oceanic crust and the exhumation of oceanic core complexes [*Dean et al.*, 2015]. Much remains to be understood about the nature of transitional crust in these distal zones of ultra-slow extending/spreading margins, the deformation processes which bring mantle to the seafloor, and the processes which control the eventual onset of seafloor spreading.

This chapter presents new wide-angle seismic data, coincident with the multichannel seismic images of *Dean et al.* [2015]. These data extend c. 90 km west of the Peridotite Ridge and reveal new insights into the nature of the basement within the COT at the Deep Galicia margin.

3.2 Tectonic setting

The Iberia – Newfoundland ultra-slow spreading rift system is responsible for the opening of the North Atlantic Ocean. Rifting at this margin occurred in two primary phases, the earliest occurred in the Late Triassic - Early Jurassic [*Pérez-Gussinyé et al.*, 2003; *Tucholke et al.*, 2007; *Mohn et al.*, 2015]. Magnetic anomaly modelling and stratigraphic records show that rifting progressed from south to north [*Masson and Miles*, 1984; *Whitmarsh and Miles*, 1995; *Mohn et al.*, 2015]. During the first rifting phase, several fault-bound rift basin were formed in pure-shear environments on the proximal margins of the rift system (e.g. Lusitanian, Porto and Galicia Interior basins) [*Murillas et al.*, 1990; *Péron-Pinvidic et*

al., 2007; *Tucholke et al.*, 2007]. A second major episode of rifting initiated in the Late Jurassic - Early Cretaceous. During this period of extension, thinning and deformation of the continental lithosphere shifted from a broad region to focused areas at the distal margins, where the continental crust would eventually rupture [*Tucholke et al.*, 2007; *Mohn et al.*, 2015]. Extension focused on the future Iberian distal margin and resulted in the continental crust thinning to less than 10 km. In its entirety, this thinning occurred over distances of 100 – 200km [*Reston*, 2009b]. Conversely, at the conjugate Newfoundland margin, thinning was abrupt, focused over a distance of ~50 km, and is suggested to give rise to the asymmetric rift geometry [*Hopper et al.*, 2004; *Van Avendonk et al.*, 2006; *Van Avendonk et al.*, 2009]. Some authors have suggested that this structural asymmetry may be exaggerated by the final line of continental breakup, leaving the bulk of thinned crust on the Iberian margin [*Reston*, 2009b; 2010].

Focused extension and embrittlement of the continental crust on the Iberian margin led to the formation of concave downward detachment faults which exhumed mantle rock to the seafloor [*Whitmarsh et al.*, 2001c; *Lavier and Manatschal*, 2006; *Péron-Pinvidic et al.*, 2007; *Reston*, 2007a]. Initial seafloor half-spreading rates are calculated to be 7 mm/yr, and it is proposed that this ultra-slow rate has resulted in either the exhumation of large areas of mantle materials, or anomalously thin oceanic crust [*Whitmarsh et al.*, 1996; *Dean et al.*, 2000; *Srivastava et al.*, 2000; *Hopper et al.*, 2004; *Shillington et al.*, 2006; *Van Avendonk et al.*, 2006; *Pérez-Gussinyé*, 2013]. Timing of the eventual continental breakup and the onset of seafloor spreading between Iberia and Newfoundland is still widely debated, and varies along the margin [*Peron-Pinvidic et al.*, 2013]. In the southern Iberia Abyssal Plain, *Dean et al.* [2000] used seismic refraction and reflection data to identify the earliest oceanic crust, corresponding to the M3 magnetic anomaly (~130 Ma). Consistent with this interpretation, *Russell and Whitmarsh* [2003] interpreted the M3 anomaly to be the first widespread sea-floor magnetic anomaly. However, IODP drilling in the southern Iberia Abyssal Plain, and the conjugate Newfoundland margin, revealed the presence of serpentinised mantle peridotite at, or seaward of the M3 magnetic anomaly [*Whitmarsh et al.*, 2001c; *Tucholke and Sibuet*, 2007]. *Sibuet et al.* [2007] attributes these linear anomalies to the ability of serpentinites to record magnetic reversals. *Minshull et al.* [2014] revisited seismic constraints in the southern Iberia Abyssal Plain and assigned an age of 125-127 Ma to the earliest oceanic crust.

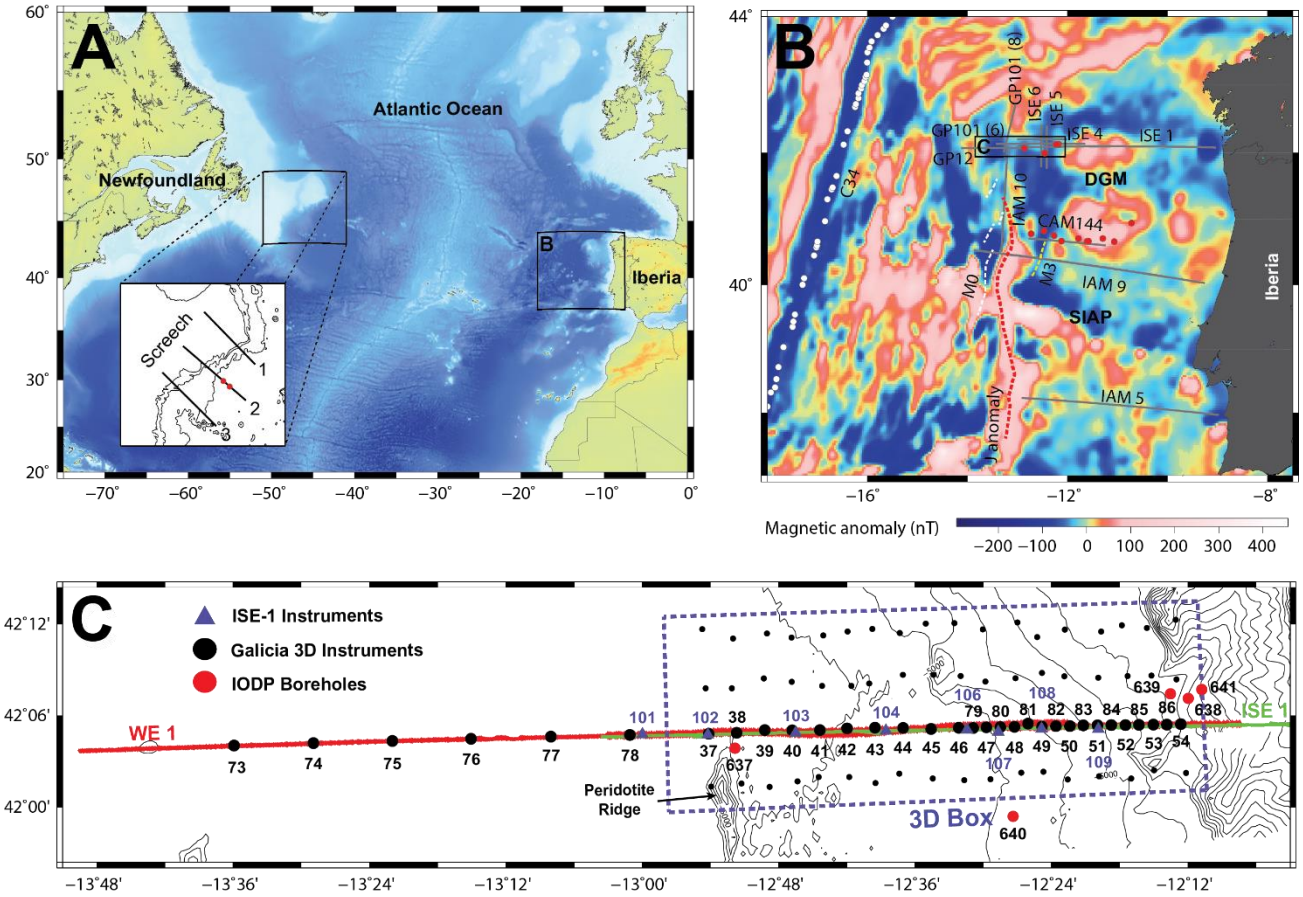

Figure 3-1: Maps of the study area. A) Bathymetric map of the North Atlantic Ocean, showing the conjugate Newfoundland and Iberia rifted margins. Inset shows the location of SCREECH seismic lines, indicated by grey lines [Funck et al., 2003; Shillington et al., 2006; Van Avendonk et al., 2006]. Red circles indicate the location of ODP boreholes. B) Magnetic anomaly map [Maus et al., 2009] over the Iberia rift margin. Previous seismic experiments are illustrated by grey lines, GP [Reston et al., 1996; Whitmarsh et al., 1996], ISE [Sawyer et al., 1997], IAM [Pickup et al., 1996; Dean et al., 2000] and CAM144 [Chian et al., 1999]. Picks of isochron C34 are shown as white circles [Klitgord and Schouten, 1986]. White dashed line represents the interpreted location of magnetic anomaly M0 [Srivastava et al., 2000], yellow dashed line represents the interpreted location of magnetic anomaly M3 [Whitmarsh and Miles, 1995]. Red dashed lines represent the location of the interpreted J anomaly [Beslier et al., 1993]. C) Map of the Galicia-3D seismic experiment. ODP Leg 103 sites are indicated by red circles [Boillot et al., 1987]. ISE-1 shooting profile is indicated by a green line; ISE-1 OBH are illustrated by blue triangles [Zelt et al., 2003]. WE-1 shooting profile is illustrated by a red line; large black circles indicate the location of WE-1 OBS/H.

Typically the onset of oceanic spreading can be identified by the first magnetic field reversal (isochron) recorded by the earliest oceanic crust. However, the late stages of continental extension and the eventual breakup of the continent, at the Iberia-Newfoundland margin, occurred during the Cretaceous constant polarity interval (121-83 Ma), resulting in a lack of strong magnetic reversals which would enable the clear identification of oceanic crust [*Bronner et al.*, 2011; *Granot et al.*, 2012]. The J anomaly is the most prominent magnetic anomaly observed within the COT at both the Iberia and Newfoundland margin

(Figure 3-1B). This anomaly is interpreted as the beginning of the M sequence of seafloor spreading anomalies (M1-M3), or alternatively as the result of a pulse of magmatism that led to continental breakup before seafloor spreading [*Sibuet et al.*, 2007; *Bronner et al.*, 2011]. The J anomaly is well defined in the southern Iberia Abyssal Plain, but rapidly decreases in amplitude north of IAM-9, and is not observed at the Deep Galicia margin.

In the Southern Iberia Abyssal Plain (Figure 3-1B), south of the Deep Galicia margin, wide-angle seismic data (Figure 3-1B) reveals a very broad continent-ocean transition, which possesses a ~190 km wide zone of exhumed mantle between extended continental crust and the onset of anomalously thin oceanic crust [*Dean et al.*, 2000; *Minshull et al.*, 2014]. The SCREECH seismic experiment (Figure 3-1A) has also revealed the presence of exhumed mantle at the eastern margin of the Grand Banks, the direct conjugate margin to the southern Iberia Abyssal Plain [*Van Avendonk et al.*, 2006]. The zones of exhumed continental mantle observed at the Grand Banks margin are found to be varied in width; 80 km on SCREECH line 3 and ~25 km on SCREECH line 2, to the north [*Shillington et al.*, 2006; *Van Avendonk et al.*, 2006]. Both of these margins have been sampled by drilling; at the Newfoundland margin by ODP leg 210 (inset Figure 3-1A) [*Tucholke et al.*, 2004]; and at the Iberia margin by ODP legs 149 and 173 (Figure 3-1B and 3-1C) [*Sawyer et al.*, 1994; *Whitmarsh et al.*, 1998]. Sites from these drilling expeditions are situated within the COT at each margin and many sites recovered serpentinised mantle peridotite. Sites 1277 and 1070 were drilled on outer highs, at the oceanward limit of the COT at the Newfoundland and Iberia margins, respectively, and recover exhumed mantle interspersed with intrusive mafic material.

At the Deep Galicia margin, continued extension of the continental lithosphere was accommodated by a complex pattern of faulting, resulting in extreme crustal thinning from ~30 km to just a few km over distances of 100 - 200 km [*Reston*, 2009b]. Initial extension is inferred to have been accommodated on high angle normal faults, forming large rotated fault blocks (10-20 km wide) where the crust was between 20-30 km thickness [*Ranero and Pérez-Gussinyé*, 2010]. How continued extension was accommodated by fault structures is still debated, with sequential and polyphase faulting being the two primary mechanisms proposed [*Ranero and Pérez-Gussinyé*, 2010; *Reston and McDermott*, 2014]. The latter authors propose that with continued extension, blocks of continental crust, bound by normal faults, were rotated to low angles to a point where the faults locked up, and new

preferentially oriented faults were cut through the existing faults and fault blocks [*Reston*, 2007b; *Reston and McDermott*, 2014]. In the sequential faulting mechanism, continued extension either reactivated existing faults, rotating them to lower angles, or cut new preferentially oriented faults through the thinned crust, but not cutting previous faults. Deformation at any one time is focused on a single fault, with successive faults cutting through crust thinned by the preceding fault, resulting in a migrating rift center and the formation of hyperextended crust, giving rise to an asymmetric rift system [*Ranero and Pérez-Gussinyé*, 2010; *Pérez-Gussinyé*, 2013].

As the crust continued to extend, thin and cool, the ductile mid and lower crust became progressively brittle, becoming completely brittle once the continental crust was < 10 km thick, commonly referred to as hyperextension, coupling the entire crust and enabling concave down listric faults to penetrate through to the underlying mantle [*Pérez-Gussinyé and Reston*, 2001; *Pérez-Gussinyé et al.*, 2003; *Pérez-Gussinyé*, 2013]. Such faults acted as conduits, allowing the hydration of the upper mantle and formation of a layer of structurally weak serpentinised mantle [*Pérez-Gussinyé and Reston*, 2001]. As a result, listric faults (responsible for hydrating the mantle) soled out into this structurally weak layer, forming a large detachment fault, known as the S reflector, oriented at a low angle (< 20^{o}) [*Reston et al.*, 2007]. In the final stages of rifting, serpentinised subcontinental mantle was exhumed to the seafloor along the S reflector. Immediately seaward of the S reflector is the Peridotite Ridge, which is suggested to mark the landward limit of oceanic crust [*Sibuet et al.*, 1995; *Whitmarsh et al.*, 1996]. The Peridotite Ridge was sampled by ODP site 637 during ODP leg 103, and returned serpentinised mantle peridotite [*Boillot et al.*, 1987]. At the Flemish Cap, the conjugate to the Deep Galicia margin, data from the SCREECH 1 seismic profile was used to interpret a ~50 km wide transition zone comprised of anomalously thin oceanic crust underlain by partially serpentinised upper mantle [*Hopper et al.*, 2004]. These existing studies of the Iberia – Newfoundland margin show that the continent-ocean transition decreases in width with northward progression along the margin, despite the fact that the transition zone has not yet been delimited, oceanward, at the Deep Galicia margin.

3.3 Data acquisition and processing

3.3.1 GALICIA-3D and ISE-1 – Wide angle and reflection datasets

The Galicia 3D project was a joint reflection and wide angle seismic experiment performed between 1 June 2013 and 2 August 2013. 3D multichannel reflection seismic was recorded over an area of 65 x 25 km by the RV Marcus G. Langseth, while an array of 72 ocean bottom seismometers and hydrophones (OBS/H), from the UK Ocean Bottom Instrumentation Facility (OBIF) [*Minshull et al.*, 2005] and GEOMAR, recorded wide angle seismic arrivals. This survey area, referred to as the 3D Box, encompasses geologic features of interest such as the S reflector detachment fault, hyper-extended continental crust and the Peridotite Ridge.

The focus of this study is on a 2D seismic line, a subset of the Galicia 3D dataset, which runs through the 3D Box and extends an additional ~90 km westward (Figure 3-1C); the entire length of which is 157 km and is referred to as Western Extension 1 (WE-1). Thirty-two OBS/H were deployed on the WE-1 multichannel seismic profile, which is coincident with the western limit of the ISE-1 seismic line (Figure 3-1C) [*Sawyer et al.*, 1997; *Zelt et al.*, 2003] . The easternmost section of WE-1 consisted of 17 instruments within the 3D Box, spaced densely at ~1.7 km intervals, with the intention to produce a high detail 2D velocity model of the seismic structure above and below the S reflector. The central section of WE-1 comprised 9 OBS, spaced at distances of ~3.4 km, covering the Peridotite Ridge and the sedimentary basins on its western and eastern flanks. The western section of WE-1 comprised 6 OBS, spaced ~9.7 km apart. The intention of this western section was to produce seismic images and a velocity model westward of the Peridotite Ridge in order to resolve the nature of basement and potentially identify the landward limit of oceanic crust. OBIF and GEOMAR instruments record at a frequency of 250 Hz and 200 Hz, respectively. Two of the 32 OBS were not retrieved, while another three instruments returned no usable data. The seismic source comprised two 3,300 cu. in. air gun arrays, towed at a depth of 9 m. A total of 2,727 shots were recorded along WE-1. Within the 3D box the two gun arrays were fired alternately every 37.5 m (a shot interval of ~16 s), intended for high resolution 3D reflection imaging. Outside of the 3D box, the 2D line was shot by a single 3,300 cu. in. gun array every 150.0 m (an interval of ~64 s), with the aim of yielding data with a higher signal-to-noise ratio, for the purpose of tomography modelling.

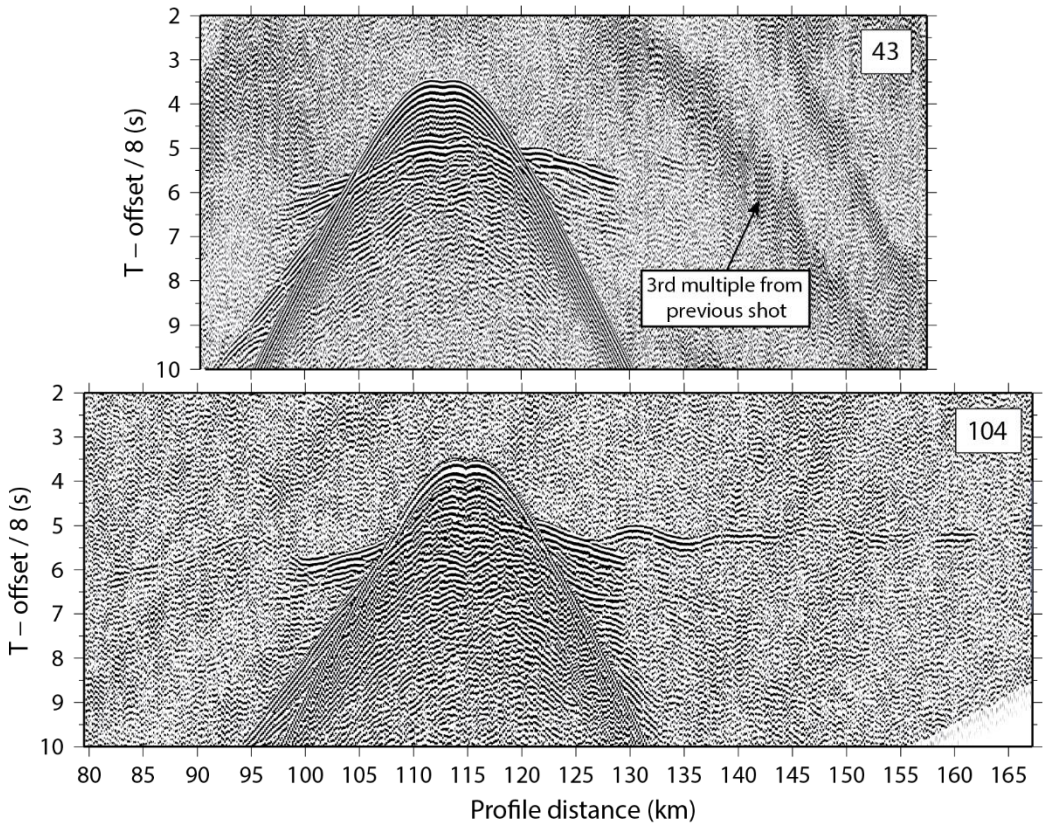

Figure 3-2: Data comparison between Galicia-3D OBS (43) and ISE-1 OBH (104), highlighting the additional noise introduced by a sub-optimal shooting in interval (~16 s) and smaller source array. These instruments are located within 1.3 km of one another and should exhibit seismic arrivals from common subsurface structure.

Several other datasets have been collected at the Galicia margin, most notably the Iberia Seismic Experiment (ISE) dataset, collected in 1997, which consists of wide-angle and MCS data [*Sawyer et al.*, 1997; *Zelt et al.*, 2003]. ISE-1 is a 2D profile, coincident with the eastern section of WE-1; the western limit of the shooting line terminates 10 km west of the Peridotite Ridge, and extends 335 km eastward. Eight OBH from this study lie along the eastern section of WE-1, spaced 4–10 km apart (8 km on average). Seismic shots, from an 8,385 cu. in. gun array, were fired every 60 s, approximately four times the period of the seismic shots within the 3D box of Galicia-3D experiment. Greater shot intervals in the ISE experiment produce seismic records with higher signal-to-noise ratio (Figure 3-2), enabling travel-time picks to greater offset, and thus improving the depth of tomographic imaging within the 3D box. For these reasons, the ISE-1 data were used to complement the WE-1 dataset. The final tomography modelling utilized a total of 34 OBS/H.

3.3.2 Data processing

For each instrument, clock drifts were determined and corrected for using GPS synchronized clocks. OBS/H were relocated to adjust for any variation in the deployment position during the ~5 km descent through the water column. The relocation procedure minimized the least squares misfit between the observed direct water wave arrival to each instrument and those calculated for depths determined from bathymetry collected during the Galicia-3D survey. On average each instrument was relocated by 315 m. Within the 3D Box there is a low signal-to-noise ratio (Figure 3-2), which is a result of poorly attenuated noise in the water column from the previous shot. In order to improve the signal-to-noise ratio, a minimum phase Ormsby band-pass filter (2-4-8-16Hz) was applied to all receiver gathers.

3.4 Data analysis

3.4.1 Phase identification and picking

In order to build a compressional velocity model of WE-1, the P wave arrivals through the subsurface must be correctly identified. These arrivals were best observed on the hydrophone channel of the OBS/H and therefore this channel was used for travel-time picking. Confident identification of refracted and reflected arrivals through post-rift sediments is made difficult by the depth of the sea-floor (4.2 – 5.3 km), a thin sedimentary cover along the seismic profile (< 1.0 – 2.0 km) and interference from high-amplitude earlier seismic arrivals. Where sediment refractions were identified, they have apparent velocities up to 3.0 km s^{-1}. We identified and picked 758 sediment refraction picks and 655 reflection picks from a prominent inter-sedimentary reflector. Crustal refractions east of the Peridotite Ridge have apparent velocities > 4.5 km s^{-1}, and highly varied travel-time arrivals owing to extreme basement topography (rotated fault blocks). A reduction velocity of 8 km s^{-1} was applied to help correlate the boundary between crustal and mantle arrivals, with mantle arrivals appearing horizontal in reduced data sections (Figure 3-3). However, beneath the S reflector, the mantle is serpentinised, which results in mantle arrivals with apparent velocities varying from ~6.0 km s^{-1} to ~8.0 km s^{-1}. West of the Peridotite Ridge all instruments, excepting 73, exhibit seismic arrivals with apparent velocities > 7.0 km s^{-1} arriving at short offsets of 13.0 km or less. Between these high-velocity arrivals and the

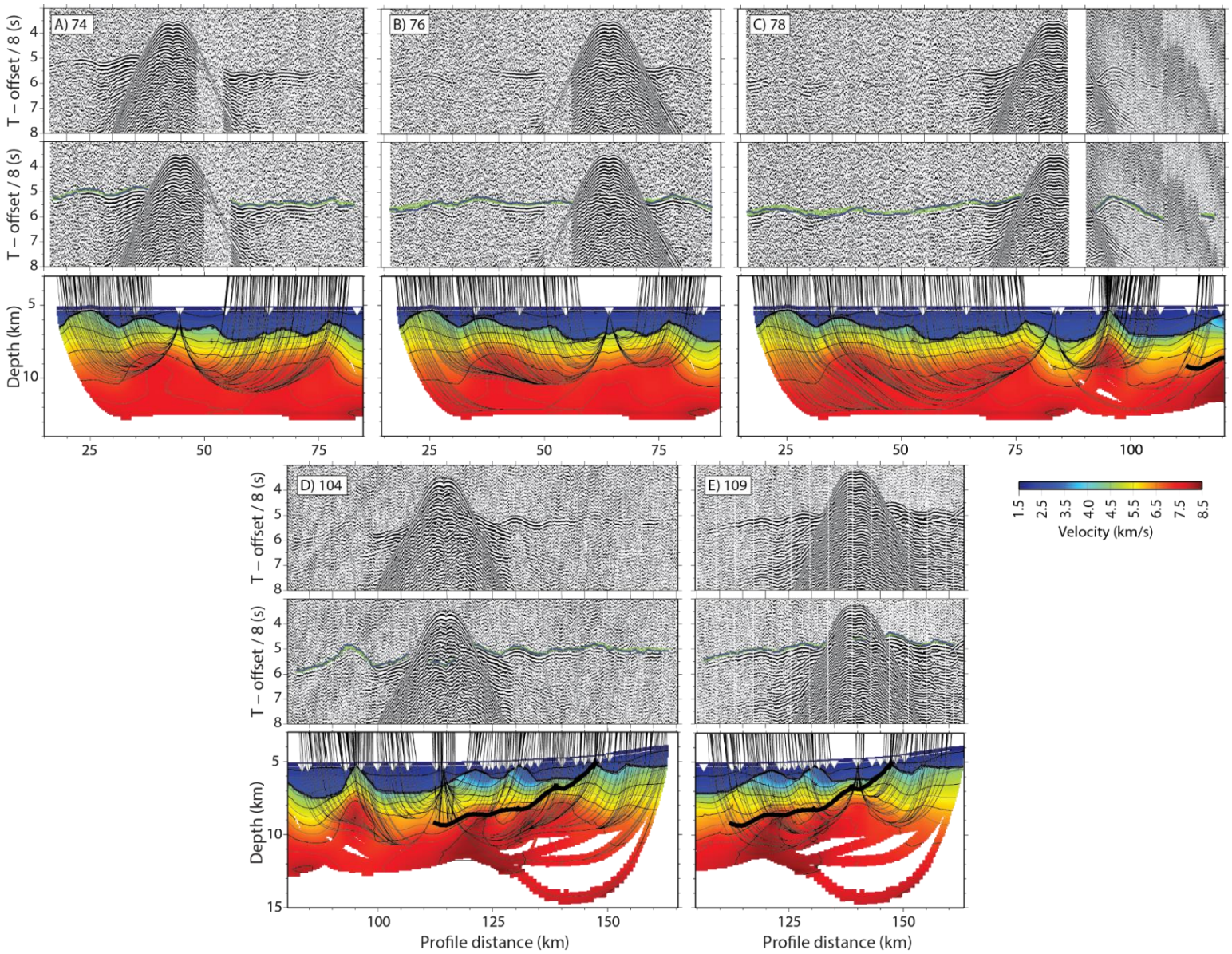

Figure 3-3: Observed and modelled data for instruments 74, 76, 78, 104 and 109. Top panels: Receiver gathers limited to offsets exhibiting identifiable first arrivals. Receiver gathers are filtered using a minimum phase Ormsby band-pass filter (2-4-8-16 Hz). Middle panels: Receiver gathers with observed and calculated travel times illustrated. Green bars indicate seismic arrival picks and their associated uncertainty, blue squares indicate the calculated travel times through the final velocity model. Bottom: Calculated ray paths through final TOMO2D velocity model. Thick black lines are the resolved S-reflector from TOMO2D modelling. Plots of the velocity model have a vertical exaggeration of 4.5.

Data Set	Pick Uncertainty (Relative to instrument offset)	Average Pick Uncertainty
WE-1 (16 s)	40 ms + 1.5 ms/km	± 60.0 ms
WE-2 (64 s)	30 ms + 1.0 ms/km	± 54.9 ms
ISE-1	30 ms + 0.5 ms/km	± 44.6 ms

Table 3-1: Travel-time picking uncertainties assigned to the WE-1 and ISE-1 datasets, and the average picking uncertainty.

direct arrival, limited linear refractions with apparent velocities of 4.5 km s^{-1} – 5.0 km s^{-1} are observed. We assume that the apparent velocity of 4.5 km s^{-1} is associated with the top of the reflective basement. The travel-times of these high-velocity seismic arrivals show high lateral variability, which correlates strongly with the basement topography observed in the seismic reflection data. First arrival travel-times observed west of the Peridotite Ridge quickly reach apparent velocities of > 7.0 km s^{-1}, with little evidence of velocities indicative of continental crust; we refer to these as basement arrivals (Pb). We identified and picked 9,517 first arrival travel-times from prominent seismic refractions through the crust, basement and mantle (e.g. Pg, Pb and Pn). The velocity contrast between thin continental crust and exhumed mantle (the S reflector) generates reflections which are considered to be PmP arrivals. A total of 1,187 near-vertical reflections from the S reflector (PmP) were identified and picked after the direct arrival, without the application of a band-pass filter; band pass filtering causes the coda from the direct arrival and other arrivals to coalesce with the S-reflection coda, prohibiting accurate identification.

Picking uncertainties are assigned for each dataset, based on the inspection of individual traces and their offset from the recording OBS/H. Table 3-1 details the pick uncertainty, relative to offset, assigned to each dataset and the average pick uncertainty.

3.4.2 Sedimentary arrivals

A lack of clear refraction and reflection arrivals from the sedimentary layering resulted in a tomographic inversion with little constraint in the post-rift sedimentary layers, a lack of definition at the top of the basement and a sparse resolution of sedimentary velocities Therefore for the sediment cover along WE-1, we developed a forward model using the code of *Zelt and Smith* [1992]. This model utilizes top basement depths from the MCS images of *Dean et al.* [2015], reflected arrivals from the top of basement, a consistent

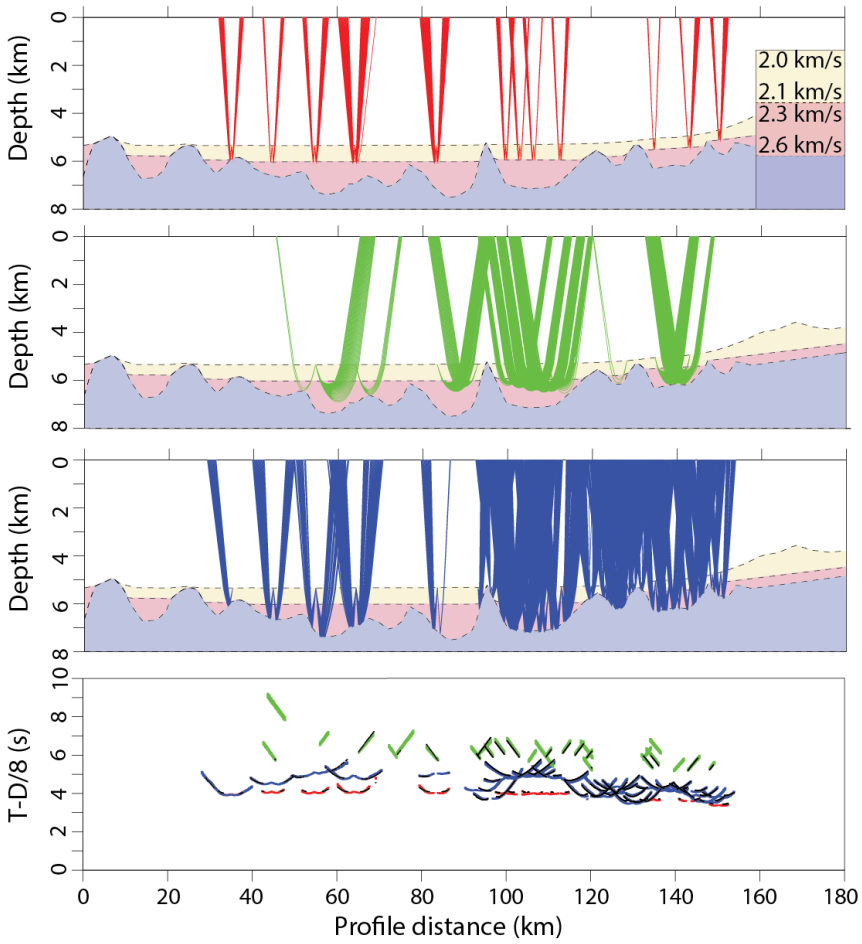

Figure 3-4: Sediment velocity model. From top to bottom: ray paths of inter-sedimentary reflections, ray paths of refractions through the lower sedimentary layer, ray paths of basement reflections, fit of calculated travel times (black points) with observed travel times (coloured points).

inter-sedimentary layer boundary, and limited refracted arrivals from the lower sedimentary layer. We assumed that seismic velocities are laterally homogeneous along the profile. Model layers and their associated velocities were adjusted to minimize the misfit between calculated and observed travel-times. The final sediment velocity model (Figure 3-4) has a RMS travel-time misfit of 67 ms and a chi-squared ($\chi 2$) value of 1.38. Sediment velocities in the upper layer increase from 2.0 to 2.1 km s^{-1}, while in the bottom layer these velocities increase from 2.3 to 2.6 km s^{-1}.

3.4.3 Basement arrivals

Tomographic modelling of crustal structure was performed using "TOMO2D", the joint reflection and refraction inversion algorithm of *Korenaga et al.* [2000]. This method allows the determination of a 2D velocity field by simultaneous inversion of both first arrival travel-times and later reflected arrivals from a geological interface. The iterative

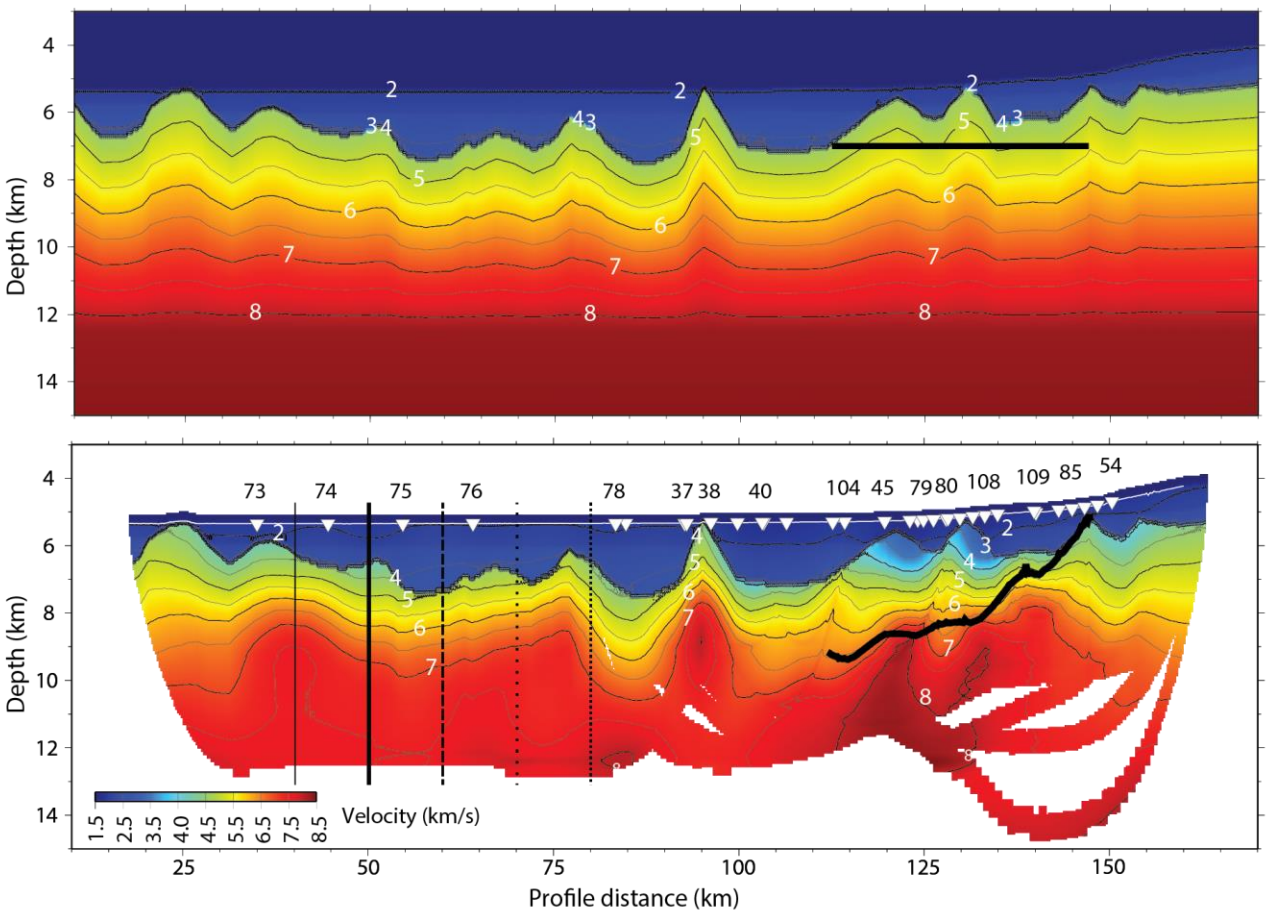

Figure 3-5: TOMO2D velocity modelling. Top: Input velocity model to the TOMO2D joint inversion process. Thick black line represents the arbitrary surface, which represents the S reflector. Bottom: Final TOMO2D velocity model after 10 inversion iterations. Thick black line represents the modified S-reflector after the inversion process. White inverted triangles illustrate the location of ocean bottom instruments used in this inversion process; a select number of instruments are labelled. Black vertical lines of varying thickness and dashes indicate the location of 1D velocity profiles illustrated in Figure 3-12. Plots have a vertical exaggeration of 4.5.

tomographic inversion process requires an input velocity and interface model, and observed refraction and reflection travel-times.

The input velocity model is defined by a sheared mesh which hangs from the seafloor bathymetry. Model cell size is 250 m in the horizontal direction, while the vertical size increases from 25 m directly below the seafloor, to 250 m at the base of the model at 15 km depth. We used the sediment velocity model from forward modelling to define the shallow structure in the input model, below which velocity smoothly increases from 4.5 km s^{-1} (below the top of reflective basement) to 8.3 km s^{-1} at 12.5 km model depth, and 8.4 km s^{-1} at 15.0 km depth. The velocity of 4.5 km s^{-1} at the top of basement was chosen based on observations of refracted arrivals observed on instruments west of the Peridotite Ridge.

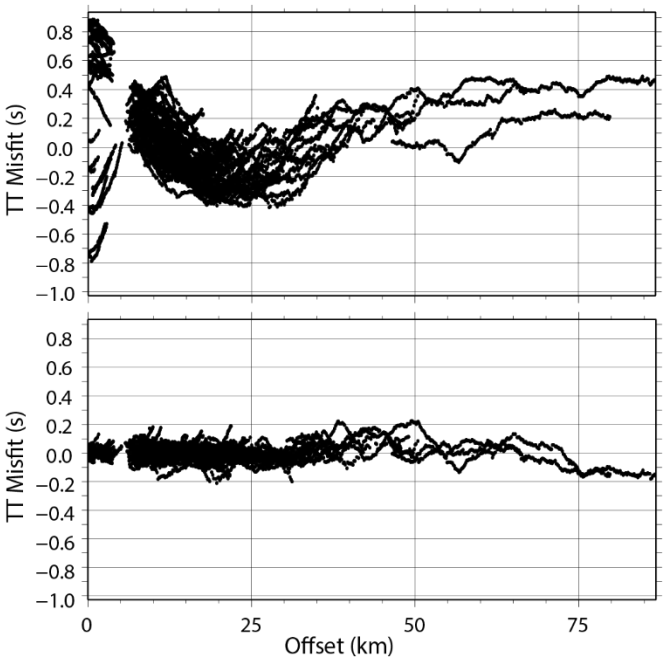

Figure 3-6: Travel time misfit between the observed seismic travel-times and the calculated travel times through the (top) input and (bottom) final compressional velocity models. Travel-time misfit is plotted against absolute offset from the recording instruments as black points.

In this model the S reflector is treated as the Moho and a floating reflector, representing the surface of the S reflector, is arbitrarily defined as a horizontal line at a depth of 7 km, with node spacing of 250 m. Extensive parameter testing was undertaken in order to find the simplest, geologically reasonable model with low travel-time misfit to the observed data. From these results we selected horizontal correlation lengths that increase from 2.0 km at the seafloor to 4.0 km at the base of the model, and vertical correlation lengths increasing from 0.5 km at the seafloor to 1.0 km at the base of the model. A depth weighting kernel of 0.2 was selected to favor velocity perturbations over interface depth perturbations. Sedimentary velocities were allowed to vary through the inversion process. Travel-time pick and misfit statistics for the final 2D velocity model (Figure 3-5) are detailed in Table 3-2.

	Travel-time picks	**RMS travel-time misfit**	**Chi-square (χ^2)**
Overall	10,717	53 ms	0.97
Refracted arrivals (Pg, Pb and Pn)	9,530	53 ms	1.01
S reflection arrivals (PmP east)	1,187	31 ms	0.65
PmP arrivals (PmP west)	100	65 ms	-

Table 3-2: Travel-time pick and misfit statistics

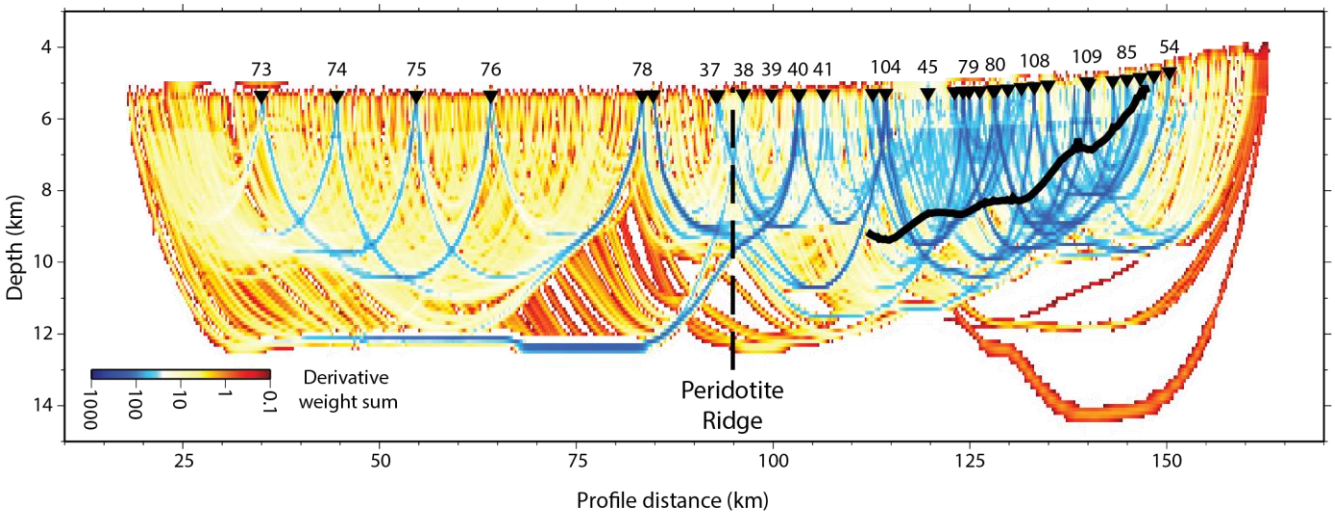

Figure 3-7: *Derivative weight sum of seismic rays traced through the TOMO2D velocity model. Higher DWS values indicate areas where a higher density of rays have sampled model cells. Thick black line is the S reflector. Vertical dashed line indicates the axis of the Peridotite Ridge. Selected instrument numbers are indicated. Plot has a vertical exaggeration of 4.5.*

No individual instrument has a RMS travel-time misfits exceeding 98 ms. Individual travel-time misfits rarely exceed 200 ms, and exhibit a significant reduction in travel-time misfit between the input and final velocity models (Figure 3-6).

3.4.4 Resolution and accuracy

Tomography modelling produces a non-unique model, with uncertainty introduced from travel-times picking, the input velocity model and the model parameterization. Therefore it is critical to assess the resolution and accuracy of the final velocity model.

3.4.4.1 Derivative weight sum

Ray coverage through the final velocity model is represented by the derivative weight sum (DWS). There is an excellent ray coverage east of the Peridotite Ridge (95 – 150 km) at depths between 6 and 10 km (Figure 3-7), encompassing the S reflector. Moderate ray coverage is observed west of the Peridotite Ridge (20 – 95 km) at depths of 6 – 10 km. Below 10 km depth the ray coverage is often moderate to poor, with many of the model cells being sampled solely by unidirectional ray paths. High derivative weight sums west of the Peridotite Ridge are observed at a depths between 12.0 - 12.5 km, and show rays travelling through a limited range of depths. These rays come solely from instrument 38 and 40, east of the Peridotite Ridge, which have RMS travel-time misfits of 37 ms and 81 ms, respectively.

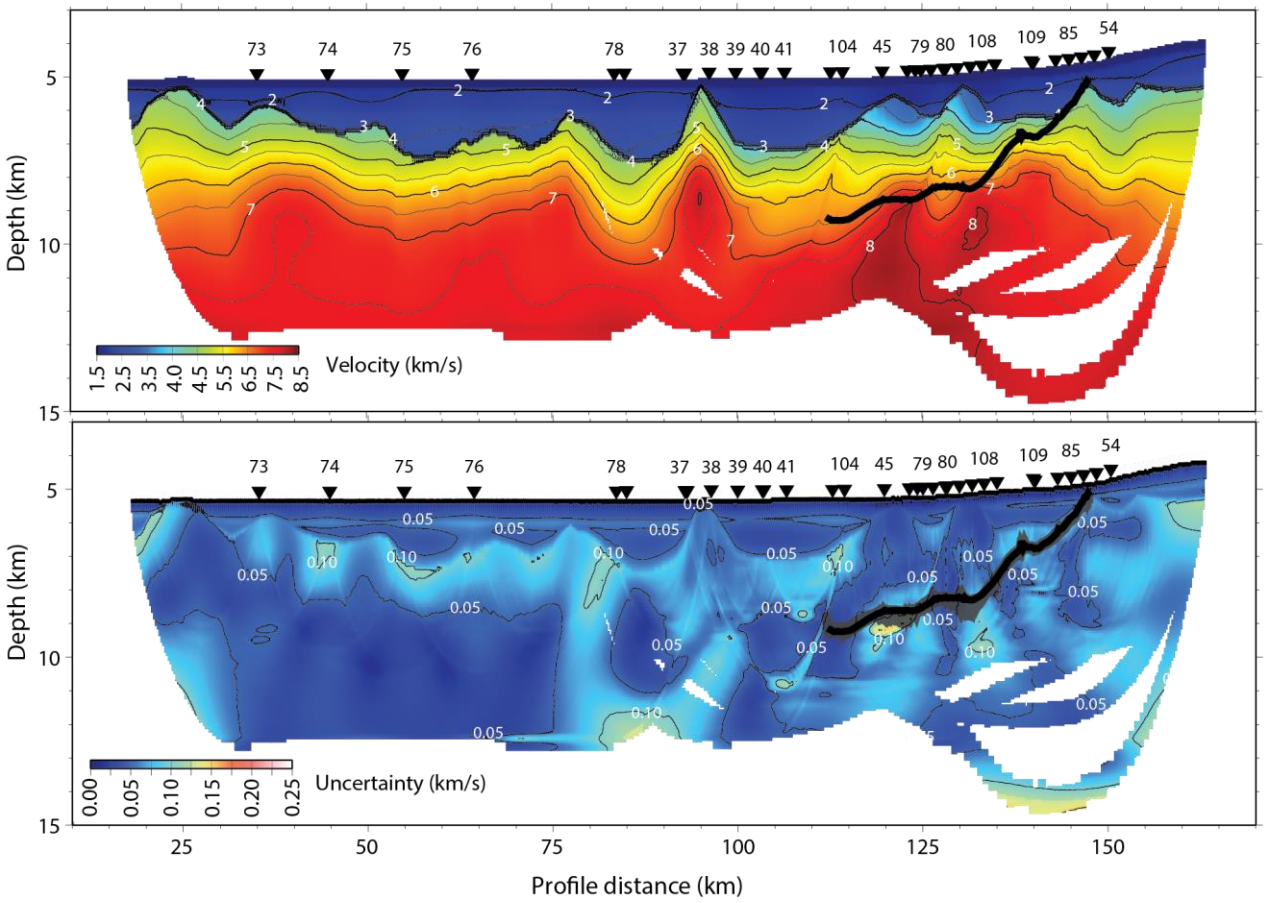

Figure 3-8: Monte Carlo uncertainty test results. Top: Average velocity model from the 100 model realizations. Thick black line illustrates the average S reflector surface. Bottom: Velocity uncertainty of the average velocity model. Uncertainty is taken as one standard deviation of the 100 model realizations from the average velocity model. Gray envelope represents the range of all resolved S Reflection surfaces. Black inverted triangles illustrate the location of ocean bottom instruments. Plots have a vertical exaggeration of 4.5.

3.4.4.2 Monte Carlo uncertainty analysis

Monte Carlo uncertainty testing [*Korenaga et al.*, 2000] enables us to assess quantitatively the uncertainty associated with the final compressional velocity model. Uncertainty in the velocity model arises from a combination of error in data picking, the starting model used, and the geometry and execution of the seismic experiment [*Zhang and Toksöz*, 1998; *Sallarès et al.*, 2011]. For our compressional velocity model we performed one hundred inversion realizations, which required the generation, and tomographic inversion, of 100 randomized input velocity models, randomized reflector depths, and "noisy" travel-time datasets. Input velocity models were generated by randomizing the original input model by ± 5% the original velocities, resulting in velocities of ± 0.10 km s^{-1} at the top of the sedimentary layers, ± 0.23 km s^{-1} at the top of reflective basement, and ± 0.42 km s^{-1} at the base of the model. The depth of the input reflector, representing the S reflector, was

randomized by ± 2.0 km. "Noisy" travel-time datasets were generated by adding randomized timing errors, including a common receiver error (± half the maximum receiver error, with a maximum of ± 58 ms), and picking errors (± half the individual pick error) [*Zhang and Toksöz*, 1998; *Korenaga et al.*, 2000]. Then, the tomographic inversion was repeated for randomized velocity model, reflector depth, and noisy travel-time dataset triples, using the same inversion parameters which generated the final velocity model (Figure 3-5). The mean deviation of all 100 realizations can be interpreted as a statistical measure of the uncertainty in the averaged velocity model (Figure 3-8) [*Tarantola*, 1987]. Through a large area of the model the velocity uncertainty is observed to be < ± 100 ms^{-1}. East of the Peridotite Ridge there are lobes of higher velocity uncertainty, with the most prominent reaching ± ~150 ms^{-1} and corresponding to the high-velocity lobe directly below the S reflector, between profile distances of 120 – 125 km. West of the Peridotite Ridge, a zone of low uncertainties (< ± 50 ms^{-1}) between 30 – 75 km profile distance, underlies higher uncertainties (± 50 – 100 ms^{-1}) at the top of the basement, and extending to depth between 75 – 85 km profile distance.

3.4.4.3 Checkerboard testing

Checkerboard tests (Figure 3-9) enable us to determine quantitatively the scale of resolvable structure in the final velocity model [*Zelt and Barton*, 1998]. Sinusoidal velocity perturbations of ± 5% were introduced in a checkerboard pattern to create reference models. Rays were traced through these reference models using a forward ray tracing method and the same shot-receiver geometry as the original inversion, producing synthetic travel-times through each reference model. Random timing errors were added to these synthetic travel-times, as described in the previous section, and were then inverted with the original model inputs and parameters [*Zhang and Toksöz*, 1998; *Korenaga et al.*, 2000]. The difference between these inversion results and the final velocity model were used to determine the length scale of structure resolved in the final velocity model.

Large-scale anomalies (25 km x 5 km) appear to be well resolved throughout the model at depths of 5 – 10 km, with the exception of the western and eastern limits, where the model is resolved by unidirectional ray paths. West of Peridotite Ridge (95 km profile distance), resolution below 10 km depth is poor for anomalies smaller than 25 km x 5 km, likely as a result of the limited ray coverage at this depth and the unidirectional rays from instrument 38 and 40. Anomalies below 10 km, east of the Peridotite Ridge, are recovered to a greater

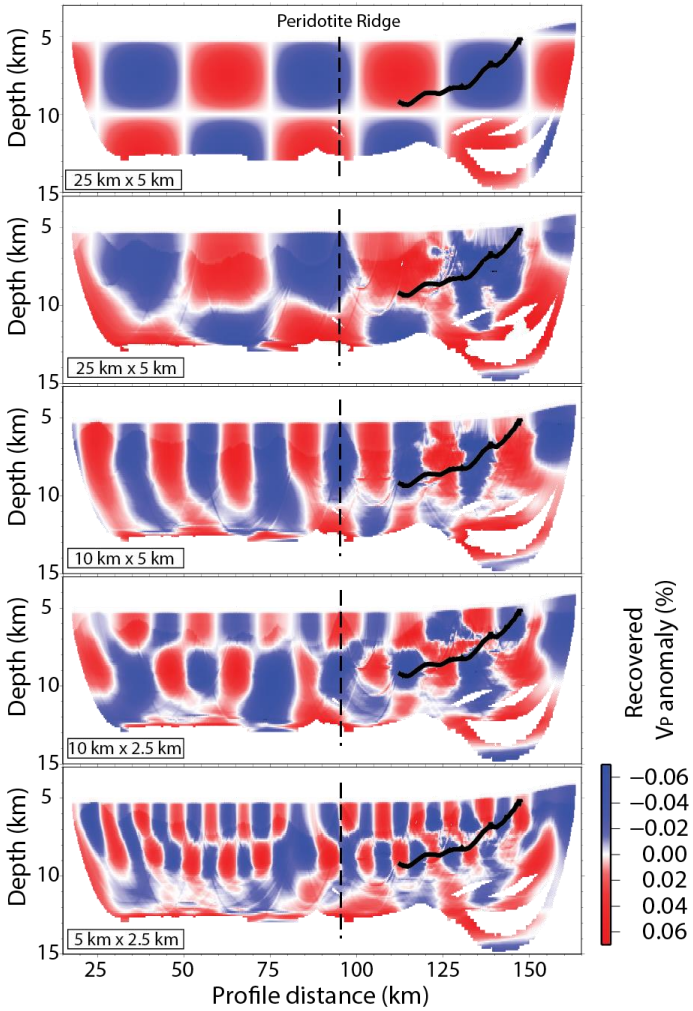

Figure 3-9: Checkerboard resolution test results. Top: input velocity anomalies for the 25 x 5 km checkerboard in order to demonstrate the boundaries between cells. Recovered velocity anomalies from the checkerboard tests are below. Second from top to bottom the anomaly dimensions are: 25 x 5 km, 10 km x 5 km, 10 km x 2.5 km and 5 km x 2.5 km, horizontally and vertically, respectively. Vertical dashed line indicates the axis of Peridotite Ridge. Plots have a vertical exaggeration of 4. 5.

degree than those westward, but are not as well resolved as those at shallower depths. Small-scale anomalies (10 km x 2.5 km and 5 km x 2km) are well resolved throughout the model to depths of 10 km, with the exception of anomalies at 80 – 90 km profile distance, where a gap in the seismic profile has resulted in limited ray coverage in this region. Resolution of small-scale anomalies is excellent above the S reflector, where ray coverage is densest, with the boundaries between tiles of opposite anomaly polarity exhibiting a reasonable match between the input and recovered velocity anomalies (Figure 3-7). The results of these checkerboard tests give confidence to the interpretation of large, basement scale velocity features west of the Peridotite Ridge, as well as the interpretation of smaller structures on the 5.0 x 2.5 km scale, associated with the S reflector and continental hyperextension east of the Peridotite Ridge.

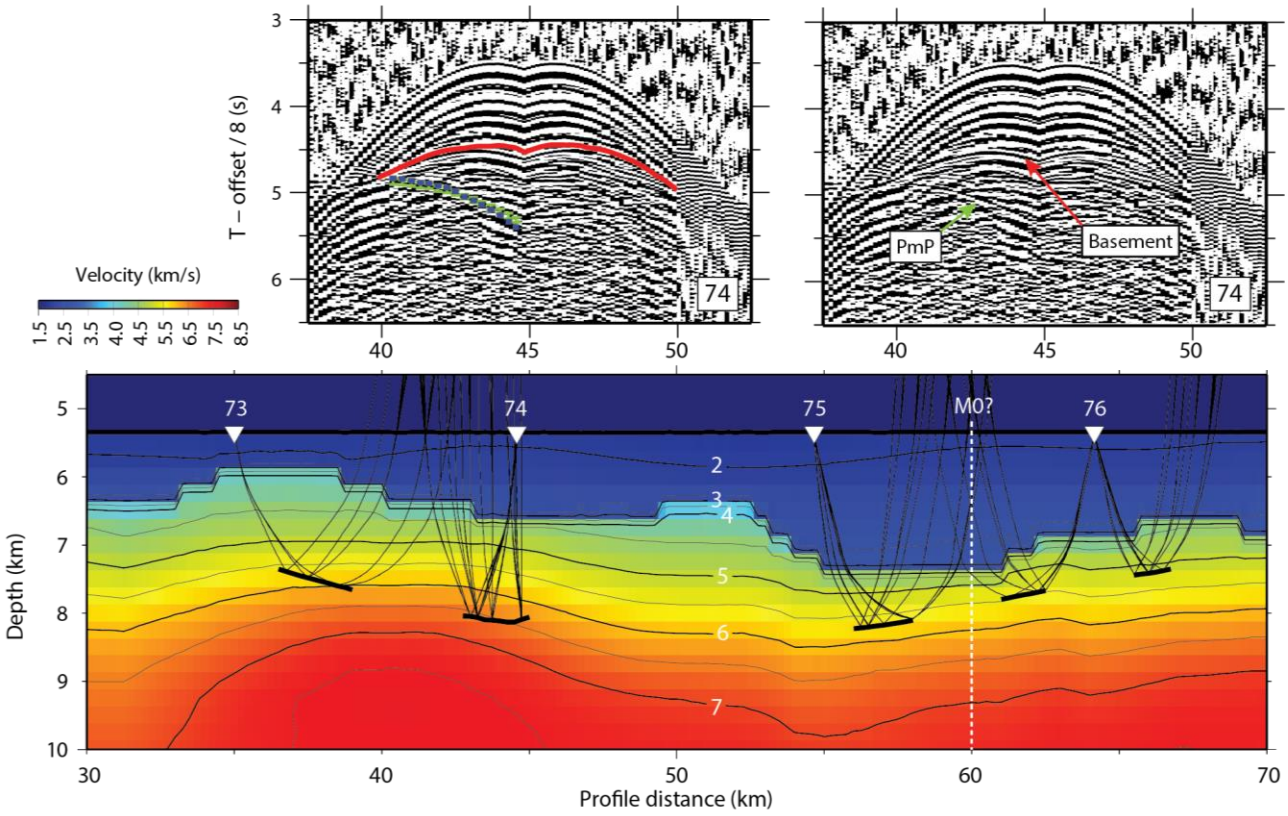

Figure 3-10: Modelled depth of the Moho from limited PmP arrivals on instruments 73, 74, 75 and 76, west of the Peridotite Ridge. Top: Receiver gathers from instrument 74; green bars indicate PmP travel time picks and their associated uncertainties; blue squares indicate the modelled travel times through the velocity model; red line illustrates wide-angle basement reflection. Bottom: Final compressional velocity model, limited to 30 – 70 km profile distance, illustrating the resolved Moho boundary. The location of M0 (white dashed line) is as interpreted by Srivastava et al. [2000].

3.4.5 Moho reflections west of the Peridotite Ridge

Limited but clear reflected arrivals were observed at short offsets (mostly after the direct water arrival) in the receiver gathers of the four westernmost instruments (Figure 3-10), west of the Peridotite Ridge. One hundred clear PmP picks were identified from the receiver gathers of these four instruments (using an Ormsby band-pass filter of 1-2-20-40 Hz). In order to model the approximate depth of this interface, the PmP travel-time picks were added to the travel-time picks from modelling in **3.4.3** and inverted with TOMO2D, using the same parameter set and input models. Locally, the same horizon which defined the initial S reflector (7 km depth throughout the initial model) was adjusted in depth through the tomographic inversion, in order to match the modelled and observed PmP reflection travel-times (Figure 3-10). An RMS misfit of 65 ms was achieved for these arrivals (Table 3-2).

These PmP arrivals are observed after basement reflections in the seismic receiver gathers (Figure 3-10), and must represent a velocity discontinuity. Such a discontinuity is not expected within serpentinised mantle, and if it were a mid-crustal discontinuity, we would expect to see a Moho reflection beneath. Therefore we interpret these arrivals as reflections from the base of a thin crustal layer.

3.4.6 Gravity model

Conversion of the final velocity model to density, using empirical velocity-density (V_p-ρ) relationships, enables the calculation of the free-air gravity anomaly along the WE-1 profile [*Brocher*, 2005]. Comparison of this calculated anomaly with shipborne gravity observations permits validation of our velocity model, and can highlight areas where the model may be unreliable, or where there is significant out-of-plane structure. To avoid edge-effects, the velocity model was extended eastward, westward and to a depth of 25 km. The tomographic velocity model for the coincident ISE-1 seismic profile [*Zelt et al.*, 2003], was incorporated into our model and extends an additional ~250 km eastward (domain B, Figure 3-11). West of the WE-1 seismic profile there are no available geophysical or geological constraints, so the 1D velocity structure at 30 km model distance was extrapolated to -200 km (domain C, Figure 3-11). Mantle velocities (8.0 km s^{-1}) below the WE-1 model and domain C, were extended to 25 km depth in order to match the depth of the ISE-1 velocity model (domain D, Figure 3-11).

We used an assumed density of 1.03 g/cm^3 for the water column (< 1.55 km s^{-1}), and 3.30 g/cm^3 for the mantle (>= 8.0 km s^{-1}). Velocities within these bounds were converted to densities using the empirical Nafe-Drake relationship of *Ludwig et al.* [1970]. This relationship is most accurate when converting the compressional velocities of water saturated sediment to density, but also provides a good first order approximation of non-mantle rock densities [*Brocher*, 2005].

Free air gravity anomalies were calculated by summing the gravity anomaly of each model cell, approximated as an infinite cuboid out of plane, with a density contrast to a background density of 3.3 g/cm^3 (Figure 3-11). A clear regional trend is observed in the difference between the calculated and observed free air gravity anomaly, likely rising from deeper mantle structures or assumptions made in creating the extended density model. To correct for this regional trend, a linear trend was fit to this difference and subtracted from

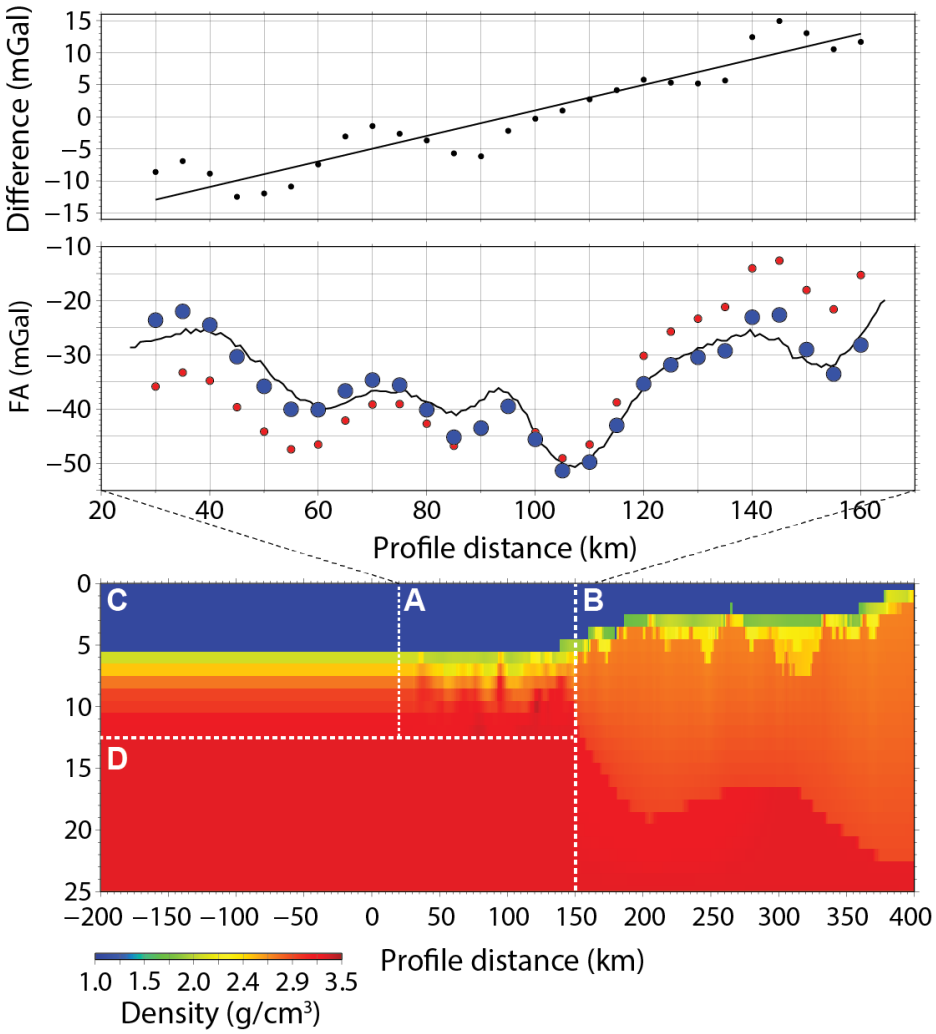

Figure 3-11: Results of the gravity modelling. Top: Small black dots illustrate the misfit between observed and calculated free-air gravity anomalies, black line shows the linear trend fitted to this misfit, which represents the regional gravity trend. Middle: Black line shows the observed ship-borne free-air gravity anomaly, small red circles show the calculated free-air gravity anomaly, and large blue circles show the regionally corrected free-air gravity anomaly calculations. Bottom: Extended density model. Region A is the density model converted from the final TOMO2D velocity model. Region B is the density model converted from the compressional velocity model of Zelt et al. [2003]. Region C is an extrapolation of the 1D density profile from 30 km profile distance. Region D is an extrapolation of mantle densities to 25 km depth in order to match the depth of region. Plot has a vertical exaggeration of 9.

the calculated free air gravity anomaly. This linear trend shows a decrease of 0.2 mGal/km oceanward. Without this correction the model had a RMS misfit to the observed anomaly of 8.0 mGal, decreasing to 2.7 mGal after trend removal, which is comparable to typical shipborne gravity uncertainties [*Bell and Watts*, 1986]. Therefore gravity data provide further support for our crustal velocity model.

3.5 Discussion

The final TOMO2D velocity model (Figure 3-5) enables the interpretation of many distinct features including: the S reflector east of the Peridotite Ridge; rotated and thinned continental blocks topped with syn- and pre-rift sediment; thickening continental crust at the eastern end of the WE-1 profile; the Peridotite Ridge, which reaches the seafloor in the center of the profile; a relatively homogeneous basement west of the Peridotite Ridge; and a sparsely sampled Moho interface at shallow depths. To investigate these features in greater detail, we divide the profile into two parts bounded by the Peridotite Ridge.

3.5.1 West of the Peridotite Ridge

3.5.1.1 Velocity model and data features

Receiver gathers from the instruments west of the Peridotite Ridge bear a strong resemblance to those from the IAM-9 seismic line, situated over the zone of exhumed continental mantle in the southern Iberia Abyssal Plain [*Dean et al.*, 2000]. Apparent velocities > 7.0 km s^{-1} at short offsets are indicative of mantle or serpentinised mantle at shallow depths, while a lack of deep and clear PmP phase arrivals indicates the absence of full thickness oceanic crust (7 km thick) along the profile. However, sparse Moho reflections identified after the direct arrival, on the four western most instruments, indicate the presence of an anomalously thin crust (Figure 3-10). We interpret this crust as oceanic because it appears highly magnetized [*Sibuet et al.*, 1995] and its seismic reflection characteristics differ markedly from those of thinned continental crust further east of the Peridotite Ridge [*Dean et al.*, 2015].

The final TOMO2D velocity model (Figure 3-5) shows that west of the Peridotite Ridge the basement velocity structure is relatively homogenous between 40 and 90 km model distance. There is slight variation in the velocities in what is interpreted as the top of basement, with lower velocities of 4.0 km s^{-1} at 30 – 52 km model distances, and higher velocities of 5.0 km s^{-1} at 55 – 75 km model distance. The 7.5 km s^{-1} velocity contour typically lies at round 12 km depth, but rises to shallower depths of 9 km and 10 km at profile distances of 40 km and 65 km, respectively. At the western limit of the model (< 30 km), velocity contours have a more uniform spread, and vary little from the input velocity model. Modelled PmP reflections reveal a thin oceanic layer that thickens seaward,

from 0.5 km thick at 67 km profile distance, to 1.5 km thick at 36 km profile distance (Figure 3-10). No clear PmP arrival can be identified on instrument 78, which suggests that the oldest oceanic crust lies between instrument 76 and 78 (64 km and 83 km profile distance, respectively). Many of the seismic arrivals from this thin oceanic layer are masked by the direct water arrival and first arrivals from the shallow underlying mantle, and therefore cannot be resolved using first arrival travel-times alone.

At its thinnest, the interpreted oceanic crustal layer has velocities between 4.5 and 5.5 km s^{1}, and at its thickest has velocities between 4.0 and 6.5 km s^{-1}. Because the Moho velocity discontinuity has been smoothed out, these maximum velocities may be over-estimated. Velocities of 4.0 – 6.5 km s^{-1} are consistent with those commonly observed in oceanic layer 2 [*White et al.*, 1992]. Variations in the thickness of oceanic crust are commonly attributed to variations in the thickness of oceanic layer 3, while layer 2 typically remains constant [*Mutter and Mutter*, 1993]. This leads us to conclude that oceanic layer 3 is absent in the oceanic crust modelled along WE-1.

3.5.1.2 Velocity profiles

One-dimensional velocity profiles through the velocity model west of the Peridotite Ridge give further insight into the nature of the unidentified basement (Figure 3-12). All of the 1D velocity profiles exhibit two distinct velocity trends, below the top of basement, which are identified based on their common velocity gradients. The upper trend extends to depths of 2.8 - 3.5 km within the unidentified basement. Velocities smoothly and rapidly increase from ~4.5 km s^{-1} to 7.3 – 7.6 km s^{-1} in this layer, and present velocity gradients ranging between 0.8 s^{-1} and 1.2 s^{-1}, with an average velocity gradient of 1.0 s^{-1}. Despite Moho reflections being identified and modelled within this depth range, we do not observe any significant velocity discontinuities, likely owing to the smooth nature of the TOMO2D modelling process. Below this top trend, compressional velocities smoothly increase toward mantle velocities of 8.0 km s^{-1}, and with a much lower velocity gradient of 0.14 s^{-1} on average. These thicknesses and velocity gradients are nearly identical to those observed by *Dean et al.* [2000] in the zone of exhumed continental mantle in the southern Iberia Abyssal Plain, and are consistent with a decreasing serpentinisation of mantle material with depth [*Carlson and Miller*, 2003]. In our model, where Moho reflections are not observed and exhumed mantle is interpreted (e.g., east of instrument 76, Figure 3-13), velocities of 4.6 km s^{-1} at the top of basement correspond to 100 % serpentinisation of mantle material,

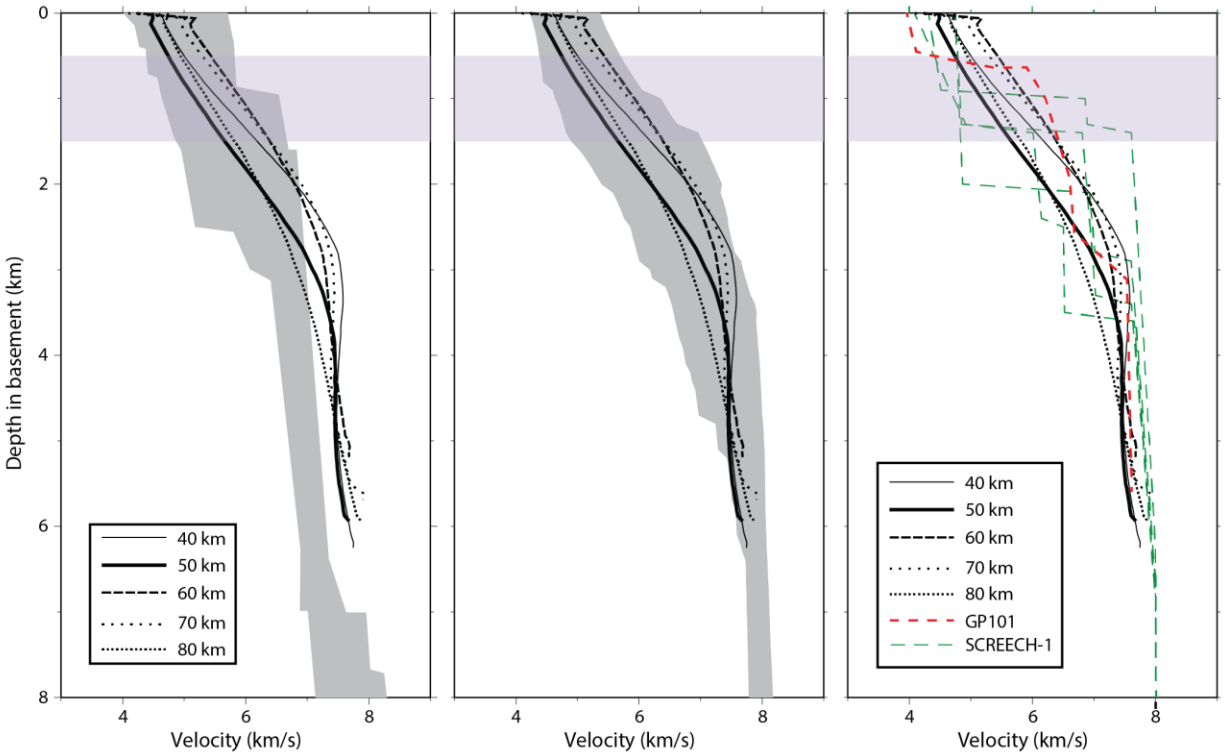

Figure 3-12: 1D velocity profiles through the final TOMO2D velocity model (Figure 3-5). Light blue shading indicates the depths at which the Moho, below our thin oceanic crust, is identified. Left: The 1D velocity profiles compared to the velocity envelope for Atlantic oceanic crust aged 59 -170 Ma [White et al., 1992]. Centre: The 1D velocity profiles compared to the velocity envelope for velocity models within the COT from previous studies, as compiled by Minshull [2009]. Right: The 1D velocity profiles compared with velocity profiles through thin oceanic crust on the SCREECH-1 compressional velocity model of Funck et al. [2003] (green dashed lines) and the GP101 model of Whitmarsh et al. [1996] (red dashed line).

decreasing to < 20 % at depths of 2.8 – 3.5 km below top basement [*Carlson and Miller*, 2003]. Velocities at depths > 2 km below the top basement sit outside the envelope for all ages of Atlantic oceanic crust, but agree strongly with the velocities observed within zones of transitional crust at both the southern Iberia Abyssal Plain and Newfoundland margins (Figure 3-12). Velocities from our model also agree with the velocity profiles through the models of thin oceanic crust, overlying serpentinised mantle, observed along GP101 at the Deep Galicia margin, and SCREECH-1 at the conjugate Flemish Cap margin (Figure 3-12) [*Whitmarsh et al.*, 1996; *Funck et al.*, 2003; *Hopper et al.*, 2004]. These velocity models are derived by forward ray-tracing of seismic arrivals through discrete crustal layers, resulting in velocity jumps at layer boundaries, while our tomographic model produces a smooth velocity transition with depth. Seismic velocities reach 8 km s^{-1} corresponding to unaltered mantle material, at around 6 km below the top of basement in our model, which is

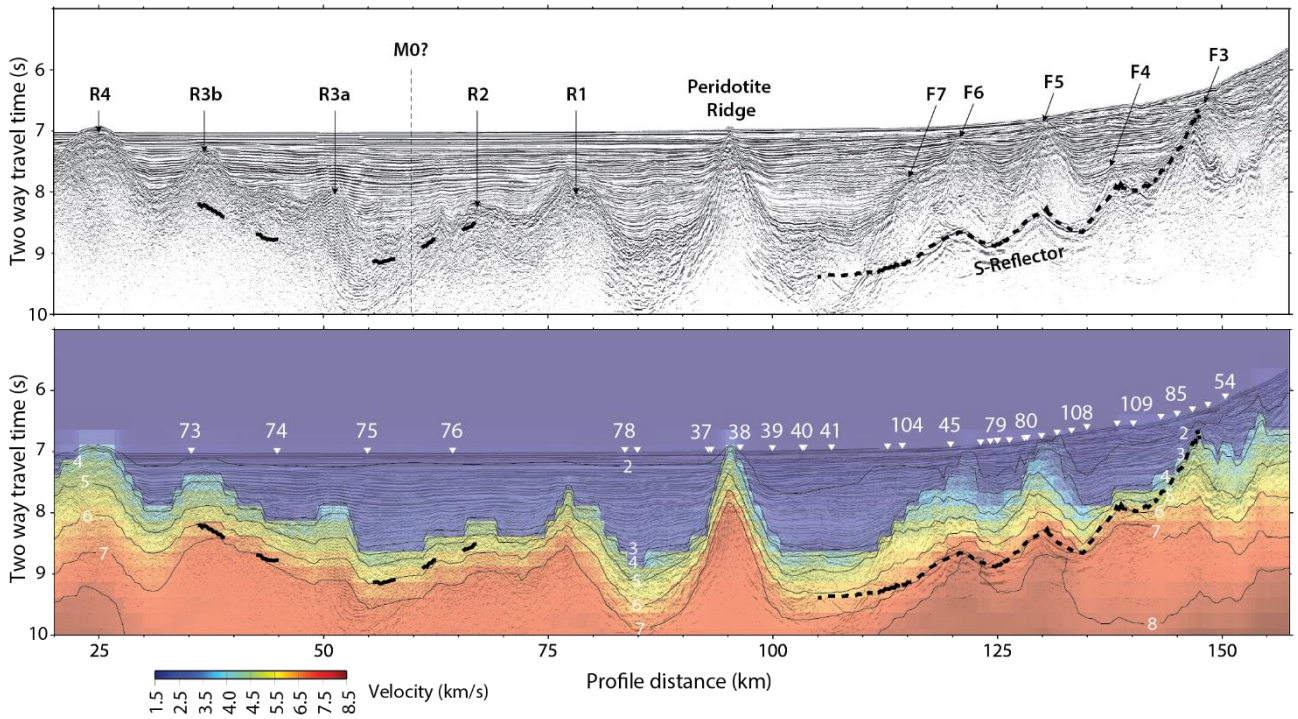

Figure 3-13: *Comparison of velocity model and seismic reflection imaging Top: Kirchhoff time-migrated multichannel seismic image of WE-1 from Dean et al. [2015]. Normal faults F3 – F7, identified on the coincident ISE-1 profile by Borgmeyer [2010], are indicated east of the Peridotite Ridge with arrows. Ridge structures identified west of the Peridotite Ridge by Dean et al. [2015] are indicated by arrows. M0 magnetic anomaly is indicated by a dashed black line [Srivastava et al., 2000]. Bottom: The same image overlain by the time-converted compressional velocity model. White inverted triangles illustrate the location of ocean bottom instruments. Thick dashed black line illustrates the time converted S reflector; thick black line illustrates areas where the Moho is sampled.*

consistent with other studies of exhumed and serpentinised peridotites at rifted margins (Figure 3-12).

From the velocity and seismic characteristics west of the Peridotite Ridge, we interpret that there is < 25 km of exhumed mantle (between the Peridotite Ridge and instrument 76, Figure 3-13), before the onset of thin oceanic crust overlying serpentinised mantle material. This thin oceanic layer thickens oceanward, but does not reach full thickness within our resolved velocity model. This interpretation is broadly consistent with previous interpretations of thin oceanic crust abutting the Peridotite Ridge and overlying serpentinised mantle [*Sibuet et al.*, 1995; *Whitmarsh et al.*, 1996]. However, *Whitmarsh et al.* [1996] used data from only three OBS along a 150-km-long margin-normal seismic profile and from three OBS along an 80-km-long margin-parallel profile. The authors from this study did not identify PmP arrivals from the base of the anomalously thin oceanic crust, while PmP arrivals from the base of full thickness oceanic crust (parallel to margin) were

clearly identified only on one of the instruments west of the Peridotite Ridge. Our model shows a layer, identified by its constant velocity gradient, with a thickness of 2.8 – 3.5 km. This thickness is very similar to that of the thin oceanic crust described by *Whitmarsh et al.* [1996], and also correlates well with the layer of scattered reflectivity identified by *Dean et al.* [2015] (Figure 3-13). However, the base of this layer does not coincide with the Moho depths determined from limited PmP arrivals in our model, and probably represents a change in the nature of mantle serpentinisation below the thin oceanic crust.

Our interpretation of an anomalously thin oceanic crust is consistent with observations of thin oceanic crust at other ultra-slow spreading margins. Seismic refraction studies at the Gakkel Ridge (<10 mm/yr full spreading rate) have revealed oceanic crust 1.4 – 2.9 km thick, with little to no evidence of oceanic layer 3, overlying partially serpentinised mantle rock [*Jokat et al.*, 2003; *Jokat and Schmidt-Aursch*, 2007]. Velocity modelling of the Southwest Indian Ridge (~12 mm/yr full spreading rate) allowed for the interpretation of an oceanic crust which is 2.2 – 5.4 km thick, with serpentinised mantle rock proposed to comprise some of the oceanic layer 3 (0.5 – 3.0 km thick) [*Minshull et al.*, 2006]. Wide angle seismic studies of the Mohns Ridge (16 mm/yr full spreading rate) also revealed the presence of a thin oceanic crust ~4 km thick, with an oceanic layer 2 thickness of 1.4 – 1.7 km thick [*Klingelhöfer et al.*, 2000]. This new interpretation at the Deep Galicia margin contributes to the evidence that thin oceanic crust is the norm, as opposed to the exception, at ultra-slow spreading margins.

3.5.1.3 Reflection imaging

Dean et al. [2015] identify and describe the morphology of five ridge like basement structures in the reflection seismic images along WE-1 west of the Peridotite Ridge (indicated by R1 – R4 in Figure 3-13). Unlike the reflection imaging of continental crust east of the Peridotite Ridge, west of the Peridotite Ridge the reflection data exhibits scattered reflectivity and a diminished presence of coherent structural reflections within the basement. Ridges 1 – 3a exhibit asymmetric structure with limited elevation above the surrounding basement topography, have little internal structure, and smooth to sub-angular basement expression. Ridges 3b and 4 are symmetric in structure, with smooth surfaces that rise high above the surrounding basement topography. The rough, or hummocky, morphology of ridges 1 – 3a is consistent with the accretion of magmatic crust at ultra-slow spreading ridges, such as that seen along sections of the Southwest Indian

Ridge [*Cannat et al.*, 2006]. Conversely, smooth basement ridge structures, like that of ridges 3b and 4, are also observed in areas of the Southwest Indian Ridge, and are interpreted to be the exhumation and exposure of altered mantle-derived rocks [*Cannat et al.*, 2006]. *Dean et al.* [2015] proposed a synthesis model for the generation of these ridges, suggesting that ridges 1 - 3a were formed through mantle exhumation and interspersed magmatism, while ridge 4 resembles an oceanic core complex (OCC). Our results support the interpretation of ridges 1 – 3a as magmatic in origin, and that this magmatic layer overlies serpentinised mantle. High P-wave velocities are expected at shallow depths in oceanic core complexes, due to presence of gabbro or ultramafic material (~6.0 km s^{-1} and >7.5 km s^{-1}, respectively) [*Blackman et al.*, 2009]. Velocity modelling of OCC at the Atlantis platform, along the Southwest Indian Ridge, revealed P-wave velocities of 5.8 km s^{-1} at the seafloor, increasing to 6.5 km s^{-1} at 1.4 km depth; at the Parece Vela Basin, in the Philippine Sea, P-wave velocities of 6.0 km s^{-1} were modelled at depths of 500 m; at 26°N along the Mid-Atlantic Ridge P-wave velocities are modelled as 4.0 km s^{-1} at the seafloor, increasing to 7.0 km s^{-1} within 1 km below [*Muller et al.*, 2000; *Canales et al.*, 2007; *Ohara et al.*, 2007; *Sohn et al.*, 2007]. These velocity structures are markedly different to that resolved in ridge 4 along WE-1, where P-wave velocities increase from 4.0 km s^{-1} at the seafloor, to 6.0 km s^{-1} (i.e.: seismic velocity of gabbro) ~2.7 km below, which is significantly deeper than the previously described OCC. Therefore, our data do not support the interpretation that this ridge is an oceanic core complex. We suggest that all of these ridge features are formed through magma-limited accretion of thin oceanic crust.

3.5.1.4 Conjugate margin

Thin oceanic crust is also observed on the SCREECH-1 profile at the Flemish Cap, which in many reconstructions is conjugate to both WE-1 and ISE-1. Magmatic crust, 3-4 km thick, is interpreted to have been accreted in direct contact with the termination of extended continental crust, defining a sharp COT [*Hopper et al.*, 2004]. This initial oceanic crust is highly faulted, with rotated fault blocks, bound by normal faults dipping seaward every ~1.5 km. Further seaward oceanic crust becomes extremely thin (~1.3 km thick) and is underlain by serpentinised mantle, much like the thin oceanic crust which we have interpreted at the Deep Galicia margin. In the reflection seismic images of WE-1 (Figure 3-13) and its interpretation west of the Peridotite Ridge, block-bounding faults, similar to those observed along SCREECH-1, are not imaged [*Hopper et al.*, 2004]. Such

faults may be present, but sub seismic in nature and unresolved in the Kirchhoff time migration images (Figure 3-13). Such faulting would provide the required mechanism to hydrate, and consequently enable the serpentinisation, of the underlying mantle. Additionally, in the seismic reflection images, there is little evidence for a strong and coherent Moho reflection from the base of the thin oceanic crust, which is evidence in support of a weak velocity contrast across this boundary.

3.5.1.5 Dating the earliest oceanic crust

A lack of linear seafloor spreading magnetic anomalies and drill sites, west of the Peridotite Ridge, make it difficult to assign an age to the earliest oceanic crust seen at the Deep Galicia margin. *Srivastava et al.* [2000] interpret a magnetic anomaly, west of the Peridotite Ridge, as spreading anomaly M0 (~126 Ma, according to timescale of *Gradstein et al.* [2012]) (Figures 3-10 and 3-13). However, caution must be applied to this interpretation, as *Sibuet et al.* [1995] fit a model to the same magnetic data, showing that the topography of a highly magnetized (5 A/m), and thin oceanic crust (~1 km), recording no magnetic field reversals, can also explain the observed magnetic anomaly. *Sibuet et al.* [1995] also state that no magnetic field reversals were expected, as oceanic crust in this region formed during the Cretaceous constant polarity interval, later than the M series of seafloor spreading magnetic anomalies. Age constraints could alternatively come from the drilling of the Peridotite Ridge, which was sampled by site 637 of IODP Leg 173 (Figure 3-1C), and returned serpentinised mantle peridotite intruded with amphibole-diorites, gabbros and pyroxenites [*Boillot et al.*, 1987]. Dating of samples from Site 637, and other drill and dive sites along the Deep Galicia margin, show that the mafic rocks were emplaced at around 122 Ma, synchronous with the end of rifting [*Schärer et al.*, 1995; *Chazot et al.*, 2005]. This date is younger than that of the M0 magnetic anomaly, and suggests an upper bound to the age of oceanic crust west of the Peridotite Ridge of 122 Ma. This date also enables us to estimate a spreading rate for the accretion of this oceanic crust. Site 637 is approximately 280 km from the nearest magnetic isochron (C34), which is the first clear seafloor spreading magnetic anomaly after the Cretaceous constant polarity interval, and has an age of 84 Ma [*Bronner et al.*, 2011; *Gradstein et al.*, 2012]. The required half spreading rate is 7.4 mm/yr, classifying the spreading here as ultra-slow, which is consistent with the observed mantle exhumation and onset of thin oceanic crust. South of the Deep Galicia margin, at the southern Iberia Abyssal Plain, the formation of oceanic crust 6 - 7 km

thick is interpreted to have begun at 127 – 125 Ma, while north of the Deep Galicia margin, at the Goban Spur, a final breakup age of 100 Ma is proposed [*Gerlings et al.*, 2012; *Minshull et al.*, 2014]. These breakup dates, decreasing in age from south to north, are consistent with the observation of a northward propagating rift margin [*Masson and Miles*, 1984]. At the Flemish Cap, conjugate to the Deep Galicia margin, oceanic crust is observed to have accreted just after the M0 magnetic anomaly along SCREECH-1, at around 123.5 Ma, which is consistent with our interpretation [*Hopper et al.*, 2004; *Van Avendonk et al.*, 2006].

3.5.2 East of the Peridotite Ridge

3.5.2.1 Comparison with existing models

Inversion of the WE-1 wide-angle seismic dataset has yielded a velocity model east of the Peridotite Ridge which strongly correlates with the structure observed in reflection imaging and the classical interpretations of the hyperextended Deep Galicia margin (Figure 3-14C). Additional to the velocity model developed in this study, two coincident compressional velocity models have previously been produced east of the Peridotite Ridge (Figure 3-14). All three models have been developed using different modelling techniques. The preferred model of *Zelt et al.* [2003] (Figure 3-14A) was developed using wide-angle and zero-offset MCS picks, from the ISE-1 profile, inverted simultaneously using the *Zelt and Smith* [1992] algorithm. This model utilized a priori information by defining a six-layer starting model including the water column, three sedimentary layers, a crustal layer and a mantle layer, constrained by MCS imaging along the ISE-1 seismic line. The model of *Bayrakci et al.* [2016] (Figure 3-14B) is a two-dimensional slice, coincident with WE-1 and ISE-1, of a larger three-dimensional compressional velocity model developed using data from the full array of instruments within the 3D box of the Galicia-3D seismic experiment (see **3.3**). This three-dimensional velocity model was developed using first arrival seismic travel-times, inverted using a non-linear iterative tomographic technique (FAST) [*Zelt and Barton*, 1998]. In the following description of the structure east of the Peridotite Ridge, we primarily describe the results of our tomographic modelling, with comparison to those of *Zelt et al.* [2003] and *Bayrakci et al.* [2016], which we will refer to as the ISE and G3D models, respectively.

Velocities in the rotated continental fault blocks, bound by normal faults (illustrated as F3-F7 in Figure 3-13), and the pre- and syn-rift sedimentary layers above, appear to have been

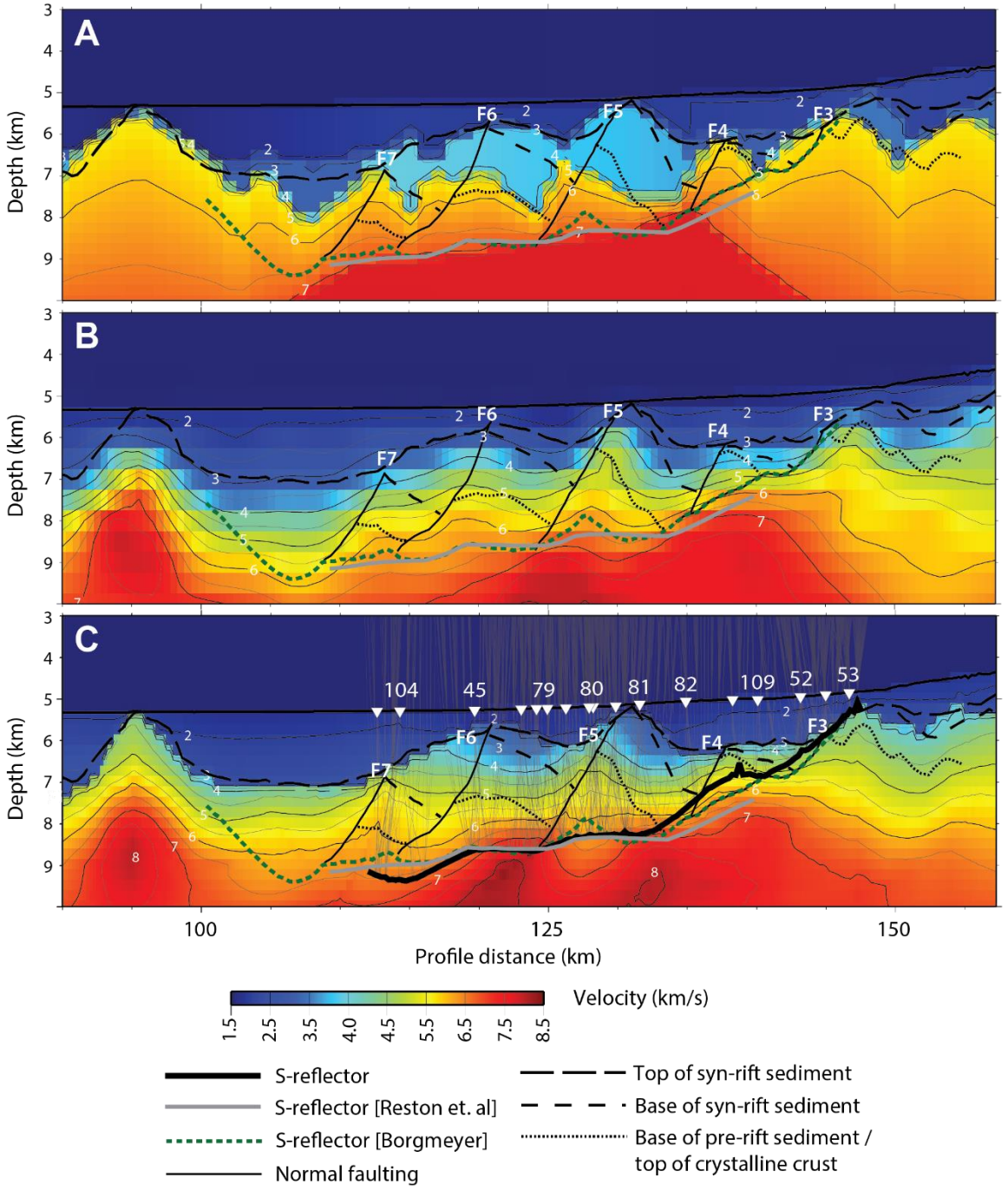

Figure 3-14: Comparison of existing velocity models east of the Peridotite Ridge, and their correlation with reflection seismic interpretations. A) Velocity model from Zelt et al. [2003] along ISE-1. B) Slice through the 3D model of Bayrakci et al. [2016] using Galicia-3D data. C) Final TOMO2D velocity model along WE-1. Horizon and fault surfaces are from depth migrated images along ISE-1 in Borgmeyer [2010], and GP12 in Reston et al. [1996]. Thick solid black line is the S reflector resolved by the reflected rays (thin black lines) from the TOMO2D inversion process. Inverted triangles are the instruments used to resolve the S reflector. Plots have a vertical exaggeration of 3.

well resolved. The velocity structure exhibits landward dipping contours, but due to model limitations, cannot match the steep boundaries interpreted between pre-rift sediment, syn-rift sediment, and crystalline crust layers. The tops of the fault-bounded blocks are better defined at shallow depths than in the G3D velocity model, owing to finer model cells

at shallow depths in our model when compared to the G3D model, and the a priori information used in the WE-1 input model. Velocities increase from ~3.0 km s^{-1} at the top of syn-rift sediment, to ~4.5 km s^{-1} at the top of pre-rift sediment, and to ~6.5 km s^{-1} at the base of crystalline crust, directly above the S reflector. The S reflector follows the 6.0 – 7.0 km s^{-1} velocity contours between profile distances of 112 – 135 km, and has an excellent match with the interpretations of depth-migrated multi-seismic along GP12 and ISE-1 [*Reston et al.*, 1996; *Borgmeyer*, 2010], as well as the G3D velocity model. These velocities are interpreted to correspond to ~30 – 60 % serpentinisation of mantle peridotite [*Carlson and Miller*, 2003]. At its eastern limit (> 132 km) the S reflector cuts through lower seismic velocities associated with the continental crust, before terminating at the seafloor at ~147.5 km profile distance. The western limit of the S reflector shallows toward the Peridotite Ridge, before terminating at 112 km.

The S reflector exhibits undulations along profile in our tomography model, which have a moderate correlation with the rotated continental fault blocks juxtaposed above this detachment surface in both our velocity model and the G3D velocity model. It is possible that smoothing in the velocity model has resulted in seismic pull-up and/or push-down, which is observed as the undulations in the resolved S reflector. Below the S reflector a pattern of high and low-velocity regions are observed. The most prominent high-velocity region observed below the S reflector reaches 8.0 km s^{-1}, 100 m below the S reflector at 122 km profile distance, rapidly decreasing eastward to a zone with a velocity of 6.5 km s^{-1} at 128 km profile distance, before again increasing to 7.2 km s^{-1} at 132 km profile distance. These velocities are interpreted to correspond to different degrees of serpentinisation of the mantle peridotite along the S reflector, with 8.0 km s^{-1} being unaltered, 6.4 km s^{-1} indicating ~45 % serpentinisation and 7.2 km s^{-1} representing ~20 % serpentinisation [*Carlson and Miller*, 2003]. The 6.5 km s^{-1} velocity zone occurs between normal faults marked as F5 and F4, and we propose that this low-velocity zone the result of fluid transport along fault F4, resulting in the pattern of variable hydration and serpentinisation of the upper mantle along the S reflector [*Bayrakci et al.*, 2016]. However, the high-velocity lobe situated at the terminus of fault F5 is problematic for this interpretation. Movement along the S-detachment could have shifted this low-velocity zone laterally eastward, but this contradicts the idea that the velocity variation below the S reflector is a result of preferential mantle hydration by fault fluid transport, which occurs when the faults are displaced. However, the G3D velocity model shows an offset in these high and low-velocity

patterns, when compared with the velocity model from this study, with the low-velocity lobes situated down-dip of the terminus of normal faults, giving strong evidence in favor of fault controlled mantle hydration [*Bayrakci et al.*, 2016]. The difference in the models could be explained by the more complete azimuthal coverage of the G3D velocity model enabling this structure to be resolved in the third dimension, where our 2D model is unable to do so. The Monte Carlo uncertainty results also shows that the uncertainty of this structure in our model is highest throughout the model, reaching ± 0.15 km s^{-1} (Figure 3-8). In contrast, the S reflector is modelled as a seaward dipping interface, free of undulations, in the lower-resolution ISE velocity model.

The velocity within the Peridotite Ridge reaches a maximum of ~8.0 km s^{-1} in both the model from this study and the G3D model, indicating the presence of unaltered mantle peridotite at the center of the Peridotite Ridge. This is a much higher velocity than modelled in the ISE model, where the maximum velocity is 6.0 – 6.5 km s^{-1}. However, the velocities in our model and the G3D model form closed-contour high-velocity blobs, with lower velocities below the Peridotite Ridge, which is difficult to interpret.

At the eastern limit of the ISE model, the Moho is modelled as an abrupt velocity jump from 7 km s^{-1} to 8 km s^{-1} across a landward dipping horizon. The Moho is not included as a layer boundary in our tomographic model, or the G3D model, so such an abrupt velocity jump is not possible in the tomography model of this study and that of the G3D study. However, the 7 km s^{-1} velocity contour of both models show a strong correlation with the Moho modelled in the ISE model.

3.6 Conclusions

Our final compressional velocity model has resolved the structure of continental hyperextension, detachment faulting, the Peridotite Ridge, and a thin oceanic crust overlying serpentinised mantle material. There is a strong correlation between the structure resolved in our velocity model and that observed in coincident seismic reflection data. The final model is further validated by the close fit between the observed and calculated free-air gravity anomaly. The primary findings from this study are as follows:

1. West of the Peridotite Ridge, exhumed mantle is present over a short distance (< 25 km), landward of the onset of an anomalously thin oceanic crust (0.5 – 1.5 km thick), which thickens seaward. Evidence for the presence of serpentinised mantle material below this thin oceanic crust comes from seismic velocities increasing smoothly from 5.5 – 6.5 km s^{-1} to 7.3 – 7.6 km s^{-1}, with a velocity gradient of 1.0 s^{-1}. Below this, velocities increase slowly into mantle velocities of ~8.0 km s^{-1}, with an average velocity gradient of ~0.14 s^{-1}.
2. We assign an upper bound to the age of the thin oceanic crust of 122 Ma, based on the dating of materials recovered from the Peridotite Ridge. This age is consistent with continental breakup progressing from south to north along the margin.
3. The S reflector detachment surface possesses undulations that correlate with the pattern of high and low-velocity regions below this surface. This velocity structure is interpreted to be the result of preferential mantle hydration along normal faults, acting as conduits between the seafloor and the S reflector. Typically the S reflector lies between the 6.0 and 7.0 km s^{-1} velocity contours, which corresponds to serpentinisation of mantle peridotite of 60 – 30%, respectively.

Chapter 4: Resolving the fine-scale velocity structure of continental hyperextension at the Deep Galicia margin using full-waveform inversion

Author contributions. This chapter has been submitted for publication as an article in the peer-reviewed journal *Geophysical Journal International*. The author list for this article is: Davy, R., Morgan, J., Minshull, T., Bayrakci, G., Bull, J., Klaeschen, D., Reston, T.J., Sawyer, D., Lymer, G., and Cresswell, D. TM, DK, TR, DS and others designed the seismic experiment. RD carried out the full-waveform inversion, with guidance from JM and TM. GL and DC provided seismic interpretations. All authors contributed feedback on the text.

Abstract

Continental hyperextension during magma-poor rifting at the Deep Galicia margin is characterised by a complex pattern of faulting, thin continental fault blocks, and the serpentinisation, with local exhumation, of mantle peridotites along the S reflector, interpreted as a detachment surface. In order to understand fully the evolution of these features, it is important to image seismically the structure and to model the velocity structure to the greatest resolution possible. Travel-time tomography models have revealed the long-wavelength velocity structure of this hyperextended domain, but are often insufficient to match accurately the short-wavelength structure observed in reflection seismic imaging. Here we present the results of two-dimensional (2D) time-domain acoustic full-waveform inversion applied to seismic data collected during the Galicia-3D seismic experiment at the hyperextended domain of the Deep Galicia margin. We have attained an increase in the resolution of subsurface velocities, with particular improvement observed in the westernmost continental fault blocks, with a clear rotation of the velocity field to match steeply dipping reflectors. Below the S reflector we observe a sharpening in the pattern of relative velocities, indicative of preferential mantle serpentinisation. This study supports the hypothesis that normal faulting acts to hydrate the upper mantle peridotite, observed as a systematic decrease in seismic velocities, consistent with increased serpentinisation. Based on observed P-wave velocities, the approximate extent of mantle peridotite serpentinisation ranges from 0% (unaltered) to 70%. We used several quality assurance procedures to assess the velocity model, including comparison of the observed and modelled waveforms, checkerboard tests, testing of parameter and inversion strategy, and comparison with the migrated reflection image. Our results confirm the feasibility of applying full-waveform inversion to deep and sparse crustal datasets.

4.1 Introduction

In recent years there has been an increase in the availability of high-density seismic datasets and a significant increase in the power of computers. These combined factors have enabled a broadening application of seismic full-waveform inversion (FWI). FWI provides a powerful extension of popular seismic travel-time tomography methods, with the ability to resolve subsurface velocity structure to half the seismic wavelength, which can be an order

of magnitude smaller than possible with travel-time tomography for a typical crustal target [*Wu and Toksöz*, 1987; *Williamson*, 1991; *Virieux and Operto*, 2009]. Three-dimensional FWI has yielded impressive results on marine seismic datasets, producing high resolution velocity models which can be used directly for geological interpretation or for the migration of reflection seismic data to produce detailed images [e.g. *Sirgue et al.*, 2010; *Ratcliffe et al.*, 2011; *Jones et al.*, 2013; *Mispel et al.*, 2013; *Mothi et al.*, 2013; *Warner et al.*, 2013]. The vast majority of such studies have utilised seismic data recorded on either hydrophone streamers or ocean bottom cables (OBC), in relatively shallow marine environments (water depth < 1,000 m). Both hydrophone streamers and OBC possess a high density of receivers, enabling dense sampling of the subsurface for the FWI process [*Warner et al.*, 2013]. However, the maximum depth of investigation for these methods is restricted to approximately a third to a sixth of the maximum source-receiver offset, limiting their use for studies of crustal scale targets or those in deep water environments [*Warner et al.*, 2010; *Morgan et al.*, 2013].

These limitations can be overcome in deep water environments by applying FWI to wide-angle seismic datasets recorded by ocean bottom seismometers and hydrophones (OBS/H). A limited number of studies have previously applied FWI to OBS/H datasets. *Dessa et al.* [2004] and *Operto et al.* [2006] presented the first results of frequency-domain FWI applied to OBS data, utilising a 2D deployment of 100 instruments at the Nankai Trough, east of Japan. The velocity structure of compressional tectonic features within the accretionary prism and the down going oceanic crust were resolved, where they had not previously been observed in travel-time tomographic models. *Kamei et al.* [2012] applied frequency-domain FWI to a separate deployment of 54 OBS at the Nankai trough, resolving the fine scale velocity structure of megasplay faulting. *Morgan et al.* [2016] demonstrated the application of three-dimensional (3D) time-domain FWI on an array of 21 OBS situated across the Endeavour oceanic spreading centre of the Juan de Fuca Ridge, revealing low-velocity zones interpreted to represent a magmatic-hydrothermal reaction zone [*Arnoux et al.*, 2017]. These studies have made use of relatively dense OBS deployments (~1 km spacing), or a 3D seismic shooting configuration, both of which are not always possible in academic experiments. However, a recent study by *Jian et al.* [2017] has demonstrated the successful application of FWI to a sparse 2D dataset, utilising only three OBS, at the Southwest Indian Ridge. Here, the authors were able to resolve the structure of an axial magma chamber, not resolved by travel-time tomography. We look to build

upon these studies by applying FWI to a comparatively sparse and deep dataset, in order to further demonstrate the feasibility of the technique in areas where only 2D or older datasets are available.

Here we apply an acoustic 2D FWI to a sparse wide-angle dataset collected on 19 OBS/H at the Deep Galicia margin in the North Atlantic, with the aim of resolving the fine-scale velocity structure of continental hyperextension. Continental fault blocks within this hyperextended domain can possess dimensions as small as a few kilometres, beyond the limit of what is resolvable with travel-time tomography, making this an ideal target for FWI [*Davy et al.*, 2016]. We investigate the robustness of our FWI result by testing several parameters influencing the inversion, including the offsets and time windowing of the input data, and uncertainties in the sediment velocity model. Our result cannot be quality checked using 3D phase plots, and so we utilise alternative quality assurances, including checkerboard tests, waveform comparisons, and correlation with reflection seismic imaging. Given the nature of both the dataset and our crustal target, this application of FWI provides an excellent case study to explore the practical limits of this increasingly popular technique.

4.2 Background

4.2.1 Tectonic setting

The Iberia – Newfoundland ultra-slow rift system was active during the early stages of the opening of the North Atlantic Ocean. The first significant phase of rifting at this margin initiated during the Late Triassic - Early Jurassic [*Pérez-Gussinyé et al.*, 2003; *Tucholke et al.*, 2007; *Mohn et al.*, 2015]. This initial period of rifting saw the formation of fault-bound continental rift basins on the proximal margins of the rift system (e.g. Lusitanian, Porto and Galicia Interior basins) [*Murillas et al.*, 1990; *Péron-Pinvidic et al.*, 2007; *Tucholke et al.*, 2007]. The second phase of significant rifting initiated in the Late Jurassic - Early Cretaceous, and saw the continued extension and thinning of the continental lithosphere. This deformation shifted from a broad region, and became focused in the distal margins, where the continental crust eventually thinned to < 10 km in thickness and ruptured in the Early-Mid Cretaceous [*Tucholke et al.*, 2007; *Reston*, 2009b; *Mohn et al.*, 2015].

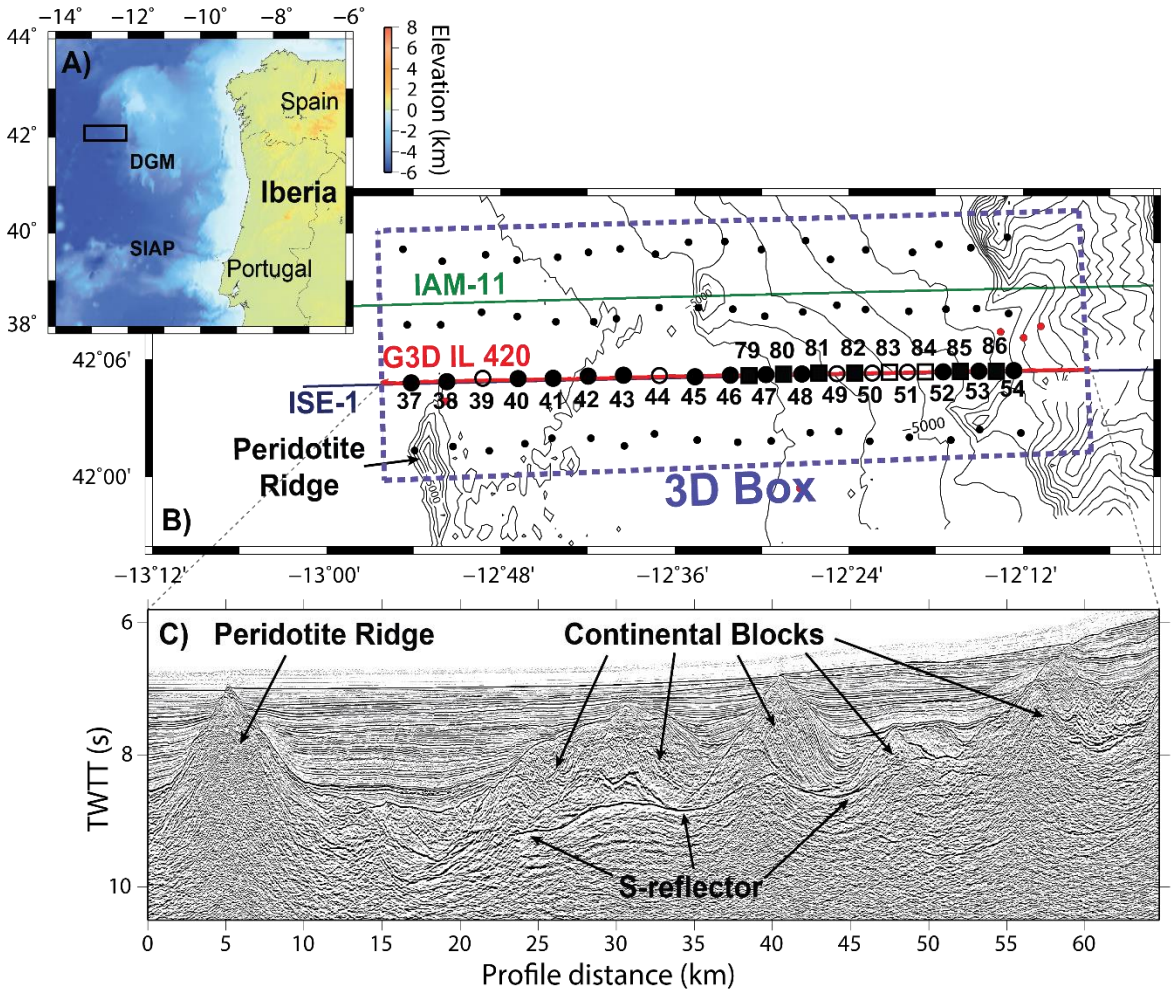

Figure 4-1: Maps of the study area. A) Bathymetric map of the Deep Galicia margin (DGM) and the Southern Iberia Abyssal Plain (SIAP) with the relative location of Fig. 4-1B (black rectangle). B) Map of the Galicia-3D seismic experiment. Galicia 3-D inline 420 seismic profile is illustrated by a red line; large black circles indicate the location of OBIF OBS along seismic inline 420; large black squares indicate GEOMAR OBH; unfilled circles and squares indicate instruments which recovered no data or were excluded from the FWI process. Purple line indicates the ISE-1 seismic profile; green line indicates the IAM-11 seismic profile; ODP Leg 103 sites are indicated by red circles [Boillot et al., 1987]. C) Kirchhoff pre-stack time-migrated multichannel seismic image of inline 420, highlighting features of the Deep Galicia margin.

Rifting at the Deep Galicia margin (Figure 4-1A) has resulted in the extreme thinning of the continental crust over distances of 100 – 200km. Unaltered crust landward of the proximal rift margin is ~30 km thick and has been thinned through a complex pattern of faulting to only a few km at the distal limits of the margin [*Zelt et al.*, 2003; *Reston*, 2009b]. Initial extensional deformation is inferred to have occurred as high-angle normal faulting, which formed large fault-bound blocks between 10 and 20 km wide, thinning the crust to between 20 and 30 km thick [*Ranero and Pérez-Gussinyé*, 2010]. With continued extension of the margin, these continental fault blocks rotated to low-angles, at which point their bounding faults locked up [*Ranero and Pérez-Gussinyé*, 2010]. The faulting mechanism responsible

for how continued extension was accommodated still remains controversial. *McDermott and Reston* [2015] propose that the crust deformed through polyphase faulting, where new preferentially oriented normal faults overprinted existing faults and fault blocks. *Ranero and Pérez-Gussinyé* [2010] suggest that the continued deformation occurred as a sequential pattern of faulting, where new preferentially oriented normal faults were successively formed through the thinned crust, but did not cut the preceding fault. Both of these proposed mechanisms lead to the extreme thinning of the continental crust.

As the margin extended and thinned at an ultra-slow rate (< 10 mm/yr half spreading rate), it allowed time for the entire crust to cool conductively, resulting in the normally ductile mid and lower crust becoming progressively embrittled [*Srivastava et al.*, 2000; *Pérez-Gussinyé and Reston*, 2001; *Pérez-Gussinyé et al.*, 2003]. Once the crustal thicknesses reached < 10 km, the entire crust became brittle and coupled, a phenomenon known as continental hyperextension. A fully embrittled crust enabled normal faults to form through the entire crust, from the seafloor to the underlying mantle [*Pérez-Gussinyé and Reston*, 2001; *Pérez-Gussinyé et al.*, 2003; *Pérez-Gussinyé*, 2013]. These faults acted as conduits, delivering seawater to the upper mantle and forming a layer of serpentinised mantle, which is an inherently weak material [*Pérez-Gussinyé and Reston*, 2001; *Reston et al.*, 2007; *Bayrakci et al.*, 2016]. With continued extension these faults soled out into the structurally weak layer of mantle serpentinite, forming a large and low angle (< 20^{o}) detachment fault, known as the S reflector (Figure 4-1C), which also corresponds to the crust-mantle boundary in the distal margin [*Reston et al.*, 2007]. It has been shown recently that these faults, which sole into the S reflector, preferentially hydrate the upper mantle which results in varying degrees of mantle serpentinisation, observed as a pattern of high and low P-wave velocities [*Bayrakci et al.*, 2016; *Davy et al.*, 2016]. In the final stages of rifting, serpentinised subcontinental mantle was exhumed to the seafloor along the S reflector, and was also emplaced west of this hyperextended domain, forming a structure known as the Peridotite Ridge [*Beslier et al.*, 1993], before the onset of seafloor spreading [*Davy et al.*, 2016]. Sedimentation of this margin occurs at all stages of the rifting process, giving rise to pre-, syn- and post-rift sedimentary units, which are mentioned throughout our interpretations [*Ranero and Pérez-Gussinyé*, 2010].

4.2.2 Seismic data set

This study investigates a 2D subset (3D inline 420) of the Galicia-3D seismic experiment, which was performed at the Deep Galicia margin, west of Spain (Figure 4-1A) between 1 June 2013 and 2 August 2013 (Figure 4-1B); (see *Davy et al.* [2016] and *Dean et al.* [2015] for further details on the wide-angle and multichannel seismic survey parameters, respectively). Multichannel seismic reflection data were recorded by the RV *Marcus G. Langseth* towing four streamers of ~6 km length, spaced 200 m apart, and at a depth of 15 m. Each streamer had 468 channels spaced at 12.5 m intervals. The seismic source comprised two 3,300 cu. in. air gun arrays, towed at a depth of 9 m and fired alternately every 37.5 m (a shot interval of ~16 s), optimal for high resolution 3D reflection imaging, but sub-optimal for wide-angle studies. Wide-angle seismic arrivals along this 2D profile were recorded by 26 ocean bottom seismometers and hydrophones (OBS/H) from the UK Ocean Bottom Instrumentation Facility (OBIF) [*Minshull et al.*, 2005] and GEOMAR (Figure 4-1B). The eastern 17 OBS/H were spaced densely at ~1.7 km intervals, with the intention to produce high resolution 2D velocity models of the geologic structure above and below the S reflector. The western 9 OBS/H, spaced at distances of ~3.4 km, cover the Peridotite Ridge (Fig 1C) and the sedimentary basins on its western and eastern flanks. Two of the 26 OBS/H were not retrieved, while another five instruments returned no usable data.

Most of the OBS/H in the Galicia-3D seismic experiment recorded seismic shots with a complete azimuthal coverage, allowing these instruments to be accurately relocated by minimising the travel-time misfit between the observed and calculated direct water wave arrival. However, eight OBH along this line were deployed for a shorter period and only recorded shots from a single seismic profile, limiting their ability to be relocated accurately in the cross-line direction (OBH 79-86). On average each instrument was relocated by 299 m.

4.3 Full-waveform inversion

The theory behind FWI and its application to seismic data was first developed in the 1980's by *Lailly* [1983] and *Tarantola* [1984]. It was shown that finite difference modelling of the wavefield through a starting medium, followed by a localised least-squares inversion, minimising the misfit between observed and modelled wavefield, could be used to recover

physical properties of the subsurface [*Tarantola*, 1987]. Initial applications of FWI were performed in the time domain, but were limited given the high computational demand of the method [*Kolb et al.*, 1986]. Three decades later and FWI is still performed based on these underlying principles, with modern codes capable of performing FWI in either the time or frequency domain, in two or three dimensions, approximating either the acoustic or elastic wave equation, and can include the effects of seismic attenuation and anisotropy [e.g., *Pratt*, 1999; *Brossier et al.*, 2009; *Warner et al.*, 2013]. It has also been shown that the maximum achievable resolution using these codes is on the order of half the seismic wavelength, making it superior to travel-time tomography [*Virieux and Operto*, 2009]. Although FWI can extract any physical property which affects the wave equation, it is most commonly used to determine the compressional velocity structure of the subsurface [e.g. *Kapoor et al.*, 2013].

FWI requires an accurate starting model (typically derived from reflection or travel-time tomography) capable of reproducing the majority of the observed wavefield to within half a seismic cycle at the lowest inversion frequency, observed seismic data, and a derivation of a source wavelet [*Virieux and Operto*, 2009]. Forward modelling of synthetic wavefields through the starting model is achieved by solving the numerical wave equation (either acoustic or elastic) through a method of finite differences [*Virieux*, 1986; *Operto et al.*, 2007]. Residual data are then calculated as the difference between the synthetic and observed data, and then the residuals are back propagated through the velocity model and subsequently cross-correlated with the synthetic data to determine a model update [*Tarantola*, 1984; *Pratt et al.*, 1998; *Virieux and Operto*, 2009]. Iteration of this process builds an increasingly resolved velocity model, capable of reproducing the observed wavefield to greater degree. As FWI is a localised inversion method it runs the risk of converging to a local minimum, commonly referred to as cycle-skipping [*Bunks et al.*, 1995; *Sirgue*, 2006]. Cycle-skipping occurs when seismic arrivals in the synthetic wavefield are more than 180^{o} out of phase with that of the observed wavefield. This results in the inversion process attempting to force a match between the observed and synthetic wavefield which is one or more cycles from the true match. In an effort to mitigate against cycle-skipping, it is common practice to start FWI at long wavelengths (low frequencies), which are easier to match within half a cycle, and systematically incorporate shorter wavelengths (higher frequencies) into the modelling, commonly referred to as multiscale

FWI [*Bunks et al.*, 1995; *Sirgue*, 2006]. A complete description of FWI and the underlying theory can be found in *Pratt et al.* [1998] and the review paper of *Virieux and Operto* [2009].

In this study we perform a 2D time-domain, acoustic, isotropic FWI, using the codes of *Warner et al.* [2013]. In this code, synthetic traces are calculated through a starting model using a finite difference method and are subsequently scaled so that their RMS amplitude matches that of their corresponding observed trace. Misfit between the respective synthetic and observed traces is calculated as the sum of squares difference for each time interval, with a misfit functional (objective function) representing the misfit over all traces. As this is a time-domain code, the inversion process matches a finite bandwidth of the observed wavefield, defined by a low-pass filter in which the maximum frequency is progressively increased during the inversion. At each bandwidth the misfit functional was minimised by an iterative gradient-based optimisation, which perturbed an input velocity model in order to match the calculated synthetic and respective observed traces, based on the phase shape and relative amplitude of individual arrivals. The code maintains a deterministic relationship between velocity and density, using Gardner's law below the seafloor [*Gardner et al.*, 1974].

4.3.1 Data pre-processing and derivation of the source wavelet

A mixture of four-component ocean bottom seismometers and single component ocean bottom hydrophones were utilised in this study; the FWI was performed on the hydrophone channel which was present for all instruments and yielded the highest signal-to-noise ratio. Spectral analysis of the hydrophone data showed that there is a reasonable signal-to-noise ratio at frequencies down to ~3.0 Hz. As we wanted to match the modelled wavefield to the observed wavefield, without cycle skipping, we included signal at the lowest frequencies possible. A minimum phase Ormsby band-pass filter with corner frequencies of 2.0, 3.0, 4.5 and 6.5 Hz was applied to the hydrophone data in order to isolate the low-frequency signal from unwanted noise (Figure 4-2A). Typical data pre-processing for the purpose of FWI may look to maintain the lower frequency data by simply applying a low-pass filter, but we needed also to diminish the effects of coherent low-frequency noise from the previous seismic shot. A top mute was applied ~0.1 s above the first seismic arrival, in order to remove the noisy water column, and a bottom mute was applied 1.8 s below this top mute (Figure 4-2B) in order to include the first-arriving

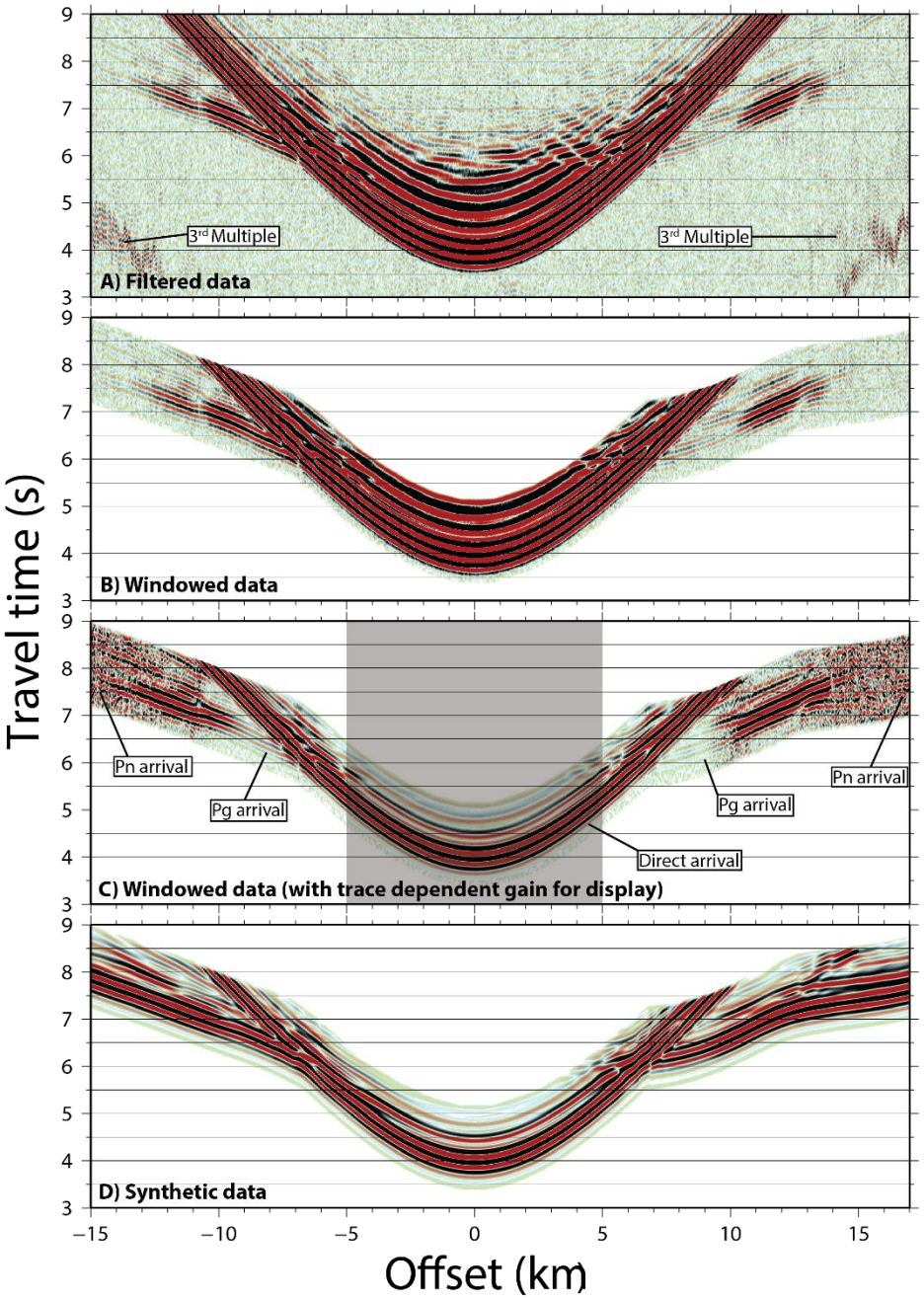

Figure 4-2: Real and synthetic data examples. A) Example receiver gather from OBS 46, filtered with an Ormsby band-pass comprised of corner frequencies 2-3-4.5-6.5 Hz. B) Receiver gather windowed 1.8 s after the first arrival for input into the inversion process. C) Receiver gather illustrated with a trace dependent gain for display purpose. Grey area indicates data which is excluded from the inversion. Identified seismic phases are indicated. D) Synthetic receiver gather for OBS46 generated using the starting velocity model in Fig 4-4A.

wavefield which, at these frequencies, is about 1.0 - 1.5 s in length (Figure 4-2A). This muting process creates a window for the input field data which incorporates the direct water arrival and refractions through the crust (Pg) and upper mantle (Pn) (Figure 4-2B).

The source wavelet was derived with a scheme that uses a Wiener filter to match the synthetic and observed direct water wave recorded on the OBS. Firstly, we produce an initial source wavelet, and in this case used a clean near-offset trace recorded by OBS 46,

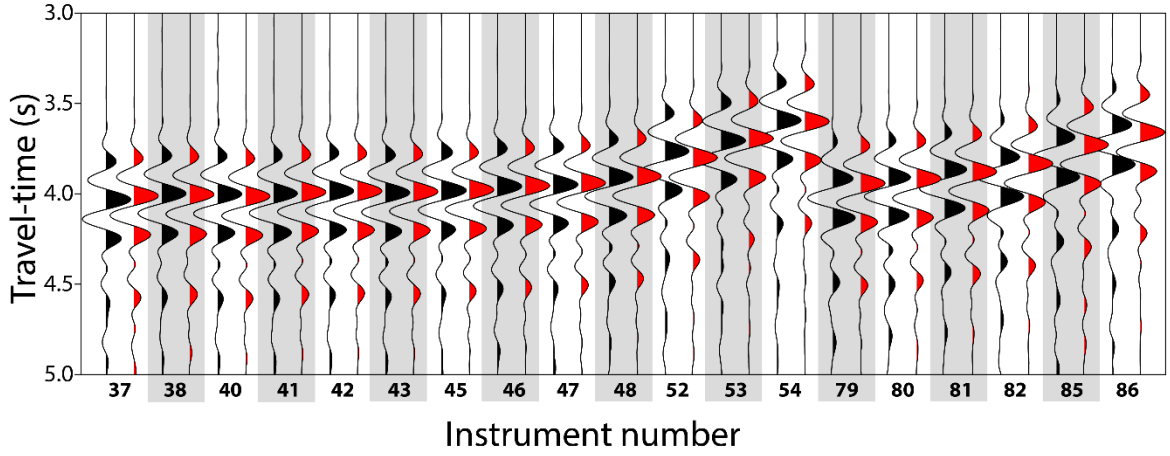

Figure 4-3: Fit between observed and synthetic direct water wave arrivals. Observed near-offset traces (black) compared with the equivalent synthetic trace (red) through the starting velocity model, for all instruments used in this study.

windowed by 1 s. This wavelet and starting velocity model is used to generate synthetic data for the trace it was derived from. We then find the inverse filter that matches this synthetic trace to the equivalent observed trace, and apply this inverse filter to the initial source to generate a new source wavelet. This new source was then used to generate the nearest-offset direct wave through the water for all OBS, and compared to the equivalent observed arrival (Figure 4-3). The excellent match between the observed and synthetic data shows that this source wavelet is appropriate for all OBS. The similarity of the waveforms for all OBS indicates that there is no significant change in the source wavelet during the survey, and that there are no significant differences in OBS response at the data frequencies used in the inversion.

4.3.2 Starting model

The starting model for the FWI process is a modified version of the 2D compressional seismic travel-time tomography model described by *Davy et al.* [2016]. This model was developed using OBS data collected from the Galicia-3D seismic experiment, supplemented with data from the ISE-1 seismic profile [*Sawyer et al.*, 1997; *Zelt et al.*, 2003], and inverted using the "TOMO2D" travel-time inversion code of *Korenaga et al.* [2000]. The final TOMO2D model has an overall travel-time misfit of 53 ms, and a chi-squared value of 0.97. We shortened this model to include only the easternmost 68 km of the seismic profile where the OBS are more closely spaced, to a depth of 12 km, and defined the model on a grid with a horizontal and vertical spacing of 50 m. FWI requires 4 - 5 model nodes per seismic wavelength [*Warner et al.*, 2013], and so with water velocities of ~1.5 km s^{-1} a node

spacing of 50 m allows inversion frequencies of up to 6.0 -7.5 Hz. In the TOMO2D analysis, a constant velocity of 1.52 km s^{-1} was used for the water column. This is sufficient for travel-time tomography, but not for reproducing consistently the first seismic arrivals to within half a cycle of those observed in the field data. Sound velocity profiles, used for the processing of the multibeam bathymetry collected during the survey, were used in place of this constant velocity approximation. The resulting model gives an accurate fit of the direct arrivals through the water-column (12.7 ms for all instruments, on average), as shown in Figure 4-3.

Sediment velocities in this starting model were determined by the forward modelling of a prominent sedimentary reflector and very limited sediment refractions, and are therefore relatively unconstrained. This is the result of the large crossover distance between the direct water wave and the refracted arrivals from the subsurface, dictated by the depth of the instrument deployment. At the deployment depths of 4,000 – 5,300 m, it is rare to observe sediment refractions as the first seismic arrival. The effect of uncertainty in sediment velocities on the final FWI velocity model is examined later in the paper.

The velocity model was smoothed in both the horizontal and vertical directions in order to remove any features that have a shorter wavelength than obtainable by FWI at the lowest inversion frequency. A 2D convolution filter, using 3 samples in the vertical direction (150 m) and 9 samples in the horizontal direction (450 m), was used for this smoothing process. Our starting model can be seen in Figure 4-4A.

4.3.3 Data selection

Using this starting velocity model, synthetic receiver gathers were produced with the same source-receiver geometry as the original seismic experiment (Figure 4-2C). Synthetic gathers were used as a quality control for the field data to be input into the FWI process. Of the 20 instruments which yielded useable data, one was rejected for being too noisy. The final instrument coverage used for the FWI is shown in Figure 4-1B.

Within the offset range between 0 m and 5,000 m the first arrivals comprise direct water waves and sub-horizontally travelling turning waves which sparsely sample the shallow sub seafloor (Figure 4-2B). When included in the inversion these arrivals tend to dominate due to their large amplitudes, and the inversion attempts to match changes in waveform structure by introducing rapid changes in shallow sub-seafloor velocities which are poorly

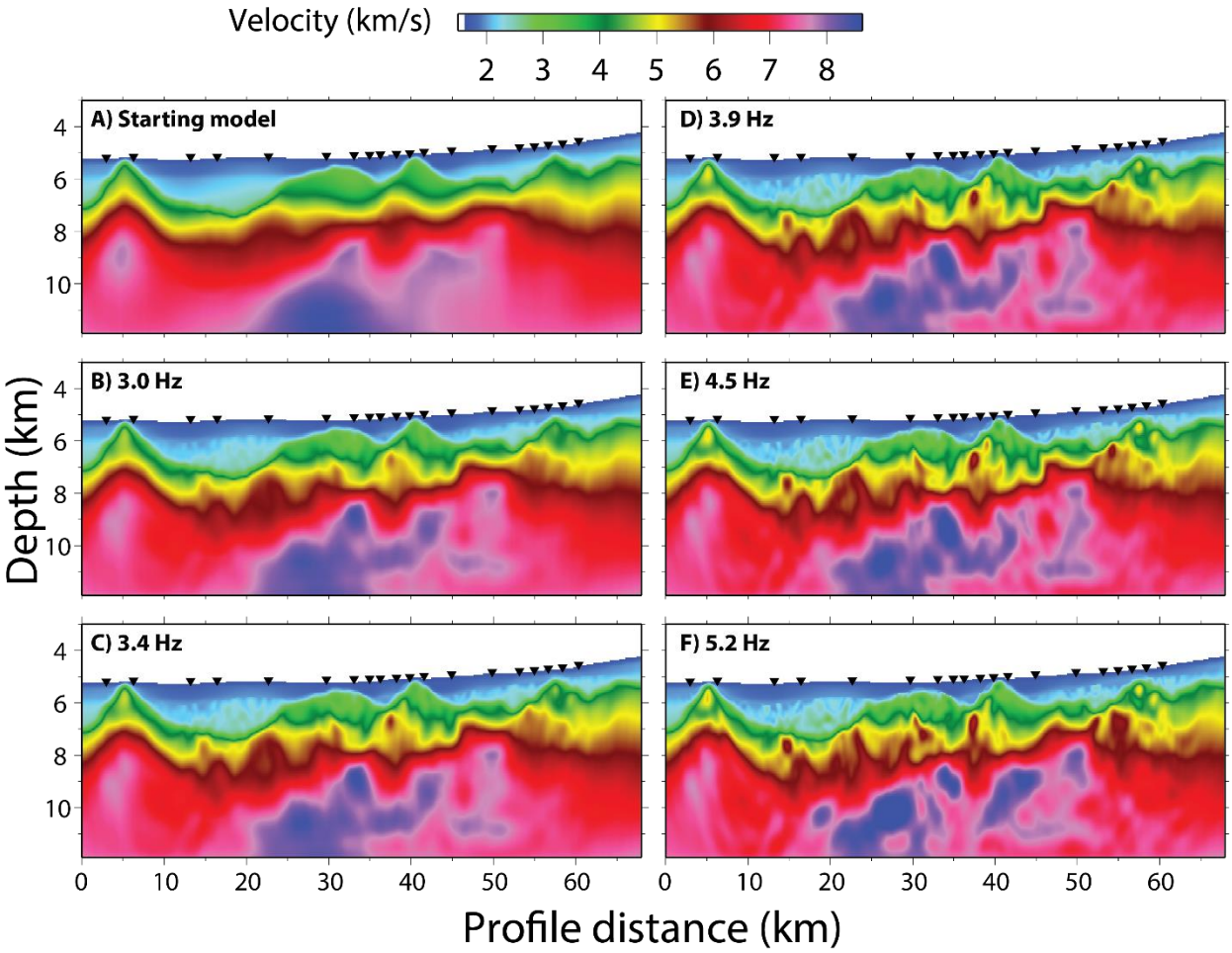

Figure 4-4: Iterative inversion models. A) Starting velocity model input to the FWI. Results of the iterative FWI process for low-pass filter frequencies of: B) 3.0 Hz; C) 3.4 Hz; D) 3.9 Hz; E) 4.5 Hz and F) 5.2 Hz. Black upturned triangles indicate the locations of utilised instruments. Vertical exaggeration is 3.2.

constrained. Pg and Pn arrivals travel sub-vertically through the shallow section below each OBS, and therefore pass relatively rapidly through this region, so their travel-times will not be significantly affected by the shallow velocity structure. Thus, it was decided to exclude this offset range (0 – 5000 m) from the inversion, and not attempt to resolve velocity in the shallow sub seafloor, which is a region of low scientific interest.

We assessed the data from each individual instrument in order to identify the maximum offsets to which the first seismic arrival could be positively identified and matched to the synthetic wavefields to within half a seismic cycle. These maximum offsets were then used as the upper bounds for data input for the respective instrument. Maximum input data offsets ranged from 13.0 to 23.0 km across the 19 instruments utilised in the inversion.

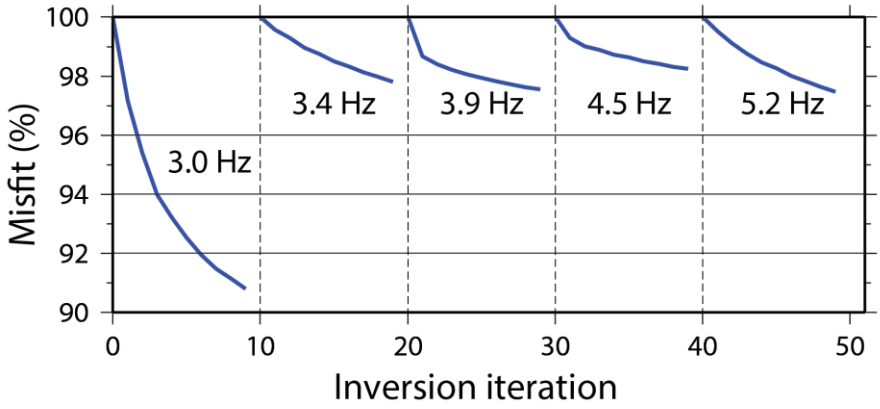

Figure 4-5: Misfit reduction versus inversion iterations for the five low-cut frequency bands, 3.0, 3.4, 3.9, 4.5 and 5.2 Hz.

4.3.4 Inversion

We assumed an isotropic medium for the inversion, based on previous joint reflection and refraction travel-time tomography [*Davy et al.*, 2016]. These joint inversions resolved the S reflector by constraining the velocity field using refraction data and determining the reflector depth using wide-angle reflections. These results showed an excellent match to the S reflector resolved in reflection imaging, where ray-paths are near vertical. This observation indicates that any anisotropy is quite weak, justifying our assumption of isotropy.

We developed the inversion by increasing progressively the cut-off frequency of the low pass filter applied to the input data, which was set at 3.0, 3.4, 3.9, 4.5 and 5.2 Hz (Figure 4-4). Velocities of below 2.0 km s^{-1} in the starting model were kept constant during the inversion to keep the water velocity and sea bottom fixed, since these parameters had been determined independently, and were confirmed by synthetic direct water waves through the starting model (Figure 4-3). Velocities were not allowed to be updated above 8.50 km s^{-1} as this was considered to be the maximum realistic value for the uppermost mantle here. The inversion process was iterated 10 times for each filter setting, with the resulting velocity model acting as the input to the next inversion iteration (Figure 4-4). After 10 inversion iterations at each bandwidth the reduction in the model misfit was less than 0.5% of the previous inversion iteration, which we believed to be a sufficient convergence (Figure 4-5). Relatively small reductions in the misfit functional were seen for each inversion frequency, see Table 4-1.

Inversion low-pass frequency	Reduction in misfit functional
3.0 Hz	9.2%
3.4 Hz	2.2%
3.9 Hz	2.4%
4.5 Hz	1.8%
5.2 Hz	2.5%

Table 4-1: Reduction in misfit functional for given inversion low-pass frequencies. Each frequency is iterated 10 times.

The complete inversion process runs through 50 iterations to produce the final inversion model (Figure 4-4F). Systematically introducing higher frequencies of input data into the inversion process gradually increases the resolution of the resulting velocity model (Figure 4-4A-F).

Testing of the inversion parameters included examining the effects of: the maximum data offsets used, the length of the time window around the first seismic arrival, and uncertainty in the sediment velocities in the starting model. The results of these parameter tests were checked against reflection seismic images, and the observed field data, in order to make informed decisions on the best parameterisation. The next three subsections describe the results of these tests.

4.3.5 Data offsets

One of the limitations of this dataset is the range of useable data offsets. Given the deep-water setting, refractions only become first arrivals at offsets of > 5,000 m, reducing our ability to resolve shallow subsurface structure. At longer offsets (> ~12,000 m) the data become adversely affected by coherent noise from the third multiple (and higher order multiples) of the previous seismic shots (Figure 4-2A). This is problematic because the crustal targets (fault rotated continental blocks, the S reflector and uppermost mantle) are up to 5,000 m below the seafloor, but we can only expect to resolve targets at depths approximately between a sixth and third of the maximum source-receiver offset [*Warner et al.*, 2010; *Morgan et al.*, 2013]. This means that our inversion model, when using data offsets > 12,000 m, may be prone to noise-induced artefacts when attempting to resolve structure at depths greater than 2,000 – 4,000 m below the seafloor. To test whether our

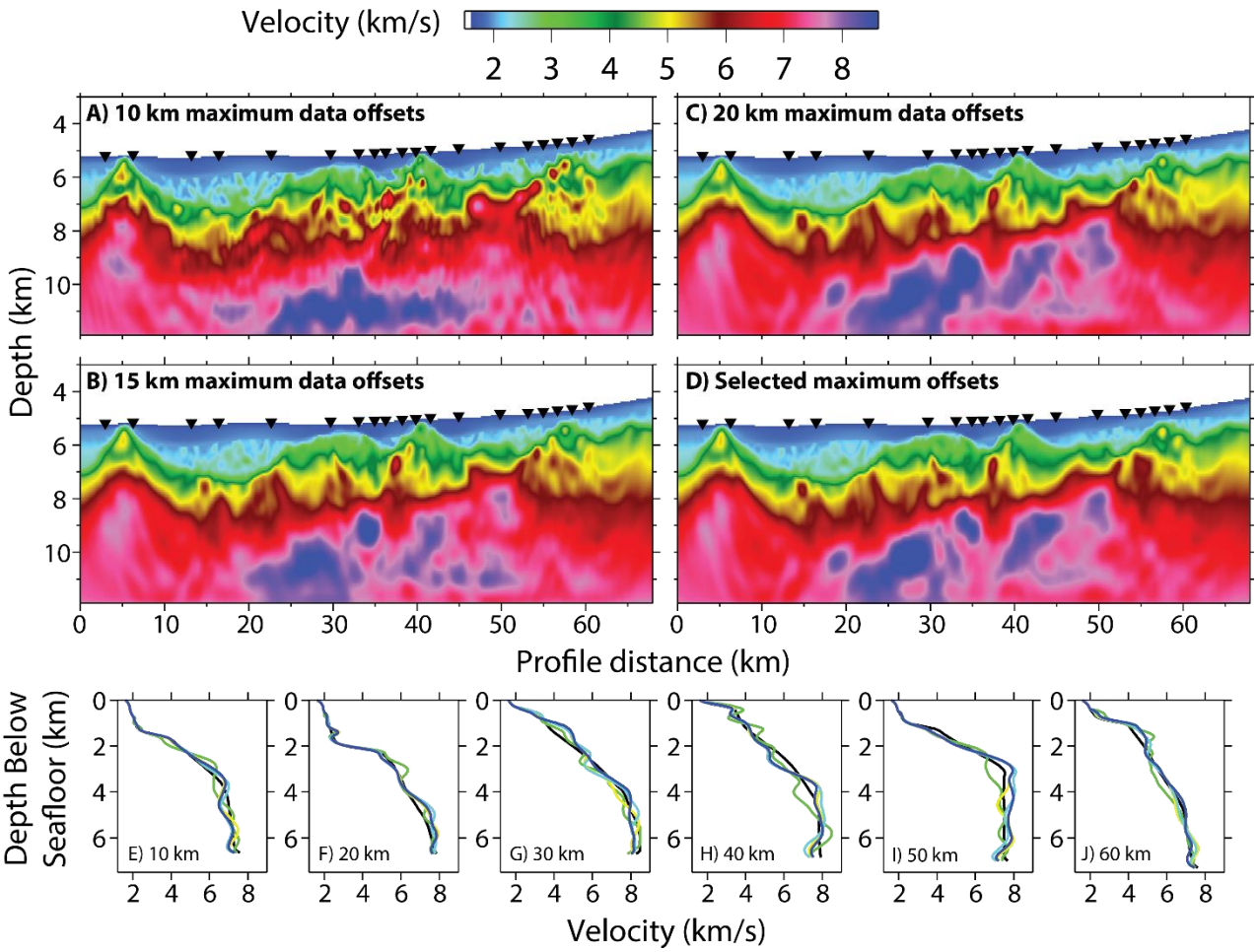

Figure 4-6: Inversion models for maximum data offsets of A) 10 km B) 15 km C) 20 km D) Instrument specific offsets. Black upturned triangles indicate the locations of utilised instruments. Vertical exaggeration is 3.2. E-J) 1D velocity profiles through the resulting models, below the seafloor, at set profile distances (10, 20, 30, 40, 50 and 60 km, respectively). Line colours are black: starting model, green: 10 km data offsets, yellow: 15 km data offsets, light blue: 20 km data offsets, blue: instrument specific data offsets.

selected maximum data offsets (between 13.0 and 23.0 km) produced a robust model, we tested arbitrary maximum data offsets of 10, 15 and 20 km for all instruments used in the inversion. All other inversion parameters were identical to those described in **4.3.4.** Figure 4-6 shows the resulting models and 1D profiles at set distances through each model.

When limiting input data offsets to 10 km (Figure 4-6A), the resulting velocity model has many closed velocity contours, high lateral and depth variability, and features which would be described as non-geologic. This is expected given the sparse coverage and relatively shallow depth of penetration when offsets are limited to 10 km, as waves are expected to only travel to depths of 1.6 – 3.3 km below the seafloor. It can be seen in the 1D plots (Figure 4-6E-J) that the model utilising 10 km data offsets has a good correlation with the trends of the other models to depths of ~1.2 – 3.0 km below the seafloor, as would be

expected. The only exception to this is at ~40 km profile distance (Figure 4-6H). Below these depths, the 10 km offset model varies from the other models by up to 1.38 km s^{-1} (e.g. 3.0 km below the seafloor at 50 km profile distance), because the model is unconstrained at these depths.

The remaining three models share common features and velocity values. These models appear much smoother than that produced using data offsets up to 10 km. The 1-D velocity profiles confirm that the models have common trends with depth, throughout the model (Figure 4-6E-J), but we observe that the model utilising offsets of 15 km deviates from our final inversion model and that using maximum offsets of 20 km, at depths greater than 4 km below the seafloor on profiles at 10, 30 and 50 km. Again, these deviations are unsurprising given that the expected depth of penetration when using maximum offsets of 15 km is up to 2.5 – 5.0 km.

This similarity, especially between models using 15.0 and 20 km offset of input data, indicates that incorporating data with coherent noise yields results which are comparable to those inversions which exclude noisy data altogether. This derivation also suggests that the FWI is relatively insensitive to noise.

4.3.6 Data windowing

Data input into the inversion process were top and bottom muted, allowing a 1.8 s window of data to be matched in the inversion process. The purpose of this time window is to include only the primary compressional seismic phase arrivals (i.e. Pg and Pn, Figure 4-2A), while excluding mode-converted later arrivals, which cannot be reproduced by the acoustic wave approximation [*Jaiswal et al.*, 2008]. Windows of 1.8 s were selected, based on inspection of the length of the band passed first-arriving waveform (Figure 4-2A). To investigate the effect of the data window length, the inversion process was run also with data windows of lengths 1.0, 1.5, 2.0 and 2.5 s (Figure 4-7). It appears that longer window lengths introduced more complicated structure to the resulting velocity model, a result of the inversion process trying to fit the later parts of the seismic coda and later arrivals. Using a time window of 1.0 s resulted in a smooth model, which is geologically reasonable, but failed to match reflections in the seismic images as well as inversion model using a time window of 1.8 s. At the other extreme, a time window of 2.5 s resulted in a rough model with a significant number of closed velocity contours, which are geologically unlikely for

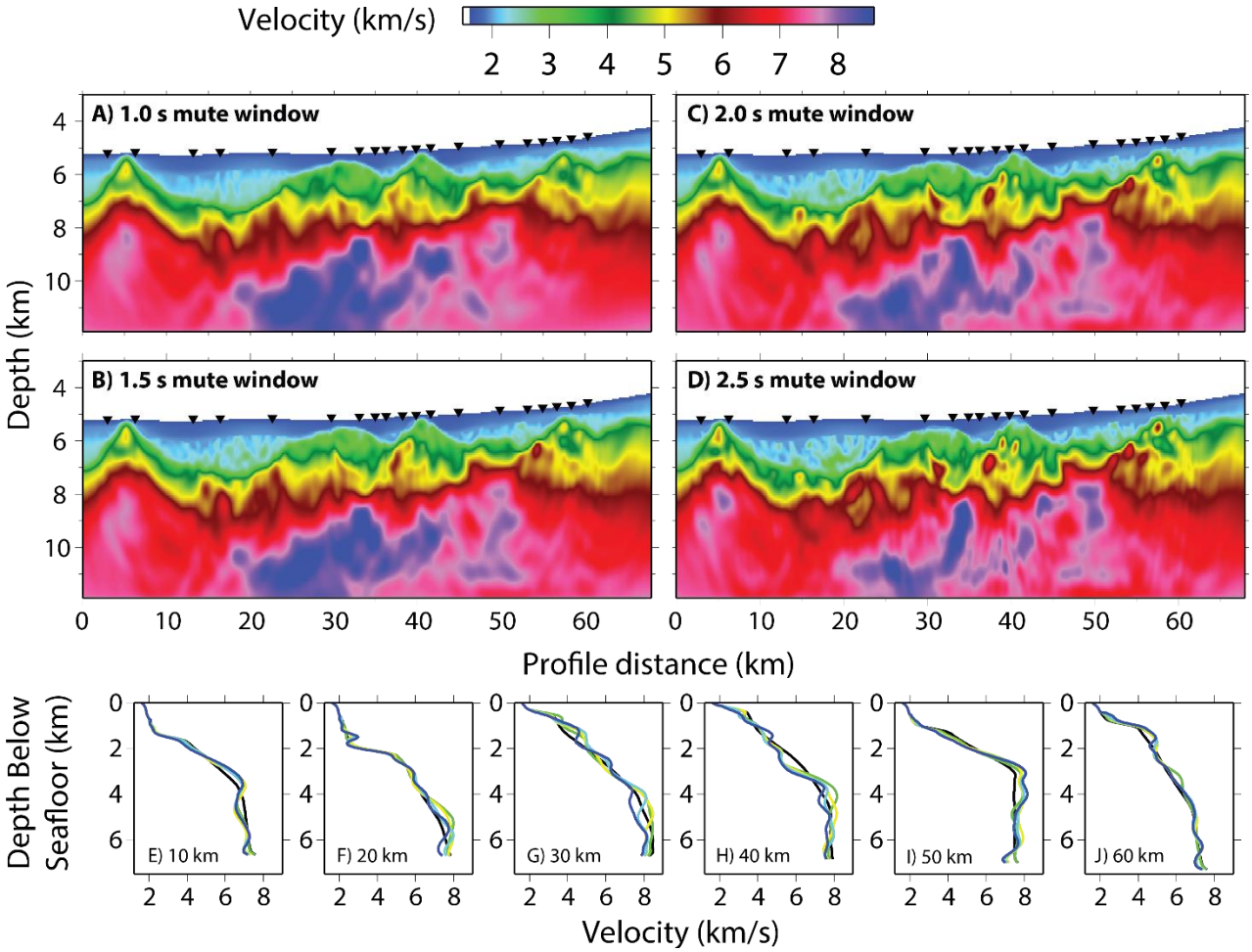

Figure 4-7: Inversion models for varying mute windows of A) 1.0 s B) 1.5 s C) 2.0 s D) 2.5 s. Black upturned triangles indicate the locations of utilised instruments. Vertical exaggeration is 3.2. E-J) 1D velocity profiles through the resulting models, below the seafloor, at set profile distances (10, 20, 30, 40, 50 and 60 km, respectively). Line colours are black: starting model, green: 1.0 s, yellow: 1.5 s, light blue: 2.0 s, blue: 2.5 s.

this setting. We also observed a significant decrease in seismic velocity in the resolved upper mantle in the central section of the profile, with an increasing window length (depths of 9.0 – 10.5 km, 25.0 – 32.0 km profile distance, Figure 4-7C-D; deeper than 4.0 km below seafloor in Figure 4-7G). Despite these differences, the overall velocity structure observed in the plots and the trends of the 1D velocity profiles, remained relatively constant. Consistency in the resulting FWI models and the observed depth-velocity profiles, when using time windows of 1.0, 1.5 and 2.0 s for FWI, indicates that our chosen time window of 1.8 s is appropriate.

4.3.7 Sedimentary velocities

As mentioned earlier in this section, the post-rift sediment velocities in the starting model were poorly constrained, so it is important to test the effects of variable post-rift

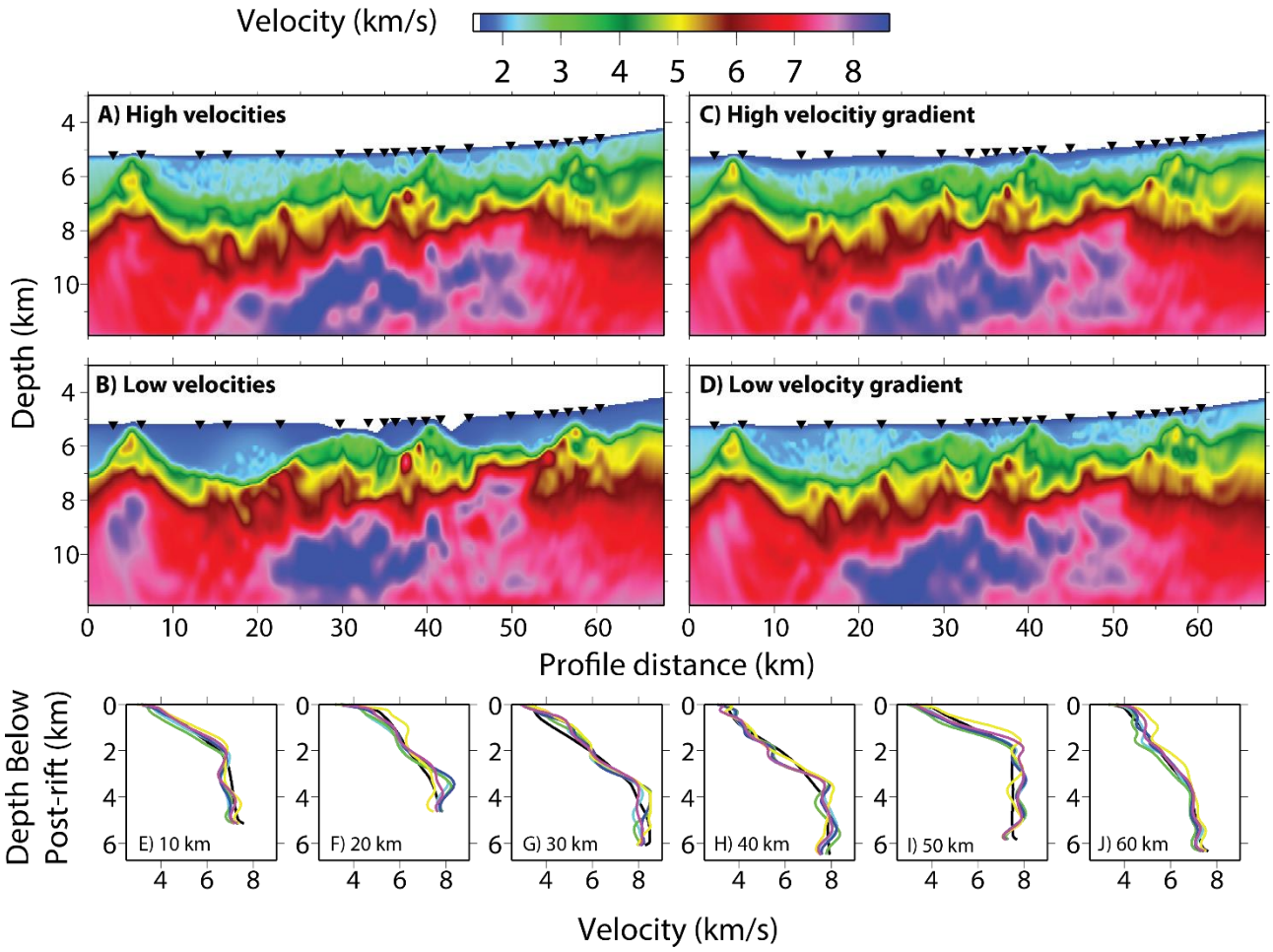

Figure 4-8: Inversion models for varying sediment velocity models, as described in section 3.7: A) High velocities B) Low velocities C) High-velocity gradient D) Low-velocity gradient. Black upturned triangles indicate the locations of utilised instruments. Vertical exaggeration is 3.2. E-J) 1D velocity profiles through the resulting models, below post-rift sediment, at set profile distances (10, 20, 30, 40, 50 and 60 km, respectively). Line colours are black: starting model, green: high velocities, yellow: low velocities, light blue: high-velocity gradient, blue: low-velocity gradient.

sedimentary velocities in the starting model. In the original model, the post-rift sediments were defined by two discrete sedimentary layers, the top which has velocities increasing from 2.00 to 2.15 km s^{-1}, while the bottom layer has velocities increasing from 2.30 to 2.60 km s^{-1}. These layers were constrained by inter-sedimentary reflectors and limited sedimentary refractions.

To test the uncertainty in sedimentary velocities in our starting model, we performed the TOMO2D travel-time inversion of *Davy et al.* [2016] with starting models possessing low sediment velocities (1.80 – 2.00 km s^{-1}), high sediment velocities (2.60 – 3.00 km s^{-1}), a low-velocity gradient (2.30 – 2.50 km s^{-1}) and a high-velocity gradient (1.80 – 3.20 km s^{-1}). All travel-time inversion parameters remained identical to that described in *Davy et al.*

[2016]. The outputs of these travel-time inversions were then used as the starting models for the FWI process, with the inversion results observable in Figure 4-8.

With the exception of the low sediment velocity model, the general velocity structure below the post-rift sediments remains consistent. Where post-rift sediment velocities are low, higher velocities are observed directly below the top of the syn-rift sediments, and vice-versa where the post-rift sediment velocities are high. This phenomenon is amplified in areas of thicker post-rift sediment (i.e.: at 10, 20 and 50 km profile distance). For example, at 50 km profile distance the difference between the low and high sediment velocity models is 1.75 km s^{-1} at 1.65 km below the base of the post-rift sediment (Figure 4-8I). This result indicates that variations in the starting post-rift sedimentary velocities are compensated for by the velocities below the post-rift sediment. Despite the differences between the models, the general trend of the velocity variations with depth below the post-rift sediment are consistent, and consistent structural features are recovered in the final velocity model, except for the model with low velocity post-rift sediments (Figure 4-8B). Along the representative depth-velocity profiles (i.e.: 10, 20, 30, 40, 50 and 60 km profile distance), the depth-averaged range of velocities recovered for the full range of starting models, excluding the low-velocity post-rift sediment velocity model, is 0.12 km s^{-1}. We conclude that the sediments are unlikely to have such low velocities, and thus the overall velocity structure of the inversion models below the post-rift sediment are minimally effected by uncertainty in the post-rift sedimentary velocities.

4.3.8 Assessing the modelled wavefield

One of the measures of the success of FWI is determined by how accurately the observed wavefield is reproduced, and this is done by comparison with the synthetic wavefield. Figure 4-9 shows the propagation of the source wavelet through the final inversion model to produce the synthetic wavefield. In this example, we have reversed the source and receiver configuration and are treating the OBS 46 as the seismic source, and the shot locations as receivers. This approach demonstrates the interaction of the wavefield with subsurface structure, and gives an idea of the penetration depths of source-receiver configuration. It can be seen that eastward of OBS 46, the wavefield refracts through significant subsurface topography in the form of a rotated continental fault block, giving the first seismic arrival significant lateral variability. Conversely, west of OBS 46, the top of

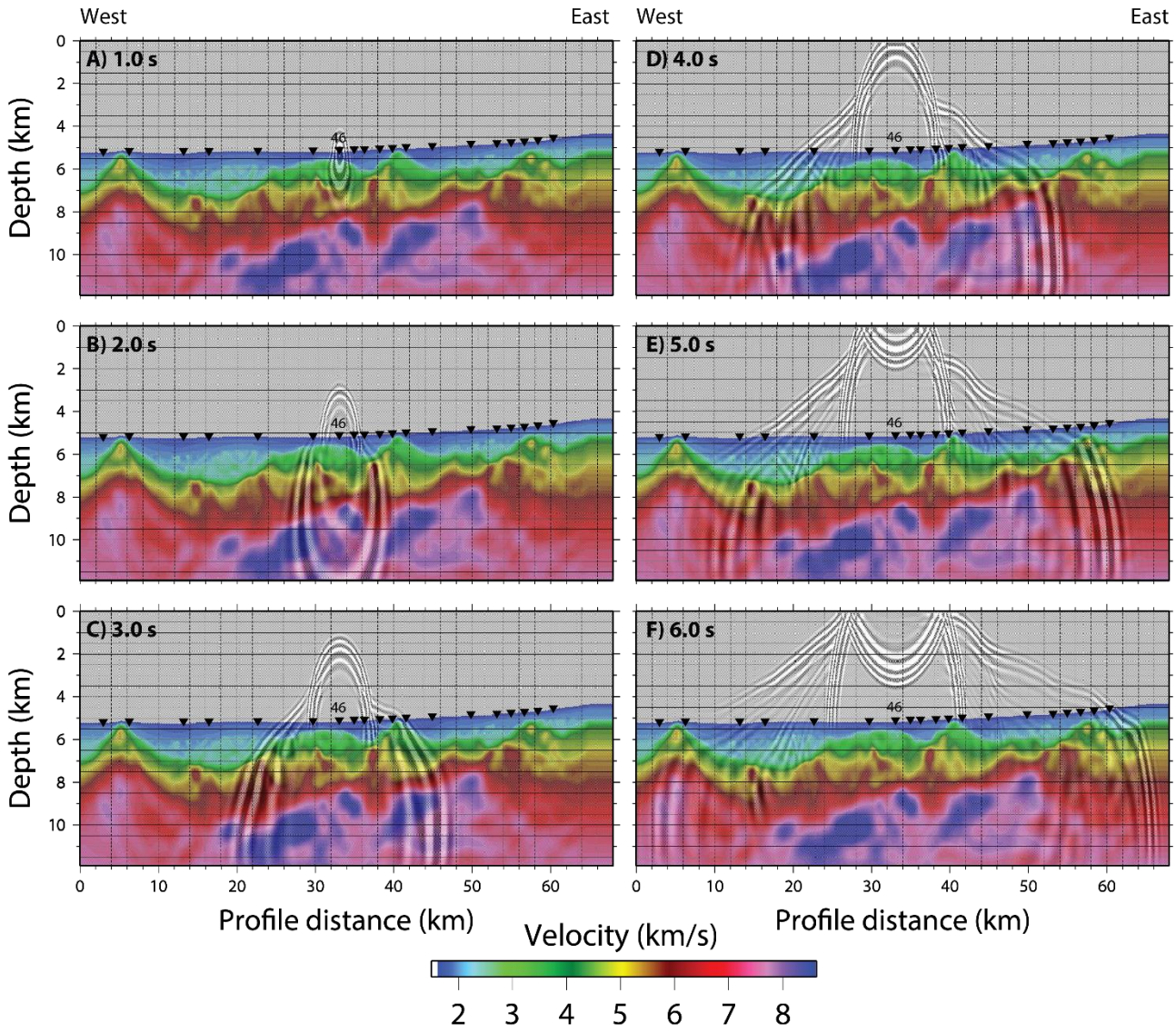

Figure 4-9: Propagation of the derived source wavelet through the final inversion model at discrete times: A) 1.0 s, B) 2.0 s, C) 3.0 s, D) 4.0 s, E) 5.0 s, F) 6.0 s. Black upturned triangles indicate the locations of utilised instruments. Vertical exaggeration is 3.2.

the rotated continental fault block dips smoothly westward, resulting in a first seismic arrival of little variation. These synthetically produced features match those in the observed wavefield (Figure 4-2A-B).

In order to compare the match between the observed and modelled wavefields, we interleaved traces from alternative offset bins of 200 m (i.e.: traces with instrument offsets between 200 – 400 m, 600 – 800 m, etc. are taken from the observed wavefield and are combined with traces with instrument offsets between 0 – 200 m, 400 – 600 m, etc. from the synthetic wavefield) (Figures 4-10-12A-B). Where the wavefields match, a continuous wavefield will be observed over distances greater than the 200 m trace bins. Where the match is poor, a discontinuous wavefield will be observed over such distances. Comparing

the observed wavefield with the synthetic wavefield through the starting model (Figures 10-12A), it can be seen that the direct water arrival (-7.0 – 7.0 km) shows high continuity, indicating that the starting velocity model has reasonably accurate water and sub-seafloor velocities. The wavefield appears to be fairly consistent at some wider offsets, for example between -11 to -15 km on OBS 46 (Figure 4-11A) and -10 to -14 on OBS 54 (Figure 4-12A), indicating that the starting model at depth is close to the true velocity structure in particular areas. There are also notable mismatches in the first seismic arrivals, outside the direct water arrival, for example at offsets between -7 and -11 km and between 7 and 13 km on OBS 46 (Figure 4-11A) and 6 to 10 km on OBS 37 (Figure 4-10A), which indicates that the velocities in sections of the thinned continental crust are not reproducing the wavefield accurately. However, these mismatches appear to be less than half a seismic cycle, which is a prerequisite to avoid cycle skipping during the FWI process. Significant improvements in the match between wavefields are observed when comparing the observed and synthetic wavefield through the FWI velocity model (Figures 4-10-12B). Areas previously mismatched (for example between offsets of 7 – 13 km on OBS 46) now appear more continuous (see arrows) indicating that the FWI process has modified the subsurface velocities in a way that moves the travel-times of these arrivals in the right direction. Where the starting model already matched the observed wavefield well there is little to no change, as would be expected.

Directly comparing traces at set offsets also shows how the synthetic waveforms are modified through the FWI process. Figures 4-10C-H, 4-11C-G, and 4-12C-G, show trace-to-trace comparisons of the observed wavefield and synthetic wavefield through the starting velocity model, while Figures 4-10I-N, 4-11H-L, and 4-12H-L, show trace-to-trace comparisons of the observed wavefield and synthetic wavefield through the final velocity model. It can be seen that despite these small changes in the inversion misfit (Figure 4-5), we observe significant improvements in the synthetic wavefield. For example, at offsets of -10.05, -7.52, 8.63 and 11.93 km on OBS 46 (Figure 4-10D-G), it can be seen that the synthetic traces through the starting model exhibit shapes close to the observed waveform, but with amplitude differences and phase shifts within half a seismic cycle. After the FWI, the synthetic traces have relative amplitudes and phases that match well the observed traces (Figure 4-10J-M), indicating that the new velocity model is a more accurate representation of the subsurface.

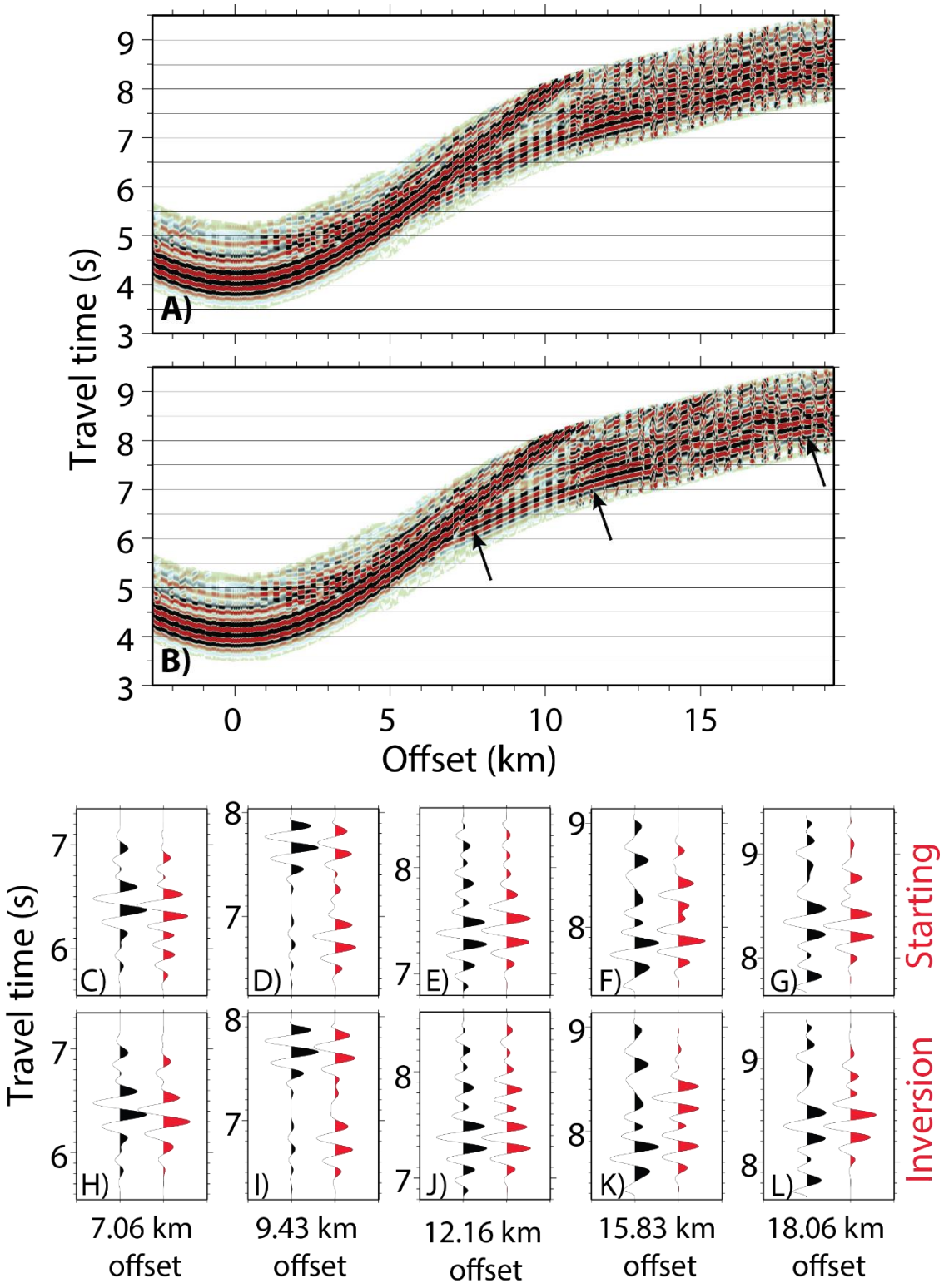

Figure 4-10: OBS 37 quality assurance. A) Observed data interleaved with synthetic through the starting model in alternative offset bins of 200 m. B) Observed data interleaved with synthetic through the inversion model in alternative offset bins of 200 m. Arrows indicate areas of improved match. C-L) Comparing observed and synthetic traces at select instrument offsets. C-G) Black traces: observed data, red traces: synthetic data through the starting model. H-L) Black traces: observed data, red traces: synthetic data through the FWI model.

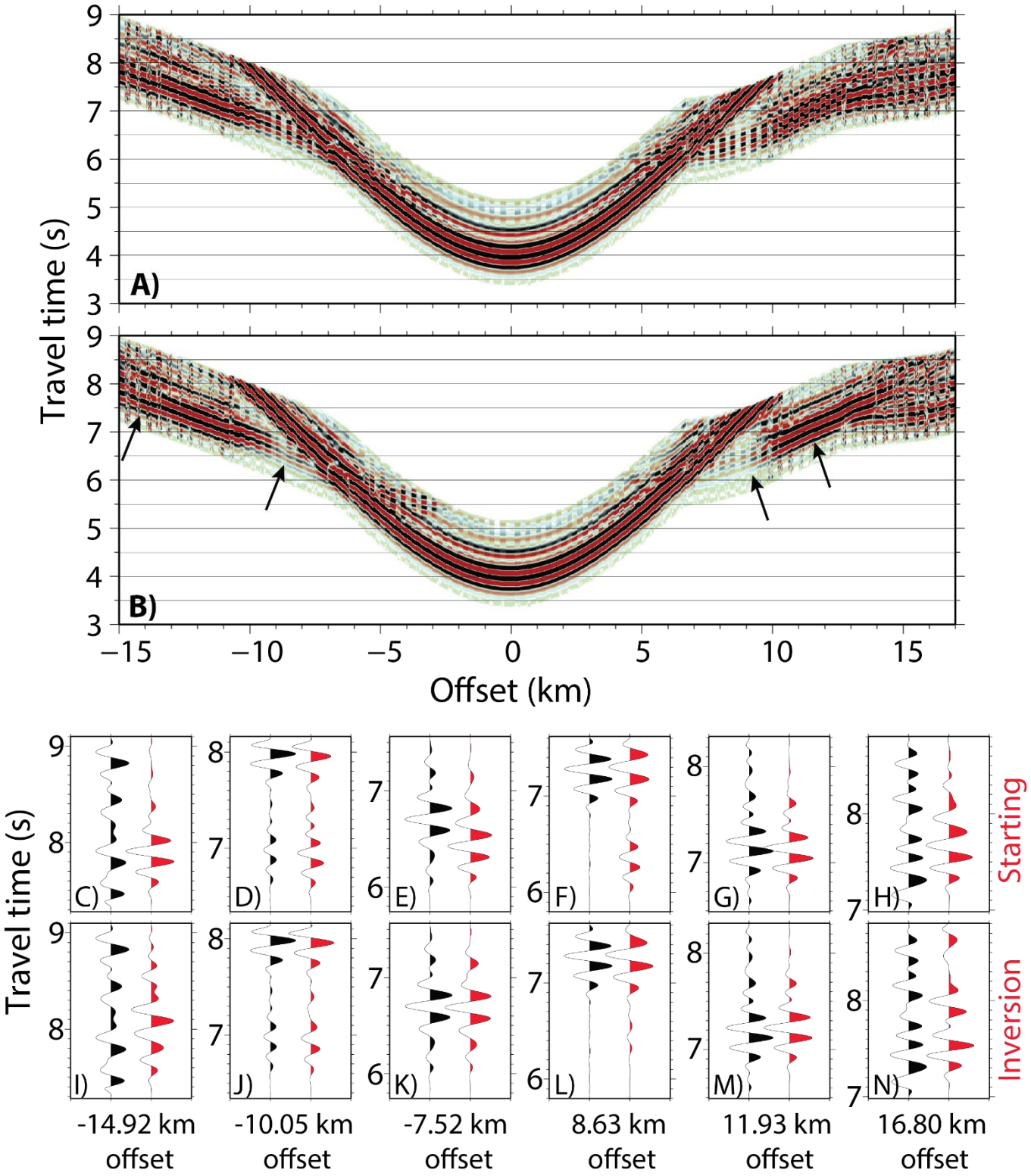

Figure 4-11: OBS 46 quality assurance. A) Observed data interleaved with synthetic through the starting model in alternative offset bins of 200 m. B) Observed data interleaved with synthetic through the inversion model in alternative offset bins of 200 m. Arrows indicate areas of improved match. C-N) Comparing observed and synthetic traces at select instrument offsets. C-H) Black traces: observed data, red traces: synthetic data through the starting model. I-N) Black traces: observed data, red traces: synthetic data through the FWI model.

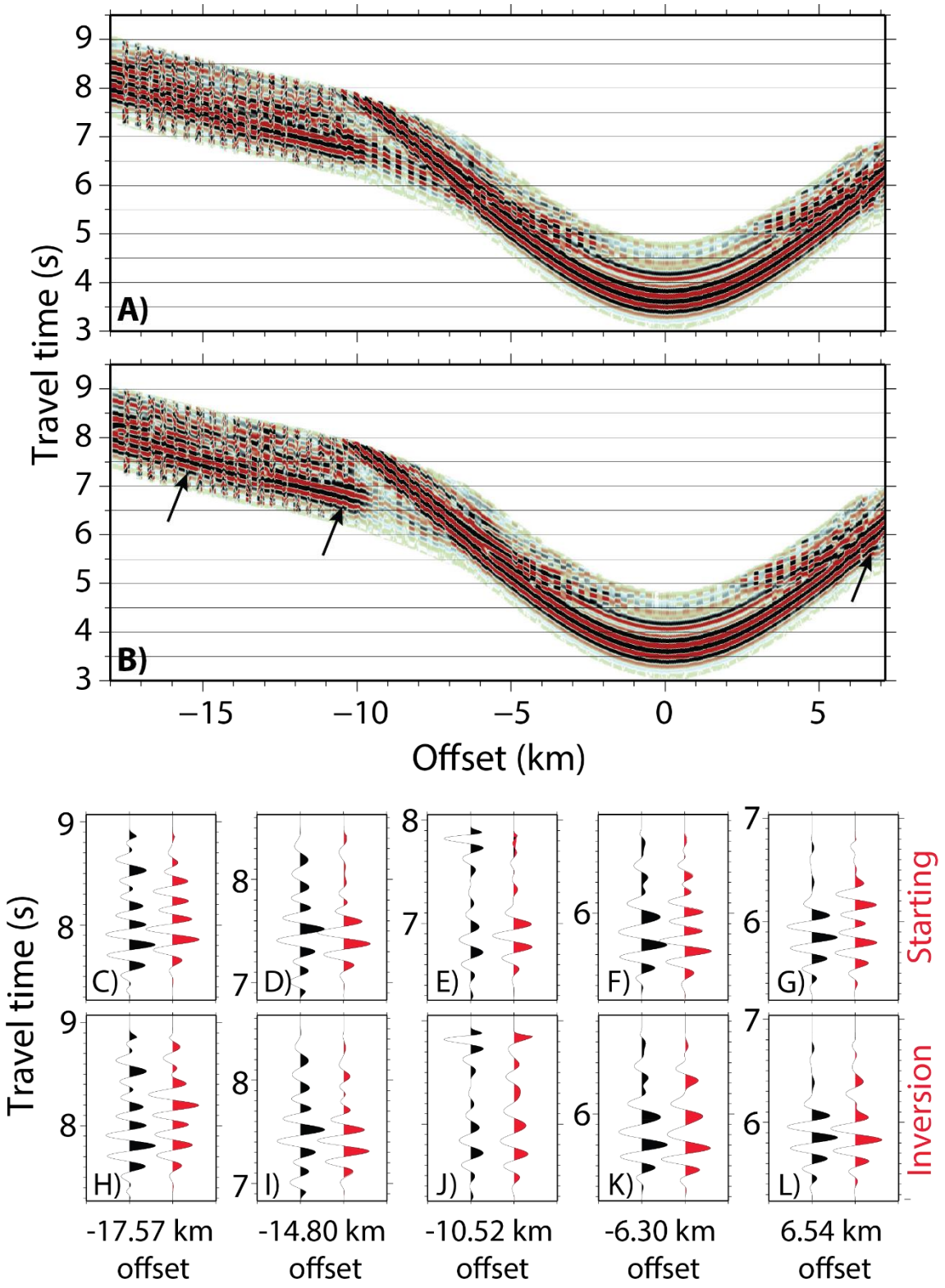

Figure 4-12: OBS 54 quality assurance. A) Observed data interleaved with synthetic through the starting model in alternative offset bins of 200 m. B) Observed data interleaved with synthetic through the inversion model in alternative offset bins of 200 m. Arrows indicate areas of improved match. C-L) Comparing observed and synthetic traces at select instrument offsets. C-G) Black traces: observed data, red traces: synthetic data through the starting model. H-L) Black traces: observed data, red traces: synthetic data through the FWI model.

Observed traces at the furthest input offsets (i.e.: -14.92 and 16.80 km on OBS 46, 18.06 km on OBS 37, and -17.57 km on OBS 54, Figures 4-11I, 4-11N, 4-10L, and 4-12H, respectively) are being affected by coherent noise, and FWI is struggling to match these more complicated waveforms. It appears that the trace at -14.92 km on OBS 46 is cycle skipped in the starting model, and although the inversion has led to an improvement in the shape of the waveform it has not changed its travel-time, which should be earlier. The onset of reduced performance of FWI at longer offsets reinforces the decision to limit the offsets of the input data, based on visual inspection of the match between the observed data and synthetic data from the starting model.

4.3.9 Checkerboards

The maximum achievable resolution of the final FWI velocity model was assessed by a series of checkerboard tests [*Zelt and Barton*, 1998]. Alternating velocity perturbations of ± 2% were introduced into the starting velocity model in checkerboard patterns to create reference models with anomaly dimensions of 10.0 km x 2.0 km, 5.0 km x 1.0 km, and 2.5 km x 0.5 km (Figure 4-13). Small velocity perturbations of ± 2% are used in order to avoid major changes in the modelled wave-paths, which could lead to the synthetic data generated from the checkerboard and starting model being cycle skipped. Synthetic receiver gathers were then produced through these reference models by forward modelling of the wavefield, using the same shot-receiver geometry as the receiver gathers used in the FWI. These synthetic receiver gathers were windowed and inverted with identical FWI parameters. The differences between these inversion results and the unperturbed starting velocity model were used to determine the length scale of structure resolvable in the final FWI model (Figure 4-13).

There is an observable diagonal smearing of the resolved checkerboard patterns at the eastern and western limits of the model, for all scales velocity perturbation. This phenomenon occurs between checks of equal polarity, at profile distances < 10 km and > 50 km. This smearing is likely to be the result of the subsurface being sampled by unidirectional wave propagation and limited data offsets in these areas of the model.

Large-scale structure (10.0 km x 2.0 km) is very well resolved throughout the central portion of the model, but exhibits a small deterioration in the recovered anomaly amplitudes below 10 km depth. Medium-scale structure (5.0 km x 1.0 km) is still well resolved, but starts to

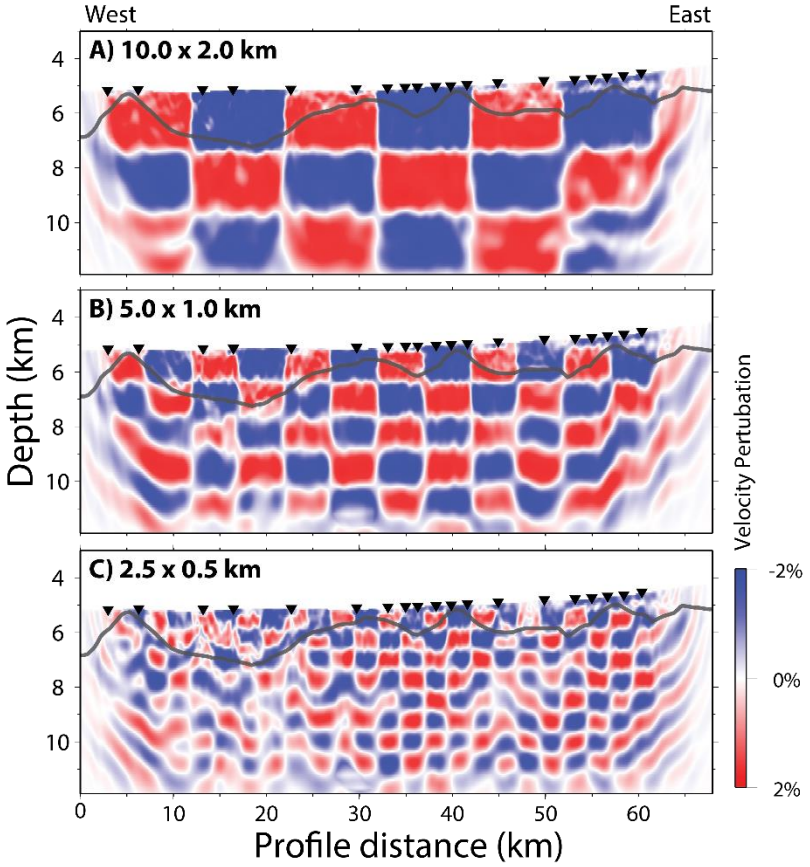

Figure 4-13: Checkerboard resolution test results. Anomaly check dimensions: A) 10.0 x 2.0 km, B) 5.0 x 1.0 km, C) 2.0 x 0.5 km. Vertical exaggeration is 3.4. Grey line represents the top of the syn-rift sediments.

exhibit slight smearing between checks where there is lower instrument coverage (e.g. 5.0 – 30.0 km profile distance), and again at depths > 10 km. Fine-scale structure (2.5 km x 0.5 km) is the least well resolved, as is to be expected, but much of the structure at this scale is still recoverable throughout the model. Fine-scale structure is particularly well resolved between profile distances of 30.0 – 42.0 km and 52.0 – 60.0 km, where the coverage of instruments is densest. Other regions of the model start to reveal a greater degree of smearing between checks, primarily between diagonally linked checks.

The results of these resolution tests exhibit a significant improvement in the achievable resolution when compared with the resolution of travel-time tomography of *Davy et al.* [2016]. However, it should be noted that these resolution tests are done with synthetically produced wavefields and thus represent the maximum achievable resolution with the given experimental geometry.

4.4 Results and discussion

The final FWI velocity model in depth can be seen in Figures 4.4F and 4.6D. Overall, the long-wavelength velocity structure remains consistent with that of the starting travel-time tomography model. Within the velocity model we observe well-defined rotated continental fault blocks which overlie the S reflector, and the Peridotite Ridge in the west. The FWI result reveals features in the velocity model with shorter-wavelengths and a greater lateral variability to those that are observed in the starting model. It appears that there has been a significant increase in the resolution of the velocity structure along this seismic line.

4.4.1 Comparison with seismic images and interpretations

In order to assess whether the FWI has resolved the velocities of fine-scale subsurface structure, we compare the final velocity model with the structure observed in reflection seismic imaging. To make this comparison we have utilised existing high-resolution 3D multichannel reflection seismic images, which have been processed through to 3D pre-stack Kirchhoff time migration. This reflection imaging was produced using the full 3D seismic volume, which has a wide azimuth of shots and receivers, and yields a high-fidelity image of the subsurface. We converted our final FWI velocity model to time, and overlaid it onto the time migrated reflection image of seismic inline 420 (Figures 4-14 and 4-15). Additionally we have overlain the interpretation of significant and relevant faults and geological horizons. Significant horizon reflections are seen from the base of the post-rift sediment, a strong intra syn-rift reflector, the top of crystalline basement, and the S reflector. These interpretations have been made consistently throughout the 3D seismic volume and are independent from both our starting and FWI velocity models. For the prominent normal faults and continental blocks observed through this section, we have adopted the naming convention of F3 – F8 and B3 – B7, respectively [*Borgmeyer*, 2010; *Ranero and Pérez-Gussinyé*, 2010] .

4.4.1.1 Long-wavelength structure

Long-wavelength features that were already present in the starting velocity model show a strong correlation with the large-scale features imaged in the reflection seismic, such as the Peridotite Ridge, the major fault-rotated continental blocks (e.g. B3 – B6) and the S reflector detachment surface (Figure 4-14D) [*Davy et al.*, 2016]. These features retain their

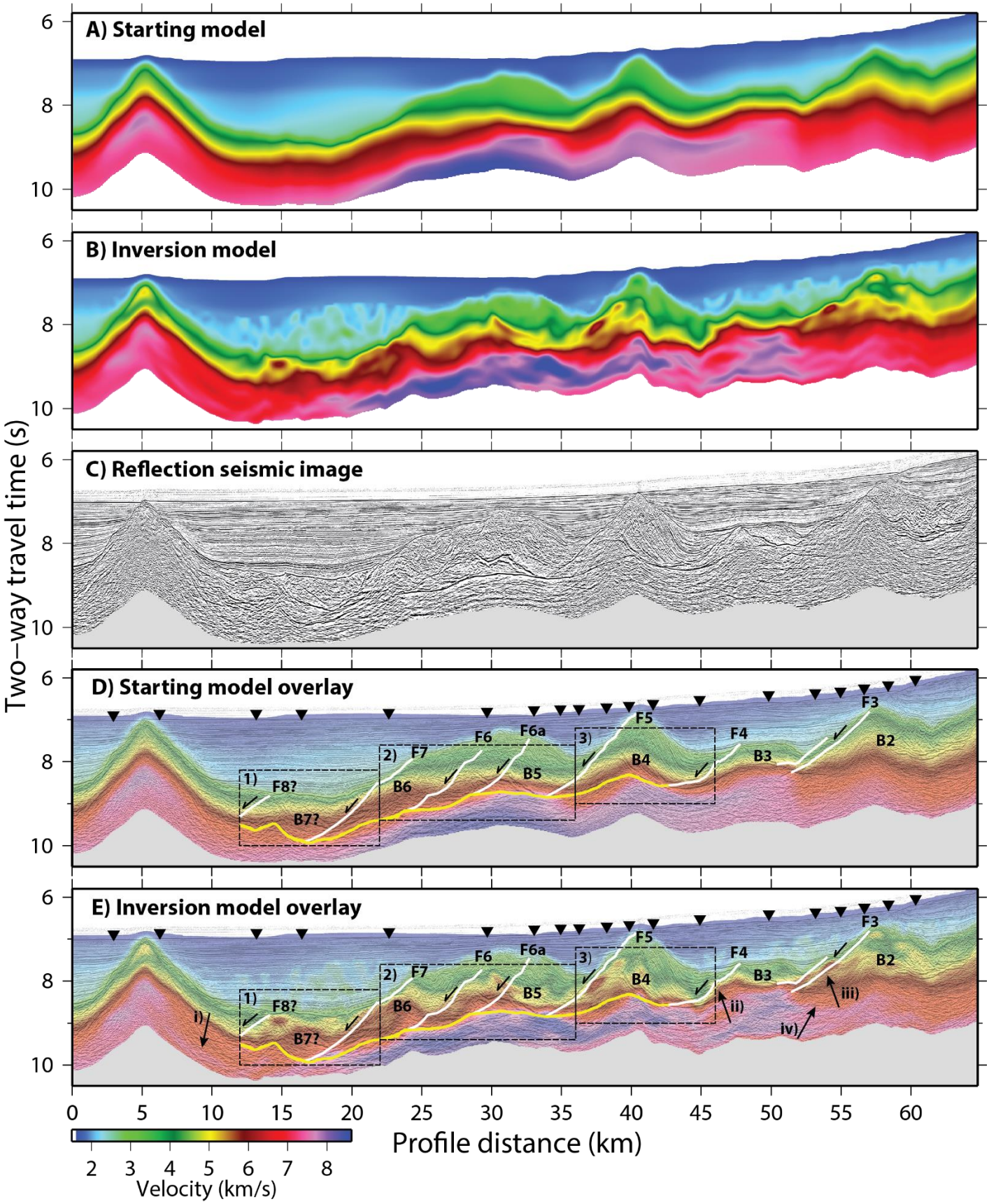

Figure 4-14: Comparison of large scale features with seismic reflection imaging. A) Starting velocity model B) Final FWI velocity model C) Kirchhoff pre-stack time-migrated multichannel seismic image of inline 420. D) Reflection image overlain with starting velocity model. E) Reflection image overlain with FWI velocity model. White lines indicate the location of interpreted normal faulting; the yellow line is the interpreted S reflector. Black upturned triangles indicate the locations of utilised instruments. Dashed black rectangles indicate the zoomed regions illustrated in Figure 4-15. Black arrows indicate regions of interest, which are discussed in the text.

long-wavelength velocity structure through the FWI process, and shorter wavelength velocity features are revealed within the previously resolved features. The most apparent and significant changes to the velocity model occur in continental fault blocks B4-B7 within the pre / syn-rift sediments and the top of crystalline basement. Areas of particular interest are identified by dashed boxes in Figure 4-14 and are shown at a larger scale in Figure 4-15. Features within these areas are discussed in detail in the next sub-section. Outside of these regions, we observed noticeable features at both the western and eastern limits of the inversion model. There is a deepening of seismic velocities between 6.0 – 7.0 km s^{-1} on the eastern flank of the Peridotite Ridge (7.0 – 12.0 km profile distance, arrow i, Figure 4-14E). This deepening could indicate that the serpentinisation of the mantle peridotite in this area is more pervasive than previous models have indicated. This area of decreased seismic velocities is coincident with the interpreted western limit of the S reflector and the suggested location of normal fault F8, which could have acted as a conduit, enabling the hydration and serpentinisation of this area.

At the eastern end of the profile, we observe top basement velocities (~5.5 km s^{-1}) resolved in both blocks B3 and B2, next to their interpreted bounding faults to the west, F4 and F3, respectively (arrows ii and iii, Figure 4-14E). These areas see an increase in velocity to those which are consistent with crystalline basement, at the up-dip end of the rotated fault blocks, indicating that we may be resolving internal structure of such blocks to a greater degree. Additionally, we see a shallowing of mantle velocities (~8.0 km s^{-1}) below block B2, which smooths out an apparent step in these velocities below continental block B2 (arrow iv, Figure 4-14E).

4.4.1.2 Continental fault blocks

The starting velocity model has minimal adherence to the interpreted geological horizons within fault blocks B4 – B7 (Figure 4-15D-F). Velocity contours cut across reflection horizons obliquely, where they would be expected to run parallel, and no sharp velocity changes are observed laterally across normal faults. Significant improvements are observed in the FWI velocity model (arrows i-xiii), Figure 4-15G-I), relative to the starting model, with an increased correlation between the velocity field and a number of the interpreted faults and reflection horizons. In some areas we also observe increased correlation between the velocity model and seismic reflections which have not been interpreted previously. Particularly good improvement is observed in the internal velocity structure of continental

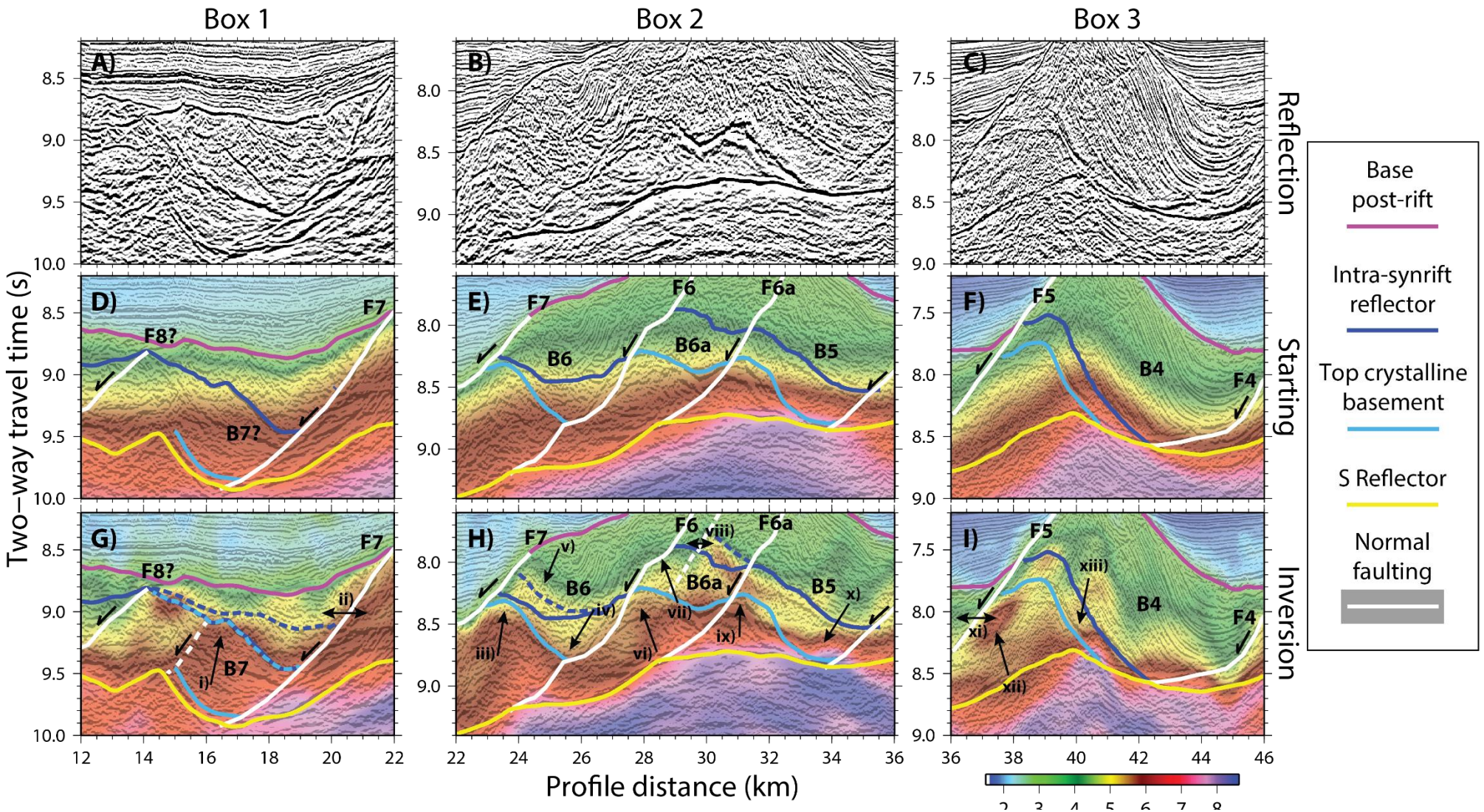

Figure 4-15: Comparison of small scale features with seismic reflection imaging. A-C) Sections of interest of the Kirchhoff pre-stack time-migrated multichannel seismic image of inline 420. D-C) Same reflection images as A-C, overlain by the time-converted starting velocity model. G-I) Same reflection images as A-C, overlain by the time-converted final FWI velocity model. Interpreted faults and horizons: white lines indicate normal faulting; yellow lines indicate the S reflector; pink line indicate the base of the post-rift sediments; dark blue indicate an intra syn-rift horizon; light blue indicates the top of crystalline basement. Black arrows indicate areas where we believe we see an increase in the match of the velocity model to s tructure observed in the reflection images, as described in the text. Double-ended arrows indicate areas with improved resolution across faulting. Dashed lines indicate the reinterpretation of faults and horizons, based on the final FWI velocity model.

blocks B6 and B7 (arrows i-v, Figure 4-15G-H) , and to a lesser degree B6a and B5 (arrows vi-x, Figure 4-15H). In these regions of the model we see a rotation of the velocity field, particularly at the top of crystalline basement, so that velocity contours run parallel to significant reflections. For example, in block B6 (Figure 4-15E), we observed starting velocities at the top of the interpreted crystalline basement of ~4.55 km s^{-1} on the up dip (western) end, and ~5.95 km s^{-1} on the down dip end (eastern). This gives a velocity difference of ~1.40 km s^{-1} along a lithological boundary where we would expect to observe a roughly constant velocity. After the inversion the velocities in these same model locations are now ~5.35 km s^{-1} and ~5.65 km s^{-1}, up dip and down dip, respectively (arrows iii and iv, Figure 4-15H). We now observe a velocity difference of only ~0.30 km s^{-1} along the same boundary. Similar improvements in the crystalline basement velocities are observed in block B7 (Figure 4-15D and G, arrow i), and less substantial improvements are also seen in blocks B6a and B5 (arrows vi and ix, Figure 4-15E and H).

Despite not resolving constant velocities along the layer boundaries within block B4 (Figure 4-15F and I), it can be seen that the FWI process has begun to introduce the appropriate higher velocities (~6.00 km s^{-1}) into the area interpreted as crystalline basement. These velocities are prominently resolved next to the westward fault, F5 (arrow xii, Figure 4-15I). This area of high velocity within the crystalline basement of B4 now exhibits a high velocity contrast laterally across normal fault F5, with the syn-rift unit of block B5 (arrow xi, Figure 4-15I). We observe a lateral velocity contrast of ~1.70 km s^{-1} over a distance of less than 1.00 km across fault F5, where the contrast had previously been ~0.75 km s^{-1}. This result indicates an increased resolution of the velocity changes across normal faults, which have juxtaposed different lithologies against one another. This improvement in the lateral velocity contrast is also observed between the crystalline basement of block B6 and the syn-rift unit of block B7, across fault F7 (arrow ii, Figure 4-15G). There is also evidence of a previously unidentified fault within block B6a, between faults F6 and F6a (Figure 4-15H). A sharp lateral velocity contrast of ~1.50 km s^{-1} (arrow viii, Figure 4-15H), and westward dipping velocity field, highlights a weak reflector which we interpret as a normal fault.

Even though these areas of the FWI model exhibit apparent improvement, there are areas where we observe velocity patterns which do not match the reflection image and its interpretation. Within fault block B4 (Figure 4-15I) a large portion of the unit interpreted

as crystalline basement remains unresolved, with uncharacteristically low velocities. In the pre / syn-rift sedimentary units of the same fault block, we observe a very chaotic pattern in the velocities, exhibiting very little correlation to imaged sedimentary reflectors. A similar uncorrelated velocity pattern is observed in the sedimentary units of block B5 (Figure 4-15I). A small, and unlikely, circular velocity inversion is observed directly east of fault F8 (Figure 4-15G). These areas all appear to be well resolved in the checkboard tests (Figure 4-13), which suggests that these artefacts do not arise as a result of the survey geometry. They may instead arise from the presence of out-of-plane arrivals affecting the FWI, and cycle-skipping in the longer-offset data that is not corrected during FWI (e.g. -14.92 km in Figure 4-11C and I). While random noise within field data will be attenuated through the FWI process, coherent noise, such as that from multiple energy, can be mapped into false velocity structure [*Pratt et al.*, 1998]. It is difficult to determine where such artefacts are to be expected, other than using qualitative model assessments, such as comparisons with reflection imaging.

The final velocity model appears to have been resolved well in areas with seismic velocities within the fault blocks of 2.80 – 5.20 km s^{-1} for the syn and pre-rift sediments, 5.20 – 6.50 km s^{-1} for crystalline basement, and 6.50 – 8.50 km s^{-1} for the very upper mantle, directly below the S reflector. These typical unit velocities, and their associated boundary velocities, enable us to reinterpret the reflection seismic image. Previous interpretations have failed to identify continental fault block B7 [e.g. *Borgmeyer*, 2010], or have interpreted it to be a completely pre / syn-rift sedimentary unit, above the S reflector (Figure 4-15G). However, seismic velocities indicative of crystalline basement (~6.00 km s^{-1}) have allowed us to reinterpret the reflection horizons in this fault block. While there are several reflections which are good candidates for the top of crystalline basement, we have interpreted that which best fits our velocity model. Where previous interpretations had indicated the presence of the intra syn-rift reflector we now interpret this as the top of crystalline basement, and the intra syn-rift reflector is reinterpreted above, along a reflector near the ~4.90 km s^{-1} velocity contour. We have also reinterpreted the intra syn-rift reflector in fault block B6 (Figure 4-15H). Velocities in this unit do not support the reflector pinching out to the west, as originally suggested, but instead suggest that it maintains a consistent thickness, following a constant velocity of ~4.90 km s^{-1} and matches a prominent reflector in the seismic image. Additionally, the intra syn-rift reflector is reinterpreted between fault F6a and the newly interpreted fault (Figure 4-15H).

4.4.2 S reflector and associated velocities

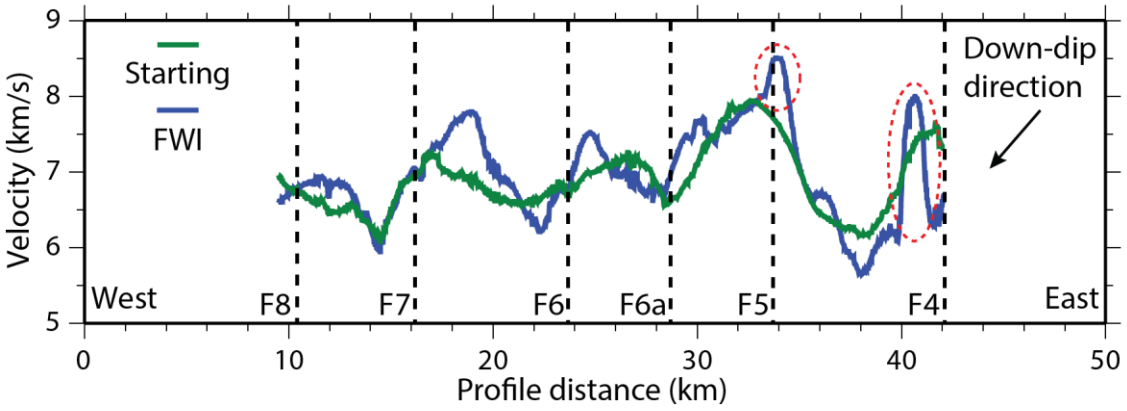

Figure 4-16: Velocities 50 ms below the interpreted S reflector. The green line indicates velocities from the starting velocity model; the blue line indicates velocities from the final FWI velocity model. Vertical dashed line indicate the locations where interpreted normal faults sole onto the S reflector. Red dashed ellipses indicate anomalous features of the inversion model.

It is difficult to gauge from these 2D plots whether there has been an improvement in the velocities associated with serpentinisation of upper mantle peridotite along and below the S reflector. The interaction between normal faulting and the P-wave velocities below the S reflector is more apparent plotted as a velocity against distance. Velocities 50 ms below the mapped S reflector are plotted against the profile distance, for both the starting and inversion velocity model (Figure 4-16). The starting model exhibits a general pattern of preferential mantle serpentinisation, which is observed as relative decreases in the seismic velocity down-dip of normal faults [*Davy et al.*, 2016]. This trend is particularly evident down-dip of faults F6 and F7. However, in this model slight increases in the velocity down-dip of faults F4, F5 and F6a can be observed, before the expected velocity decrease. These velocity increases, despite being minor, contradict the hypothesis of preferential hydration and serpentinisation of the mantle by normal faulting.

In the same figure it can be seen that the FWI result has resolved the pattern of preferential mantle serpentinisation in greater detail. Decreases in seismic velocity are now seen directly down-dip of all normal faults, F4 – F8 (Figure 4-16). This result is more consistent than the starting model with the hypothesis that normal faults act as conduits, enabling the preferential hydration and serpentinisation of upper mantle peridotites below the S reflector [*Bayrakci et al.*, 2016; *Davy et al.*, 2016]. Despite this promising result, there are unexpected features in the velocity profile of the FWI model.

We observe two short-wavelength (~2 km) features which show anomalously rapid changes in seismic velocity (highlighted by red dashed ellipsoid in Figure 4-16). The most prominent exhibits an increase in velocity of ~1.5 km s^{-1} at 41 km profile distance. This rapid change appears to be particularly anomalous, when compared with the rest of the profile, and differs greatly from the velocity trend in both the starting and inversion models. The other anomalous feature is coincident with fault F5, and reaches the models maximum allowed velocity of 8.50 km s^{-1}. We expect the velocity of unaltered upper mantle peridotite to be ~8.00 km s^{-1}, thus making this observation implausible [e.g., *Carlson and Miller*, 2003]. These features appear to be artefacts introduced during the FWI process. It is possible that these features arise due to the sparsity of data available in this experiment, or are the result of the FWI process trying to map coherent noise into the velocity model. Unfortunately, in order to resolve the velocity structure at these depths, we had to include data that were starting to be affected by coherent multiple noise.

Ignoring these anomalous short-wavelength features, we can attempt to quantify the levels of observed serpentinisation. Relative velocity decreases (from the normal fault to the nearest down-dip velocity minima) of ~1.40 km s^{-1}, ~0.60 km s^{-1}, ~0.60 km s^{-1}, ~0.70 km s^{-1} and ~1.0 km s^{-1} are observed for faults F4, F5, F6a, F6 and F7, respectively. Using the study of *Carlson and Miller* [2003] we can approximate the extent of mantle peridotite serpentinisation, based on the observed P-wave velocities. Down-dip of these faults we calculate the degree of serpentinisation, averaged over the resolution length of the FWI, to change from 30 to 70%, 0 to 20%, 30 to 40%, 30 to 50% and 30 to 60%, for faults F4, F5, F6a, F6 and F7, respectively.

4.5 Conclusions

The application of FWI has yielded a clear improvement over travel-time tomography results. From this study we find that:

- FWI can be applied to sparse and noisy OBS data in deep water environments, for the purpose of producing high-resolution velocity models of shallow crustal targets.
- The final velocity model exhibits a significant increase in resolution within the continental fault blocks of this hyperextended domain. This improvement in the velocity model has enabled the reinterpretation of the reflection seismic image.

- Increased resolution in the seismic velocities below the S reflector has further defined the pattern of upper mantle serpentinisation, a result of preferential hydration by normal faults acting as water conduits.
- The final FWI result is limited by the sparsity of data available, and the presence of coherent noise at longer data offsets.

Given a more optimised seismic shooting period we can expect that the results would have shown an even greater quality. We suggest that future marine studies targeting crustal structure take into consideration the application of FWI to their proposed datasets. While a higher density of OBS/H is desirable, we have shown that a relatively sparse profile can improve the resolution of travel-time tomography models. This approach will also allow for the improved migration of reflection seismic images, which was not investigated here. There may also be merit in applying the FWI method to existing high quality 2D OBS/H datasets where high quality travel-time tomography models have already been determined.

Chapter 5: Determining the shear velocity structure from Rayleigh wave dispersion at the Deep Galicia margin using ambient noise cross-correlation and beamforming

Author contributions. This chapter is in preparation for submission to the peer-reviewed journal the *Bulletin of the Seismological Society of America*. The author list for this article is: Davy, R., Harmon, N., and Minshull, T. RD performed all data preparation and analysis under the guidance of NH. All authors contributed feedback on the text.

Abstract

The compressional velocity structure of continental hyperextension and mantle exhumation within the continent-ocean transition at deep water rift margins has been well documented by active source seismic studies. However, geophysical studies recovering the shear velocity structure within such domains are uncommon. Here we recover one-dimensional (1-D) shear velocity information at the Deep Galicia rift margin. This was achieved by applying a suite of ambient noise cross-correlation techniques to continuous seismic data recorded by an array of 59 ocean bottom hydrophones (OBH). Fundamental Rayleigh wave phase velocity dispersion curves are found using three independent methods; ambient noise cross-correlation and frequency time analysis, 1D beamforming, and 2D beamforming. The results of all three techniques produce consistent results, giving average phase velocities through the array that increase from ~1.0 km s^{-1} at a period of 4 s, to ~3.0 km s^{-1} at a period of 14 s. 2D beamforming reveals that the primary source of the ambient noise is ocean waves crashing along the coast of the Iberian Peninsula. We invert the best average phase velocity dispersion curve and recover a mean 1D shear velocity structure of the lithosphere comprising this hyperextended domain. Mean shear velocities are found to be 0.94 ± 0.12 km s^{-1} in the sediments, 2.21 ± 0.36 km s^{-1} in the upper crust, 3.48 ± 0.36 km s^{-1} in the lower crust, and 4.25 ± 0.35 km s^{-1} in the upper most mantle, increasing to 4.45 ± 0.35 km s^{-1}, 25 km below the Moho. During the array deployment, there were 32 days of active source seismic shooting. We found that there is no discernible effect, either adverse or beneficial, to the ambient noise techniques when utilising continuous seismic data which records active source seismic shooting.

5.1 Introduction

The Deep Galicia rift margin in the North Atlantic Ocean has formed through the hyperextension of continental lithosphere, before the onset of sea-floor spreading [*Whitmarsh et al.*, 1996; *Pérez-Gussinyé and Reston*, 2001; *Davy et al.*, 2016]. Extreme extension of this margin has been accommodated by the rotation of fault bound continental blocks, which have progressively cut and thinned the continental crust [*Ranero and Pérez-Gussinyé*, 2010; *Reston and McDermott*, 2014]. Within the hyperextended domain, these normal faults have cut through to the upper mantle, enabling the hydration of the upper mantle and forming a layer of serpentinised mantle peridotite [*Pérez-Gussinyé*

and Reston, 2001]. Continued extension has resulted in the formation of a large scale detachment fault, known as the S reflector, which has locally exhumed upper mantle peridotites, and forms the crust-mantle boundary [e.g., *Reston et al.*, 2007]. The resulting margin architecture is a highly thinned and faulted continental crust, overlying the continental mantle at very shallow depths.

Active source seismic studies recovering the compressional velocity structure at such deep water margins are common [e.g. *Pickup et al.*, 1996; *Whitmarsh et al.*, 1996; *Dean et al.*, 2000; *Funck et al.*, 2003; *Hopper et al.*, 2006; *Davy et al.*, 2016]. Less common are seismic studies which recover shear velocities from the direct observation of S-waves [e.g. *Chian and Louden*, 1994; *Funck et al.*, 2003; *Bullock and Minshull*, 2005; *Eddy et al.*, 2013]. The generation of S-waves in marine seismic experiments normally relies on the conversion of P-waves at geological boundaries with significant velocity contrasts [*White and Stephen*, 1980]. Often deep water environments will have thick sedimentary units, such that there is little velocity contrast for the conversion of P- to S-waves. However, shear wave velocities can be determined indirectly through the observation of surface waves, such as Rayleigh and Love waves, whose velocities are dependent on both the compressional and shear velocities of the medium they travel through [e.g. *Campillo and Paul*, 2003; *Sabra et al.*, 2005b]. It has been shown that the cross-correlation of the ambient noise field between two or more recording stations recovers estimates of the Green's function of propagating surface waves, which can be exploited in order to determine shear wave velocities [*Sabra et al.*, 2005a; *Shapiro et al.*, 2005]. Such ambient noise methods have become increasingly popular for determining shear wave velocity structure and have been shown to yield results on multiple scales and in both terrestrial and marine environments [e.g., *Harmon et al.*, 2007; *Arroucau et al.*, 2010; *Boaga et al.*, 2010; *De Nisco and Nunziata*, 2011]

In this study we utilise an array of ocean bottom seismometers and hydrophones (OBS/H), deployed within the hyperextended domain of the Deep Galicia margin for a three month period, in order to determine the average 1D shear velocity structure. We employ three ambient noise techniques in order to recover independent estimates of fundamental Rayleigh wave phase velocity dispersion. These techniques include the calculation of noise cross-correlation functions and direct estimation of phase velocities from each cross-correlation time series, 1D beamforming using spatial coherence across the array to estimate the wavelength at each period, and two-dimensional (2D) beamforming using the

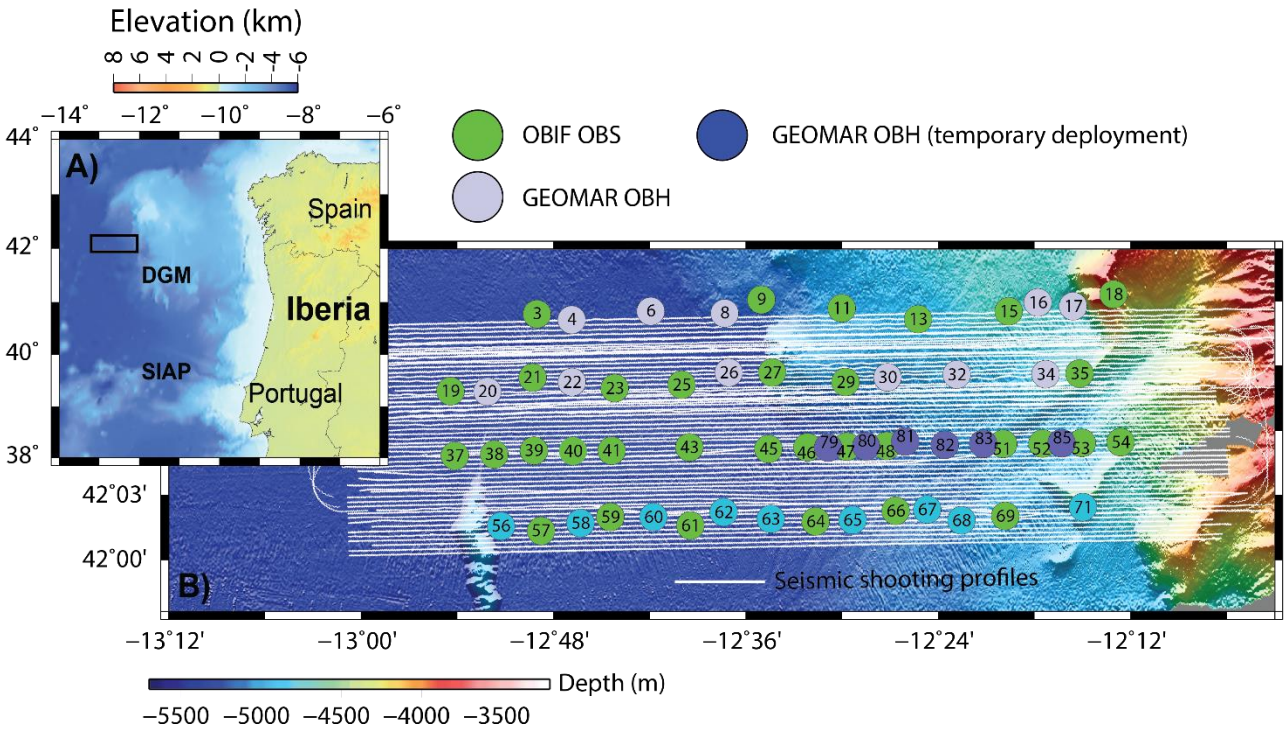

Figure 5-1: Maps of the study area. A) Bathymetric map of the Deep Galicia margin (DGM) and the Southern Iberia Abyssal Plain (SIAP) with the relative location of Figure 1B (black rectangle). B) Map of the Galicia-3D seismic experiment. Circles indicate station locations: green are OBIF OBS, light blue are GEOMAR OBS/H, purple are temporary GEOMAR OBH. White lines indicate seismic shooting profiles.

array, allowing for azimuthal variation. We invert what we determine as the most reliable of these phase velocity dispersions and recover a 1D shear velocity for the study area. This array also recorded an active source seismic experiment for approximately half the total deployment period, and so we have the opportunity to investigate the effects of the near-field signal on the application of ambient noise techniques.

5.2 Data and preparation

Here we utilise continuous seismic data recorded on OBS/H during the Galicia-3D seismic experiment, carried out between June and August of 2013. The useable array comprised 59 OBS/H stations provided by the UK Ocean Bottom Instrumentation Facility (OBIF) [*Minshull et al.*, 2005] and GEOMAR (Figure 5-1). The total length of the instrument deployment was 101 days, however, six of the stations in the array were temporary deployments and only recorded three days of data each. Excluding these temporary instruments, the average recording period for an instrument in the array was 79 days. During this deployment there were a total of 32 days where active source seismic shooting was undertaken, with a uniform distribution of shots relative to the OBS/H

array (Figure 5-1). The seismic sources used during the active experiment were two airgun arrays, each with a total volume of 3,300 cu. in., fired alternately every ~16 s. We propose that including the data recorded during seismic shooting provide an additional diffuse noise source, and can therefore be included in the cross-correlation of seismic data. It is also probable that the high-frequency seismic signal will have little effect on ambient noise seismic techniques, which exploits signal with much longer periods.

Hydrophone data is common across all instruments in the array, and we have therefore used this channel for our analysis. Both the hydrophone and geophone sensors used in the Galicia-3D survey have a limited bandwidth at short periods. The hydrophones used have a frequency response range of 2 Hz – 20 kHz, while the geophones used have a natural frequency of 4.5 Hz. Despite this, spectral analysis of the hydrophone data indicates energy is recovered up to a periods of ~14 s, which should be sufficient to recover the shear-wave structure of the upper mantle below the array. The continuous seismic data were cut into single day periods and down sampled in the time domain from 250 and 200 Hz (OBIF and GEOMAR instruments, respectively), to 1 Hz, while employing an anti-alias filter. Down sampling the seismic data drastically decreases the computational requirements, while retaining the long period signal of Rayleigh waves (> 1 s period). Prior to cross-correlation the data were band-pass filtered between 0.01 and 0.5 Hz (periods of 2 – 100 s) and normalised using a moving average window, as described in *Bensen et al.* [2007].

5.3 Noise cross-correlation and frequency time analysis

Noise cross-correlation functions (hereafter referred to as NCF) work on the principal that the time-averaged cross-correlation of two simultaneously recording seismic stations in a diffuse wavefield, will produce an approximation of the Green's function between the stations [*Shapiro and Campillo*, 2004; *Roux et al.*, 2005; *Sabra et al.*, 2005a]. We prepared the data following the methods of *Bensen et al.* [2007] in order to recover the NCFs between OBH in this study and determined the group and phase dispersions of fundamental Rayleigh waves using an automated frequency time analysis (AFTAN).

5.3.1 Cross-correlation

Continuous seismic data were processed day by day. The day-long seismograms were zero-padded, Fourier transformed into the frequency domain, and then spectrally

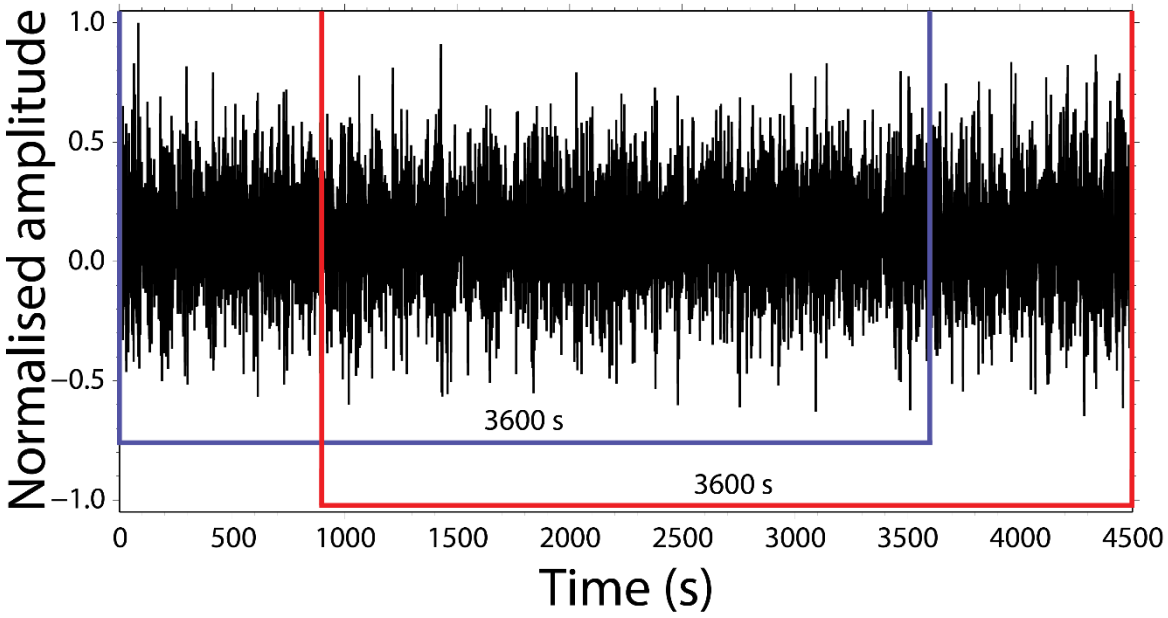

Figure 5-2: Welch's method for cross-correlation of continuous seismic data. Data is normalised and resampled from OBS21 on Julian day 180. Hour long time series, indicated by blue and red, overlap each other by 75% and are cross-correlated with the corresponding time period recorded by other instruments in the array to yield inter-station NCF.

whitened by amplitude normalisation [*Bensen et al.*, 2007]. Within each day, hour long segments (3,600 s) were cross-correlated between all station pairs. We employ Welch's method where the hour long cross-correlation segments overlap one another by 75% (Figure 5-2) [*Welch*, 1967]. This results in 93, hour long cross-correlations segments for a single day, versus 24 if Welch's method had not been implemented. This simple technique increases the coherency of the recovered NCFs each day and reduces the effect of any single high amplitude transient signal on the ensemble average [*Seats et al.*, 2012]. The NCF of these hour long segments were subsequently inverse Fourier transformed and stacked in the time domain, giving the time domain NCF between two stations for a single day (Figure 5-3A-C). The 'causal' and 'acausal' signals, representing waves travelling in opposite directions between the stations, are apparent in the daily NCF and appear to be relatively asymmetric (Figure 5-3C) [*Roux et al.*, 2005; *Yao et al.*, 2006]. This may be an early indication that the distribution of noise sources is relatively inhomogeneous in azimuth [*Sabra et al.*, 2005b]. Looking at the daily NCF as an amplitude map for the station pair OBS21 and OBS35 (Figure 5-4), we can see that the time positive causal signal appears to be consistently stronger over the period of the experiment. Interestingly this figure does not reveal any clear differences in the daily NCFs between periods of shooting (Julian days 157-167, 170-173 and 196-212) and periods of no shooting (all other Julian days).

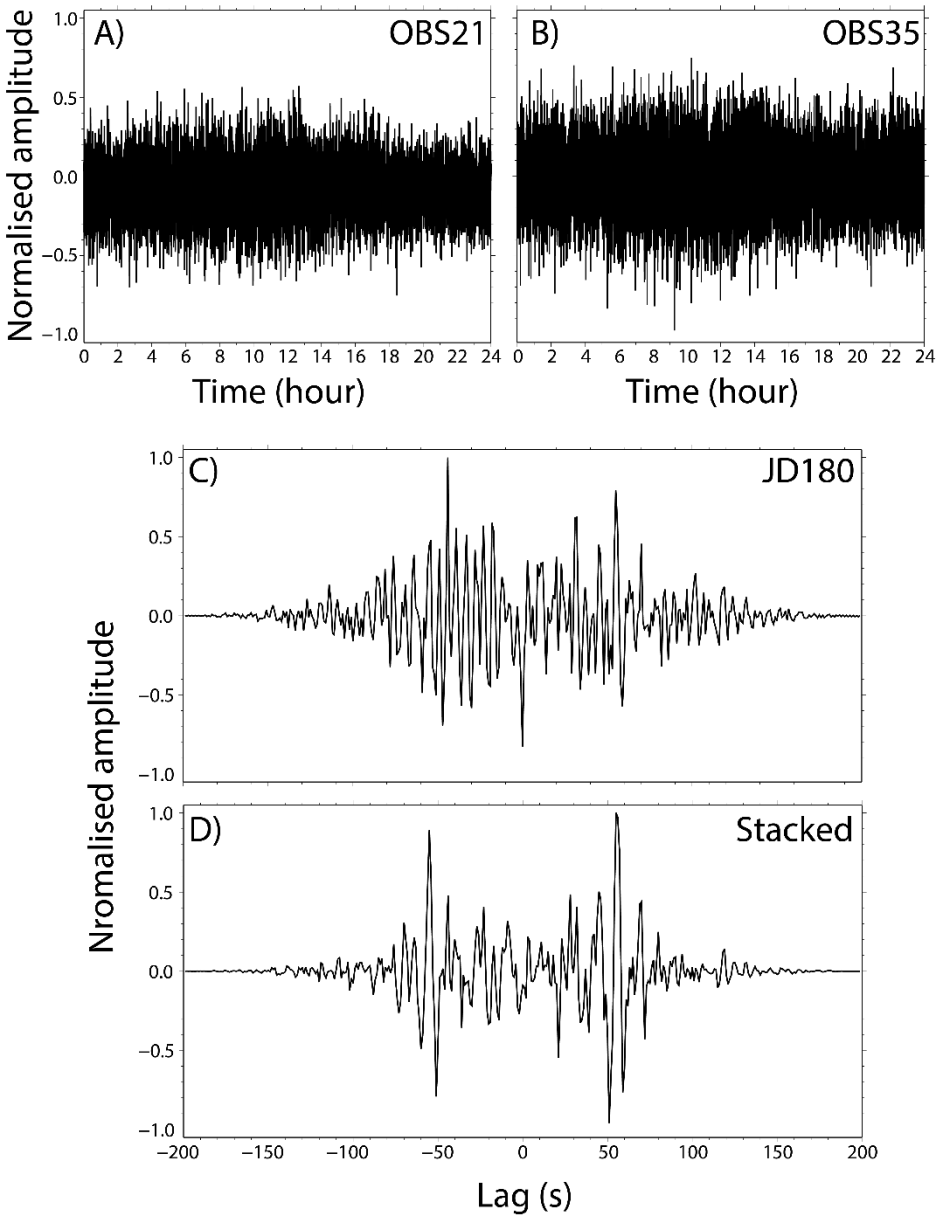

Figure 5-3: Continuous data and calculated NCF. Normalised and resampled continuous seismic data recorded on Julian day 180 by A) OBS21 and B) OBS35. C) NCF of seismic data recorded by OBS21 and OBS35 on Julian day 180. D) Stacked NCF between OBS21 and OBS35 for all days concurrently recorded.

Once the cross-correlation process had been completed for all station pairs, for every day on which they concurrently record, the daily NCFs were stacked in the time domain to give a single interstation NCF for the duration of the deployment (Figure 5-3D). This stacked NCF, averaged over the experiment duration, appears to be more symmetric. A total of 1,770 stacked NCFs were calculated for the entirety of the deployment. However, not every calculated NCF exhibits a clear impulse response corresponding to Rayleigh wave moveout. Each NCF was visually inspected for the presence of an emergent Rayleigh wave signal, rejecting any NCF that did not present a clear signal. A total of 457 NCFs were deemed to show the clear emergence of Rayleigh waves.

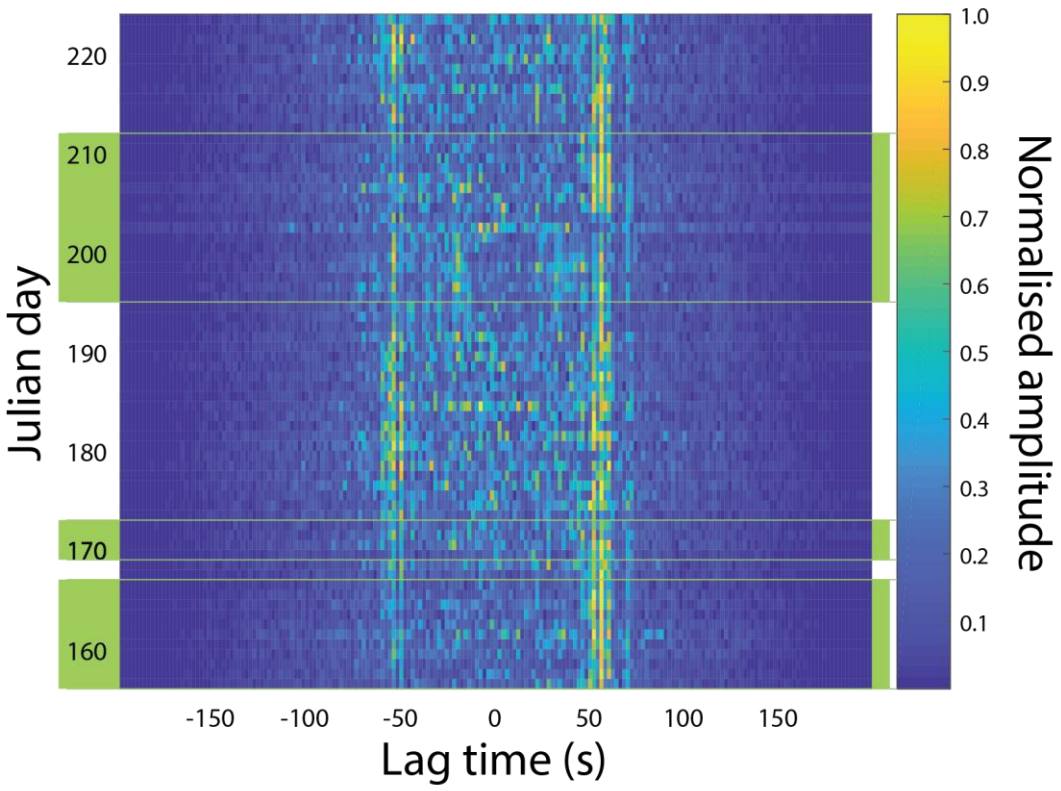

Figure 5-4: Amplitude map showing the energy in the daily NCFs between OBS21 and OBS35. NCF amplitude is averaged in bins of 2 s. Green bars and lines on the vertical axis indicate periods of seismic shooting.

We repeated the cross-correlation process, but this time separating the data into an even number of days where the instruments record seismic shooting (Julian days 157-167, 170-173, 196-212) and no seismic shooting (Julian days 147-156 and 174-195) in order to investigate any possible differences in the recovered NCFs between these two periods. Figure 5-5A-C shows the NCF between OBS21 and OBS35 stacked for periods of no shooting, shooting and the difference between the two, respectively. Visually the NCF during the non-shooting period appears to be more symmetric than that calculated for the shooting periods, which may indicate that the seismic shooting acts as an inhomogeneous noise source throughout the study area. The difference between the two NCFs (Figure 5-5C) exhibits a small amount of coherent energy 40 – 70 s, which may be the result of phase shifts due to the different signal sources. However, a lack of dominant signal in the differences indicates a negligible difference in the recovered NCF between periods of shooting and no shooting. When plotting the NCFs as a function of interstation distance for the non-shooting, shooting and combined periods (Figure 5-6A-C, respectively), we observe a clear moveout of the Rayleigh wave signal with increasing station separation. The only

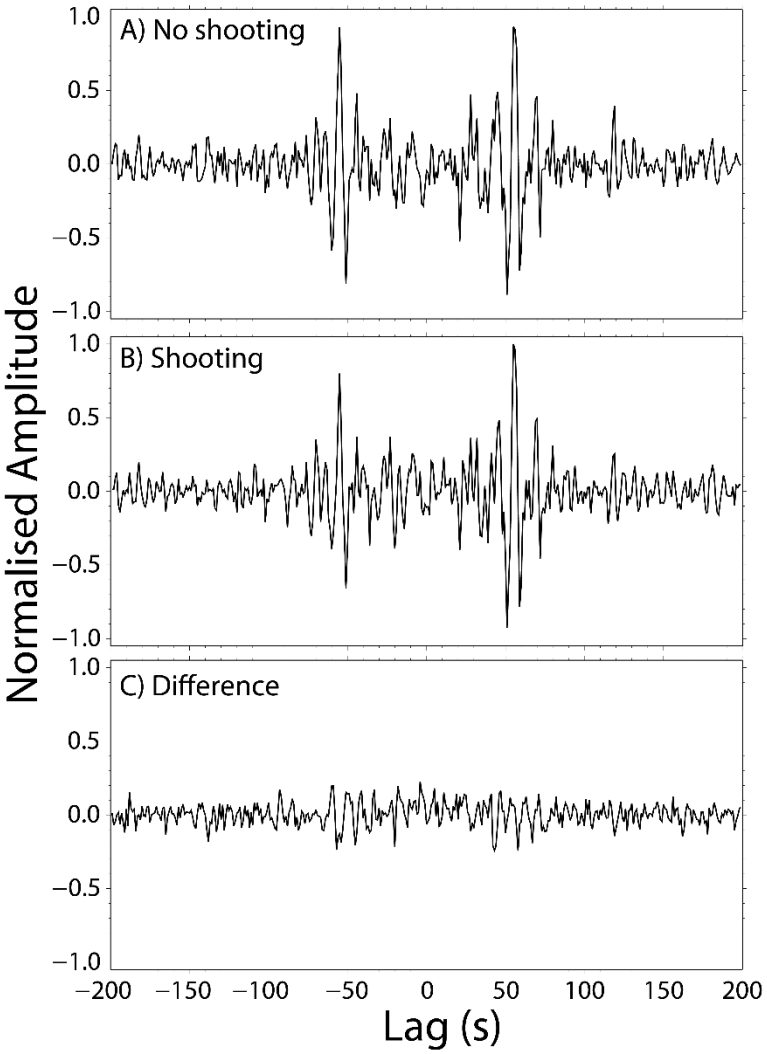

Figure 5-5: Stacked NCF calculated between OBS21 and OBS35 for A) periods of no seismic shooting, B) seismic shooting. C) The difference between these two stacked NCF.

apparent difference between the non-shooting and shooting period NCF appears to be a consistent impulse at zero lag time on the NCF stacked during the shooting periods. Based on these observations, we proceeded to determine the group and phase velocities using the combined NCF dataset.

5.3.2 Frequency time analysis

The resulting NCFs give an estimate of Green function between station pairs [*Bensen et al.*, 2007]. Using these NCF, we can recover both the group and phase velocities of fundamental Rayleigh waves using frequency time analysis (FTAN) [e.g *Dziewonski et al.*, 1969; *Levshin et al.*, 1989; *Levshin and Ritzwoller*, 2001]. FTAN is a powerful signal processing tool which can extract the group and phase velocities of surface waves from single inter station NCF.

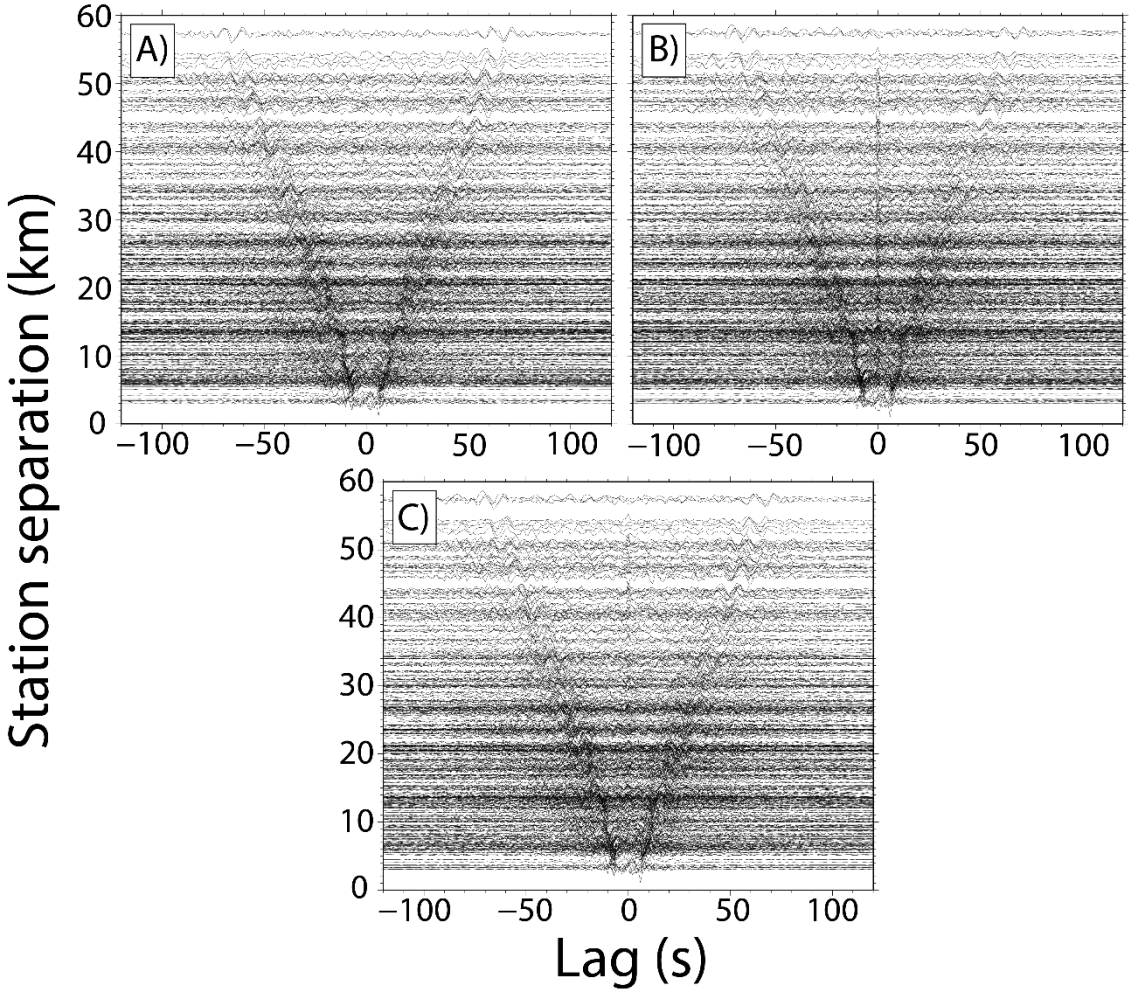

Figure 5-6: Interstation NCFs as a function of inter-station distance for stacked NCF calculate during A) periods of no seismic shooting, B) periods of seismic shooting, C) both periods combined.

Here we used the automated FTAN (AFTAN) method described by *Bensen et al.* [2007] to calculate average group and phase velocities from the 457 high-quality NCF. The AFTAN algorithm rejected 179 NCF, generating 278 FTAN results and their associated group and phase velocity dispersion curves. We subsequently calculated the mean of these FTAN results and velocity dispersion curves. In order to further refine the result we excluded any group or phase velocities which were more than one standard deviation from the mean velocity, at each of the calculated periods. We calculated the mean of these results again, and assigned the velocity uncertainty as the standard deviation of these refined velocity dispersion curves. Figure 5-7 shows the mean FTAN result, as well as the refined group and phase velocity dispersion curves.

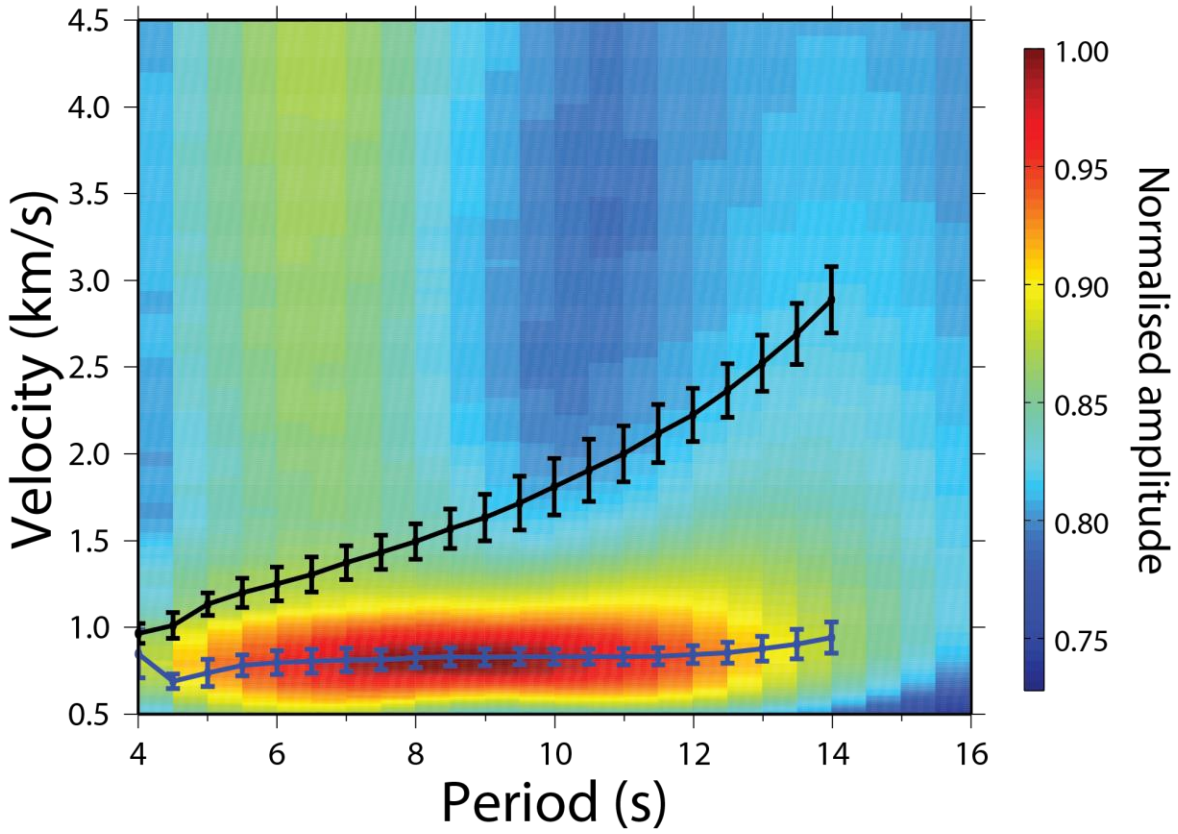

Figure 5-7: Averaged FTAN power spectra, amplitude normalised. Blue line is the mean group velocity dispersion, black line is the mean phase velocity dispersion. Error bars are a single standard deviation of their respective mean velocity curve.

5.4 Beamforming

5.4.1 1D Beamforming

Harmon et al. [2010] show that estimates of the mean phase velocity through an array can be made by finding the best fitting Bessel function to the real Fourier component of these NCF as a function of distance. This technique has no dependence on the angle of incidence of a propagating surface wave, assuming a completely homogeneous noise distribution. Here we follow the same method of fitting a Bessel function, of the form $A * J_0(\frac{\omega d}{c})$ to the real component of the NCF (calculated in **5.3.1**), where A is amplitude, J_0 is a zero order Bessel function of the first kind, ω is angular frequency, d is interstation distance, and c is phase velocity. For Rayleigh wave periods between 5.5 and 14.0 s in 0.5 s increments, we calculated J_0 (the Bessel function) for the interstation distances of all 457 useable NCF, using phase velocities between 0.5 and 4.8 km s^{-1} in increments of 0.01 km s^{-1}. We summed the causal and acausal signals of each NCF, to give only the time positive impulse. Data

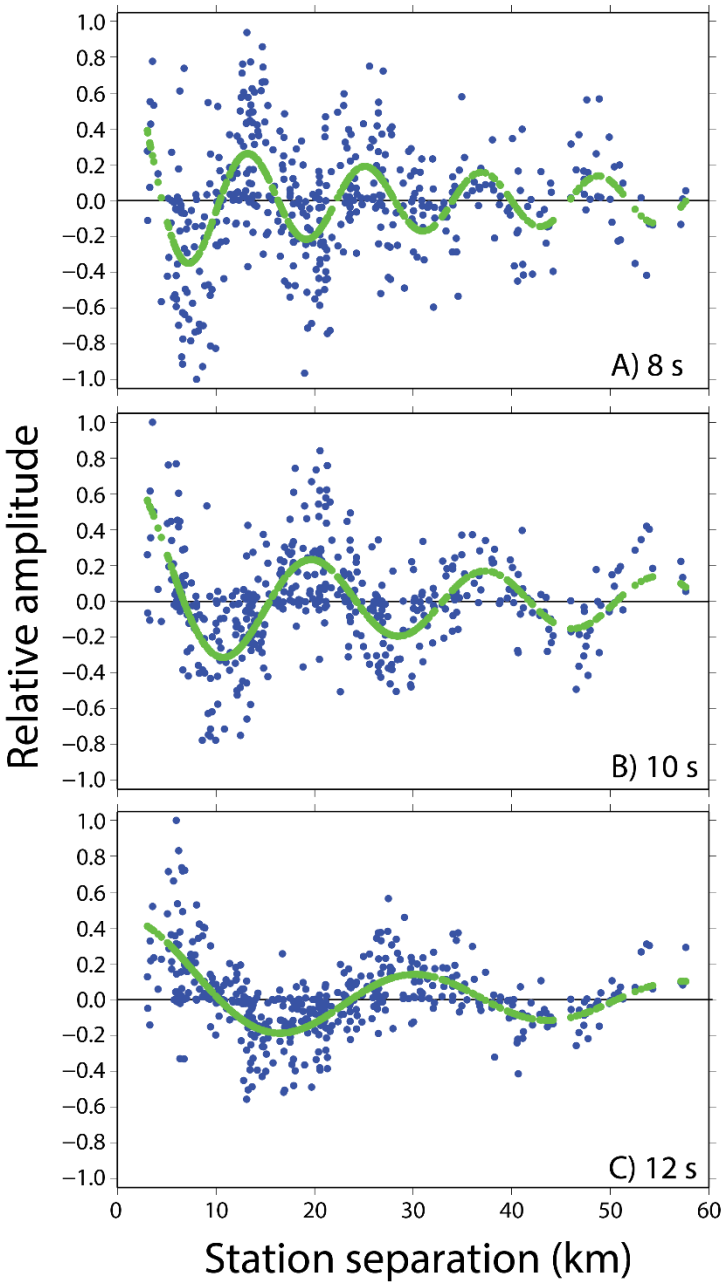

Figure 5-8: 1D beamforming results showing the best fit Bessel functions (green dots) to the real Fourier component of all interstation NCF (blue dots), for periods of A) 8 s, B) 10 s, C) 12 s.

residuals were calculated as the difference between the calculated Bessel function and the useable NCF, at each interstation distance, and at each tested phase velocity. The phase velocity which produces the minimum data residual was chosen for that given period. The high degree of scatter in the real component of the NCF means that the amplitude of the calculated Bessel function is not matched well. However, this will not affect the determination of phase velocities, as the misfit calculation is sensitive to the match of zero crossings between the calculated Bessel function and the NCF.

Figure 5-8 shows the results of the 1D beamforming, for periods of 8, 10 and 12 s. The best fit Bessel functions at periods of 8, 10, and 12 s are found using phase velocities of 1.55, 1.76 and 2.25 km s^{-1}, respectively. It can be seen that the match between the zero crossing of the real NCF components and the calculated Bessel functions is good. However, the real NCF components exhibit a significant degree of scatter for any given interstation distance, which is likely to have arisen from the assumption that noise source is homogeneously distributed for all azimuths. A dominant noise source producing waves that propagate obliquely to the interstation azimuth will see a decrease in the apparent cross-correlation times. This means that when sampling the real component of the NCF the amplitude is taken from the incorrect part of the waveform. At periods greater than 14.0 s the wavelength of the fit Bessel function exceeds the maximum interstation separations and cannot be resolved, while at periods less than 5.5 s the data scatter is such that a Bessel function cannot be fit.

5.4.2 2D Beamforming

Inhomogeneous noise distribution can be investigated by performing 2D beamforming, which includes a dependence on the azimuth of a propagating surface wave, which is assumed to be travelling as a plane wave. 2D array beamforming performs a grid search for both the phase slowness (inverse of velocity) and the azimuth of a propagating wave, and calculates a relative time shift given the stations relative position in the array. When the appropriate phase slowness (velocity) and azimuth of the observed wave is found, the time shifted signals from the array stations will stack constructively [*Rost and Thomas*, 2002].

The array data were beamformed using the method described by *Gerstoft and Tanimoto* [2007]. As was done with the calculation of NCFs in **5.3.1**, we performed the 2D beamforming procedure on the datasets which record only ambient noise, only seismic shooting and both periods combined. The continuous data from stations in the array were divided into 512 s time series and the amplitude information was removed by clipping and normalising the data, while preserving the phase data. These data were then Fourier transformed into the frequency domain and form complex-valued vectors, $v(\omega, t_i)$ for each frequency, where t_i is the start time of the Fourier transform. The cross-spectral density matrix is found by $C = \langle vv^T \rangle$, where the brackets indicate ensemble averaging over 168 of the 512 s time series, giving an average for each day. The plane wave response

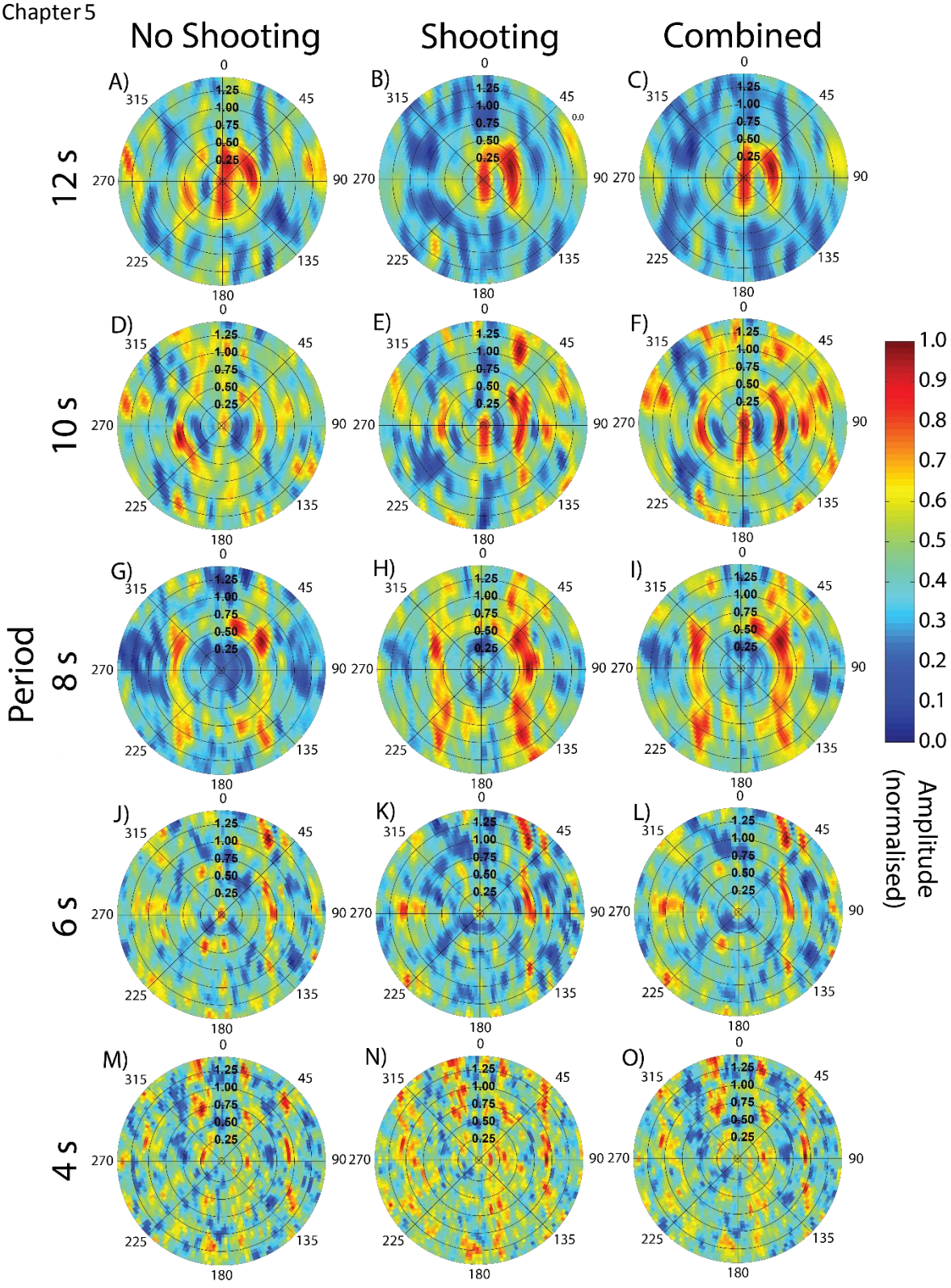

Figure 5-9: 2D beamformer outputs for periods of A-C) 12 s, D-F) 10 s, G-I) 8 s, J-L) 6 s, M-O) 4 s, during times of no seismic shooting, seismic shooting, and the combination of both. Phase slowness contours are marked between 0.25 – 1.25 s km^{-1}, azimuths vary from 0 - 360^{o}. Hot colours indicate coherent energy for the indicated phase slownesses and azimuth.

of all the stations in the array is given by $p(\omega, s, \theta, r) = \exp(i\omega s(r\ e))$, where s is slowness (1/c), r is the station coordinates relative to the array mean, and e are directional cosines of the propagating wave, $e = (\sin\theta, \cos\theta)^T$. The final beamformer output is given by

$b(\omega, s, \theta, t) = p^{\dagger}(\omega, s, \theta) C(\omega, t) p(\omega, s, \theta)$, where † is the transpose complex conjugate. For each day we produced beamformer outputs for plane waves with propagation azimuths of 0-360°, increasing in 2° bins, slowness values ranging between 0.0 – 1.5 s/km (phase velocity of 0.5 - ∞ km s^{-1}) increasing in 0.05 s/km increments, for periods between 4 and 12 s (angular frequencies of 0.52 - 1.57 $rads^{-1}$). The beamformer results were averaged and normalised over the periods where the array recorded seismic shooting, only ambient noise, and the combination of both periods (Figure 5-9).

Coherent energy from the beamforming of ambient noise sources appears along circles of constant slowness in Figure 5-9, while aliased signal typically manifests as multiple maxima in the beamformer output, which shows no correlation to a particular slowness value. At all periods of investigation the beamformer results between the three datasets show a general agreement with one another. This observation supports our conclusion that the seismic shooting has little effect on the cross-correlation of seismic data at the frequencies of investigation, which are orders of magnitude lower than frequencies of interest in reflection seismic studies. During both the quiet and shooting period, the dominant noise source recorded by the array typically comes from azimuths between 45° and 135°. This noise source is almost certainly generated by ocean waves along the coast of the Iberian Peninsula. This is the only noise source which can be identified at all investigated periods (Figure 5-9). There is also evidence of a secondary, weaker, source of coherent energy coming from the opposite direction, between 225° and 315°, predominantly seen only at longer periods (e.g., Figure 5-9A-I). This noise source could feasibly originate from ocean waves along the coast of North America. This conclusion is supported by the fact that the coherent energy from these azimuths is seen only at higher periods (> 6.0 s), which is to be expected as longer wavelength Rayleigh waves attenuate less than that of shorter period waves, over any distance.

At all periods investigated for the 2D beamforming, we observe a significant degree of anomalous energy within the results which does not coherently form along constant values of slowness. Some of these artefacts appear to be geometrically distributed within the plots, with an apparent symmetry through the axes. There also appears to be a prevalence of these artefacts forming in the north-south direction, for example at 8.0 s period distinct artefacts smeared north to south can be observed (Figure 5-9H-I). At long periods (e.g., > 10.0 s, Figure 5-9A-F) we observe a distinct anomalous region of north-south

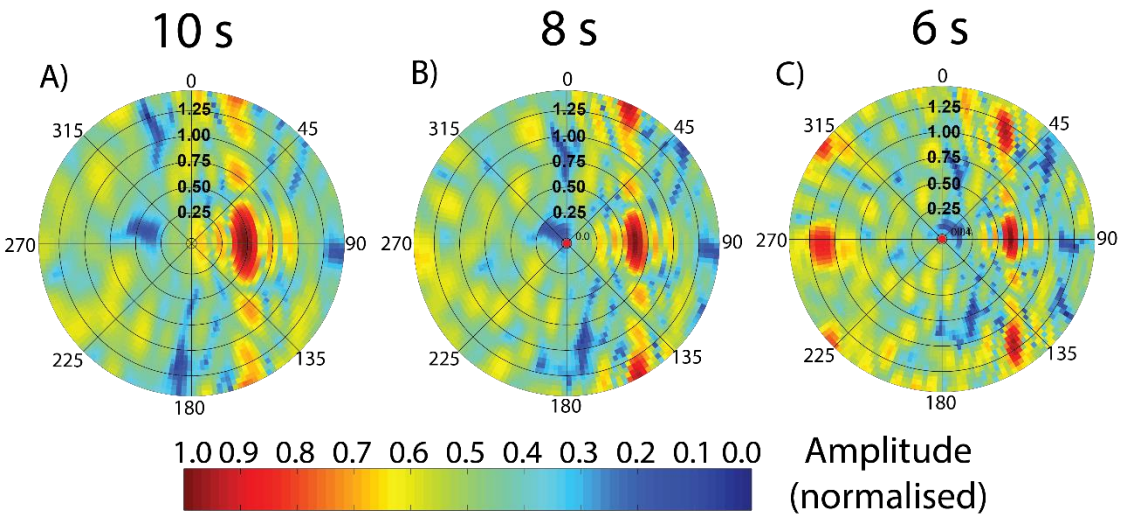

Figure 5-10: 2D beamformer outputs for synthetic plane waves At periods of A) 10 s, B) 8 s, C) 6 s. Plane wave phase slownesses are A) 0.50 s km^{-1}, B) 0.65 s km^{-1}, and C) 0.65 s km^{-1}

trending energy, passing through zero slowness. We suggest that all of these artefacts are the result of spatial aliasing, given the design of the survey. In order to prevent spatial aliasing in the beamformer results, the array must possess station spacing $< \lambda/2$ for the shortest periods of interest, and in order to resolve the longest periods of interest, the array aperture must be greater than λ [*Harmon et al.*, 2008]. For periods of 4.0 and 14.0 s, these constraints approximately correspond to a station spacing of < 2.0 km and an aperture of > 45.0 km, respectively. Within the Galicia-3D array the smallest station spacing is 2.1 km, excluding the short deployment stations. This indicates that we should expect spatial aliasing at shorter periods. Additionally, the array was designed in such a way that stations were deployed ~3.2 km apart in the east-west direction, and ~6.0 km apart in the north-south direction (Figure 5-1). The higher density of stations in the east-west direction may explain the observation of stronger aliasing in the north-south direction (Figure 5-9G-O). We can illustrate the arrays aliasing pattern by producing beamformer outputs for synthetic plane waves propagating through the array. Figure 5-10 shows the arrays response to synthetic plane waves propagating from east to west, for phase velocities between 1.5 – 2.0 km s^{-1}. Geometrically distributed maxima are seen aligned in the north-south direction, decreasing in spacing at shorter periods. These observations confirm that our results in Figure 5-9 are spatially aliased as a result of the array configuration.

For each period we used a grid search to identify the maximum beamformer output and its corresponding phase slowness (therefore phase velocity). We introduced conditional

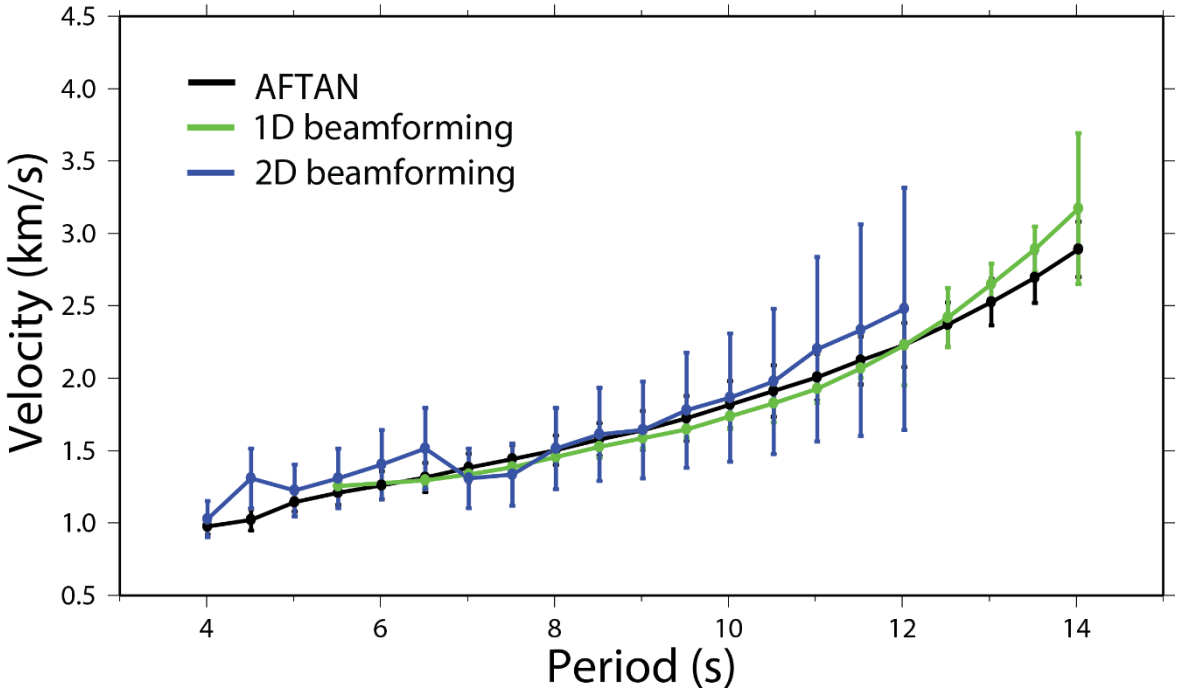

Figure 5-11: Fundamental Rayleigh wave phase velocities through the G3D array as determined from FTAN analysis (black), 1D beamforming (green), and 2D beamforming (blue).

statements into these grid searches in order to avoid selecting areas of clear spatial aliasing. For example, at a period of 12 s (Figure 5-9C), we identify a clear north-south alias feature passing through 0.0 s/km slowness, while there is coherent energy along the slowness contour of ~0.35 s/km, between 45° and 90°. The grid search for this period is given the conditions that it must find the maximum between azimuths of 30° and 135°, and at slowness values greater than 0.25 s/km. Uncertainty in the phase slowness calculated at each period is assigned as ± 1 grid node, which corresponds to ± 0.05 s/km.

5.5 1D shear velocity inversion

Three phase velocity dispersion curves have been determined using these independent techniques (Figure 5-11). All three results are in agreement with one another, within their calculated uncertainties, which gives confidence in each result. These phase velocity dispersions can be used to invert for the average 1D shear velocity structure beneath the Galicia-3D seismic array. We choose to perform the inversion using the phase velocity dispersion determined using the calculated NCF and FTAN analysis. Phase velocities from the 2D beamforming are influenced strongly by the gridding used within the method, which results in an unsmooth curve at short periods (4 – 8 s), and high uncertainty at longer periods (> 8 s) (Figure 5-11). We choose not to invert using the 1D beamformer result,

simply because it already exhibits an excellent match to the FTAN results, but covers a smaller range of periods.

We invert the phase velocity dispersion for 1D shear velocity structure, using a damped least squares inversion, following the method of *Harmon and Rychert* [2016]. The inversion operates using the following equation:

$$\delta m = (G^T C_{nn}^{-1} G + C_{mm}^{-1})^{-1} (G^T C_{nn}^{-1} \delta d - C_{mm}^{-1} [m_i - m_0])$$

where i is the inversion iteration, m is the shear velocity model, ∂m is the model update, and d is the phase velocity dispersion. G is a matrix of partial derivatives relating phase velocity to shear velocity, and is calculated using the DISPER80 algorithm of *Saito* [1988]. C_{nn} and C_{mm} are the data and model covariance matrices, respectively.

A 1D starting model was parameterised by defining layers in depth, each with a set density, and starting V_p and V_s values. We utilised a priori information from previous studies [e.g., *Bayrakci et al.*, 2016; *Davy et al.*, 2016] to set the average water depth, and define relatively thin sedimentary and crustal layers, underlain by thicker mantle layers. Starting V_p velocities were taken from established tomography models and previous studies, while V_s was estimated using an assumed V_p/Vs ratio of 1.8 [*Nishimura and Forsyth*, 1989]. V_p is held constant, allowing the V_p/Vs ratio to vary throughout the model inversion.

The results of the 1D inversion can be seen in Figure 5-12. Phase velocities input into the inversion range from 1.00 ± 0.06 km s^{-1} at 4 s period, to 2.91 ± 0.19 km s^{-1} at 14 s period (Figure 5-12A). After the inversion we observe an improvement in the model fit to the observed phase velocity dispersion, particularly at lower periods (< 8 s). The resulting 1D shear velocity model has velocities which range from 0.94 ± 0.12 km s^{-1} in the sediments, 2.21 ± 0.36 km s^{-1} in the upper crust, 3.48 ± 0.36 km s^{-1} in the lower crust, and 4.25 ± 0.35 km s^{-1} in the uppermost mantle, increasing to 4.45 ± 0.35 km s^{-1}, 25 km below the Moho (Figure 5-12B). The uncertainties associated with the shear velocity structure are relatively significant, which is a direct result of the high uncertainty associated with the estimated phase velocities. However, the uncertainties are such that we are still able to differentiate between the different lithological units within the COT. The resulting inversion model has V_p/V_s ratios of 2.12 in the sediments, 1.81 in the upper crust, 1.78 in the lower crust, 1.79 in the uppermost mantle, and 1.83 for the rest of the resolved mantle (Figure 5-13). Figure 5-12C shows the depth sensitivity kernels for the different periods of

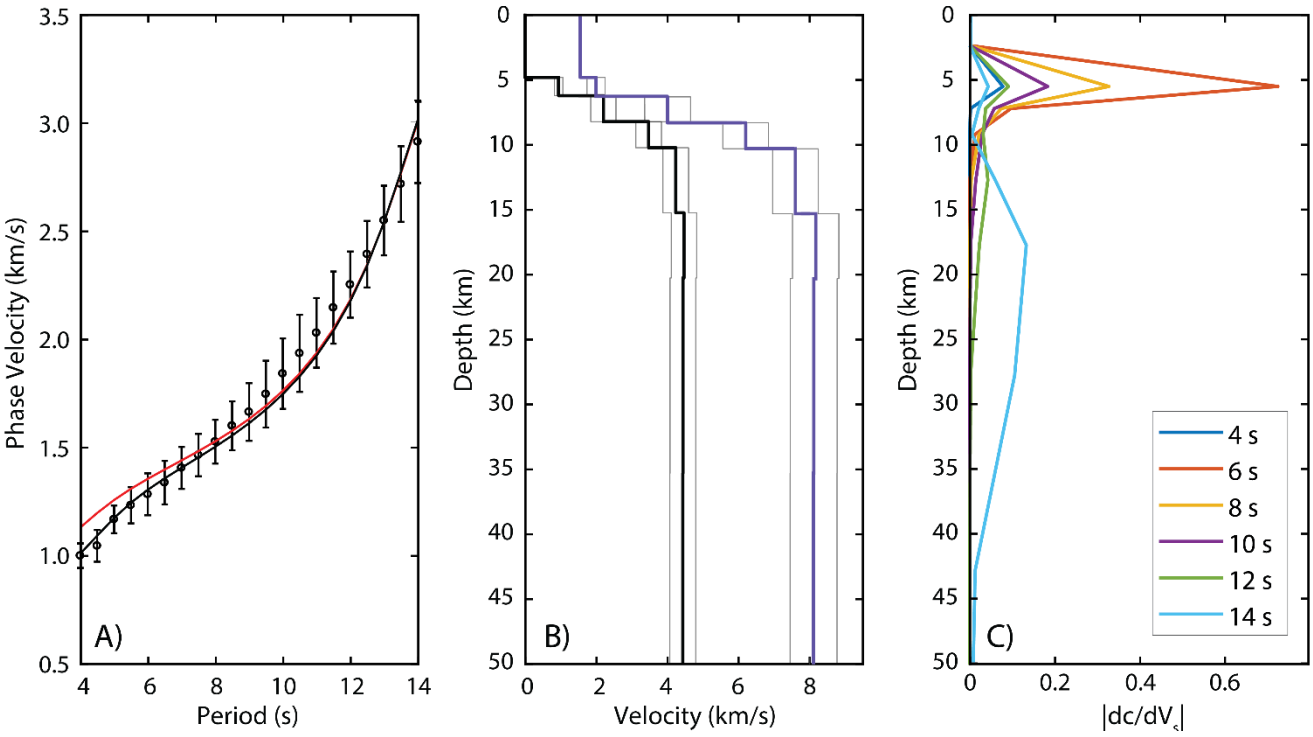

Figure 5-12: 1D shear velocity model. A) Black open circles with error bars show the phase velocity dispersion, as determined from FTAN analysis. Red line shows the fit of the starting model, black line shows fit of inverted shear velocity model to the phase velocity dispersion. B) Best fit shear velocity model (black line) and associated compressional velocities (blue line). C) Rayleigh wave sensitivity kernels for indicated periods.

Rayleigh waves, and provides insight into what periods are used to resolve the shear velocities at different depths. It can be seen that the shallow shear velocity structure (5 – 10 km depth) is determined by surface waves of short periods of 4 – 10 s, while deeper (10 - 45 km depth) shear velocity structure is resolved using the longer periods of 12 – 14 s.

5.6 Discussion

5.6.1 Shallow shear velocity structure

Recently, *Corela et al.* [2017] published a similar ambient noise tomography study of the Southwest Iberia margin, directly south of the DGM. In their study, a 3D shear velocity model was determined over the SW Iberia margin, which encompasses regions including the COT between continental crust and full thickness oceanic crust. For this reason, this study provides an excellent comparison for the results found in our study. Although the authors do not explicitly state the shear velocities of different lithologies, the typical velocities can be determined from cross sections of their 3D shear velocity model. It is

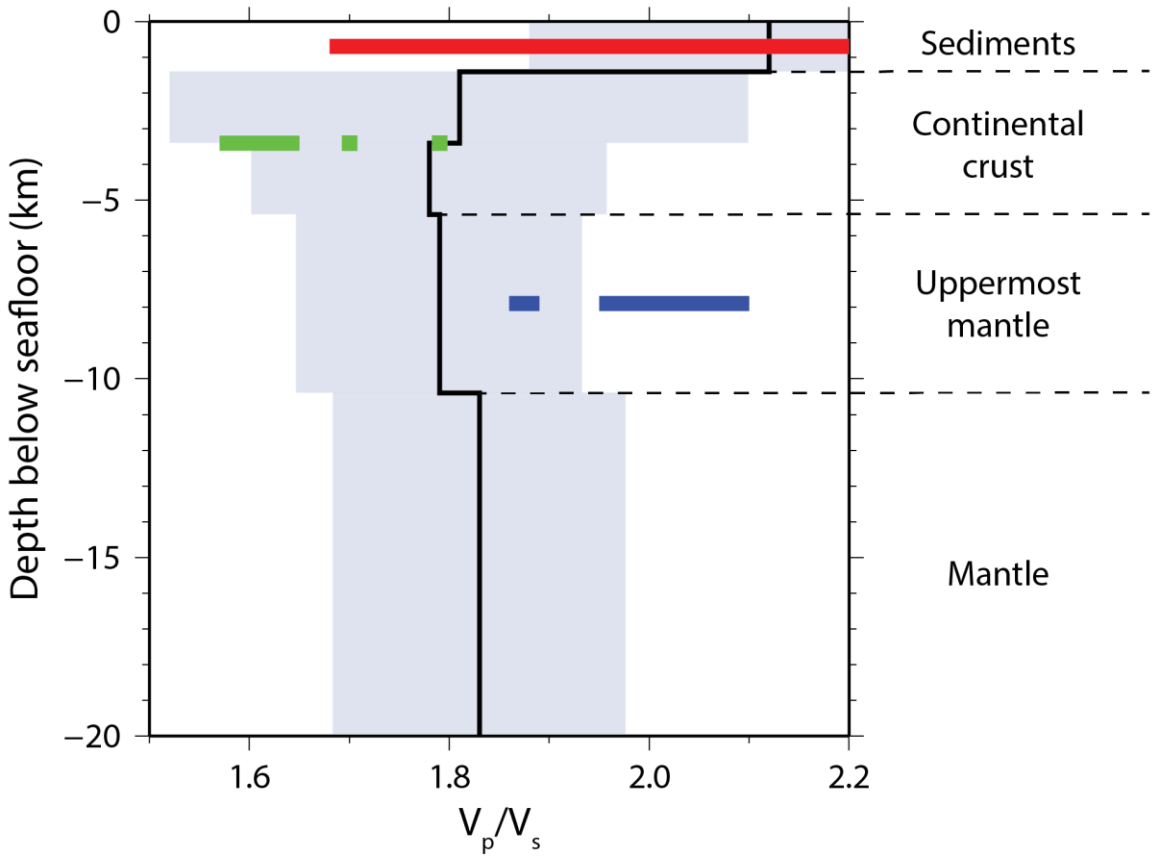

Figure 5-13: Ratio of compressional velocity to shear velocity (V_p/V_s) for the top 20 km below the seafloor. Solid black line indicates the V_p/V_s ratio from this study, shaded region is the uncertainty, red, green and blue lines show the V_p/V_s ratio from the equivalent sedimentary, continental crust and upper mantle units (respectively) from similar studies [Hamilton, 1979; Kern et al., 1993; Christensen, 1996; Gerlings et al., 2011; Eddy et al., 2013; D'Alessandro et al., 2016].

shown that sedimentary shear velocities are ~1.0 km s^{-1}, upper crustal shear velocities are ~2.4 km s^{-1}, lower crustal shear velocities are ~3.7 km s^{-1}, and upper mantle shear velocities are ~4.2 km s^{-1}. All shear velocities for the different lithologies match, within error, to those found in this study, giving confidence in the results seen in Figure 5-12.

Through the inversion process we see a significant increase in the V_p/V_s ratio of the sedimentary layer, and smaller changes at all other depths in the model (Figure 5-13). The high V_p/V_s ratio of 2.12 in the sedimentary layer is typical of water saturated sediments [*Hamilton*, 1979]. Studies returning shear wave velocities at the conjugate Newfoundland margin have found V_p/V_s ratios in the stretched continental crust of 1.57 - 1.65 and 1.79 (at the Grand Banks and Flemish Cap margins, respectively), which are consistent with granite/granodiorite [*Gerlings et al.*, 2011; *Eddy et al.*, 2013]. The V_p/V_s ratio of 1.79 at the Flemish Cap margin, the direct conjugate to the Deep Galicia margin, is in excellent agreement to the values of 1.78 - 1.81 determined within the extended continental crust of this study. The V_p/V_s ratio at the Deep Galicia and Flemish Cap margin

is relatively high when compared with in situ and lab based observations of undeformed granite/granodiorite, which typically return V_p/V_s ratios of ~1.70 [*Kern et al.*, 1993; *Christensen*, 1996]. Fracture space at the Flemish Cap and Deep Galicia margin could play host more fluids, which would reduce the bulk shear velocity of the continental crust, and hence lead to a higher V_p/V_s ratio.

Interestingly we observe little to no change in the V_p/V_s ratio between the crustal and mantle layers in the resulting 1D model, with the uppermost mantle possessing a V_p/V_s ratio of 1.79 (Figure 5-13). *Gerlings et al.* [2011] observe a similar V_p/V_s ratio of 1.86 – 1.89 within the COT at the Flemish Cap margin, and interpret this to be a combination of serpentinised mantle and volcanic material. While we do not expect to observe any volcanic material within the hyperextended domain, this observation matches our interpretation of a serpentinised upper mantle. However, other studies have also shown that partially serpentinised mantle peridotites possess high V_p/V_s ratios, typically in the range of 1.95 – 2.10, with low shear velocities between 3.05 – 3.85 km s^{-1}, depending on the degree of serpentinisation [*D'Alessandro et al.*, 2016]. Our result differs appreciably from these studies, potentially due to the high level of uncertainty in the phase velocities at higher periods. Previous travel-time tomography and full-waveform inversion results at the DGM show that mantle serpentinisation decreases rapidly below the Moho, increasing to typical mantle velocities within 5 km [*Davy et al.*, 2016]. Given that our uppermost mantle layer is 5 km thick, we can expect both higher V_p and V_s values, and a lower V_p/V_s ratio, as this layer likely to be affected by the shear velocity of unaltered mantle peridotites. Additionally there is a marked decrease in model sensitivity coinciding with the depth of the upper mantle, likely arising due to the significant velocity contrast between the lower crust and upper mantle (Figure 5-12C). Despite the low V_p/V_s, ratio, the shear velocity of 4.25 ± 0.35 km s^{-1} is consistent with the velocity of upper mantle determined within the COT at the Southwest Iberia in the study of *Corela et al.* [2017].

We must also consider that the shallow architecture of the Deep Galicia margin is 3D in nature and highly variable laterally in terms of the depths of different geological layers. Simplifying the margin structure into a 1D model will undoubtedly lead to the velocities of overlying layers influencing the determined shear velocity of one another.

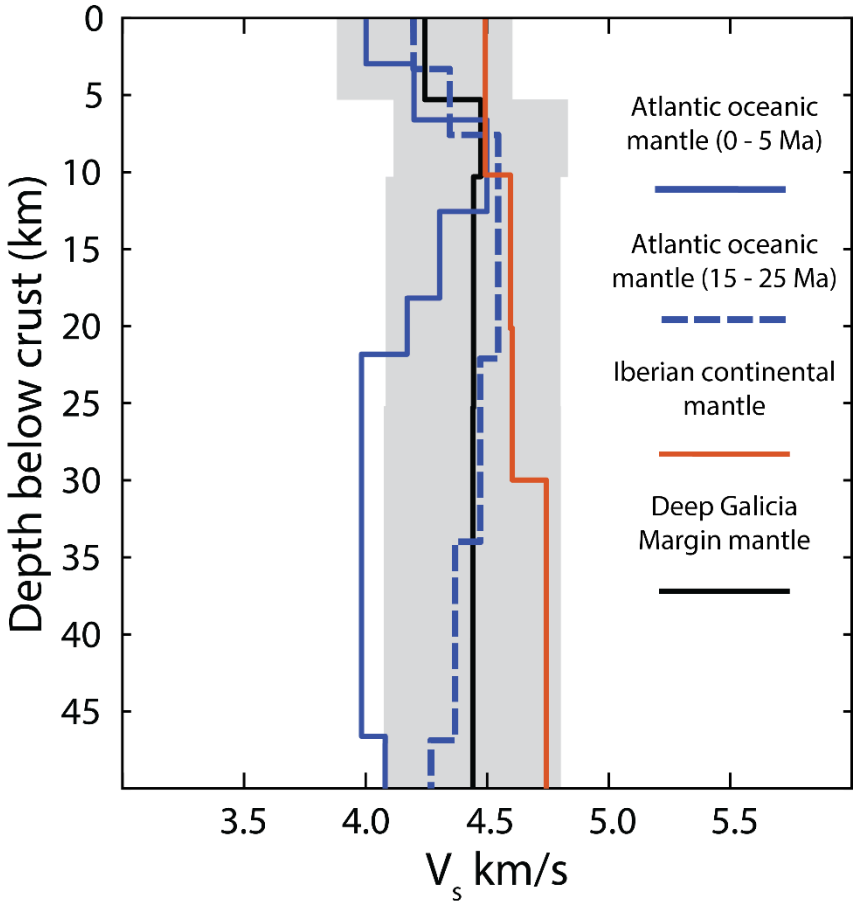

Figure 5-14: Mantle shear wave velocity comparison. Shear wave velocities are indicated by a solid blue line for oceanic mantle at the Mohns ridge aged 0 – 5 Ma, a dashed blue line for oceanic mantle at the Mohns ridge aged 15 – 25 Ma [Conley and Dunn, 2011], a solid black line for continental mantle below the Iberian Peninsula [Corchete and Chourak, 2011], a red line for mantle at the Deep Galicia margin (this study). Shaded region indicates uncertainty in the Deep Galicia margin result.

5.6.2 Deeper shear velocity structure

To our knowledge, no mantle shear velocity structures have previously been determined to depths of 50 km within the COT at the Iberia margin. In order to discuss the deeper mantle shear velocity structure determined in our study, we have compared our results with the shear velocity structure of newly formed oceanic mantle below the slow spreading Mohns ridge in the North Atlantic, and the continental mantle below the Southeast Iberian Peninsula [*Conley and Dunn*, 2011; *Corchete and Chourak*, 2011].

Figure 5-14 shows a comparison of the mantle shear velocity structure between these three domains. It can be seen that the continental mantle below the Iberian Peninsula possess the highest shear wave velocities, ranging from 4.50 – 4.80 km s^{-1}, and increasing with depth. These higher shear wave velocities are a result of the Iberian continental mantle being cool, at a high pressure, and with an absence of melt material. Conversely, the

oceanic mantle typically exhibits lower shear wave velocities, which increase with age, but does form a higher velocity (~4.50 – 4.60 km s^{-1}) "lithospheric lid" at the top of the mantle, which thickens in depth and becomes faster with age [*Conley and Dunn*, 2011]. The observed low velocities in the young oceanic domain are associated with the processes responsible for the formation of new oceanic crust, which includes low pressures in the lithosphere, increased temperatures and the production of melt materials. As the oceanic lithosphere moves away from the ridge, it cools and the shear velocities increase.

The shear velocity result from this study appears to lie between the velocities observed at these two different mantle domains, particularly at greater depths. This result can be explained by the processes associated with the rifting of continental lithosphere. Lithospheric thinning at the DGM may have led to decompression melting and melt depletion, which lowers the shear wave velocity of continental mantle [*Bown and White*, 1995]. Despite the Galicia margin being an amagmatic rift margin, low volumes of melt material in the sub-continental mantle are expected to be generated prior to continental break up and the onset of oceanic accretion [*Schärer et al.*, 1995; *Manatschal et al.*, 2001; *Russell and Whitmarsh*, 2003]. The presence of now solidified melt materials will act to lower both compressional and shear velocities. So while the subcontinental mantle within the continent-ocean transition does not possess as much melt material as at newly formed oceanic crust, it is likely to have higher levels of melt than subcontinental mantle below full thickness crust. This is consistent with the shear velocities seen between the three domains in Figure 5-14.

5.7 Conclusions

Despite the short deployment length, and restricted bandwidth of the utilised OBS/H, we have successfully recovered three consistent Rayleigh wave phase velocity dispersions from ambient noise recordings, and developed a 1D shear velocity structure within the hyperextended domain of the DGM. The primary findings of this study are as follows:

- Fundamental Rayleigh wave dispersion velocities determined through the Galicia-3D seismic array increase from 1.0 km s^{-1} at periods of 4 s, to 3.0 km s^{-1} at 14 s period. This result is consistent between the FTAN and beamforming methods, giving confidence in the result.

- The primary source of ambient noise recorded by the seismic array is from wave noise generated along the coast of the Iberian Peninsula. A secondary weaker source appears to come from the opposite direction, and is likely wave noise from coast of North America.
- Active source seismic shooting during the instrument deployment appears to have had little to no effect on the results of ambient noise analysis. This result is not unexpected given that the frequencies of investigation in this study are two orders of magnitude lower than the dominant frequency of active source shooting.
- Estimates of the 1D shear wave velocity at the DGM reveal values of 0.94 ± 0.12 km s^{-1} in the sediments, 2.21 ± 0.36 km s^{-1} in the upper crust, 3.48 ± 0.36 km s^{-1} in the lower crust, and 4.25 ± 0.35 km s^{-1} in the upper most mantle, increasing to 4.45 ± 0.35 km s^{-1}, 25 km below the Moho. These results are consistent with similar studies at the Iberia-Newfoundland conjugate margins.

Given the success of this ambient noise analysis, future work could look to expand upon these results by performing ambient noise tomography in order to produce a 3D shear velocity map of the DGM.

Chapter 6: Conclusions and future work

6.1 Conclusions

This thesis has described a seismic investigation of the continent-ocean transition at the Deep Galicia margin, using newly collected seismic reflection and refraction data from the Galicia-3D seismic experiment (G3D). This study looked to address questions regarding the transition from rifting to seafloor spreading, the nature of faulting and mantle serpentinisation within the hyperextended domain, and the shear velocity structure of such distal rift domains. These questions were addressed using a variety of conventional and novel seismic analysis techniques, which produced a compressional velocity model of the transition from continental extension to seafloor spreading, a high resolution compressional velocity model of continental hyperextension and the associated detachment faulting, and a shear velocity model of the COT. The primary findings from this study are as follows:

- Travel-time tomography models have been interpreted to show that west of the Peridotite Ridge the exhumation and serpentinisation of mantle peridotite continues over a short distance (< 25 km), before the onset of an anomalously thin oceanic crust (0.5 – 1.5 km thick), which thickens seaward. Evidence suggesting the presence of serpentinised mantle material below this thin oceanic crust comes from seismic velocities increasing gradually from 5.5 – 6.5 km s^{-1} to 7.3 – 7.6 km s^{-1}, with a velocity gradient of 1.0 s^{-1}. These results are consistent with seismic observations of the continent-ocean transition at the conjugate Flemish Cap margin, and supports other studies which have suggested that the transition to oceanic crust is largely symmetric once the continental crust has ruptured [*Funck et al.*, 2003; *Hopper et al.*, 2006, *Gillard et al.*, 2016]. It is important to note that the interpretation of thin oceanic-crust is based on the presence of shallow and short-offset sub-basement reflections. An alternative source for such reflections could be a pronounced serpentinisation front within a zone of exhumed continental mantle.
- The accretion of thin oceanic crust seaward of the Peridotite Ridge is interpreted to have begun at some time after 122 Ma, based on the dating of materials recovered from the Peridotite Ridge. This age is consistent with the rifting propagating from

south to north at the Iberia-Newfoundland rift margin and an ultra-slow seafloor spreading rate of 7.4 mm yr^{-1}. However, the nature and timing in which the Peridotite Ridge was emplaced still remains unclear. Previous studies have interpreted the presence of oceanic spreading anomaly M0 west of the Peridotite Ridge, which gives the interpreted thin oceanic crust an age of 126 Ma [*Srivastava et al*., 2000]. If anomaly M0 is truly present in the oceanic crustal domain, then it leads us to the conclusion that the emplacement of the Peridotite Ridge occurs after the onset of oceanic crustal accretion.

- Both travel-time tomography and full-waveform inversion models have resolved a pattern of high and low velocities below the S reflector in the hyperextended domain, which is interpreted to be varying degrees of mantle serpentinisation. These observations are consistent with the models of normal faulting cutting through the hyperextended crust and acting as conduits, transporting seawater and preferentially serpentinising the upper mantle. Seismic velocity is observed to decrease down-dip of these faults, corresponding to an increase in serpentinisation. Observed seismic velocities directly below the S reflector range between 5.5 and 8.0 km s^{-1}, which corresponds to serpentinisation of 70% to 0% (unaltered), respectively.
- The application of 2D full-waveform inversion to this sparse and deep seismic dataset was successfully demonstrated, and produced a seismic velocity model of the Deep Galicia margin with the greatest resolution to date. These high resolution velocity models have been used to assist in the interpretation of previously unidentified faults and crustal units in high resolution seismic reflection imaging of the hyperextended domain. It is hoped that more accurate interpretations of the hyperextended margin will aide in the understanding of the apparent extension discrepancy observed at the Deep Galicia margin.
- Despite the short array deployment and limited bandwidth of instrumentation, the application of ambient noise analysis methods has returned three consistent fundamental Rayleigh wave phase velocity dispersion curves. Additionally, the recording of active-source seismic shooting during the deployment has been shown to have little to no effect on these ambient noise results. Beamforming indicates that the predominant source of surface waves through the array during the deployment comes from the east, likely to be wave noise along the coast of the

Iberian Peninsula, with a secondary, weaker, source originating from the west, likely to be from the coast of North America. However, it is noted that these directional sources are also correlated with significant spatial aliasing in the beamformer results, as well as the east-west shooting direction of the active source survey.

- Determination of a 1D shear velocity model at the Deep Galicia margin gives shear velocities of 0.94 ± 0.12 km s^{-1} in the sediments, 2.21 ± 0.36 km s^{-1} in the upper crust, 3.48 ± 0.36 km s^{-1} in the lower crust, and 4.25 ± 0.35 km s^{-1} in the uppermost mantle, increasing to 4.45 ± 0.35 km s^{-1}, 25 km below the Moho. These results are consistent with similar studies conducted at the Iberia-Newfoundland conjugate margins, and adds to the observations of shear velocity within such domains [*Gerlings et al.*, 2011; *Eddy et al*., 2013; *D'Alessandro et al*., 2016].

6.2 Comparisons with existing rift models

Velocity models produced in this study and the interpretations we draw from them contradict many aspects of the classic rift models, and both support and contradict modern interpretations and models of magma-poor rifting and continental breakup. In the following we highlight our interpretations which support or contradict existing models:

- The original pure-shear rift model of *McKenzie* [1978] predicts uniform stretching through the continental lithosphere, resulting in symmetric conjugate margins and the direct juxtaposition of continental and oceanic crust. Simple-shear models produce asymmetric rift geometries, but also result in the direct contact of oceanic crust with continental crust [e.g., *Wernicke*, 1981; 1985]. In our models we interpret a more complicated, non-uniform, thinning of the continental crust which cannot be explained by either pure- or simple-shear alone. When the models from this study are compared to the conjugate margin, we observe significant asymmetry in the thinning of the continental crust. Our models show extreme thinning (to < 2 km) over large distances (> 100 km, when combined with the model of *Zelt et al.* [2003]), while models at the conjugate Flemish Cap margin show a much more abrupt thinning [*Funck et al*., 2003; *Hopper et al*., 2006]. Additionally, our models are interpreted to show a significant transitional zone between continental crust and oceanic crust, comprising exhumed and serpentinised mantle peridotites. These contradictions are already well established observations at the Deep Galicia margin,

and other magma-poor rift margins. Subsequent models of rifting have been modified in order to account for the complexities in extensional structures, and the pronounced zones of exhumed continental mantle [e.g. *Dean et al.*, 2000; *Pérez-Gussinyé and Reston, 2001*; *Pérez-Gussinyé et al*., 2003; *Van Avendonk et al., 2006*].

- Many contemporary rift models describe the coupling of the upper and lower continental crust, once the crust has been thinned to less than 10 km in thickness, enabling listric normal faults to cut through to the upper mantle [*Whitmarsh et al.*, 2001; *Pérez-Gussinyé and Reston, 2001*; *Pérez-Gussinyé et al*., 2003]. In our velocity models, we also interpret a rapid decrease in the thickness of continental crust, before observing faults which cut through to the upper mantle. Our velocity models show that the continental crust could be as thin as 4 km before this complete coupling of the continental crust occurs. Once the continental crust is completely coupled, these existing models describe the hydration and serpentinisation of upper-mantle peridotites by fluid flow along normal faults. Subsequently, continued extension at the margin becomes focussed in this weak layer of serpentinite, forming a large detachment fault. Our modelling results strongly support these models, revealing that the upper mantle, below the S detachment, has lower seismic velocities at the base of these faults, which we interpret as higher degrees of mantle serpentinisation, associated with the fluid flow along the faults. In this study, and the associated Galicia-3D studies (e.g. *Bayrakci et al.* [2016]), we have been able to quantify the degree of serpentinisation below the S Reflector, as well as the fluid flow along the normal faulting acting as conduits. Such quanitifcations could be incorporated as constraints in future numerical modeling of the magma-poor break-up process.
- A significant majority of the current magma-poor rift models describe detachment faulting within the hyperextended domain as being concave down, and rooted in the mantle [*Whitmarsh et al.*, 2001a; *Lavier and Manatschal*, 2006; *Péron-Pinvidic et al.*, 2007; *Péron-Pinvidic and Manatschal*, 2009]. This fault geometry enables the exhumation of continental mantle, with progressively deeper source of mantle as the exhumation progresses oceanward. This detachment geometry also results in an asymmetry between the conjugate margins, with one margin possessing a substantial zone of exhumed continental mantle, while the conjugate margin has a

more immediate onset of magmatic accretion [*Manatschal*, 2004]. However, in our tomography model the shape of the S reflector is observably concave up, contradictory to these models and interpretations. *Manatschal* [2004] presents models of both concave downward and upward detachment faults. The concave upward detachment model soles out in the crust-mantle boundary, resulting in a symmetric exhumation of continental mantle and onset of oceanic crust. This strongly supports our suggestion that mantle emplacement and magmatic accretion is symmetric after continental breakup. While this interpretation is contradictory to most contemporary models of the Iberia-Newfoundland margin, it has been suggested to occur at margins, such as the Australia-East Antarctic magma-poor margin [*Direen et al.*, 2011; *Espurt et al.*, 2012; *Direen et al.*, 2013]. *Direen et al.*, (2011) observed an absence of concave downward detachment faults as well as a pronounced rift symmetry at this margin, and explained this by symmetric mantle exhumation along a system of concave upward detachment faults, observed at both of the conjugate margins.

- Two models of faulting are currently proposed to explain the discrepancy between the observed lithospheric thinning and the amount of deformation observable in the brittle continental crust at magma-poor margins; polyphase faulting and sequential faulting. Sequential faulting describes continental crust being cut by normal faults, forming fault blocks which get progressively smaller toward the location of continental break-up [*Ranero and Pérez-Gussinyé*, 2010]. At no point in the model do new faults cut the preceeding fault. Polyphase faulting models are similar, except that the preceeding faults can be cut by new faults, giving rise to a much more complex fault geometry [*Reston*, 2007a; *McDermott and Reston*, 2015]. Our velocity models and interpretations of reflection seismic images exhibit the general shape of fault blocks described by the sequential faulting model, and even reveal a small and previously uninterpreted fault block at the most distal limit of the hyperextended domain. These observations lend favour to the argument for sequential faulting. However, our results also reveal new faults within the previously interpreted fault blocks, which reduce the width of the fault blocks and break the pattern of continually decreasing block size oceanward, contradicting the sequential faulting model. Additionally, chaotic velocity patterns in the areas of

complex reflection imaging could be indicative of significant fault overprinting, which would be expected from polyphase faulting.

6.3 Wider implications of this study

- While continental rifting and the thinning of continental crust is often observed to be largely asymmetric at magma-poor rift margins, this study suggests that once the crust has ruptured the exhumation of sub-continental mantle and the onset of oceanic crust is relatively symmetric between conjugate margins [*Ranero and Pérez-Gussinyé*, 2010; *Franke*, 2013]. This study also suggests that the exhumation of sub-continental mantle could be occurring along concave-upward detachment faults. This observation could have important implications for the understanding magma-poor rifting globally. For instance the Australian-Antarctic magma-poor margin exhibits conjugate margins with strong symmetry and an absence of concave-downward detachment faulting, which is in contrast with what is observed at the Iberia-Newfoundland margin and other North Atlantic margins [*Direen et al.*, 2011; *Espurt et al.*, 2012; *Direen et al.*, 2013]. This could suggest that magma-poor rifting is better described by concave-upward detachment faulting, or that there are two modes of detachment faulting at magma-poor margins, or that it doesn't require detachment faulting at all. The way in which mantle is exhumed at magma-poor margins may be able to account for the differences between the rift margins observed in the North-Atlantic and other margins around the globe. However, the processes responsible for the formation of ridges comprised of peridotite, isolated on only one of the conjugate margins remain enigmatic.
- Extremely limited mantle melting at the time of continental breakup not only results in mantle exhumation, but also the eventual onset of extraordinarily thin oceanic crust, which can be less than 1 km in thickness. The gradual thickening of this oceanic crust indicates an increasing melt production after lithospheric breakup [*Jagoutz et al.*, 2007]. Such thin oceanic crust has long been thought to be anomalous, but the results presented here add to the mounting evidence that this phenomenon occurs at many margins around the globe (e.g. Gakkel Ridge, Southwest Indian Ridge, Iberia-Newfoundland rift margin, the Bay of Bengal, Mid-Cayman Rise) [*Stroup and Fox*, 1981; *Mutter*, 1993; *Whitmarsh et al.*, 2001a; *Funck*

et al., 2003; *Van Avendonk et al.*, 2006; *Jokat and Schmidt-Aursch*, 2007; *Radhakrishna et al.*, 2010; *Armitage et al.*, 2011; *Singh et al.*, 2011].

- We have suggested that detachment faulting at magma-poor margins forms via an inhomogeneous distribution of seawater to the upper mantle, leading to the preferential serpentinisation of the mantle peridotites. This new knowledge should now be applied and tested in other studies of magma-poor continental hyperextension and breakup (e.g., the Porcupine Basin, the Australia-Antarctica rift system), not only to confirm this particular mechanism for the formation of detachment faulting, but to see how it varies between margins. There also remain questions pertaining to the level of serpentinisation below individual faults, and how that affects the movement along both the normal faults responsible and the detachment surface formed.
- The successful application of 2D full-waveform inversion in order to resolve a crustal target, using sparse and deep OBS/H data, should encourage the application of this method in future academic seismic experiments. The improvement in velocity resolution is highly advantageous for the interpretations of crustal targets with significant lateral and vertical variability. Higher resolution velocity models will also enable more accurate migration of seismic reflection data. We suggest revisiting existing wide-angle seismic datasets that could be good candidates for the application of full-waveform inversion. Many of these studies already possess travel-time tomography models capable of reproducing the observed wavefield to within half a seismic cycle, making the extension to full-waveform inversion straightforward.
- In this study we have used seismic velocities to infer the level of serpentinisation of mantle peridotites, while other results from the Galicia-3D study have linked fault displacement to water flux through the crust [*Bayrakci et al.,* 2016]. Such fault-enabled hydration of the upper-most mantle is not a process unique to magma-poor rift margins, and the techniques used in this study are applicable to similar settings. Hydration and serpentinisation of the mantle lithosphere also occurs along low-angle detachment faults at slow and ultra-slow mid-ocean ridges (e.g. the Atlantis Massif in the Atlantic Ocean [*Boschi et al.*, 2006] and Godzilla Mullion in the Western Pacific Ocean [*Loocke et al.*, 2013]), as well as along bending-related normal faults at subduction zones (e.g. the Tonga-Kermadec-Hikurangi trench in the

West Pacific Ocean [*Henrys et al.*, 2006] and the Middle-America trench in the East Pacific Ocean [*Ranero et al.*, 2003]). Collectively, these faulting mechanisms form an important part of the Earth's water cycle, enabling large volumes of water to be transferred from the ocean and into the solid Earth. The transport of water, stored in serpentinite and other altered minerals, into the deep Earth via subduction has significant implications for the Earth's evolution, affecting volcanism, earthquakes, metal fractionation and formation of new continental crust. Understanding where and how water enters the deep Earth, allows greater understanding of these processes.

- Processes of slow and ultra-slow spreading at mid-ocean ridges often result in the formation of low-angle detachment faults and oceanic-core complexes (e.g. the Atlantis Massif in the Atlantic Ocean and Godzilla Mullion in the Western Pacific Ocean), which exhume and serpentinise oceanic lithospheric mantle [*Boschi et al.*, 2006; *Loocke et al.*, 2013]. Many questions still remain on how these structures initiate and subsequently cease growing. Given the strong parallels between the slow extending/spreading settings and the structure of detachment faults at both magma-poor rift margins and mid-ocean ridges, it is possible that the processes responsible for each share commonality [*John and Cheadle*, 2010]. The processes of preferential mantle serpentinisation and focussed strain localisation discussed in this study could provide further insights into the formation of the low-angle detachment faults formed at mid-ocean ridges.

6.4 Study limitations

- Notable limitations in the travel-time tomography performed in Chapter 3 occur due to the way in which TOMO2D handles the smoothing of velocity models and reflection surfaces. Seismic reflections arise due to velocity contrasts within the structure of the Earth, however, the TOMO2D algorithm produces velocity models which are smooth in both the horizontal and vertical direction and are unable to introduce such velocity contrasts. Instead the algorithm treats the reflection surface as a "floating reflector", which is simply a horizon within the smooth velocity model. The depth of this reflection surface is modified using the smooth velocity field in order to produce synthetic travel-times that match the observed travel-times. This results in the velocities directly above the reflector being overestimated, and hence

leads to the depth of the modelled reflector being shallower than in reality. This is an inherent problem with the use of a floating reflector in velocity modelling. This issue could be avoided by using alternative tomography algorithms, such as RAYINVR or JIVE-3D, which utilise discrete layers within the model and are capable of reproducing the velocity contrasts responsible for seismic reflections.

- As mentioned in Chapters 3 and 4, the depths in which the instruments are deployed, combined with the significant noise in the water column, limits the ability to accurately resolve shallow sediment velocity structure in the travel-time tomography and full waveform inversion models. Error within the shallow velocity model can propagate to the deeper regions of the model and has an adverse effect on the final models. The shallow structure of these models could potentially be resolved in greater detail using data from the multi-channel seismic reflection data. Velocities determined in the processing of the reflection seismic imaging (i.e. stacking and migration velocities) could be incorporated into the wide-angle tomography models. Alternatively, refractions from the shallow subsurface are often recorded on the hydrophone streamers, which would enable the determination of shallow subsurface structures by seismic tomography.
- The full waveform inversion performed in Chapter 4 is both acoustic and isotropic, which means that we are making the assumption that differences between the observed and synthetic wavefields can explained purely by differences in the compressional velocity and density (which is tied to the compressional velocity by Gardner's Law). However, seismic waveforms are a function of many factors, including compressional velocity and density, as well as shear velocity, attenuation and anisotropy. Some authors believe that without accounting for these additional parameters, true waveform inversion is not performed. Differences in the waveform shape and amplitude are incorrectly accounted for by modification of the compressional velocity, which could lead to artefacts within the compressional velocity model. Improvements could be made by performing an anisotropic and elastic full waveform inversion. However, the data used in this study are insufficient to accurately determine and invert for a shear velocity model, and without accurate models of attenuation and anisotropy the inversion still relies on the assumption that the waveform is modified only by the compressional and shear velocities within the model.

- The limited bandwidth of the ocean-bottom seismometers and hydrophones used in this study restricts the depth resolution of both surface wave phase velocities and their inversion for compressional and shear velocity. Achievable depth resolution is approximately equal to the wavelength of a propagating surface wave. Short period data enable the resolution of velocities in thin and shallow geological layering, while long period data enable the determination of velocities at greater depths. Given that the Galicia-3D data set possesses short period data down to 4 s and long periods up to 14 s, we expect to only be able to resolve velocities in shallow layers approximately 4 km in thick or greater, and the ability to resolve velocities to a depth of approximately 42 km. This would imply that our shallow sediment and continental crustal layers are poorly resolved, and probably influenced by one another, while the velocities resolved at depths greater than 40 km are poorly constrained. Improving the depth resolution would require a greater bandwidth of data, and so future experiments should look to utilise broad-band OBS/H.

6.5 Future work

The Galicia-3D seismic dataset is a large and comprehensive academic seismic dataset and offers a wide range of research directions. In this study we produced a mixture of 1D and 2D seismic velocity models of the COT, exploring what might be considered more novel seismic techniques in such a deep water environment. Given the success of these methods, we have shown the viability of extending these methods to a 3D application to the full seismic dataset. Such investigations will provide further insight into the 3D nature of continental rifting and breakup at the DGM, and assist in the interpretation of 3D seismic reflection imaging.

6.5.1 3D Full-waveform inversion

Following the successful application of FWI to a 2D profile of the Galcia-3D seismic experiment, the next progression is to extend the application to a full 3D FWI of OBS/H data collected in the 3D Box. Although the overall spacing of the instruments in 3D Box array is larger than that of the 2D FWI profile, these instruments record a much larger catalogue of seismic shots, with a complete azimuthal coverage. This will mean that each cell in the 3D velocity model will sample many crossing wavefields, giving more

independent observations at each location within the model and hence provide greater constraint on the resolved velocities. Unlike the 2D FWI, any out-of-plane arrivals should be correctly mapped into their 3D location, reducing the frequency of anomalous features in the final velocity model. 3D FWI also offers more comprehensive quality assurance methods, including phase plots which make the identification of cycle skipping much easier.

A 3D travel-time tomography model of the 3D Box has already been determined by *Bayrakci et al.* [2016] and could be used as the starting model for 3D FWI. This model may require similar modifications as the 2D travel-time tomography model used in this study, such as a more accurate water velocity. The source-signature derived in Chapter **4** could be used in the 3D FWI, if the filters applied to the seismic data remain the same. However, it is important to ensure that the source signature does not vary during the course of the survey and that the filters applied to the 2D data set are also optimal for the full 3D dataset.

It may also be possible to recover shallow reflection and refraction data by performing downward continuation on the OBS/H data. Downward continuation of the OBS/H data can be used in order to remove the effects of the large amplitude direct-water arrival, by bringing the shot and receiver to a common datum, which in this case would be the seafloor. Without the dominant direct water arrival, the shallow sediment reflections and refractions may be observed, and could be included in the full-waveform inversion process. This would give more constraint to the shallow sediments and as a result would improve the accuracy of the deeper model. Additionally, the downward continuation assists in focusing the seismic energy and hence improves the overall resolution.

A high resolution velocity model derived from 3D FWI could be used to interpret the 3D seismic reflection imaging of hyperextended crust and S reflector, and could potentially be used for a more accurate migration of the seismic reflection data.

6.5.2 Ambient noise tomography

An absence of observable converted shear waves from the active source shooting has prohibited the determination of a 3D shear velocity model using classical travel-time tomography. However, it has been shown in Chapter **5**, that it may be possible to perform ambient noise tomography in order to recover a 3D shear velocity model of the hyperextended domain at the DGM.

In this study we determined noise cross-correlation functions for all inter-station pairs in the 3D seismic array, using those which showed an emergent Rayleigh wave signal to determine both group and phase velocity dispersion curves. Ambient noise tomography would utilise the spatial distribution of these inter-station NCFs, in order to map the Rayleigh wave group and/or phase velocities onto models defined throughout the array, at different periods of interest. Inversion of the group and/or phase velocity dispersions at grid nodes throughout the model would produce shear velocity profiles relative to depth, and hence enable the generation of a 3D shear velocity model throughout the 3D Box.

Determining the 3D shear velocity structure from ambient noise tomography offers a feasible alternative to classic travel-time tomography of observed shear waves. A shear wave velocity model determined in such a way would complement the 3D compressional velocity model, determined by travel-time tomography. Both models could be utilised to generate models of the V_p/V_s ratio, or Poisson's ratio, which would provide valuable information on the properties of structures observed within the hyperextended domain. Of particular interest would be the V_p/V_s ratio of the serpentinised mantle peridotite forming the S reflector, giving a greater constraint on the degree of serpentinisation and the water content of such material.

Appendix A

Instrument	T_{drift} (s)	$T_{duration}$ (s)	D_{rate} (s/s)	Instrument	T_{drift} (s)	$T_{duration}$ (s)	D_{rate} (s/s)
1	-1.4483	8.05E+06	-1.80E-07	**46**	0.0285	8.83E+06	3.23E-09
2	0.0000	8.19E+06	0.00E+00	**47**	-1.7777	8.86E+06	-2.01E-07
3	0.3318	8.02E+06	4.14E-08	**48**	0.0455	8.84E+06	5.15E-09
4	-0.2340	8.15E+06	-2.87E-08	**51**	0.0259	8.89E+06	2.92E-09
5	-0.1060	8.01E+06	2.23E-06	**52**	-0.5031	8.50E+06	-5.92E-08
6	0.1800	8.13E+06	2.21E-08	**53**	-0.0058	8.50E+06	-6.80E-10
8	0.3860	8.19E+06	4.71E-08	**54**	-0.2194	8.55E+06	-2.56E-08
9	-0.3763	7.98E+06	4.72E-08	**56**	0.9440	8.48E+06	1.11E-07
11	-0.2280	7.97E+06	-2.86E-08	**57**	0.2725	8.81E+06	3.09E-08
13	-0.4893	7.96E+06	-6.14E-08	**58**	-0.5630	8.48E+06	-6.64E-08
14	1.3210	8.64E+06	1.53E-07	**59**	-0.3079	8.86E+06	-3.47E-08
15	0.2944	7.96E+06	3.70E-08	**60**	-0.0180	8.48E+06	-2.12E-09
16	-0.3750	8.48E+06	-4.42E-08	**61**	0.8325	8.78E+06	9.48E-08
17	0.1080	8.48E+06	1.27E-08	**62**	0.7620	8.48E+06	8.99E-08
18	-0.1894	7.94E+06	-2.39E-08	**63**	0.0310	8.49E+06	3.65E-09
19	0.4533	8.23E+06	-6.64E-08	**64**	0.0265	8.81E+06	3.00E-09
20	0.0570	7.88E+06	7.23E-09	**65**	-0.1810	8.48E+06	-2.13E-08
21	0.4216	8.33E+06	5.06E-08	**66**	-0.4900	8.77E+06	-5.59E-08
22	125.3620	8.14E+06	1.54E-05	**67**	0.0170	8.48E+06	2.01E-09
23	0.3305	8.34E+06	3.96E-08	**68**	-0.1170	8.47E+06	-1.38E-08
25	0.2640	8.37E+06	3.15E-08	**69**	2.6222	9.01E+06	2.91E-07
26	0.4070	8.22E+06	4.95E-08	**70**	0.0000	8.47E+06	0.00E+00
27	0.0074	8.37E+06	8.84E-10	**71**	-0.1420	8.46E+06	-1.68E-08
28	0.0740	7.92E+06	9.34E-09	**72**	-0.7041	8.99E+06	-7.83E-08
29	-0.0140	8.10E+06	1.73E-09	**73**	0.0182	8.18E+06	3.19E-09
30	0.0310	8.29E+06	3.74E-09	**74**	0.3711	8.72E+06	4.25E-08
32	-0.0230	7.70E+06	-2.99E-09	**75**	-1.1464	8.71E+06	-1.20E-07
33	9.8620	8.12E+06	1.21E-06	**76**	-1.1898	8.72E+06	-1.36E-07
34	0.4100	8.50E+06	4.82E-08	**77**	0.0149	8.73E+06	1.70E-09
35	-0.0576	8.13E+06	-7.09E-09	**78**	-0.0013	8.79E+06	-1.49E-10
37	-0.2835	8.80E+06	-3.22E-08	**79**	0.0280	3.92E+05	7.14E-08
38	0.3825	8.95E+06	4.27E-08	**80**	0.0040	3.95E+05	1.01E-08
39	0.1270	8.97E+06	1.42E-08	**81**	-0.0020	3.98E+05	-5.02E-09
40	0.0227	8.73E+06	2.61E-09	**82**	0.0000	4.07E+05	0.00E+00
41	0.0041	8.74E+06	4.74E-08	**83**	0.0080	4.11E+05	1.95E-08
42	0.0126	8.78E+06	1.43E-09	**84**	-0.0130	4.16E+05	-3.13E-08
43	-0.0816	8.80E+06	-9.28E-09	**85**	0.0060	4.29E+05	1.40E-08
45	-0.4322	8.80E+06	-4.91E-08	**86**	0.0200	4.43E+05	4.52E-08

Table A-6-1: Clock drift calculations for all recovered instruments in the Galcia-3D experiment.

Appendix A

Instrument	Deployment Longitude (UTM)	Deployment Latitude (UTM)	Relocation Longitude (UTM)	Relocation Latitude (UTM)	Relocation Distance (metres)	Relocation Azimuth (degrees)
3	680249	4673134	680521	4673377	365	48
4	683226	4672733	683232	4672722	13	153
6	690003	4673646	689980	4673389	258	185
8	696334	4673631	696327	4673485	146	183
9	699447	4674874	699502	4674384	493	174
11	706378	4674374	706110	4674141	355	229
13	712971	4673626	712617	4673505	375	251
15	720721	4674542	720743	4674652	112	11
16	723200	4675365	723143	4674572	795	184
17	726241	4675140	726171	4674812	335	192
18	729692	4676263	729357	4675909	488	223
19	672980	4666330	673030	4666164	173	163
20	676162	4666398	676431	4666718	419	40
21	680008	4667695	680126	4667709	119	83
22	683390	4667382	683543	4669231	1855	5
23	687090	4666957	687253	4665755	1213	172
25	692801	4667410	692932	4667645	268	29
26	696838	4668578	696785	4668575	53	267
27	700565	4668694	700629	4668996	309	12
29	706878	4668054	706430	4667943	461	256
30	710502	4668561	710377	4668478	150	236
32	716429	4668985	716322	4668949	113	251
33	720541	4668935	720540	4667116	1819	180
34	724080	4669246	723955	4669128	172	227
35	726980	4669383	726927	4669544	169	342
37	673496	4660810	673645	4660978	226	42
38	676876	4661016	676929	4660503	515	174
39	680276	4661424	680465	4661490	200	71
40	683618	4661476	683858	4660735	779	162
41	686967	4661598	687096	4661290	333	157
42	690271	4661875	690279	4661600	274	178
43	693643	4662066	693296	4662200	371	291
45	700437	4662122	700356	4661765	367	193
46	703800	4662352	703690	4662374	112	281
47	707156	4662516	706889	4662786	380	315
48	710570	4662673	710467	4662907	256	336
51	720614	4663157	720449	4663500	381	334
52	723996	4663297	723741	4664056	801	341
53	727386	4663438	727271	4663578	182	320
54	730717	4663613	730941	4663945	400	34
56	677609	4654879	677637	4654743	138	168
57	681056	4654555	680848	4654179	429	209
58	684425	4655297	684375	4655607	314	351
59	686977	4655898	686436	4655494	675	233
60	690694	4655986	690673	4655958	35	218
61	693893	4655361	693929	4655132	232	171

62	696742	4656573	696683	4656504	92	221
63	700815	4656099	700777	4655994	111	200
64	704662	4656020	704208	4656143	470	285
65	707838	4656212	707769	4656546	340	348
66	711548	4657123	711714	4657028	191	119
67	714243	4657315	714163	4657407	121	319
68	717218	4656472	717146	4656611	157	333
69	720990	4656955	721221	4658474	1536	9
70	724922	4656835	724807	4656916	141	305
71	727655	4657923	727536	4658012	149	307
73	615939	4658199	615743	4658437	309	321
74	625589	4658663	625313	4658700	279	278
75	635140	4659095	635374	4659244	278	58
76	644672	4659561	644856	4659794	297	38
78	663945	4660426	664042	4660990	572	10
79	705554	4662369	705567	4662538	169	4
80	708834	4662588	708867	4662532	65	150
81	712180	4663099	712214	4662656	444	176
82	715588	4662913	715533	4662921	56	278
83	718894	4663092	718887	4662954	139	183
85	725634	4663360	725581	4663435	92	325
86	729032	4663503	729013	4663457	49	202

Table A-6-2: Instrument relocations for all recovered instruments in the Galcia-3D experiment

Appendix B

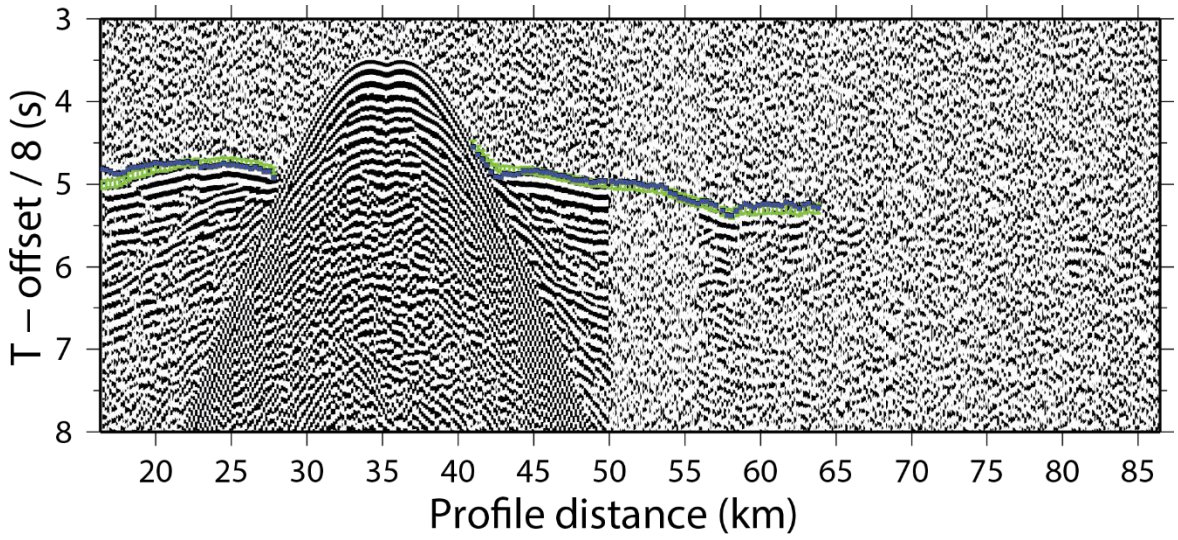

Figure B-1: Receiver gather for OBS73. Travel-time picks are green lines, TOMO2D model fit is indicated by purple dots.

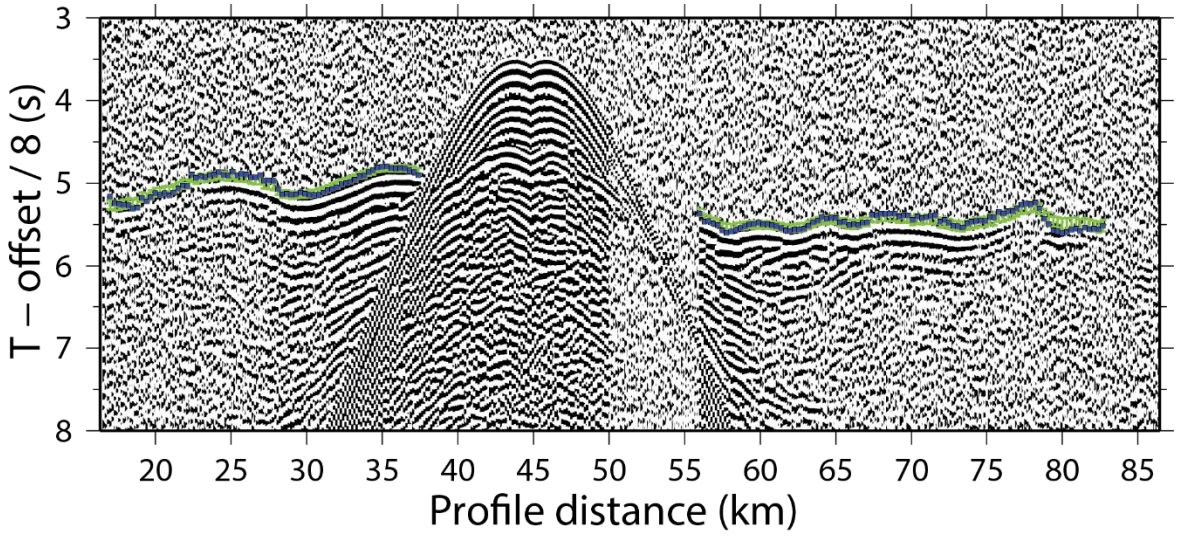

Figure B-2: Receiver gather for OBS74. Travel-time picks are green lines, TOMO2D model fit is indicated by purple dots.

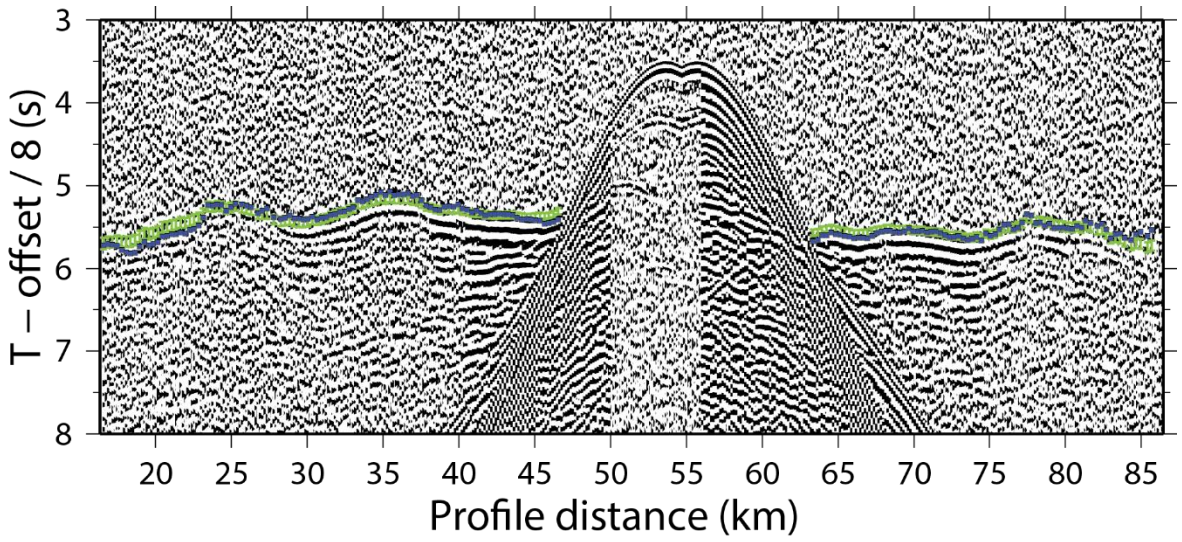

Figure B-3: Receiver gather for OBS75. Travel-time picks are green lines, TOMO2D model fit is indicated by purple dots.

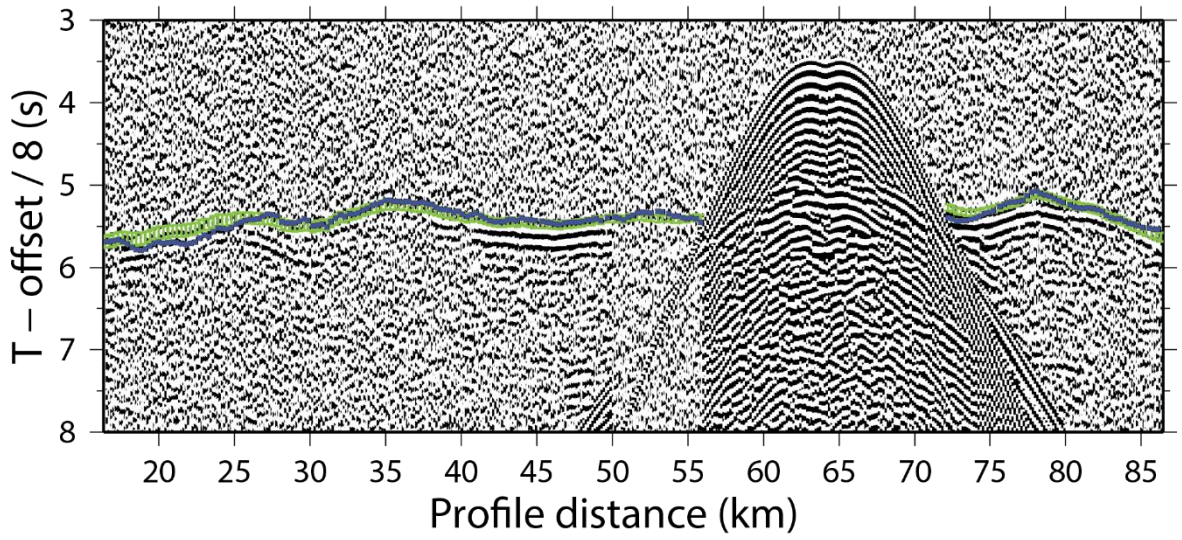

Figure B-4: Receiver gather for OBS76. Travel-time picks are green lines, TOMO2D model fit is indicated by purple dots.

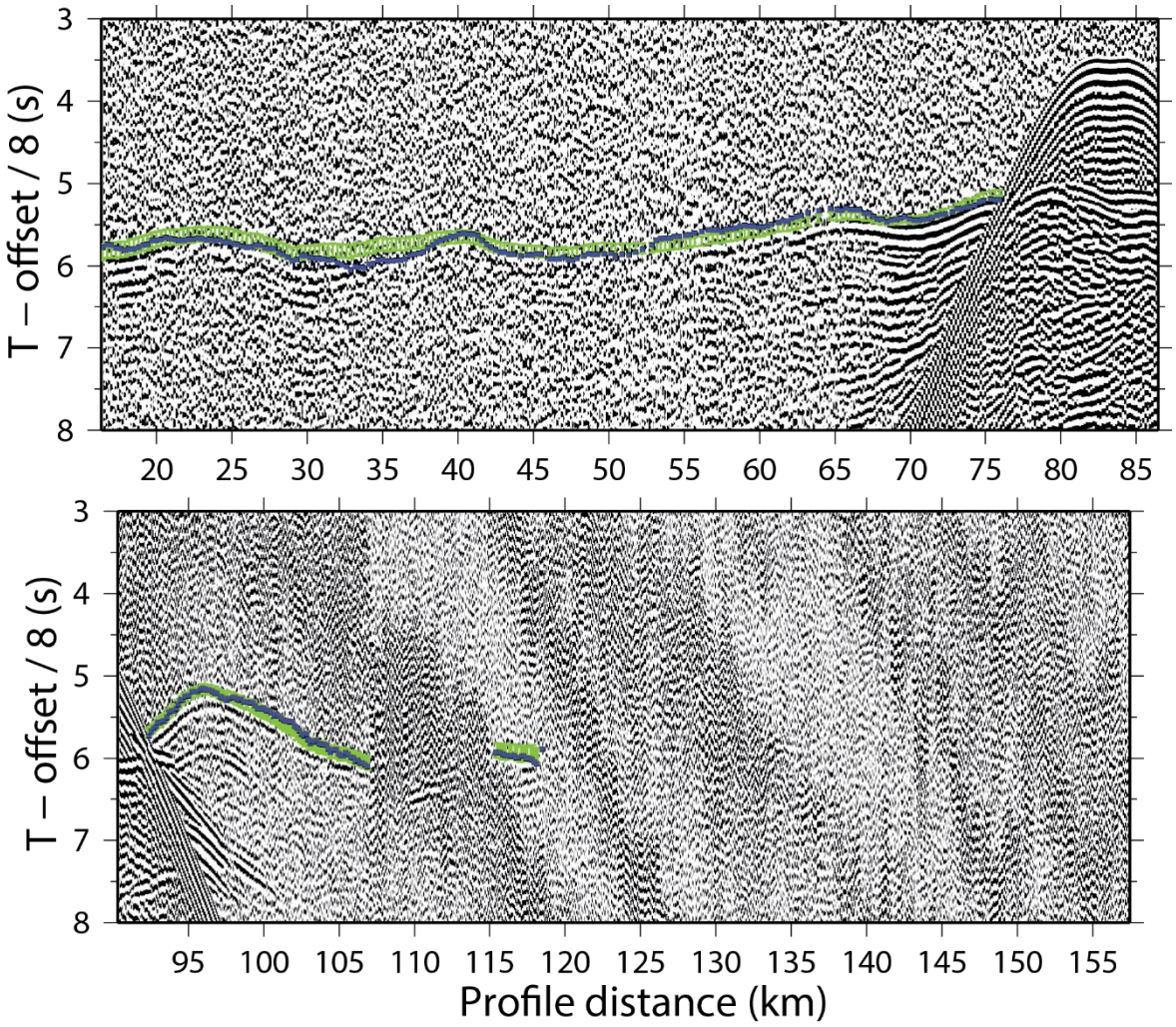

Figure B-5: Receiver gathers for OBS78. Travel-time picks are green lines, TOMO2D model fit is indicated by purple dots.

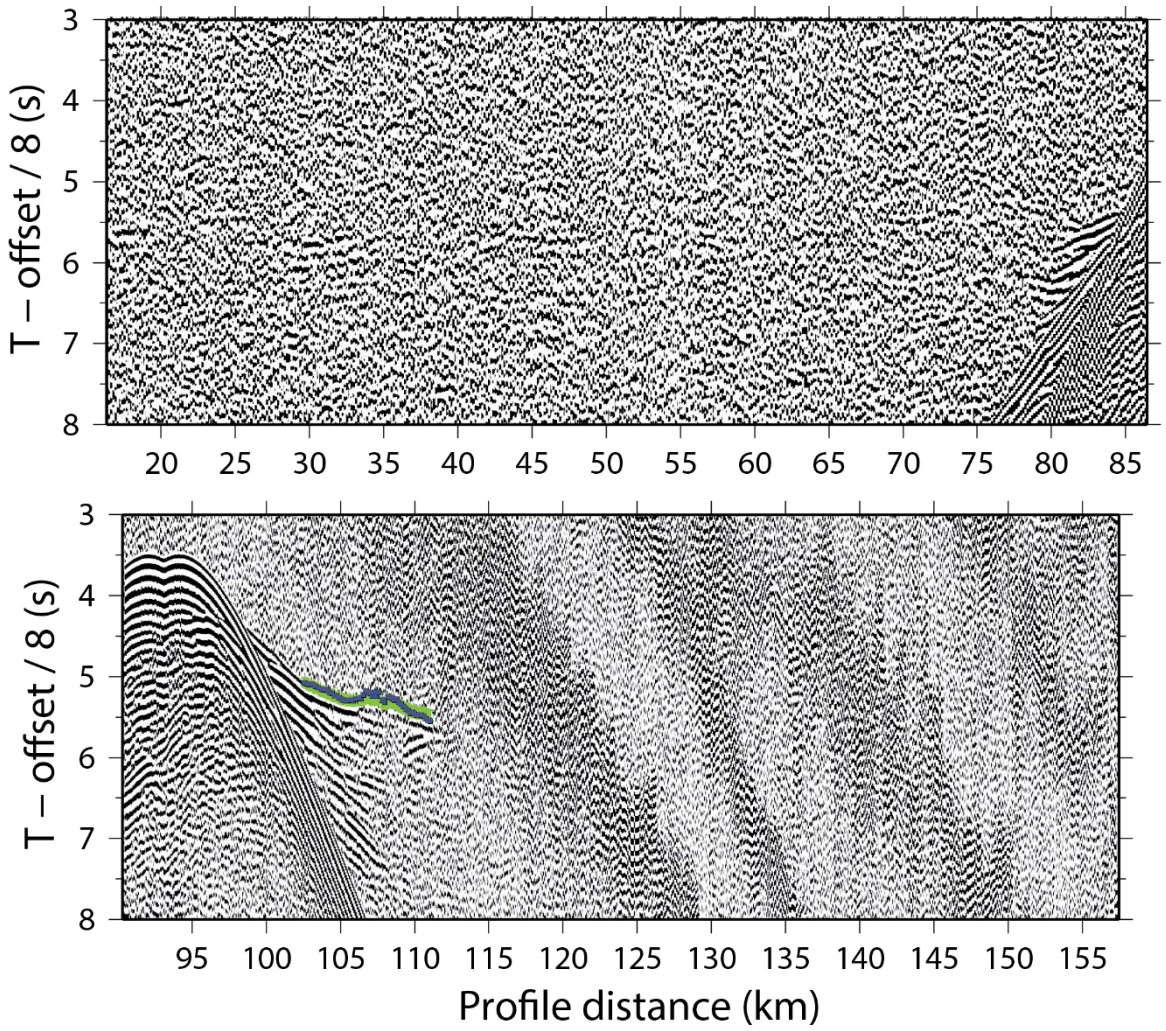

Figure B-6: Receiver gathers for OBS37. Travel-time picks are green lines, TOMO2D model fit is indicated by purple dots.

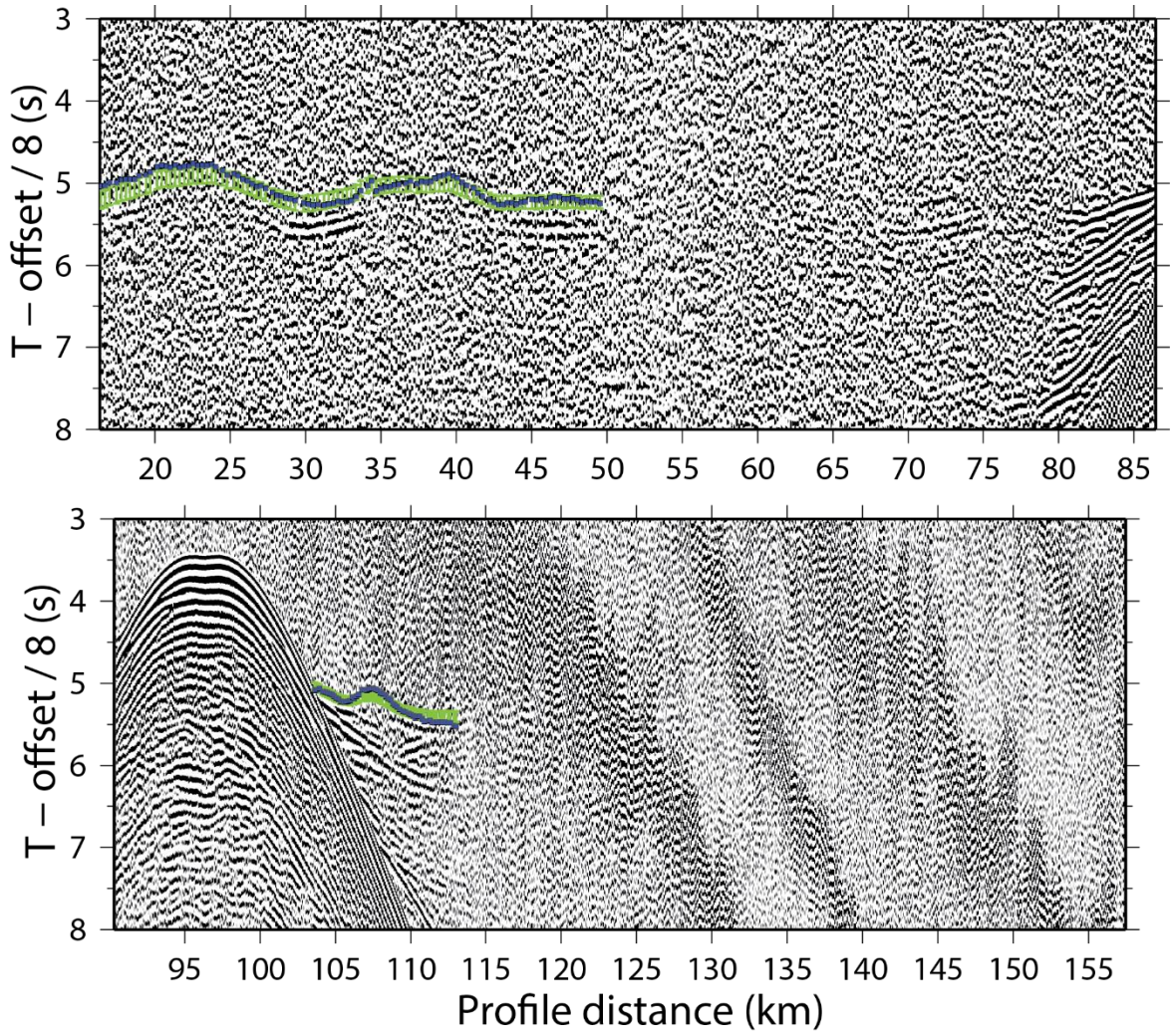

Figure B-7: Receiver gathers for OBS38. Travel-time picks are green lines, TOMO2D model fit is indicated by purple dots.

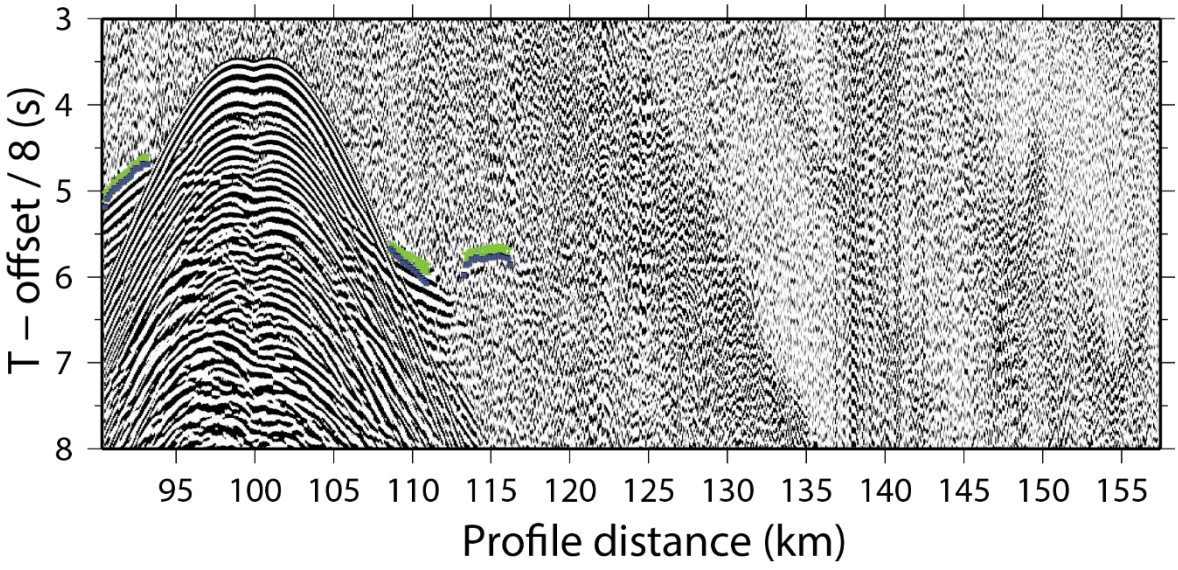

Figure B-8: Receiver gather for OBS39. Travel-time picks are green lines, TOMO2D model fit is indicated by purple dots.

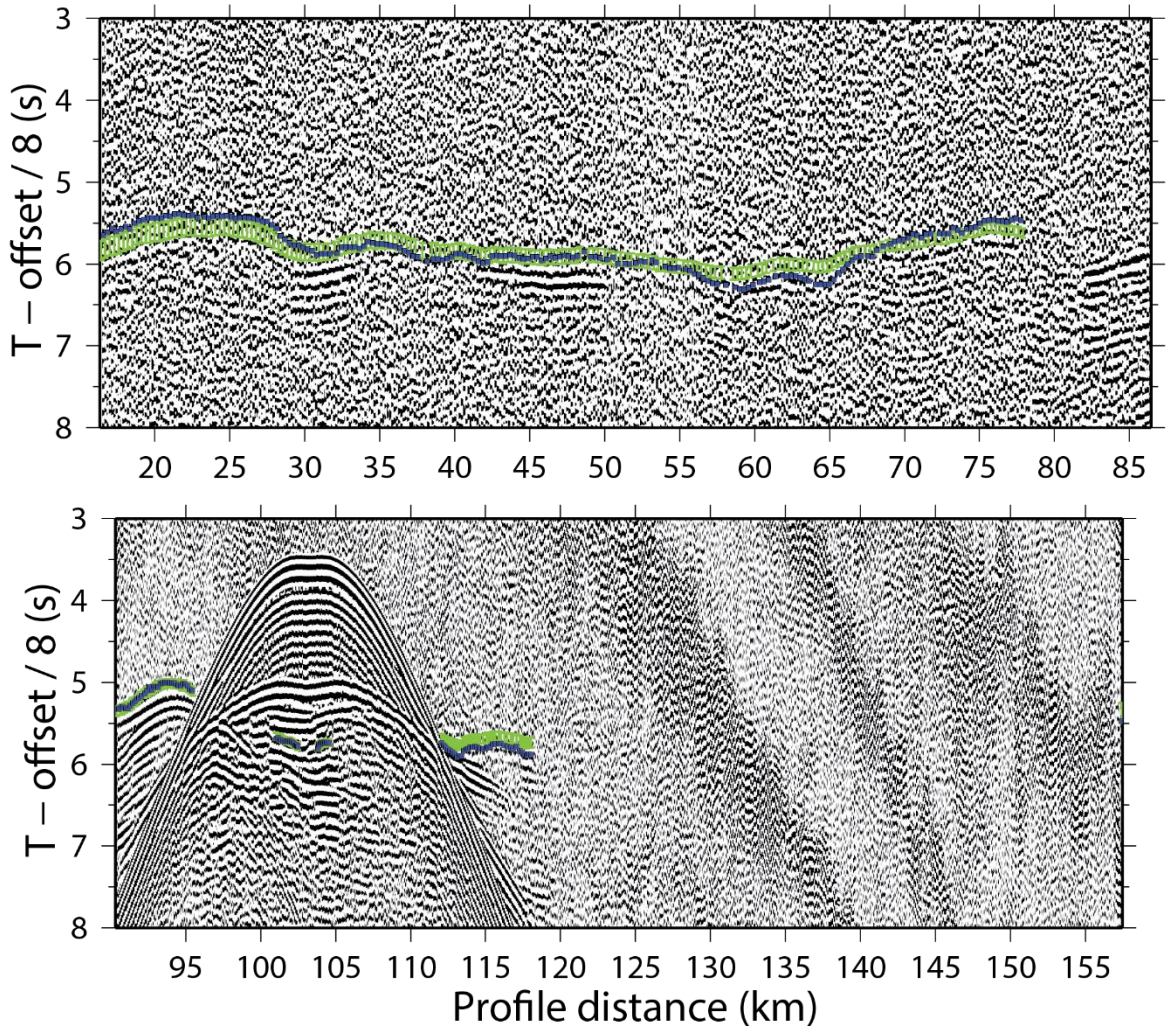

Figure B-9: Receiver gathers for OBS40. Travel-time picks are green lines, TOMO2D model fit is indicated by purple dots.

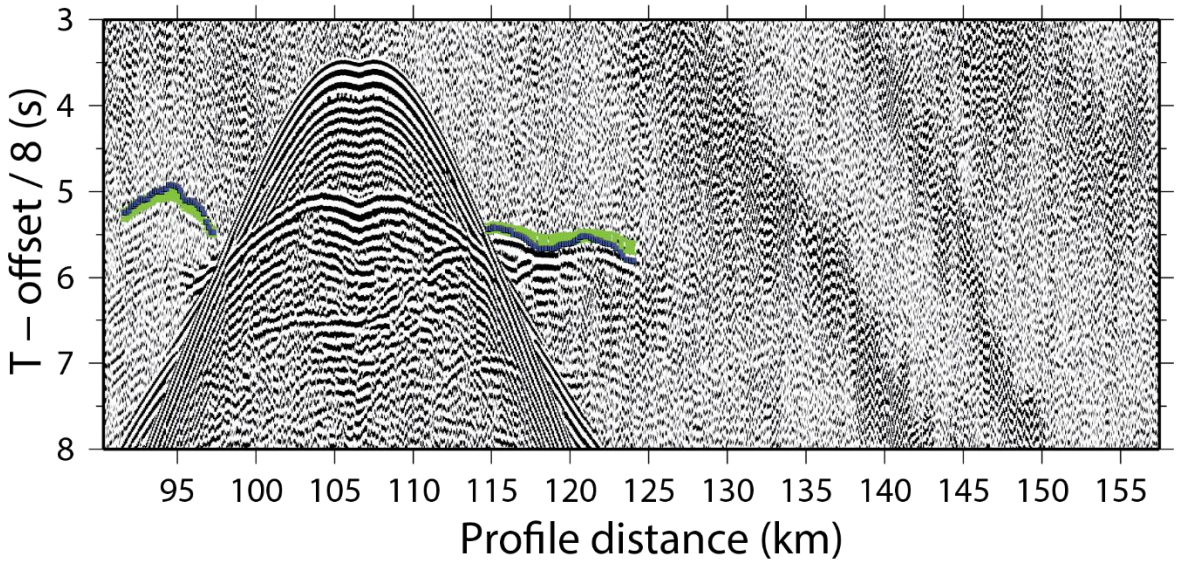

Figure B-10: Receiver gather for OBS41. Travel-time picks are green lines, TOMO2D model fit is indicated by purple dots.

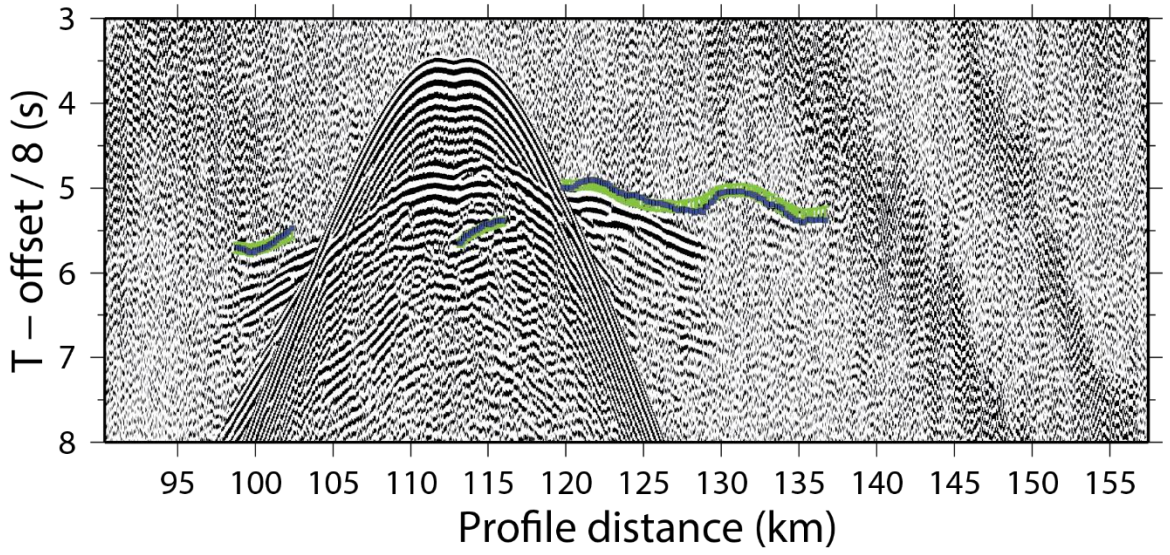

Figure B-11: *Receiver gather for OBS43. Travel-time picks are green lines, TOMO2D model fit is indicated by purple dots.*

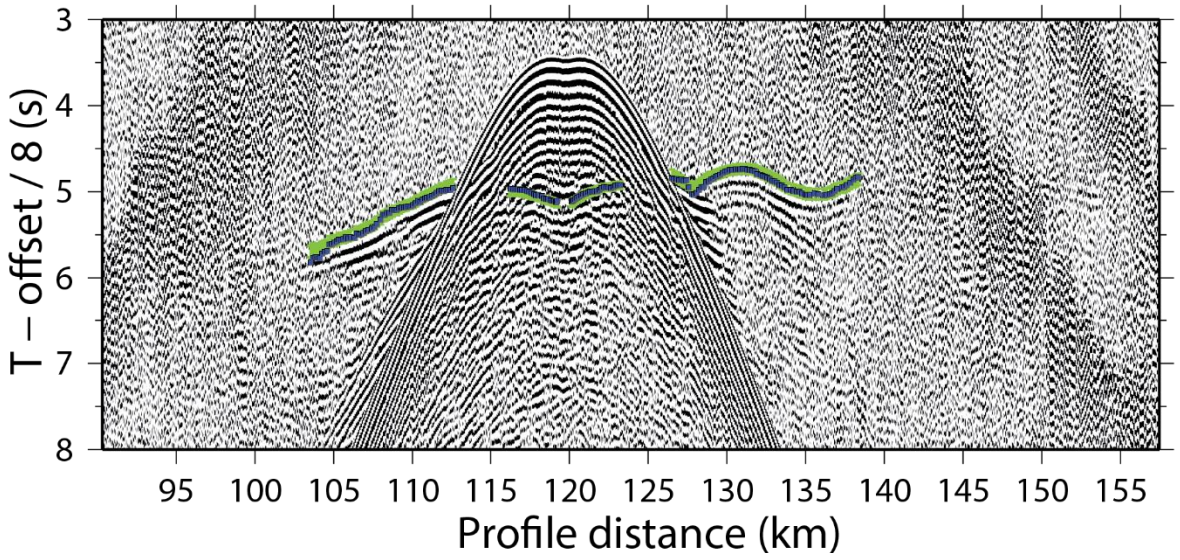

Figure B-12: *Receiver gather for OBS45. Travel-time picks are green lines, TOMO2D model fit is indicated by purple dots.*

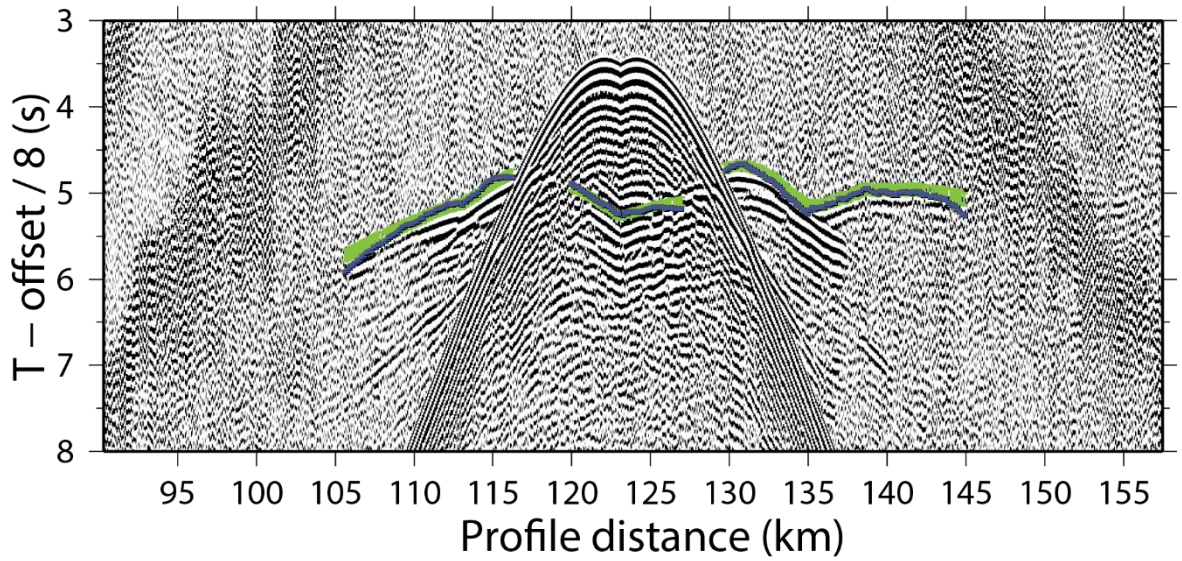

Figure B-13: Receiver gather for OBS46. Travel-time picks are green lines, TOMO2D model fit is indicated by purple dots.

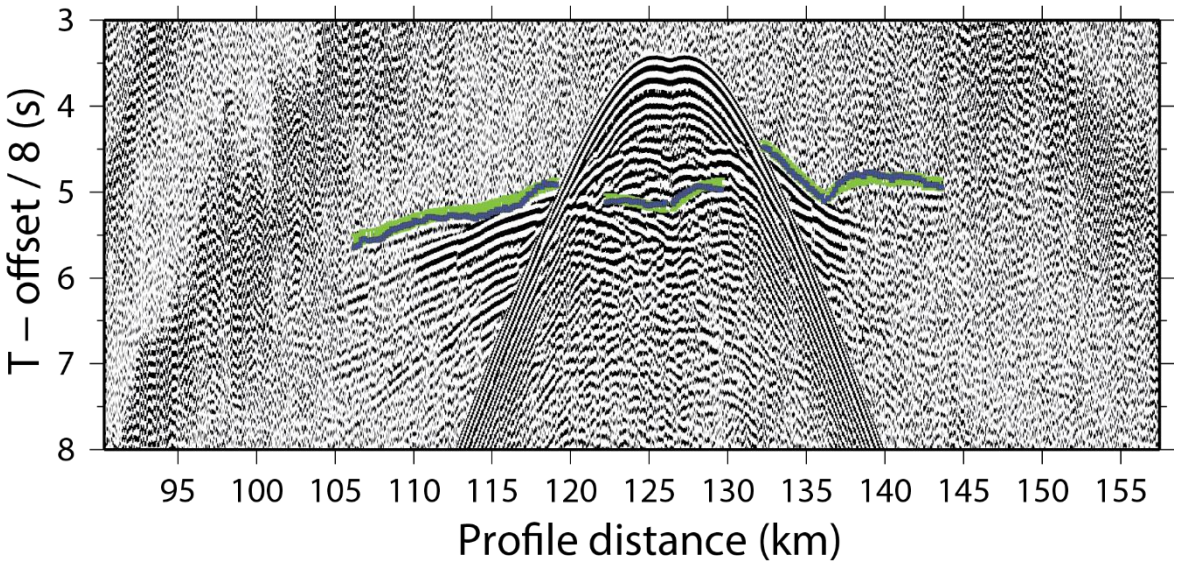

Figure B-14: Receiver gather for OBS47. Travel-time picks are green lines, TOMO2D model fit is indicated by purple dots.

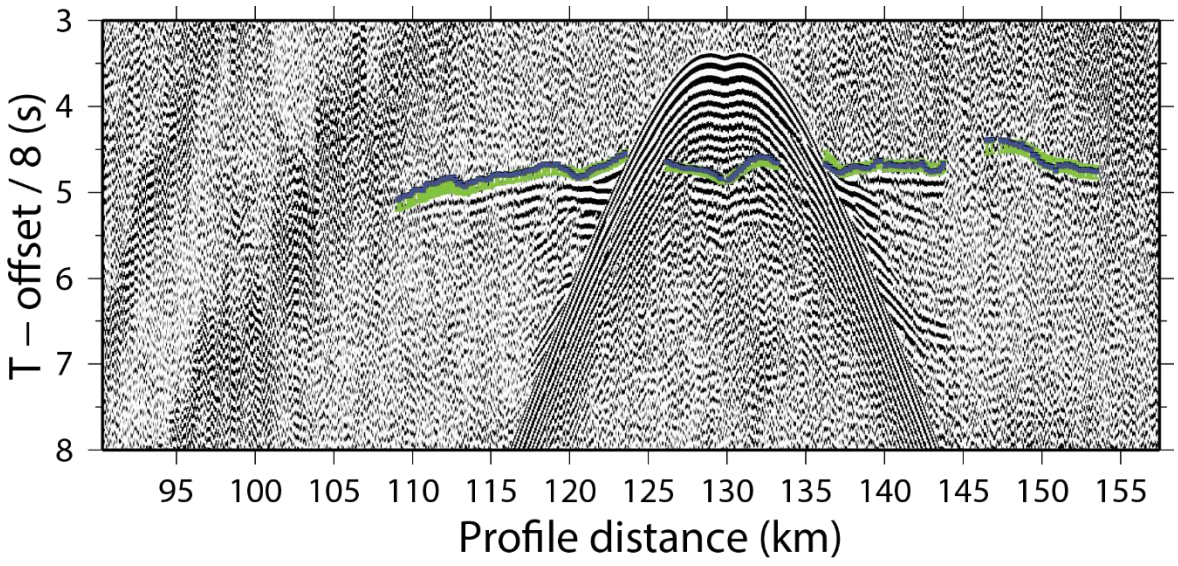

Figure B-15: Receiver gather for OBS48. Travel-time picks are green lines, TOMO2D model fit is indicated by purple dots.

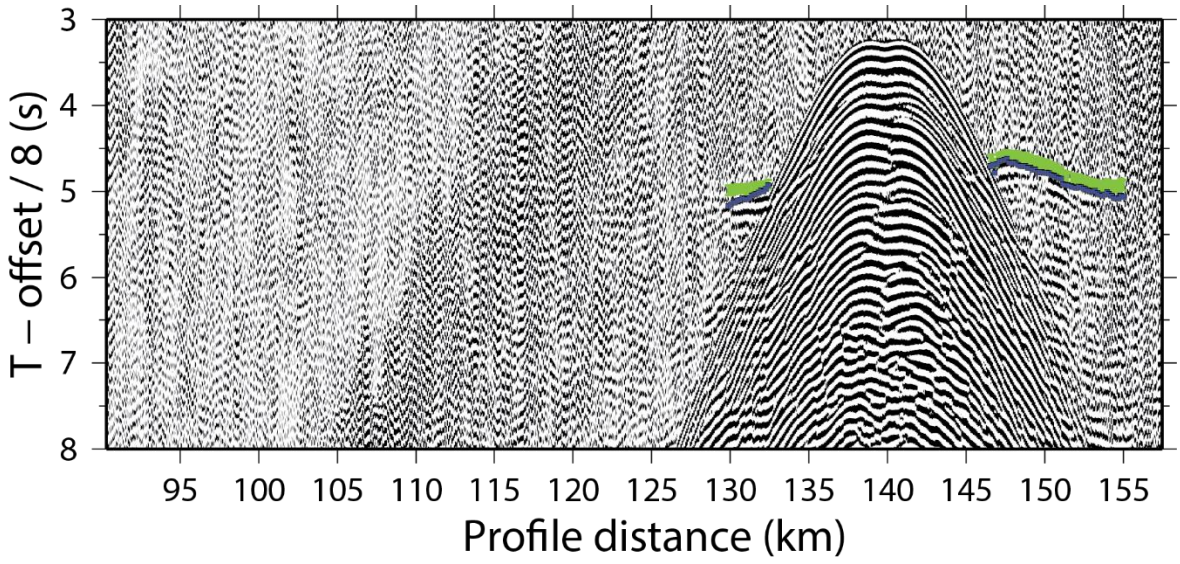

Figure B-16: Receiver gather for OBS51. Travel-time picks are green lines, TOMO2D model fit is indicated by purple dots.

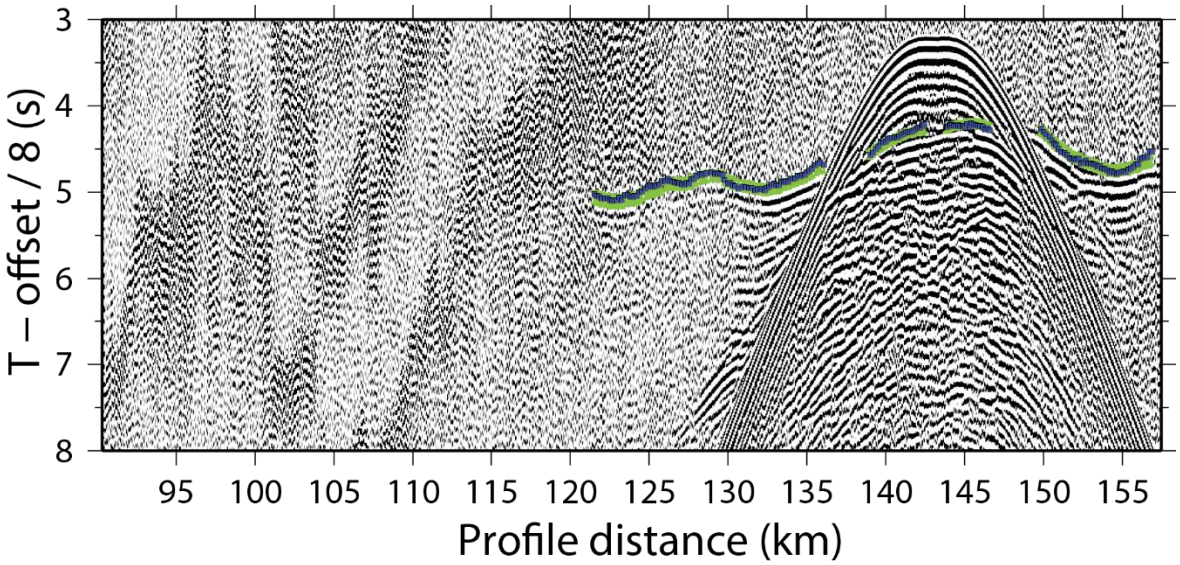

Figure B-17: Receiver gather for OBS52. Travel-time picks are green lines, TOMO2D model fit is indicated by purple dots.

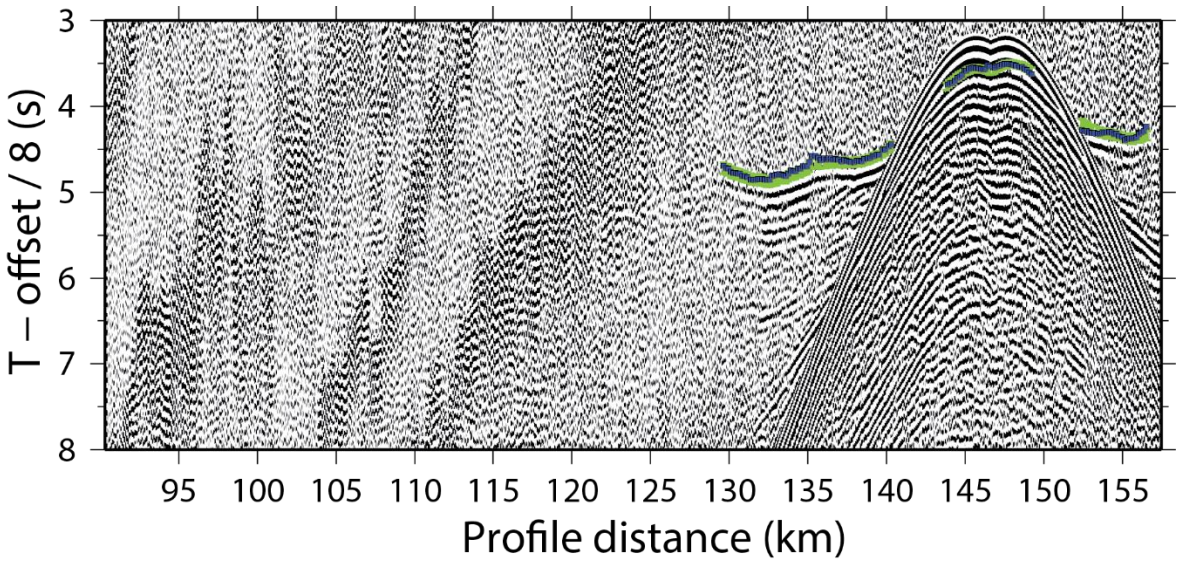

Figure B-18: Receiver gather for OBS53. Travel-time picks are green lines, TOMO2D model fit is indicated by purple dots.

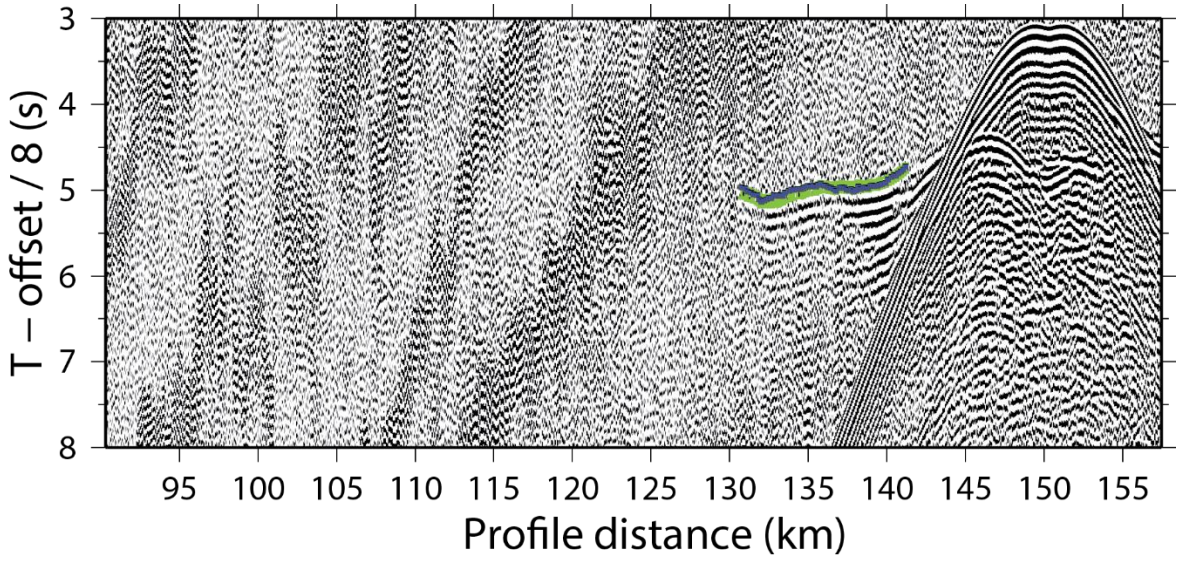

Figure B-19: Receiver gather for OBS54. Travel-time picks are green lines, TOMO2D model fit is indicated by purple dots.

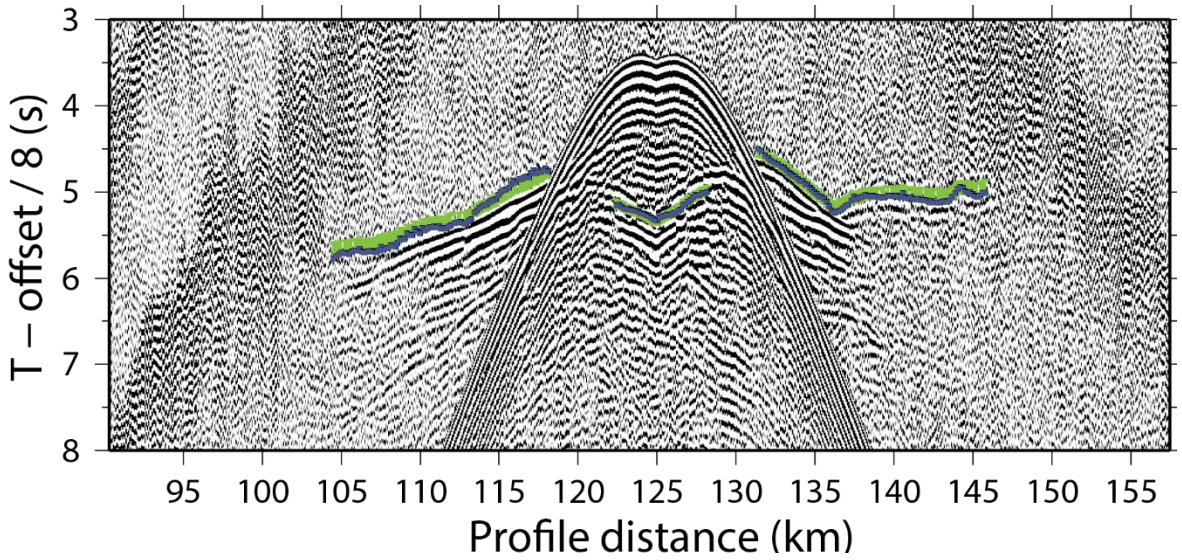

Figure B-20: Receiver gather for OBH79. Travel-time picks are green lines, TOMO2D model fit is indicated by purple dots.

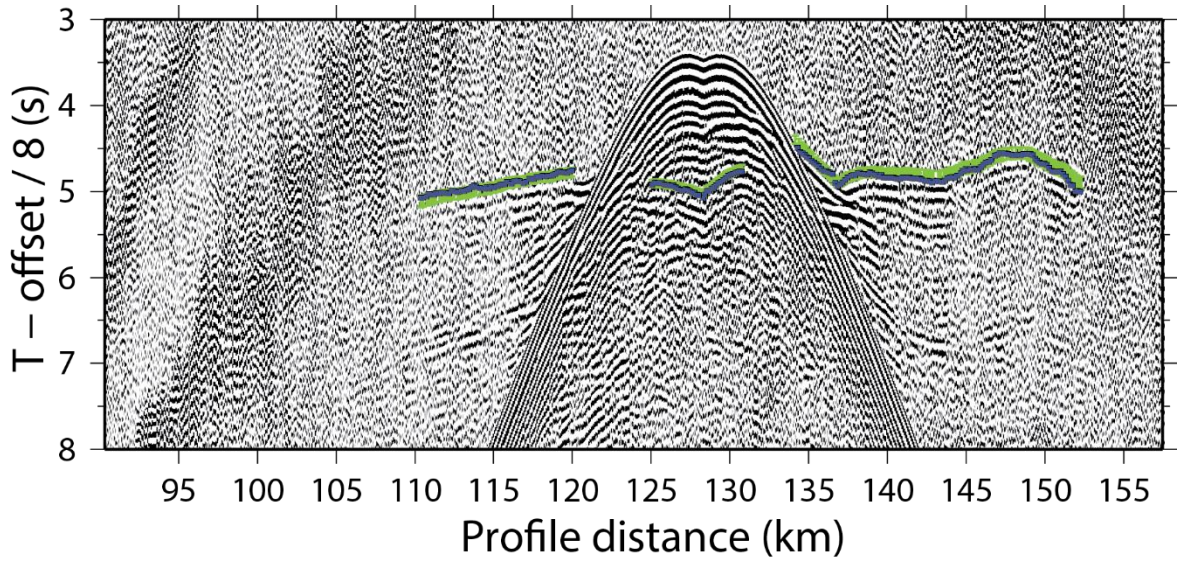

Figure B-21: Receiver gather for OBH80. Travel-time picks are green lines, TOMO2D model fit is indicated by purple dots.

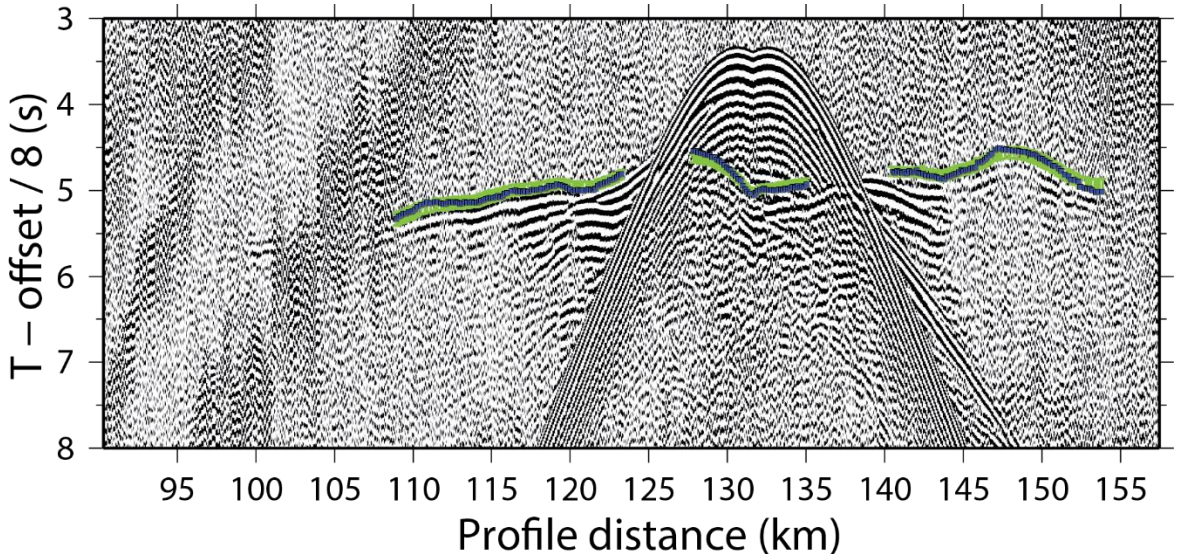

Figure B-22: Receiver gather for OBH81. Travel-time picks are green lines, TOMO2D model fit is indicated by purple dots.

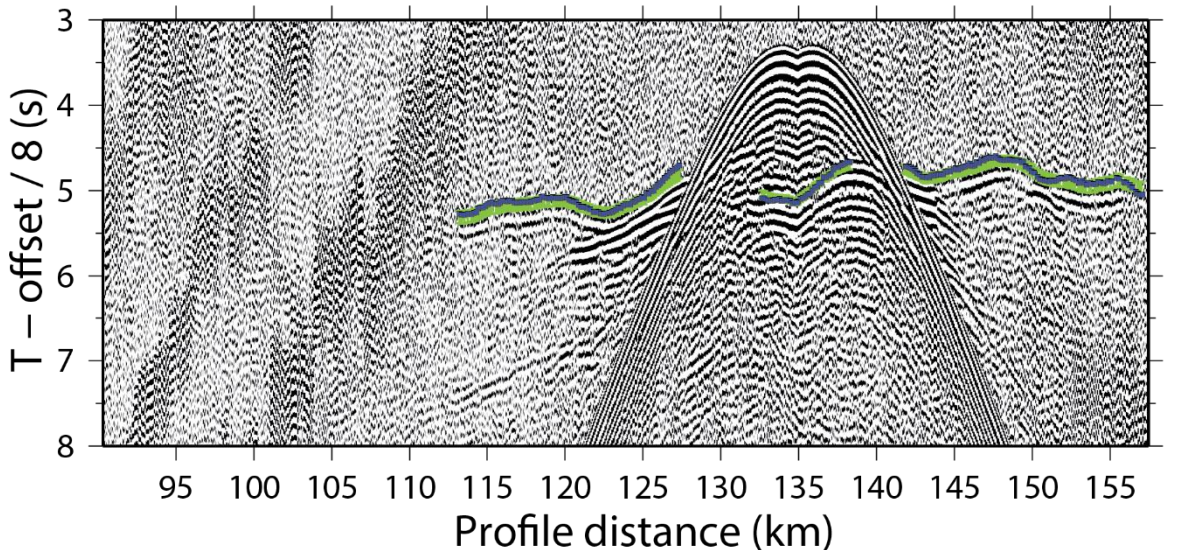

Figure B-23: Receiver gather for OBH82. Travel-time picks are green lines, TOMO2D model fit is indicated by purple dots.

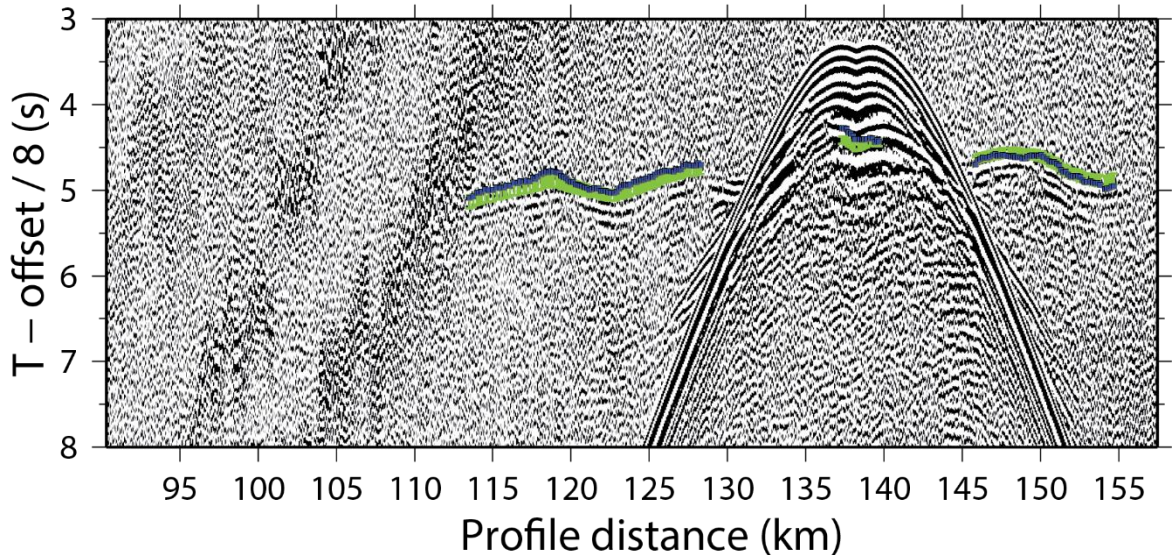

Figure B-24: Receiver gather for OBH83. Travel-time picks are green lines, TOMO2D model fit is indicated by purple dots.

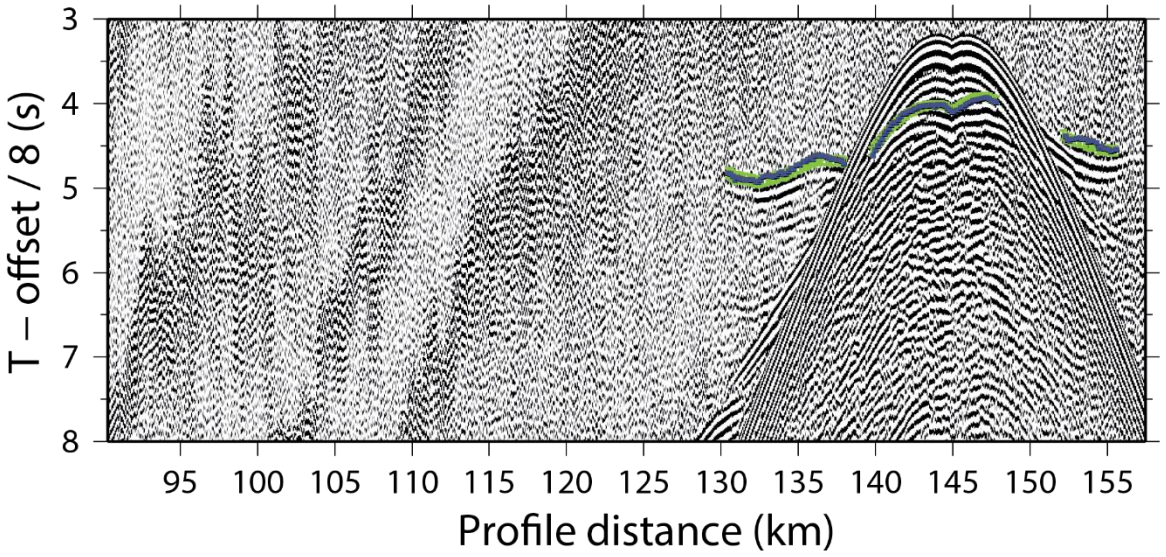

Figure B-25: Receiver gather for OBH85. Travel-time picks are green lines, TOMO2D model fit is indicated by purple dots.

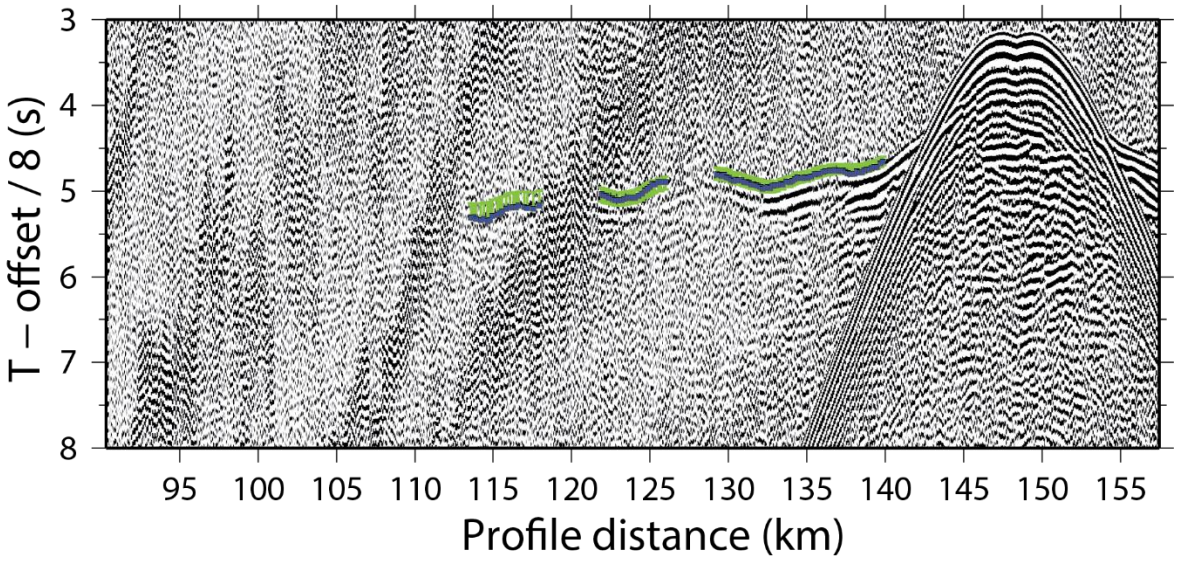

Figure B-26: Receiver gather for OBH86. Travel-time picks are green lines, TOMO2D model fit is indicated by purple dots.

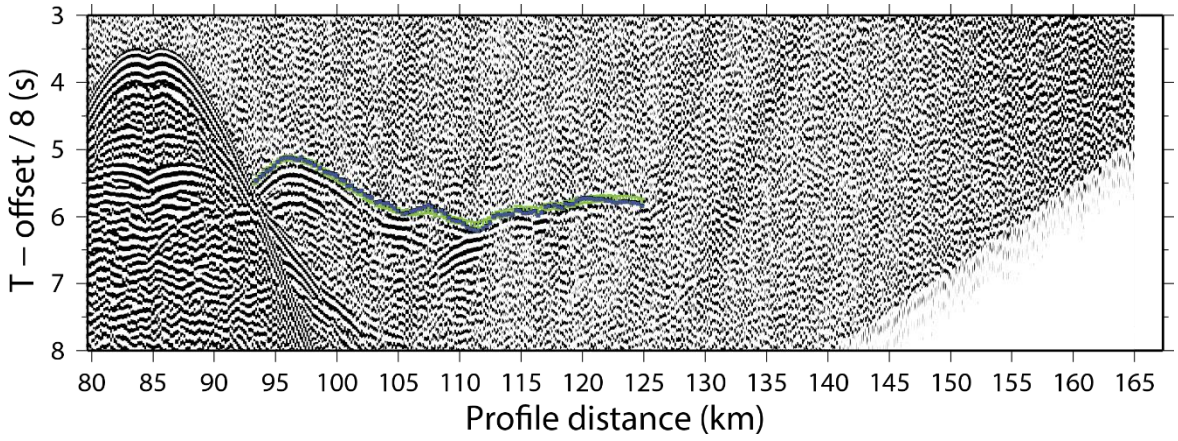

Figure B-27: Receiver gather for GEO101. Travel-time picks are green lines, TOMO2D model fit is indicated by purple dots.

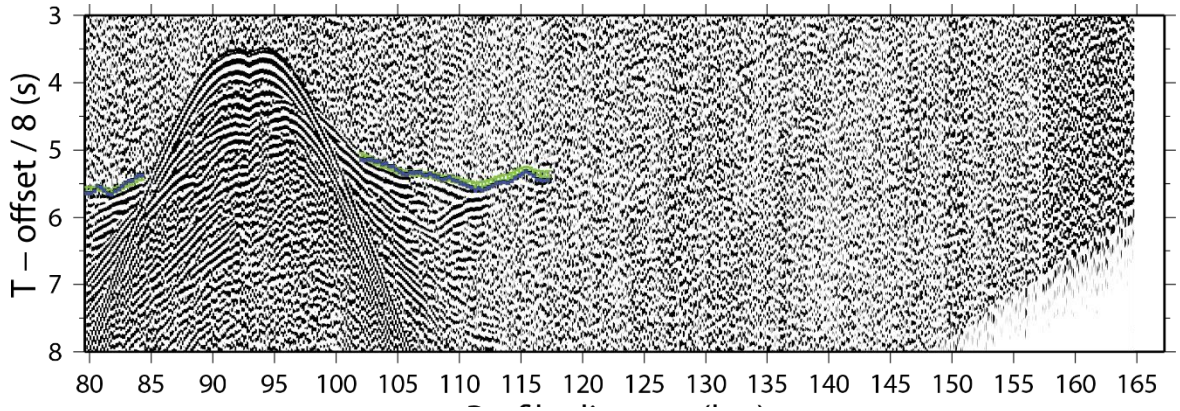

Figure B-28: Receiver gather for GEO102. Travel-time picks are green lines, TOMO2D model fit is indicated by purple dots.

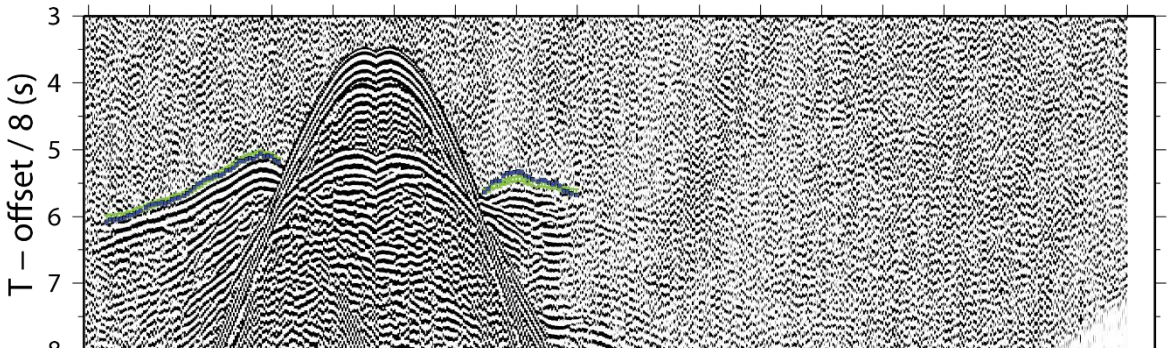

Figure B-29: Receiver gather for GEO103. Travel-time picks are green lines, TOMO2D model fit is indicated by purple dots.

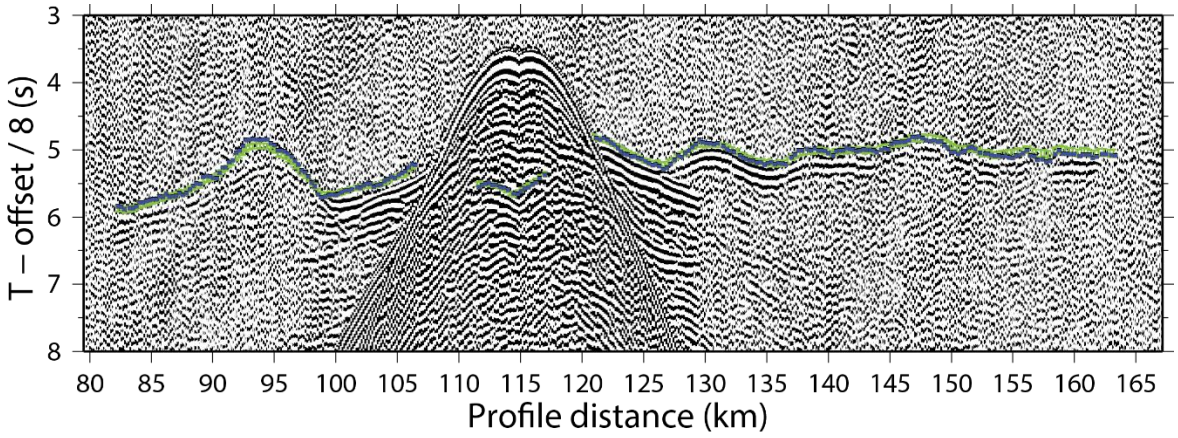

Figure B-30: Receiver gather for GEO104. Travel-time picks are green lines, TOMO2D model fit is indicated by purple dots.

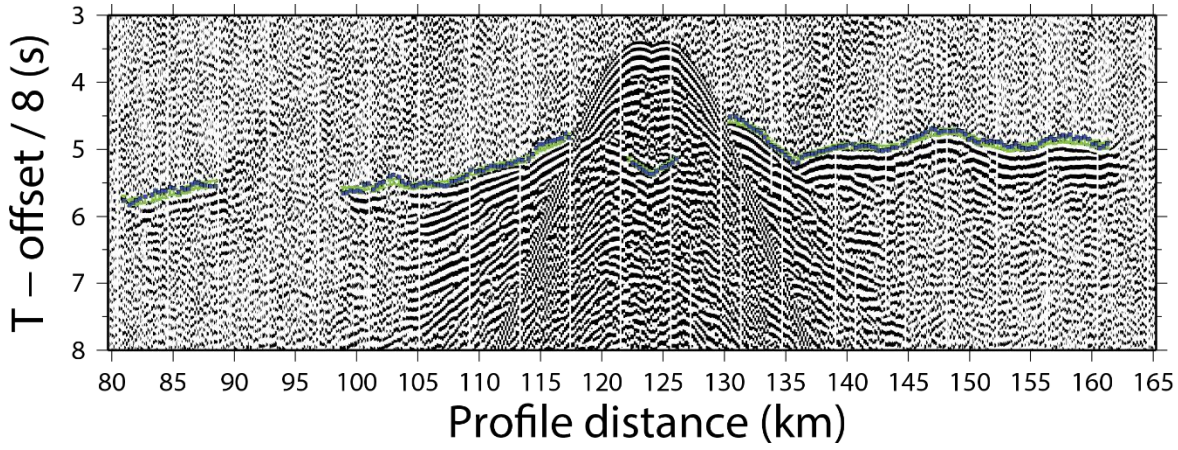

Figure B-31: Receiver gather for Ute106. Travel-time picks are green lines, TOMO2D model fit is indicated by purple dots.

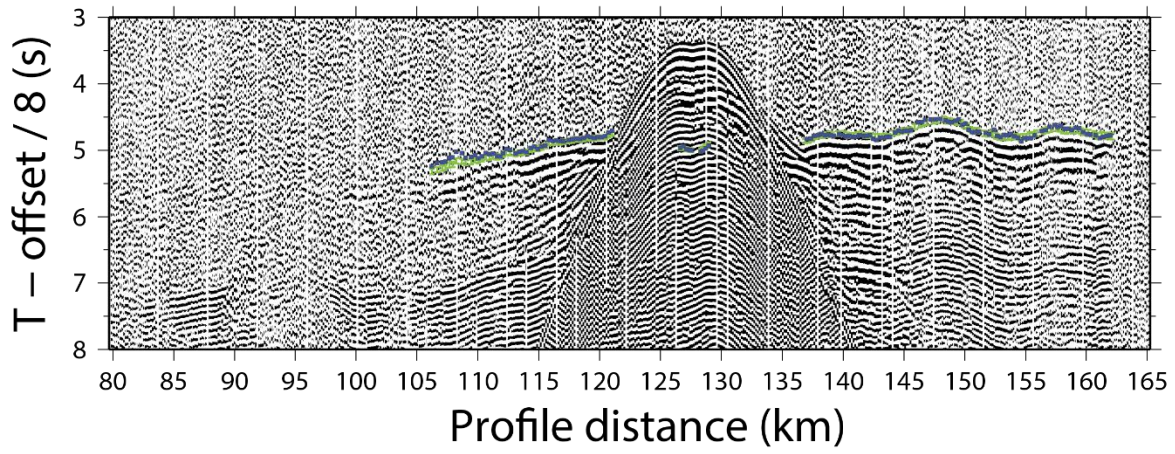

Figure B-32: Receiver gather for Ute107. Travel-time picks are green lines, TOMO2D model fit is indicated by purple dots.

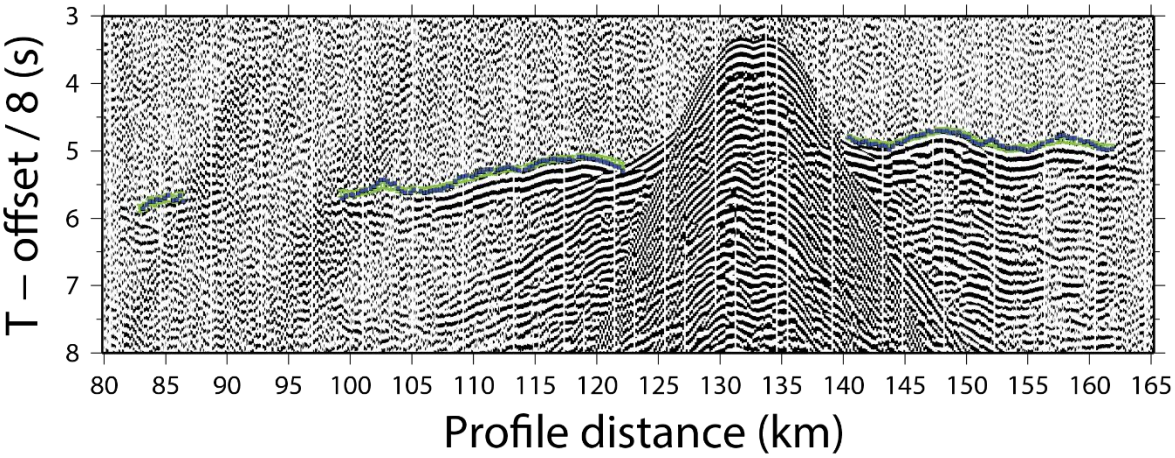

Figure B-33: Receiver gather for Ute108. Travel-time picks are green lines, TOMO2D model fit is indicated by purple dots.

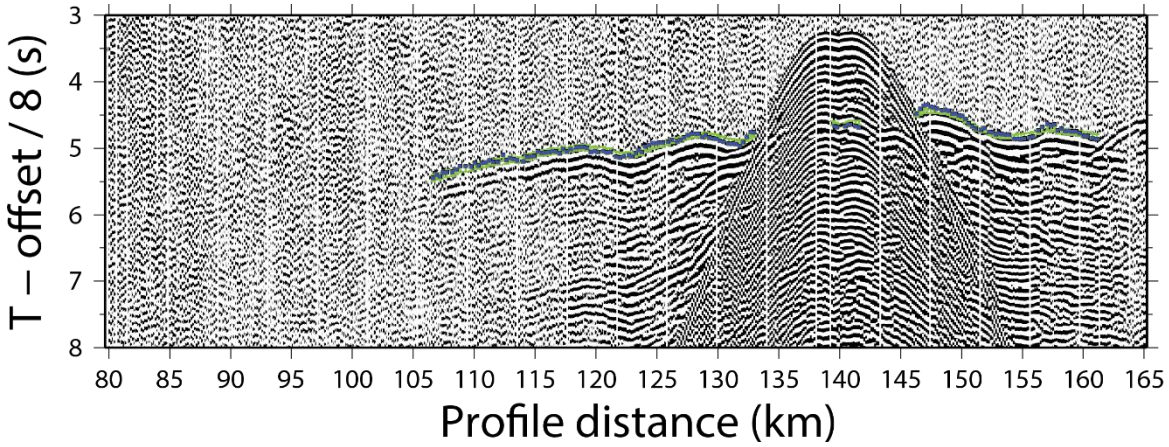

Figure B-34: Receiver gather for UTe109. Travel-time picks are green lines, TOMO2D model fit is indicated by purple dots.

Appendix C

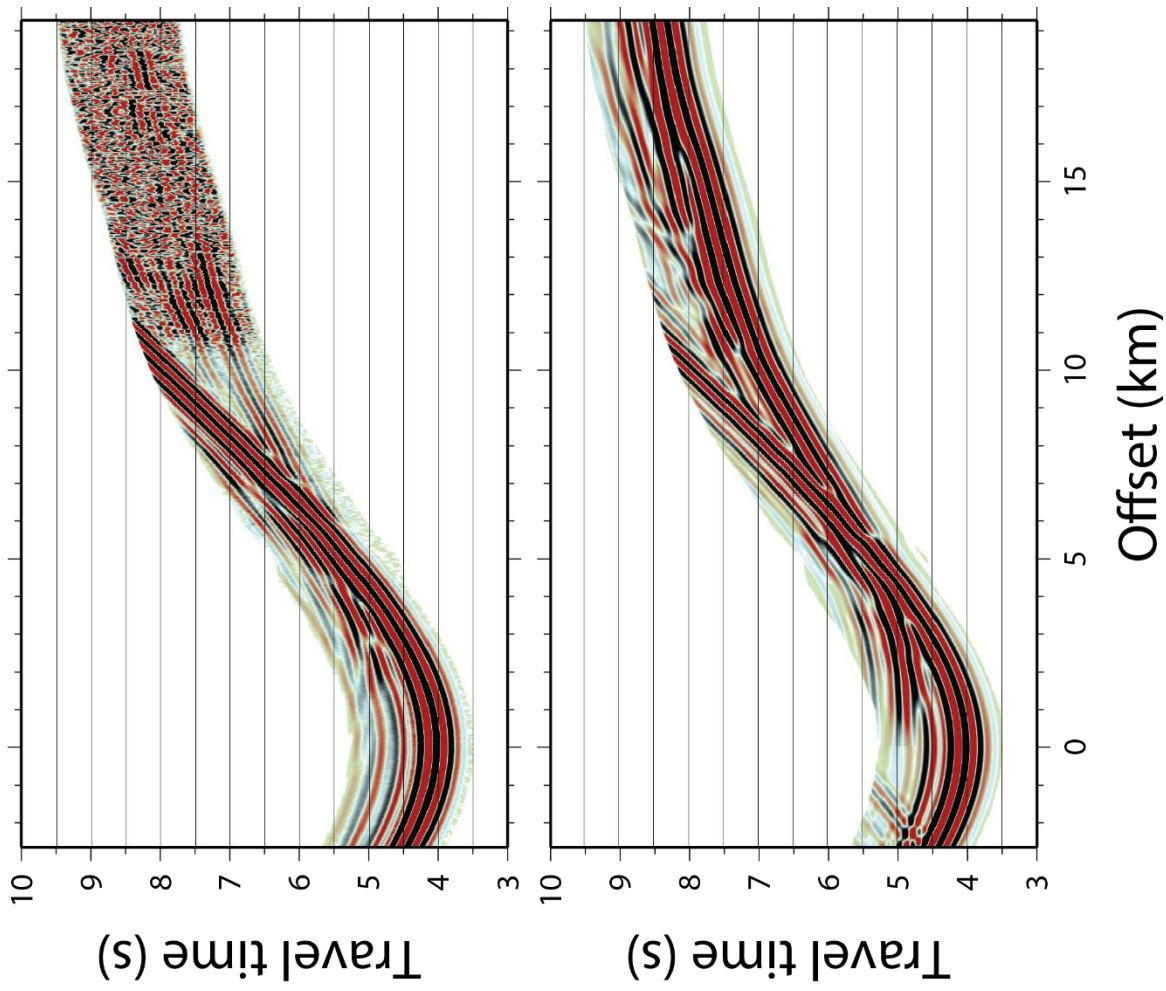

Figure C-1: Above: observed receiver gather for OBS37. Below: synthetic receiver gather for OBS37 through final FWI model.

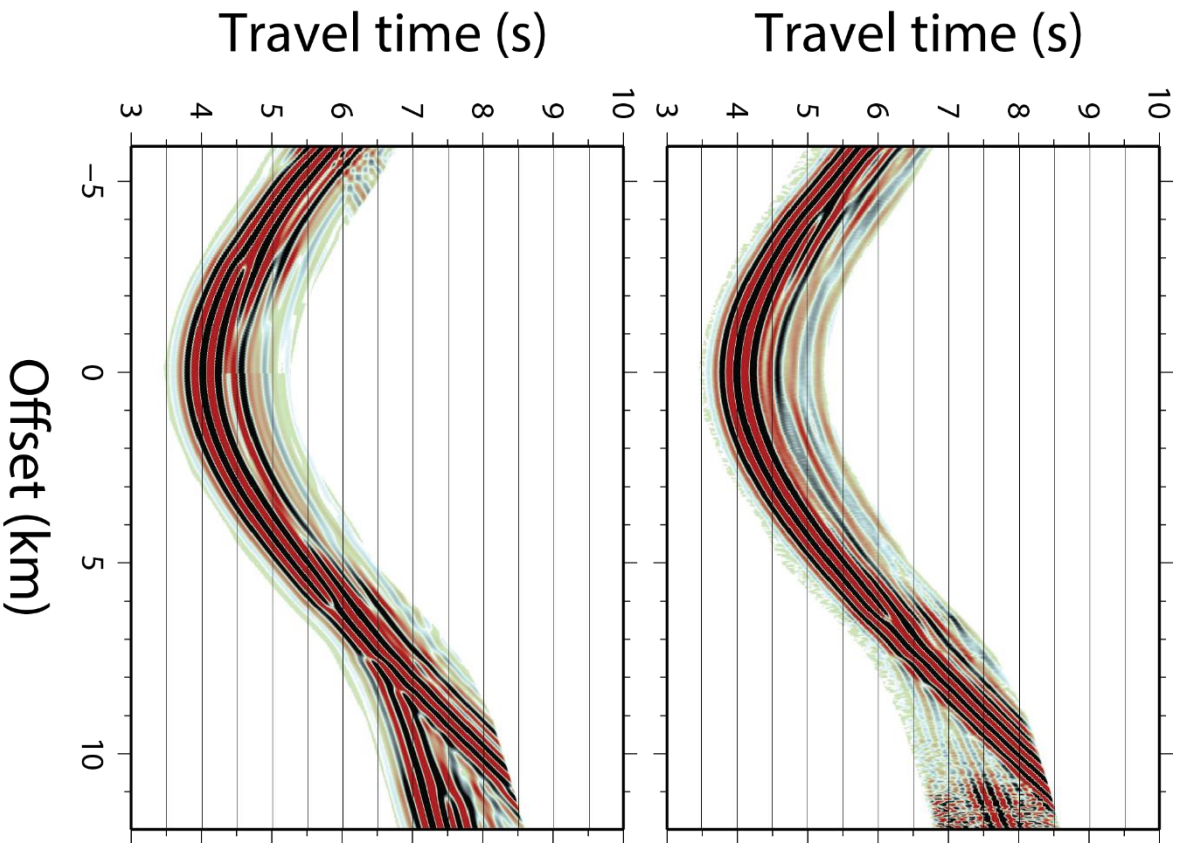

Figure C-2: Above: observed receiver gather for OBS38. Below: synthetic receiver gather for OBS38 through final FWI model.

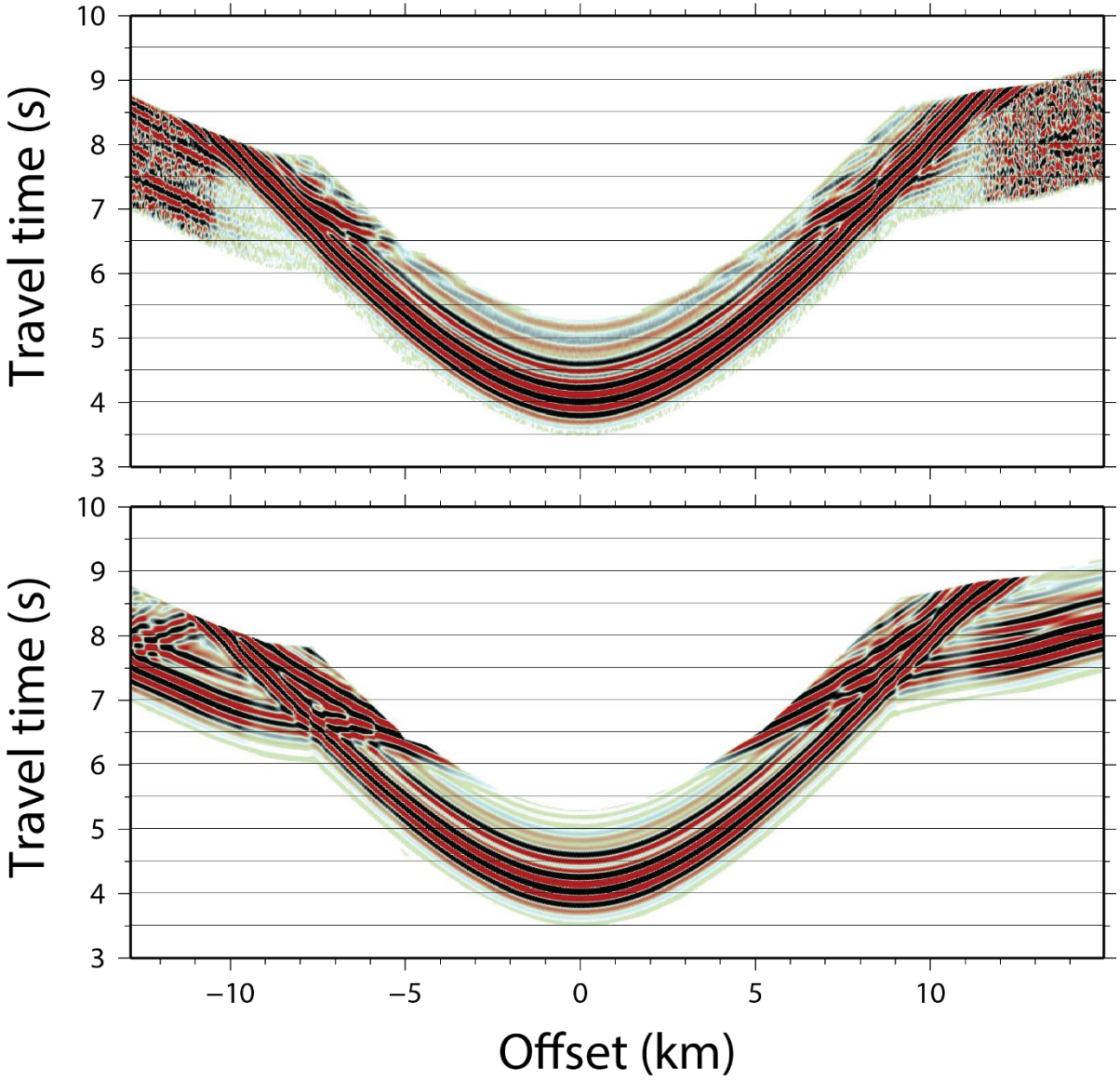

Figure C-3: Above: observed receiver gather for OBS40. Below: synthetic receiver gather for OBS40 through final FWI model.

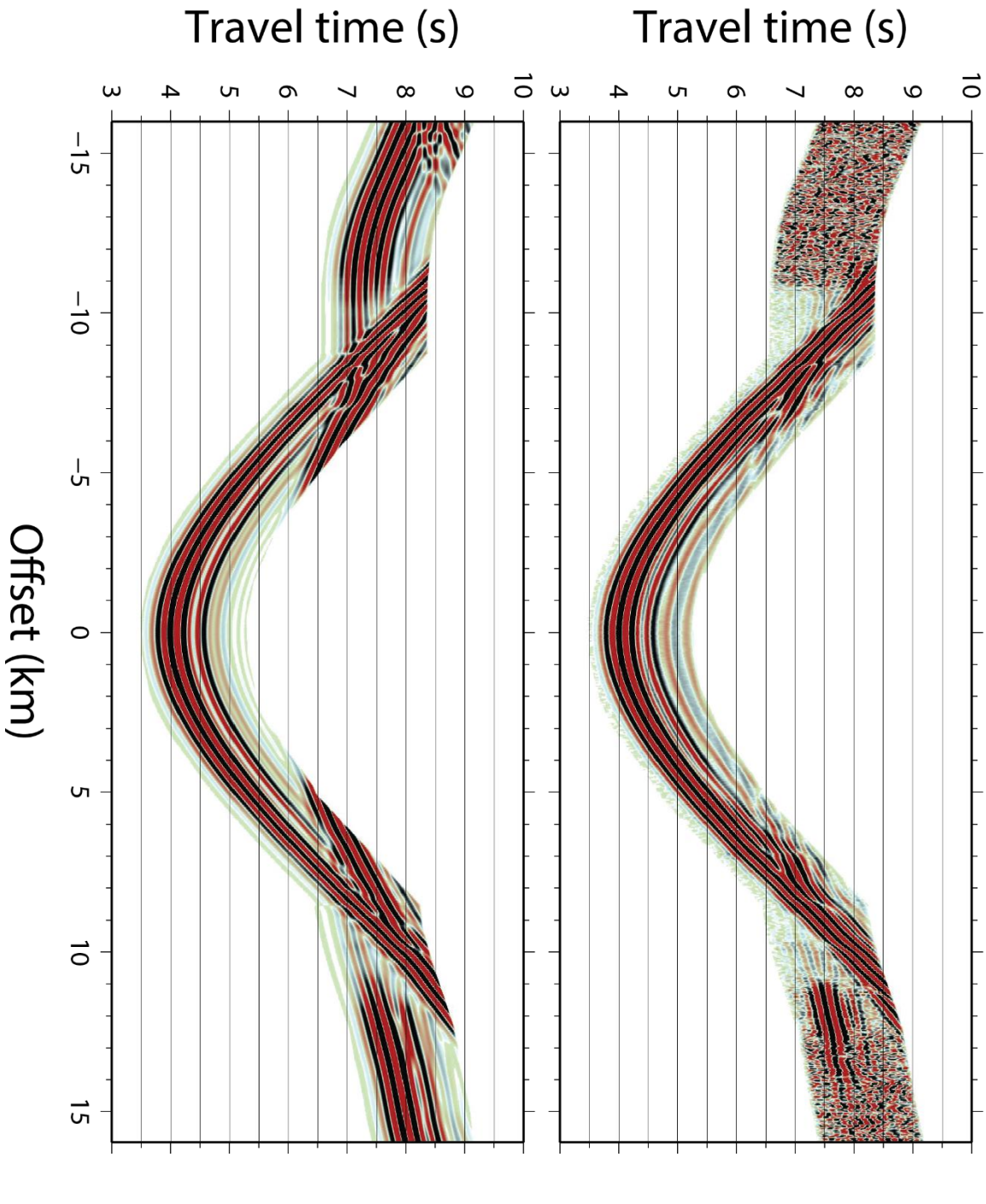

Figure C-4: Above: observed receiver gather for OBS41. Below: synthetic receiver gather for OBS41 through final FWI model.

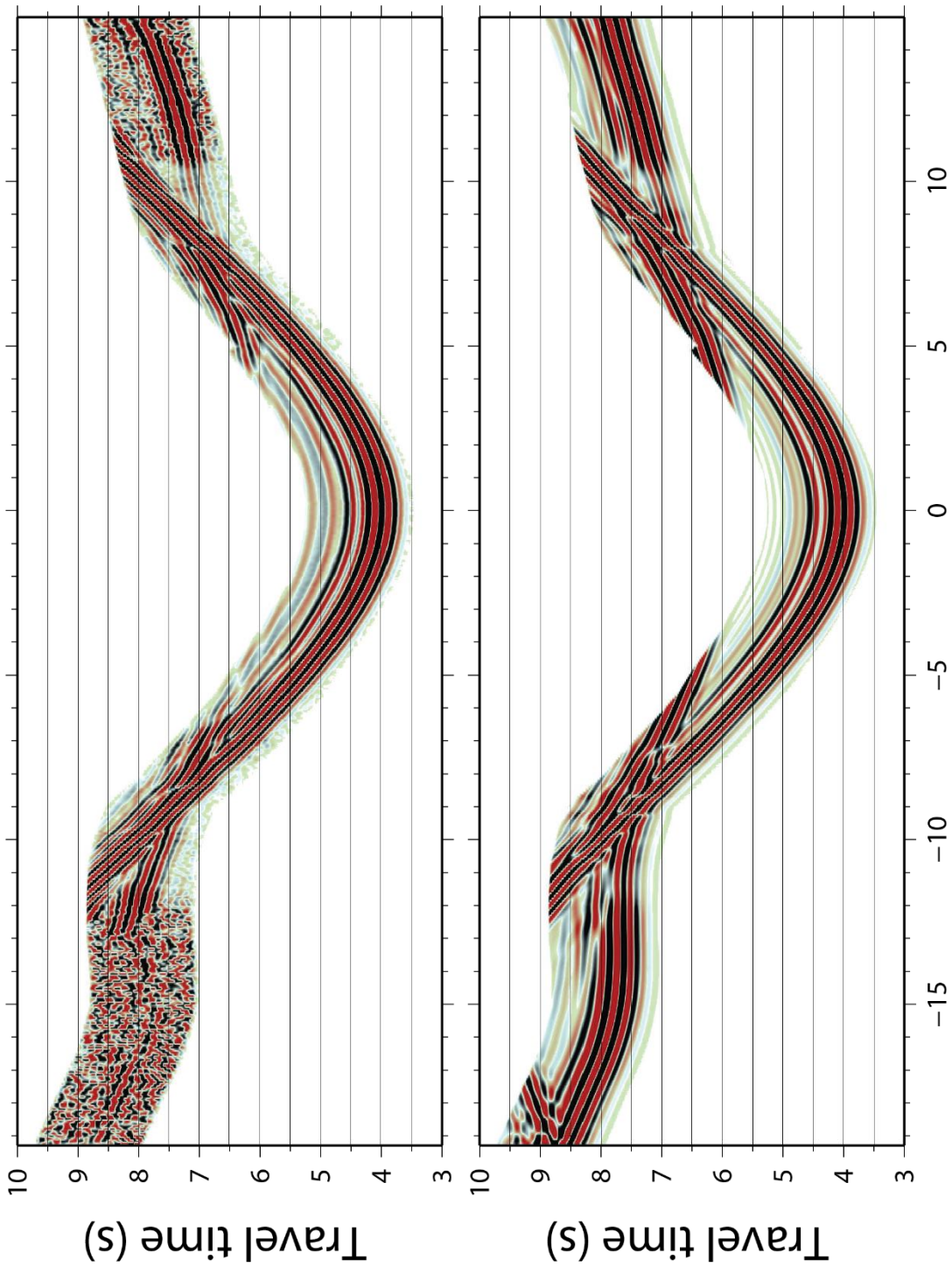

Figure C-5: Above: observed receiver gather for OBS42. Below: synthetic receiver gather for OBS42 through final FWI model.

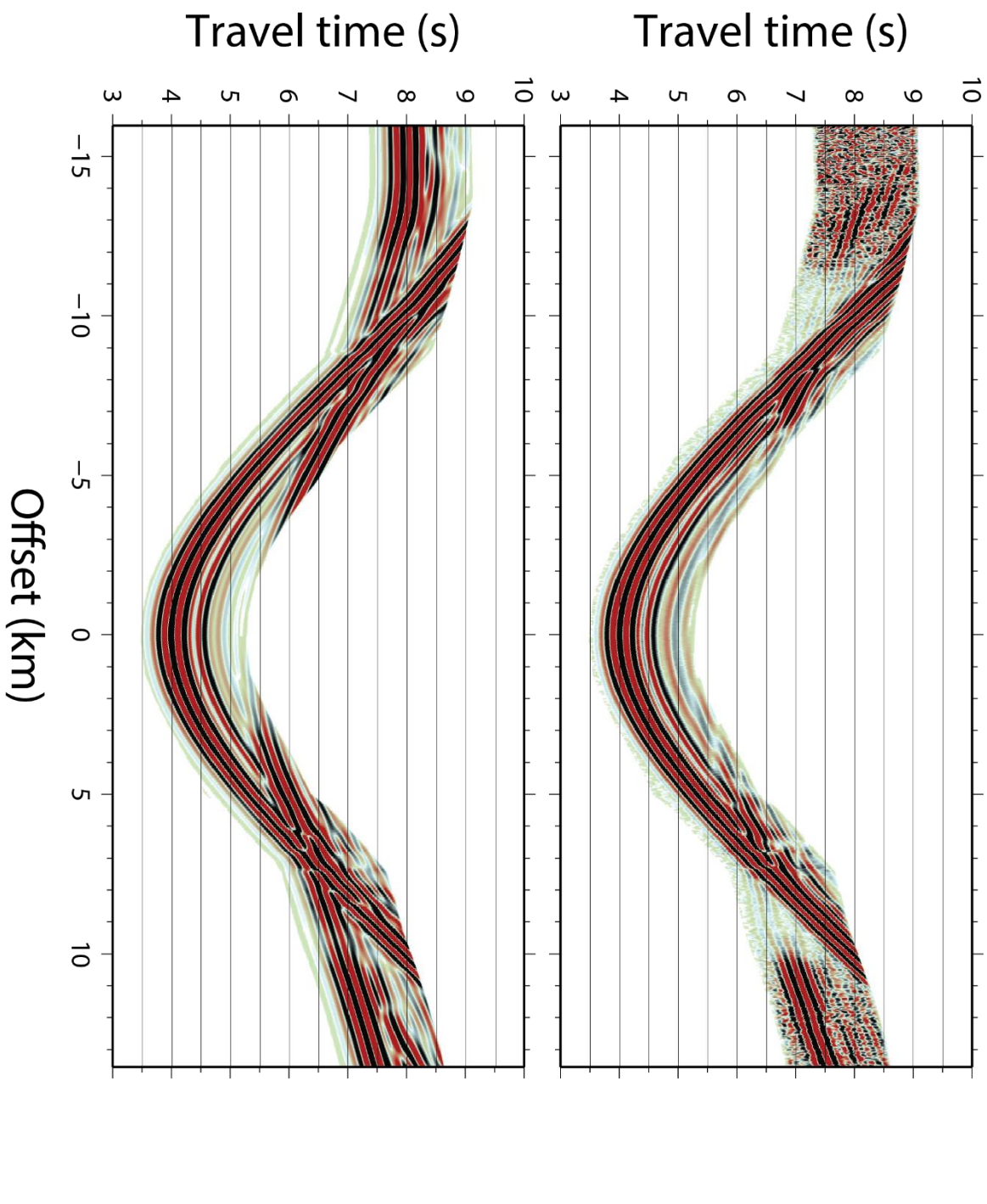

Figure C-6: Above: observed receiver gather for OBS43. Below: synthetic receiver gather for OBS43 through final FWI model.

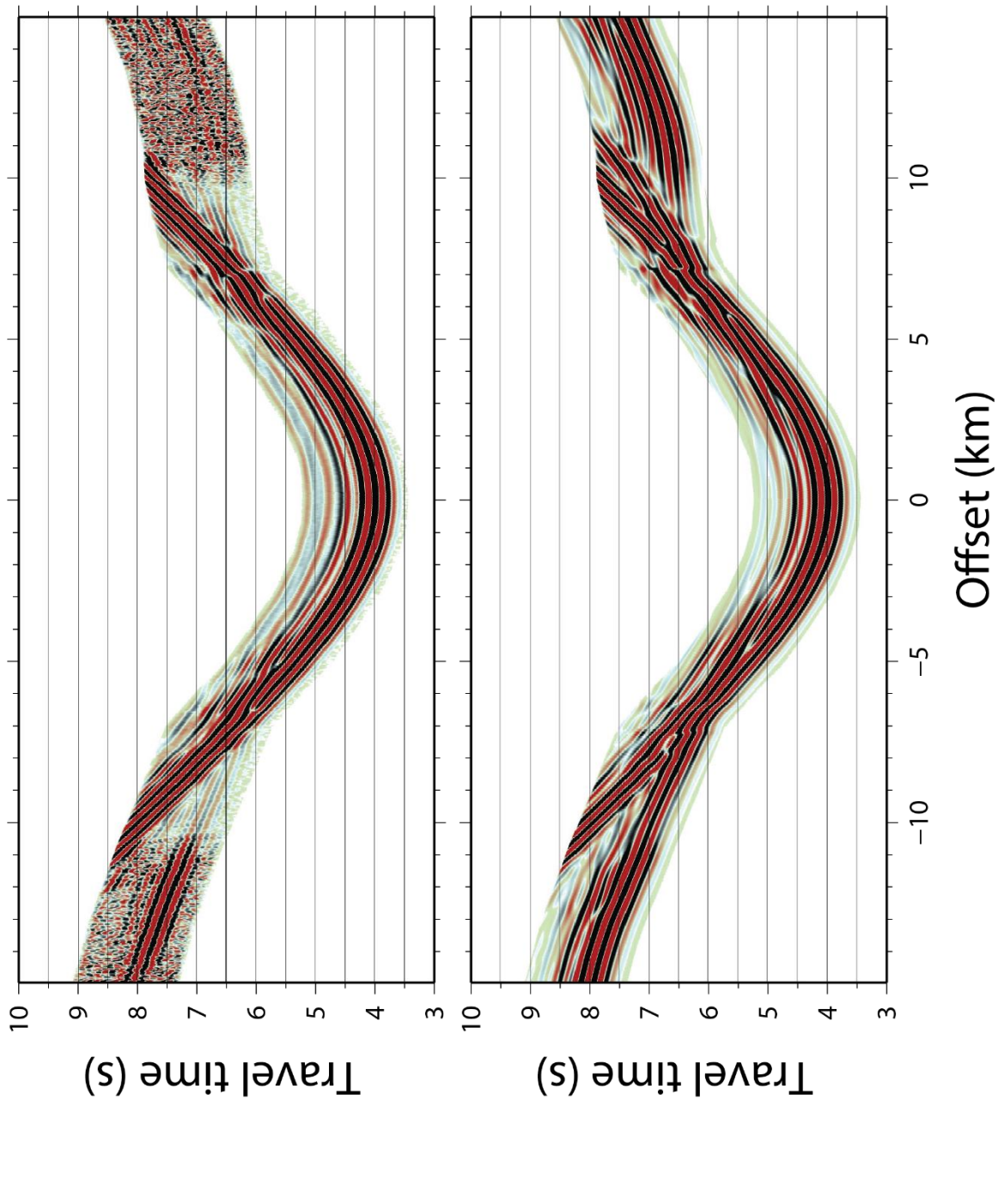

Figure C-7: Above: observed receiver gather for OBS45. Below: synthetic receiver gather for OBS45 through final FWI model.

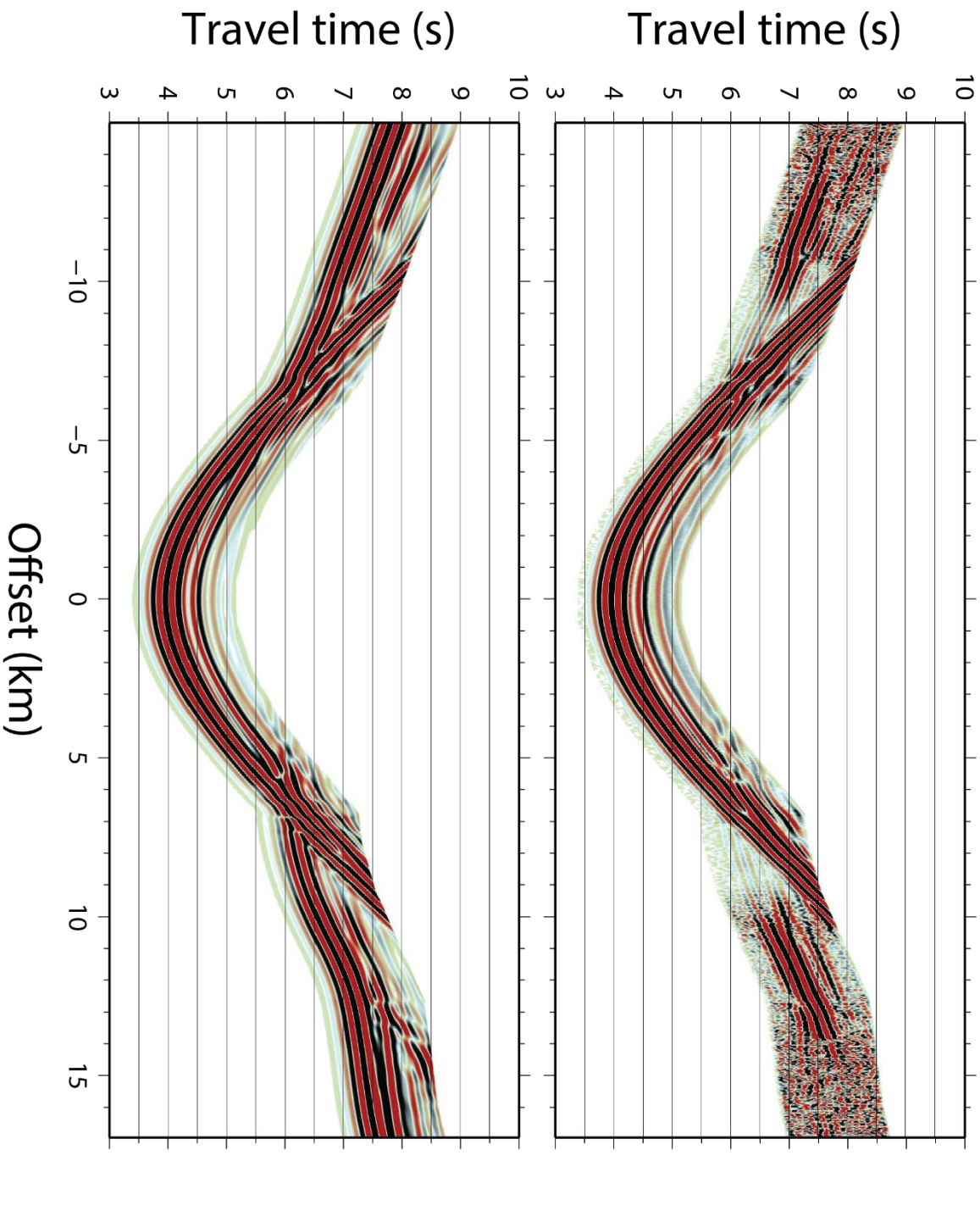

Figure C-8: Above: observed receiver gather for OBS46. Below: synthetic receiver gather for OBS46 through final FWI model.

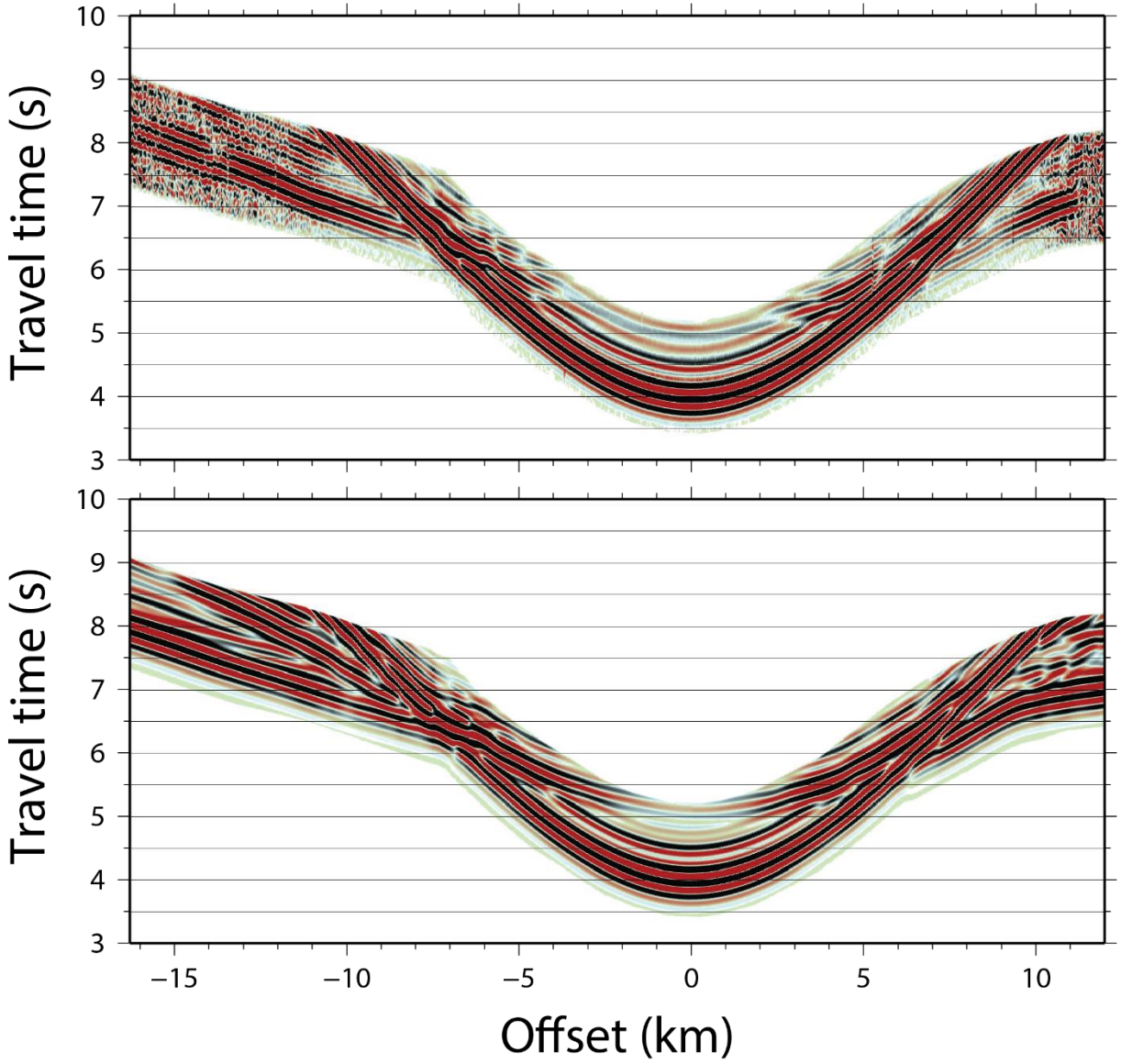

Figure C-9: Above: observed receiver gather for OBS47. Below: synthetic receiver gather for OBS47 through final FWI model.

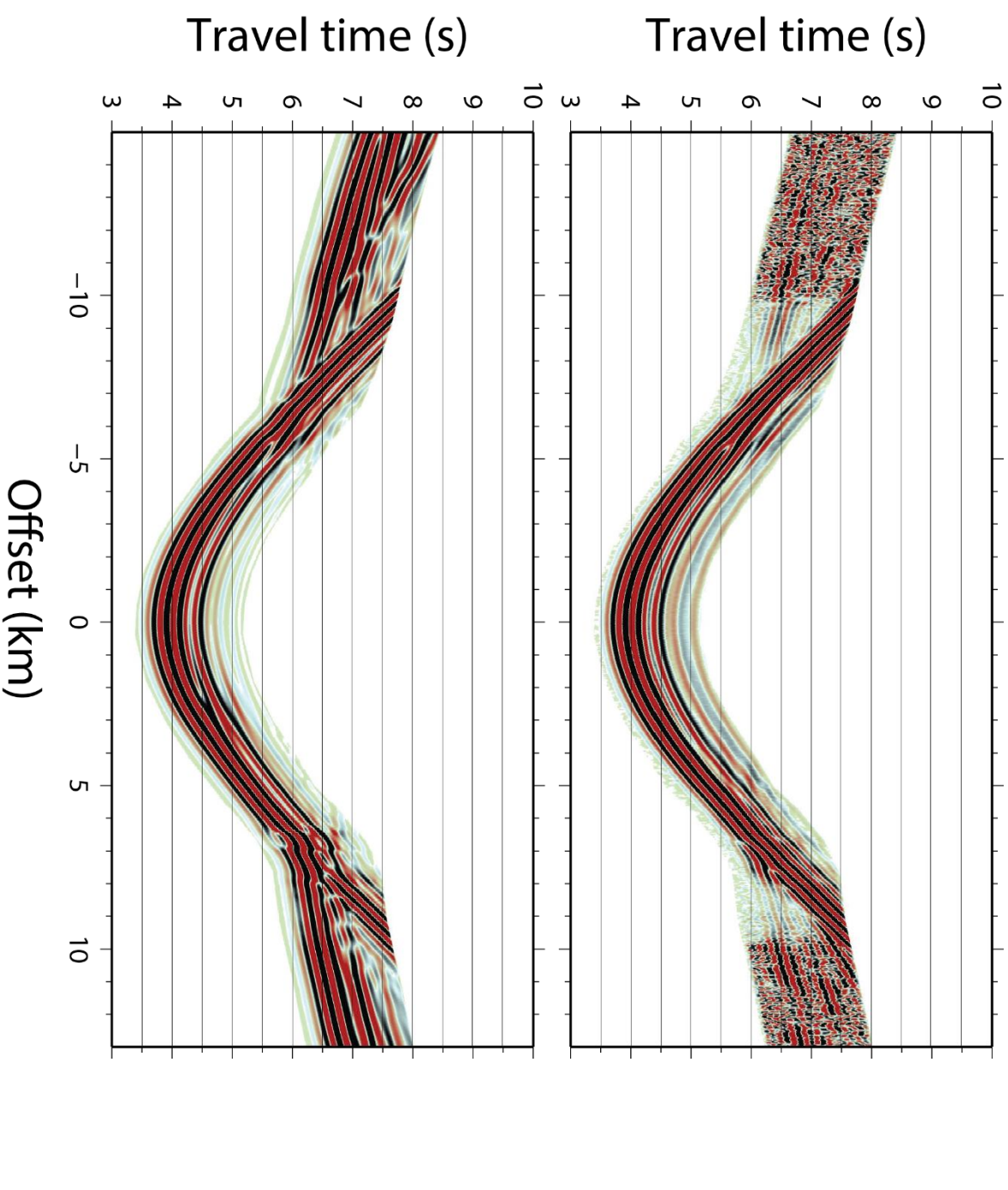

Figure C-10: Above: observed receiver gather for OBS48. Below: synthetic receiver gather for OBS48 through final FWI model.

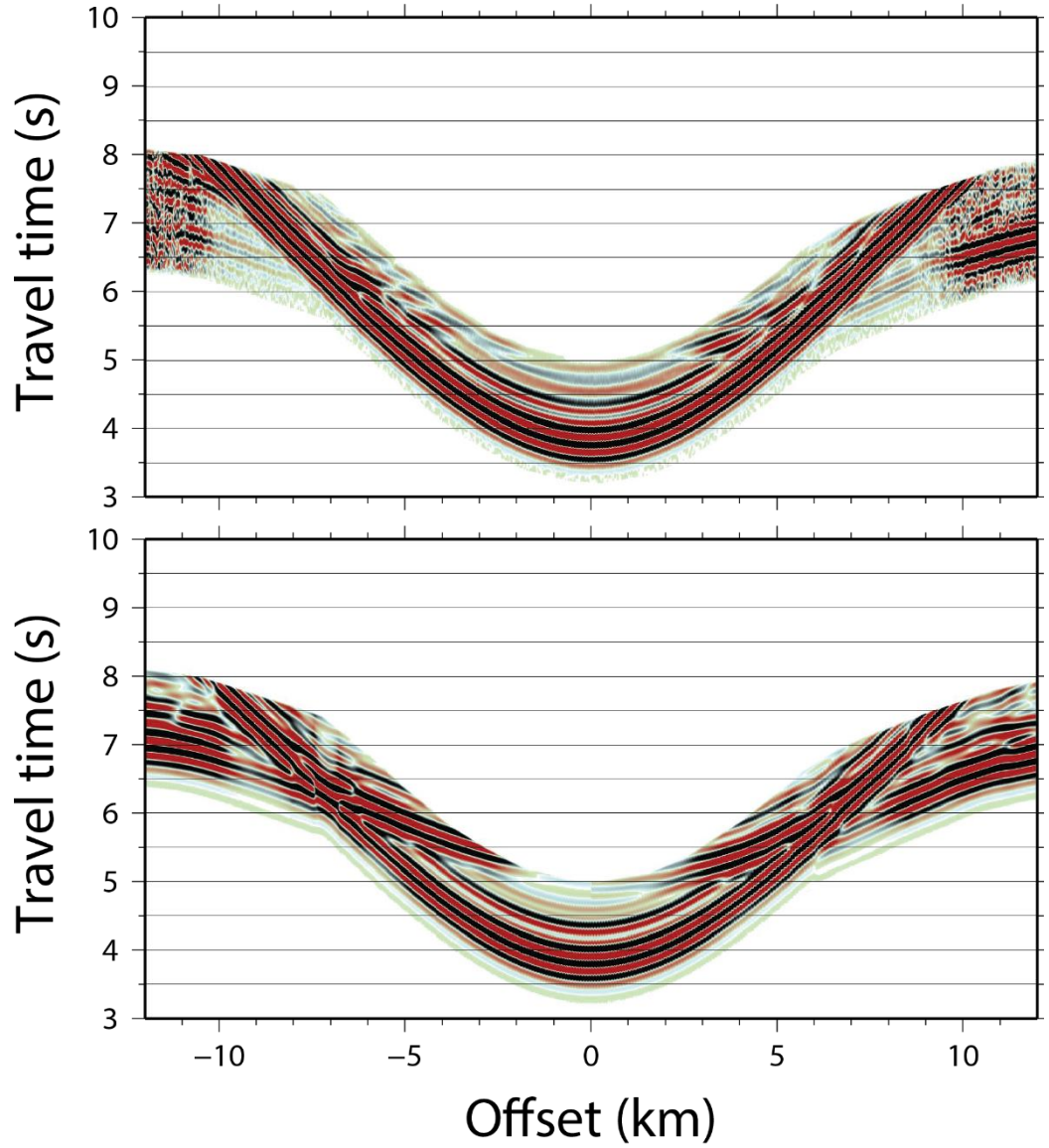

Figure C-11: Above: observed receiver gather for OBS52. Below: synthetic receiver gather for OBS52 through final FWI model.

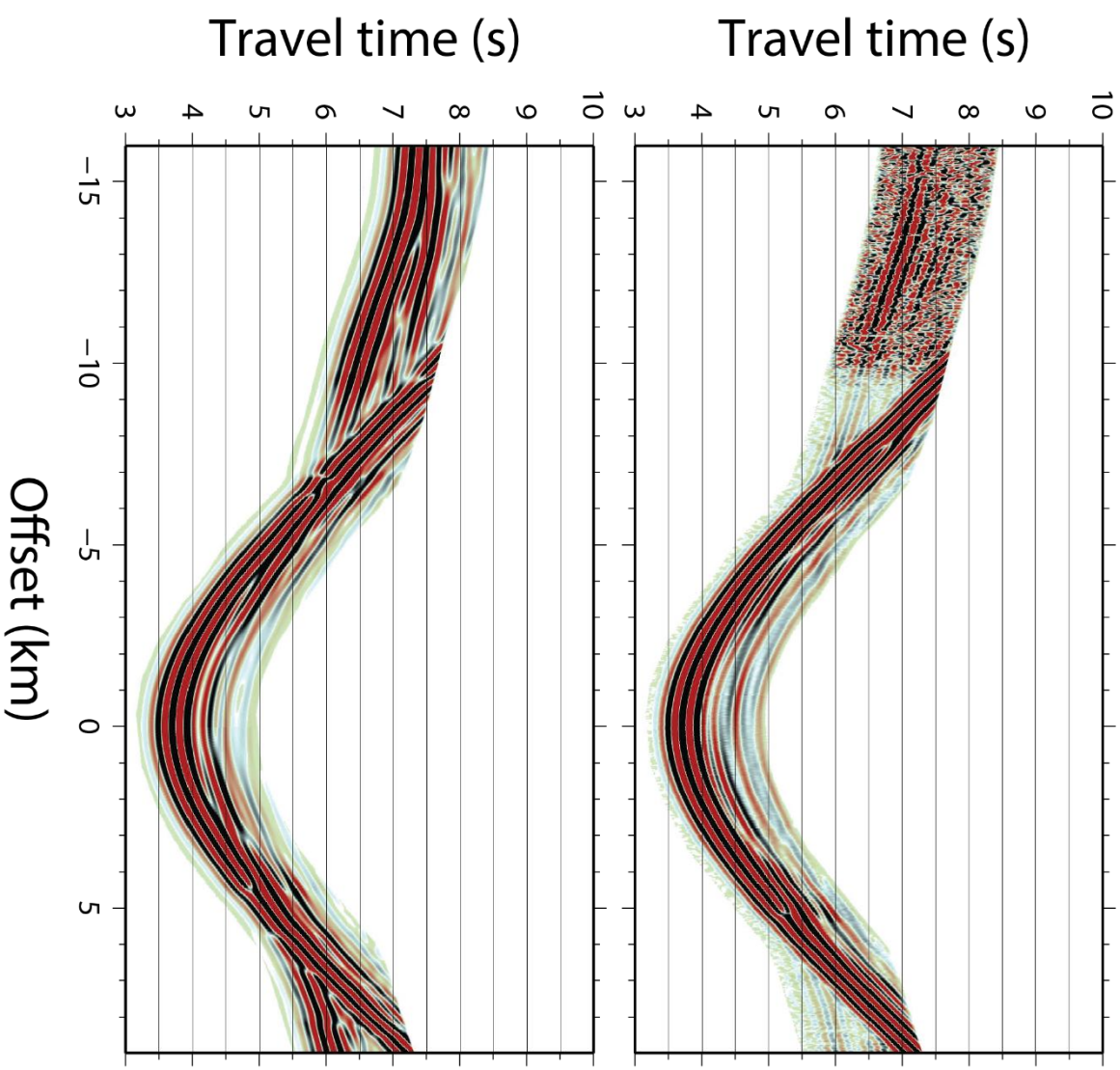

Figure C-12: Above: observed receiver gather for OBS53. Below: synthetic receiver gather for OBS53 through final FWI model.

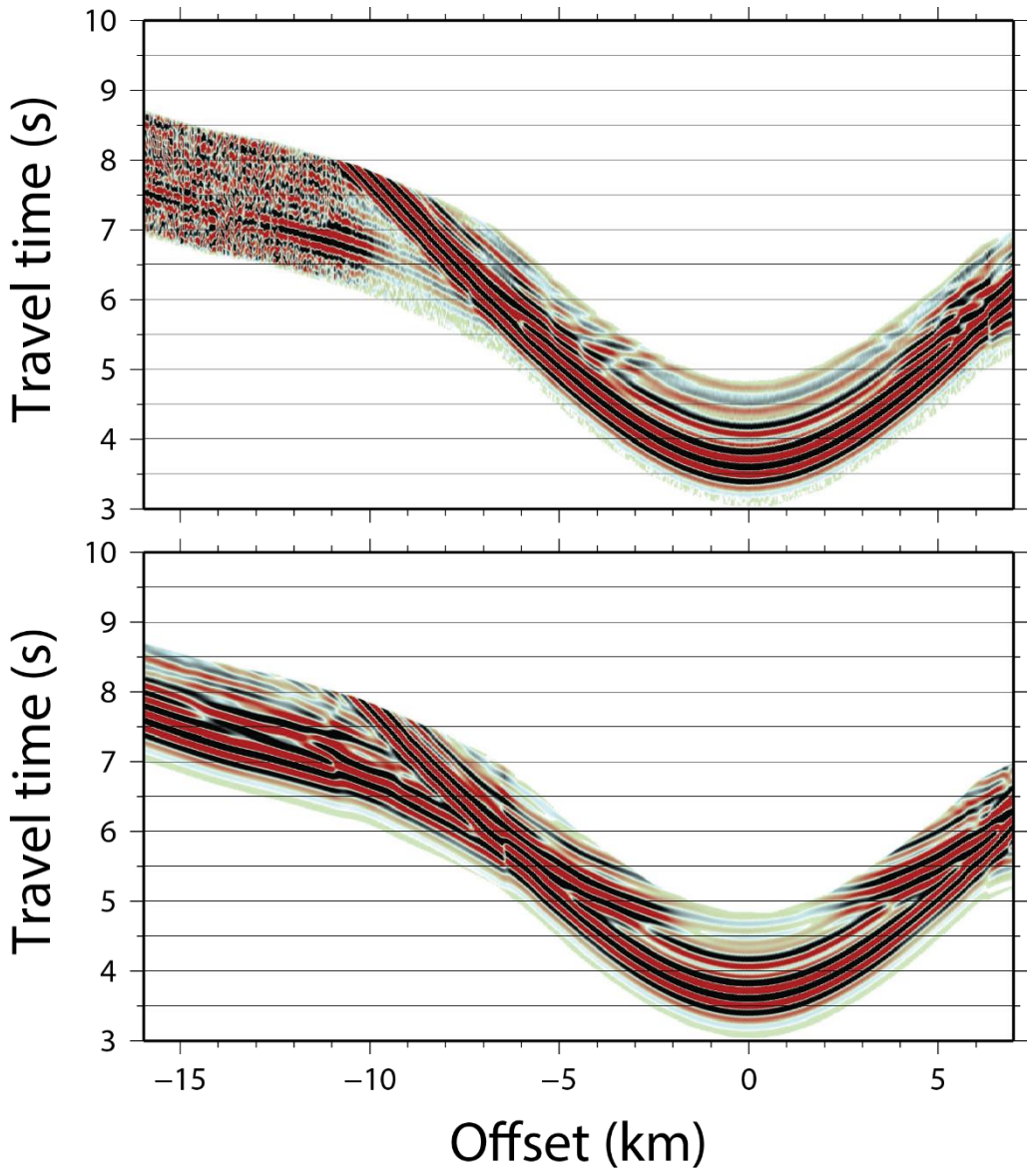

Figure C-13: Above: observed receiver gather for OBS54. Below: synthetic receiver gather for OBS54 through final FWI model.

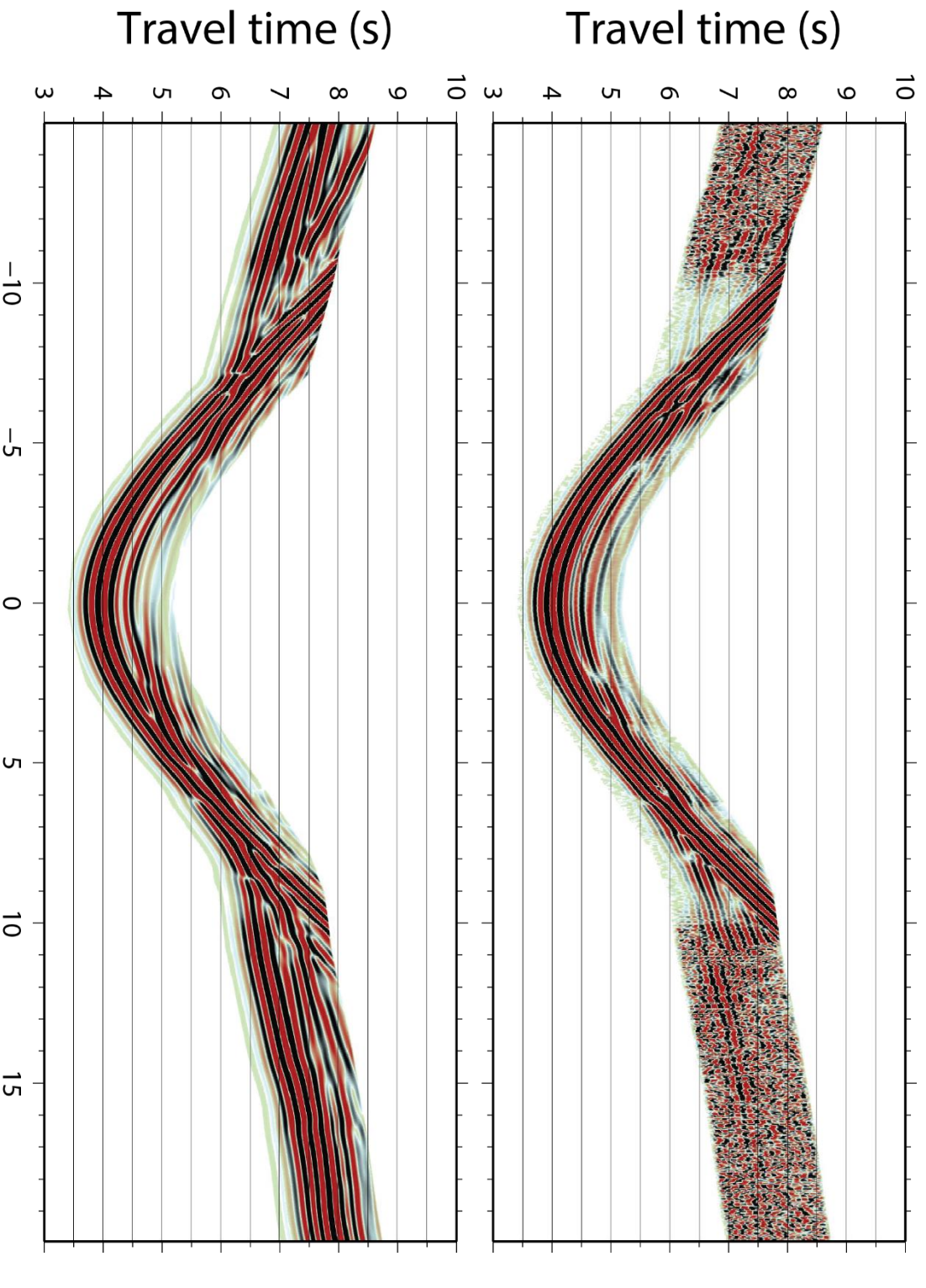

Figure C-14: Above: observed receiver gather for OBH80. Below: synthetic receiver gather for OBH80 through final FWI model.

81

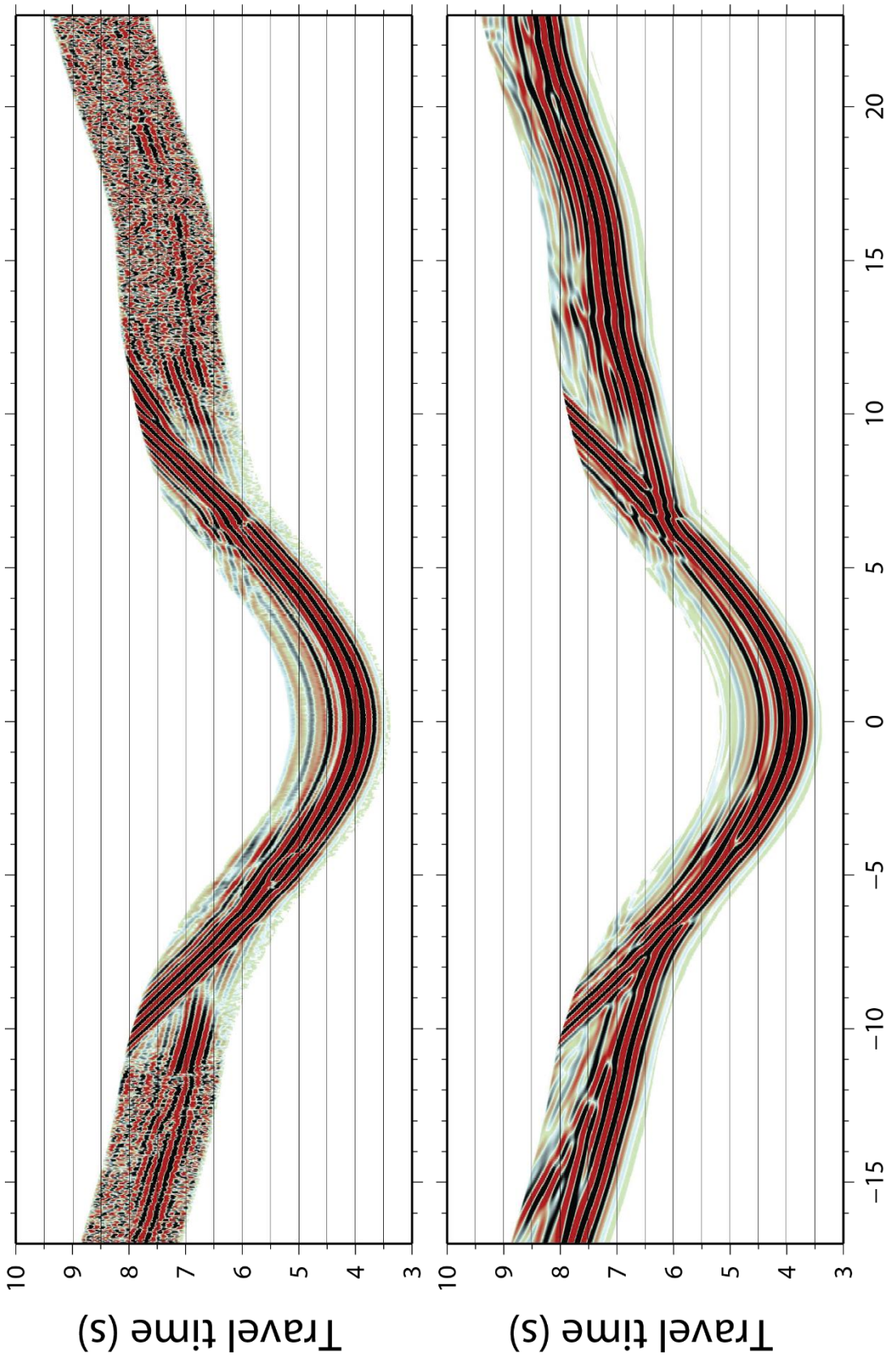

Figure C-15: Above: observed receiver gather for OBH81 Below: synthetic receiver gather for OBH81 through final FWI model.

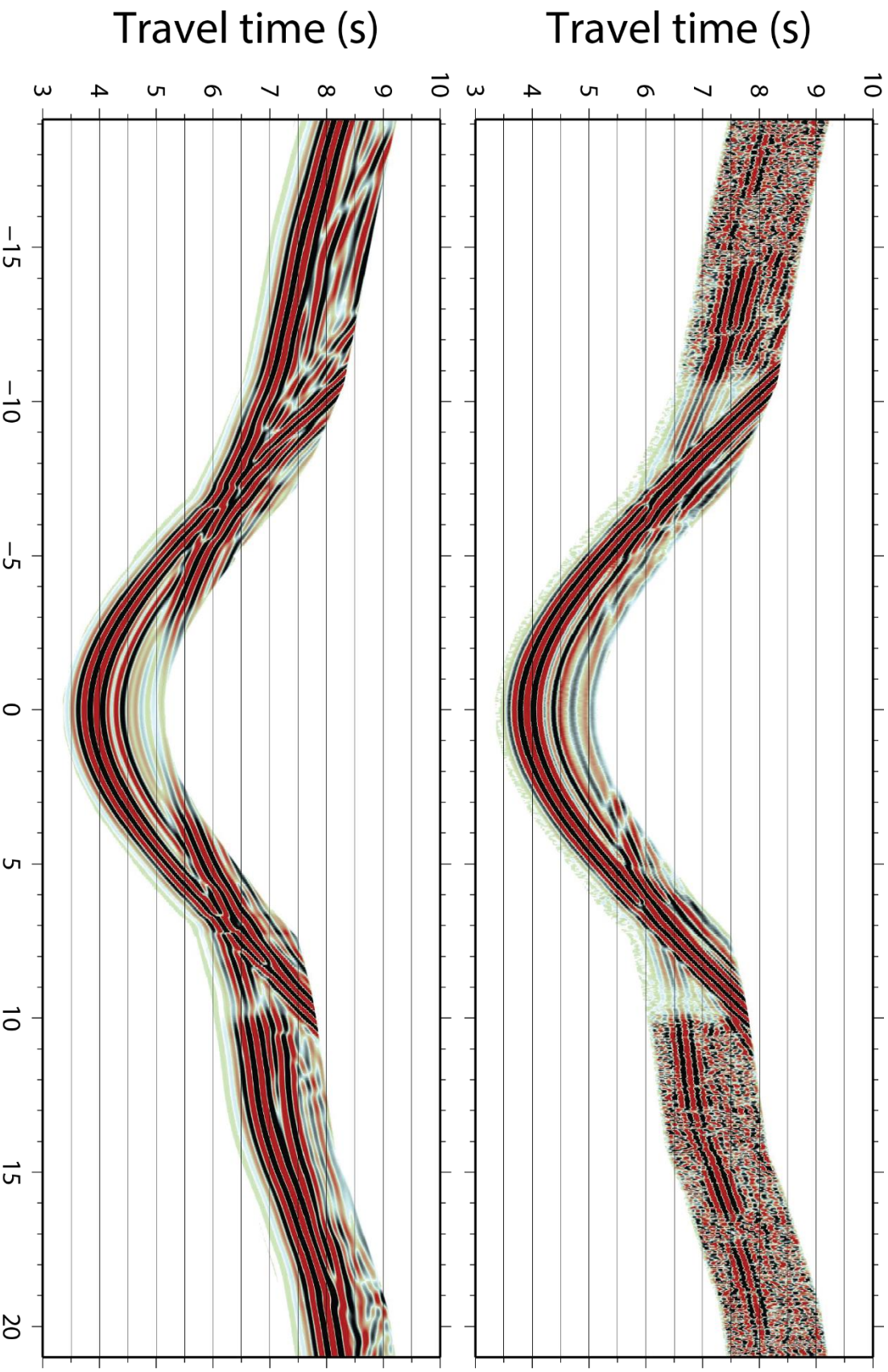

Figure C-16: Above: observed receiver gather for OBH82. Below: synthetic receiver gather for OH828 through final FWI model.

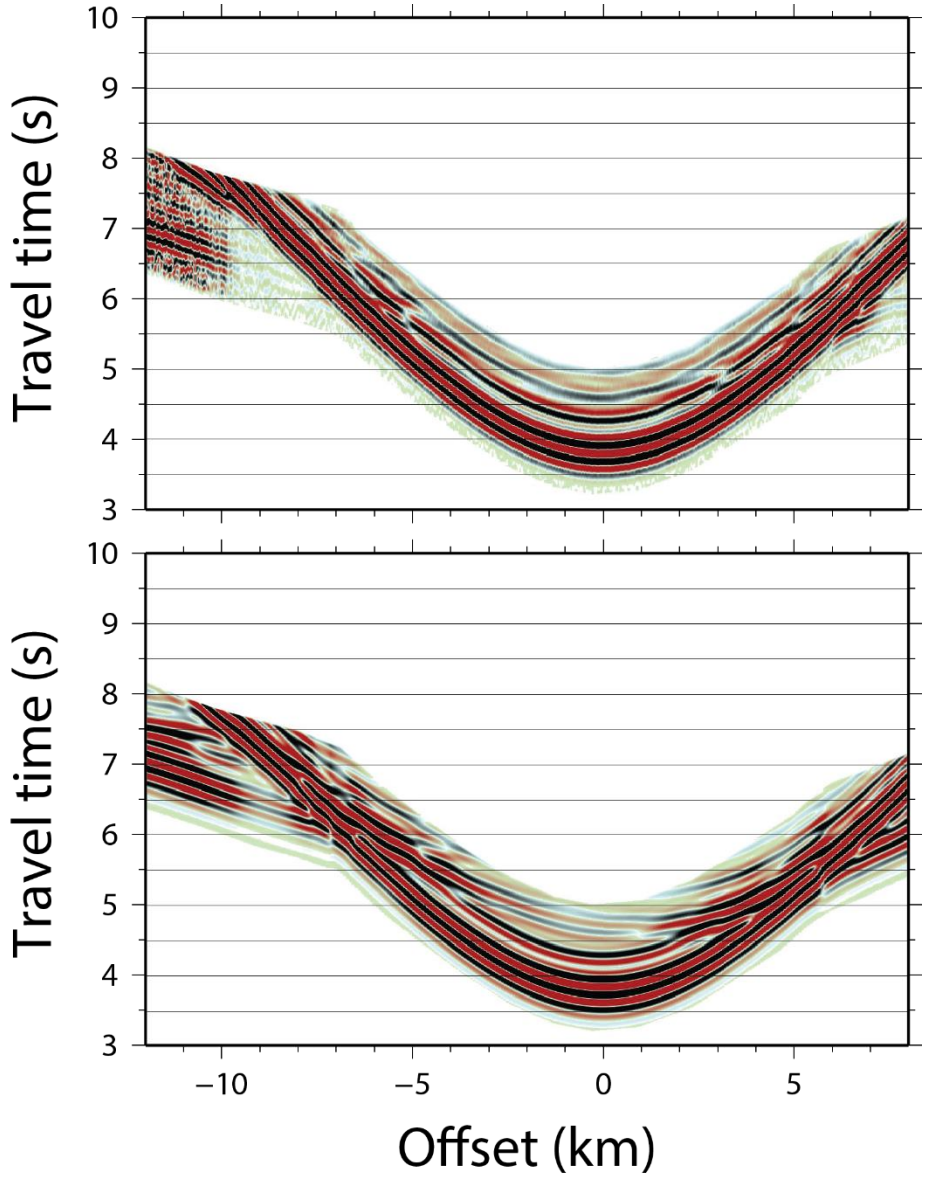

Figure C-17: Above: observed receiver gather for OBH85. Below: synthetic receiver gather for OBH85 through final FWI model.

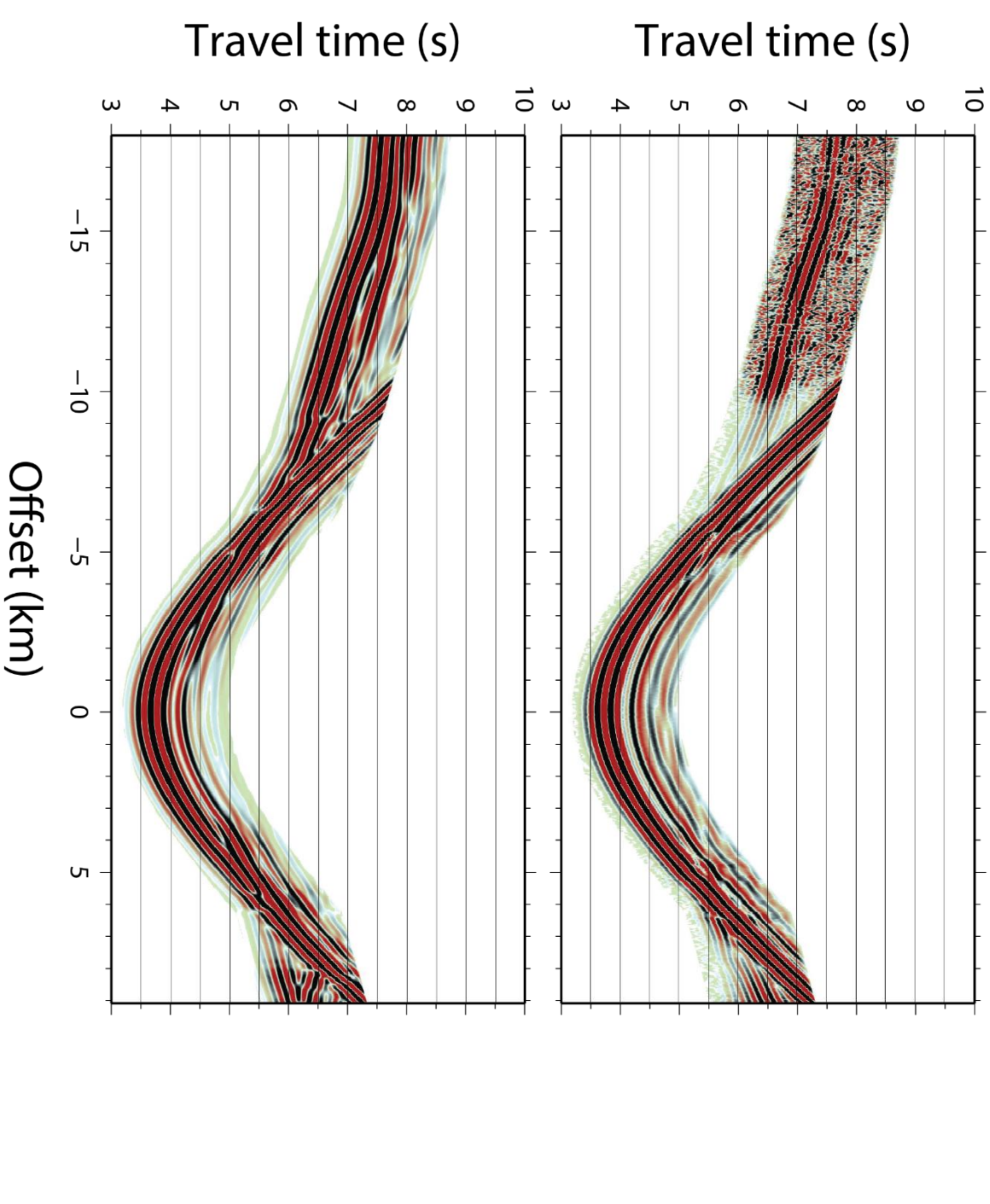

Figure C-18: Above: observed receiver gather for OBH86. Below: synthetic receiver gather for OBH86 through final FWI model.

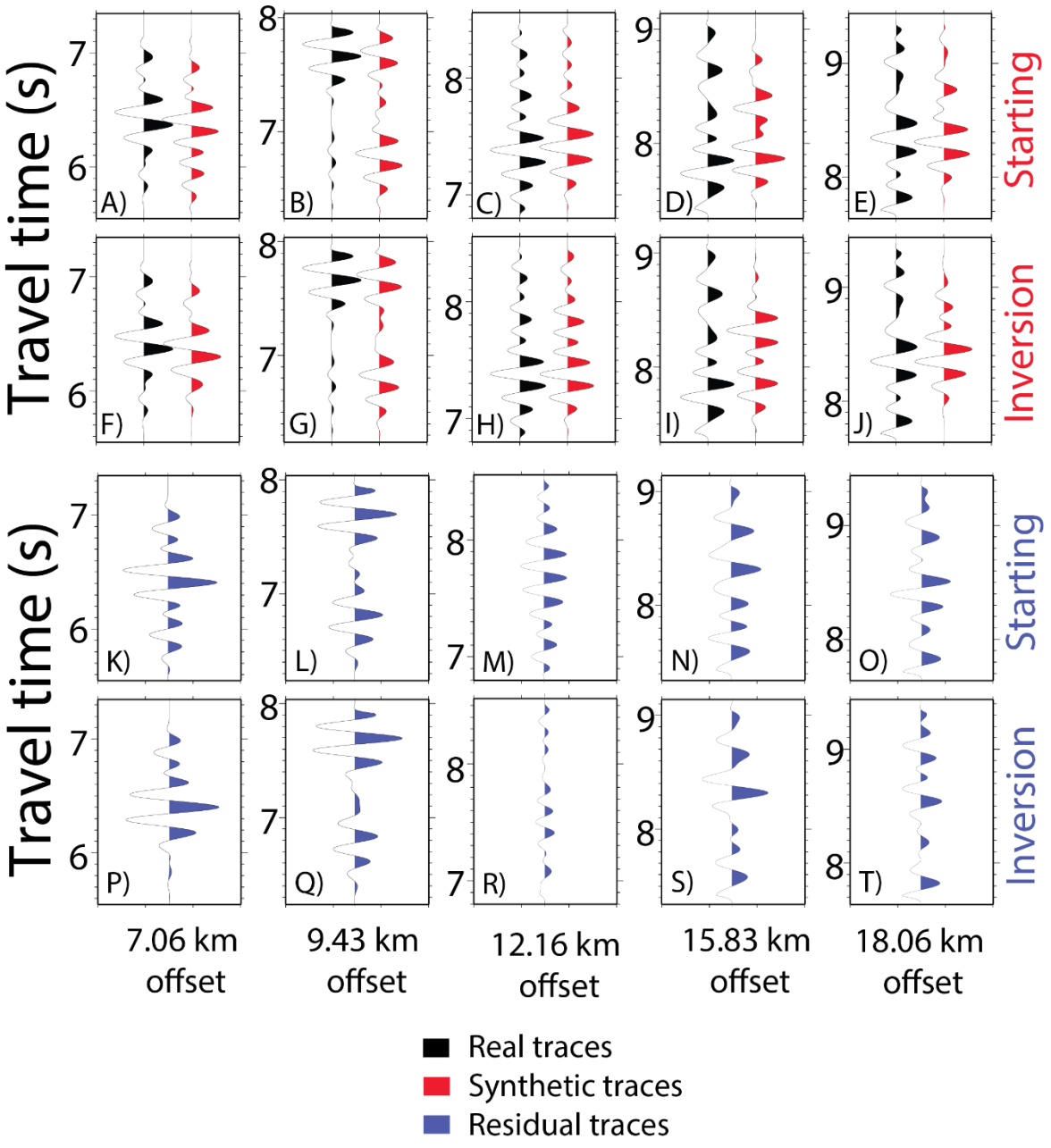

Figure C-19: *A-J) Comparing observed and synthetic traces at select instrument offsets for OBS37. A-E) Black traces: observed data, red traces: synthetic data through the starting model. F-J) Black traces: observed data, red traces: synthetic data through the FWI model. K-T) Residual data between the observed data and the synthetic data from above. K-O) Blue traces are the difference between the observed data and synthetics through the starting model. P-T) Blue traces are the difference between the observed data and synthetics through the FWI model.*

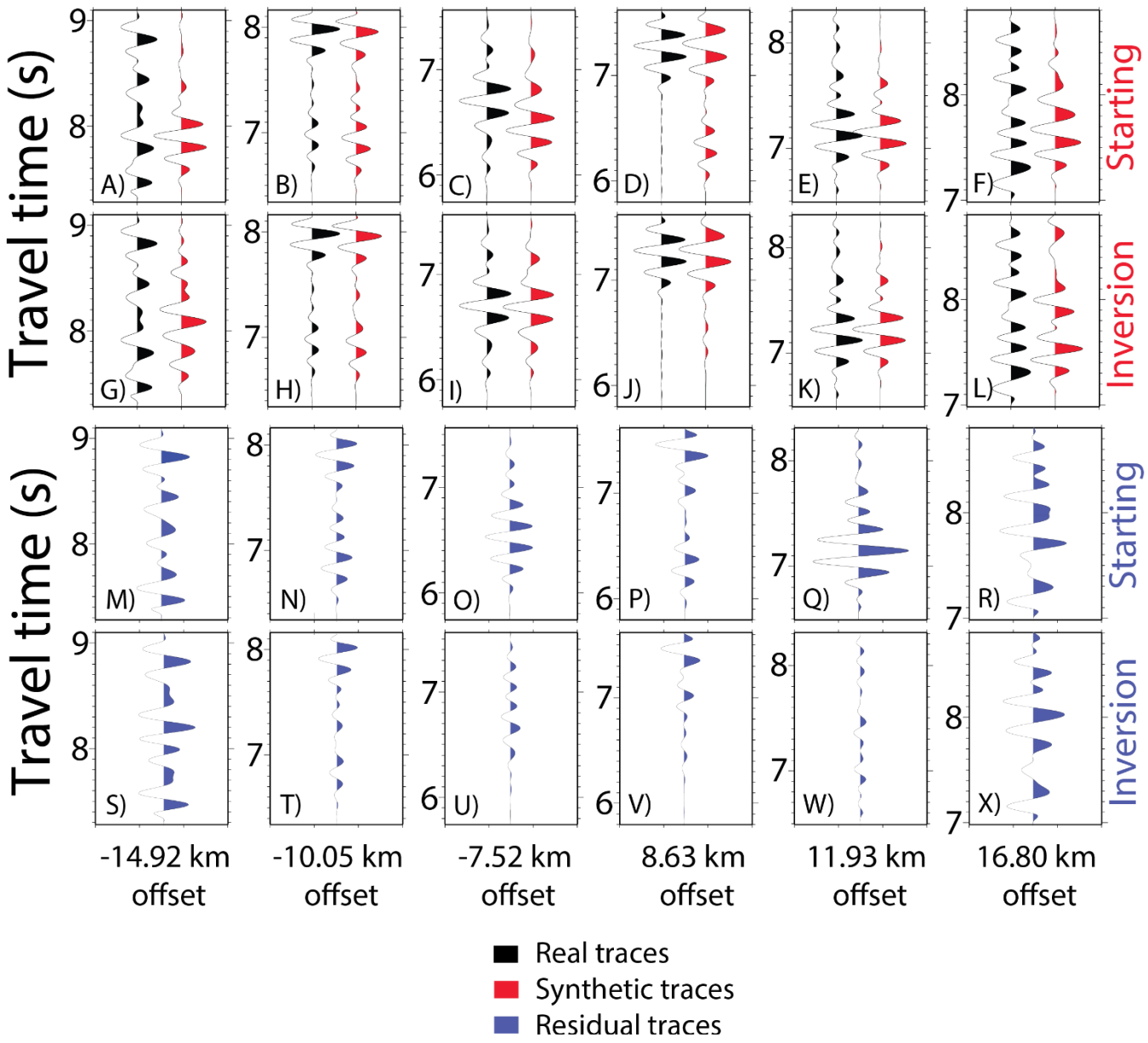

Figure C-20: *A-L) Comparing observed and synthetic traces at select instrument offsets for OBS46. A-F) Black traces: observed data, red traces: synthetic data through the starting model. G-L) Black traces: observed data, red traces: synthetic data through the FWI model. M-X) Residual data between the observed data and the synthetic data from above. M-R) Blue traces are the difference between the observed data and synthetics through the starting model. S-X) Blue traces are the difference between the observed data and synthetics through the FWI model.*

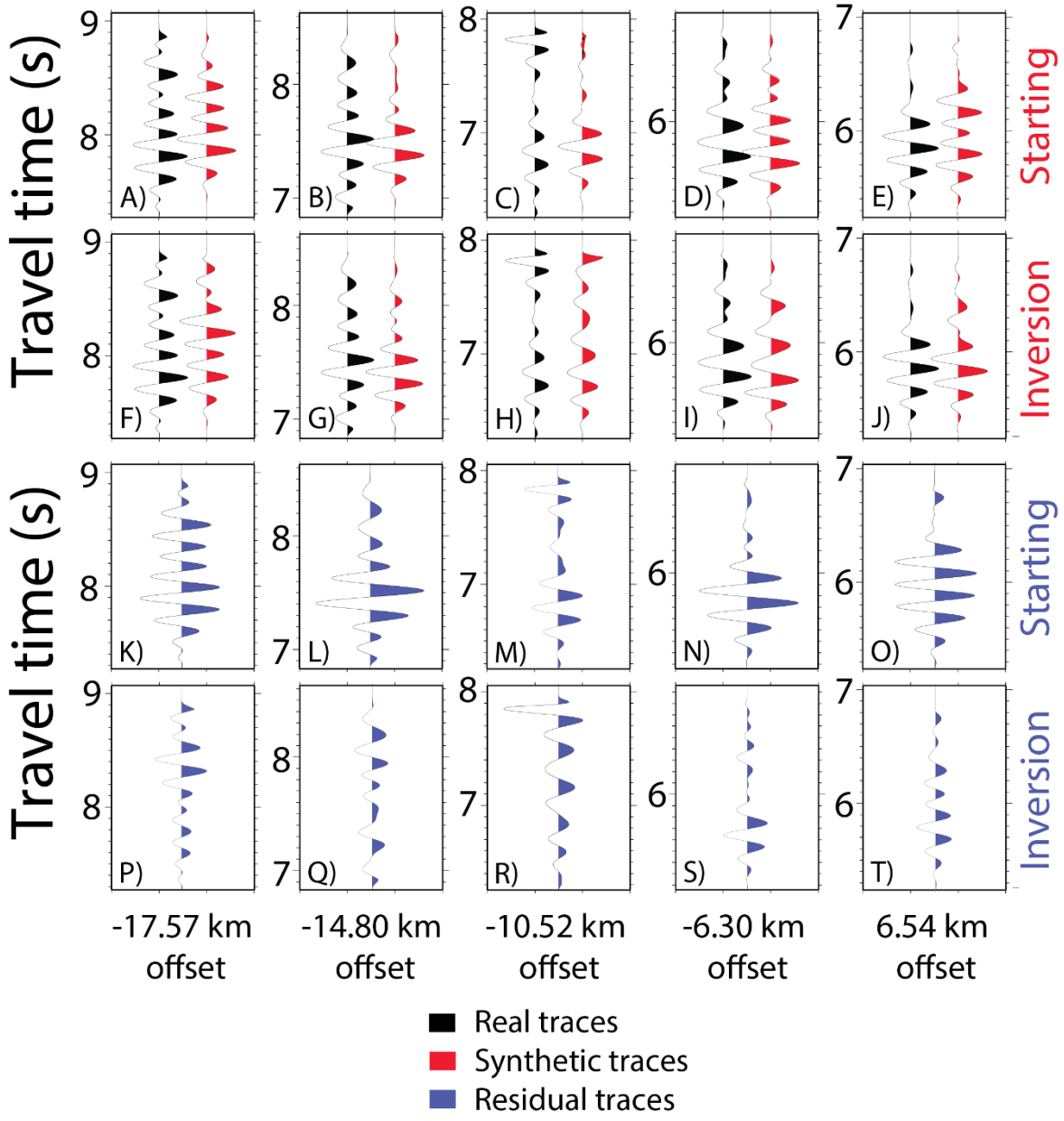

Figure C-21: *A-J) Comparing observed and synthetic traces at select instrument offsets for OBS54. A-E) Black traces: observed data, red traces: synthetic data through the starting model. F-J) Black traces: observed data, red traces: synthetic data through the FWI model. K-T) Residual data between the observed data and the synthetic data from above. K-O) Blue traces are the difference between the observed data and synthetics through the starting model. P-T) Blue traces are the difference between the observed data and synthetics through the FWI model.*

Bibliography

Anderson, E. M. (1951), *The Dynamics of Faulting, Etc.(Revised.)*, Edinburgh, London.

Armitage, J., J. Collier, T. Minshull, and T. Henstock (2011), Thin oceanic crust and flood basalts: India-Seychelles breakup, *Geochemistry, Geophysics, Geosystems*, *12*(5).

Armitage, J. J., J. S. Collier, and T. A. Minshull (2010), The importance of rift history for volcanic margin formation, *Nature*, *465*(7300), 913-917.

Arnoux, G. M., D. R. Toomey, E. E. Hooft, W. S. Wilcock, J. Morgan, M. Warner, and B. P. VanderBeek (2017), Seismic evidence that black smoker heat flux is influenced by localized magma replenishment and associated increases in crustal permeability, *Geophysical Research Letters*, *44*(4), 1687-1695.

Arroucau, P., N. Rawlinson, and M. Sambridge (2010), New insight into Cainozoic sedimentary basins and Palaeozoic suture zones in southeast Australia from ambient noise surface wave tomography, *Geophysical Research Letters*, *37*(7), L07303.

Banda, E., and M. Torne (1995), Iberian Atlantic Margins Group investigates deep structure of ocean margins, *Eos, Transactions American Geophysical Union*, *76*(3), 25-29.

Bassi, G. (1995), Relative importance of strain rate and rheology for the mode of continental extension, *Geophysical Journal International*, *122*(1), 195-210.

Bayrakci, G., T. Minshull, D. Sawyer, T. J. Reston, D. Klaeschen, C. Papenberg, C. Ranero, J. Bull, R. Davy, and D. Shillington (2016), Fault-controlled hydration of the upper mantle during continental rifting, *Nature Geoscience*, *9*(5), 384-388.

Bell, R. E., and A. B. Watts (1986), Evaluation of the BGM-3 sea gravity meter system onboard R/V Conrad, *Geophysics*, *51*(7), 1480-1493.

Bensen, G., M. Ritzwoller, M. Barmin, A. Levshin, F. Lin, M. Moschetti, N. Shapiro, and Y. Yang (2007), Processing seismic ambient noise data to obtain reliable broad-band surface wave dispersion measurements, *Geophysical Journal International*, *169*(3), 1239-1260.

Beslier, M.-O., M. Ask, and G. Boillot (1993), Ocean-continent boundary in the Iberia Abyssal Plain from multichannel seismic data, *Tectonophysics*, *218*(4), 383-393.

Bishop, T., K. Bube, R. Cutler, R. Langan, P. Love, J. Resnick, R. Shuey, D. Spindler, and H. Wyld (1985), Tomographic determination of velocity and depth in laterally varying media, *Geophysics*, *50*(6), 903-923.

Blackman, D. K., J. P. Canales, and A. Harding (2009), Geophysical signatures of oceanic core complexes, *Geophysical Journal International*, *178*(2), 593-613.

Boaga, J., F. Vaccari, and G. Panza (2010), Shear wave structural models of Venice Plain, Italy, from Time Cross Correlation of seismic noise, *Engineering Geology*, *116*(3), 189-195.

Boillot, G., S. Grimaud, A. Mauffret, D. Mougenot, J. Kornprobst, J. Mergoil-Daniel, and G. Torrent (1980), Ocean-continent boundary off the Iberian margin: a serpentinite diapir west of the Galicia Bank, *Earth and Planetary Science Letters*, *48*(1), 23-34.

Bibliography

Boillot, G., and E. Winterer (1988), Drilling on the Galicia margin: retrospect and prospect, paper presented at Proceedings of the Ocean Drilling Program, Scientific Results, Ocean Drilling Program College Station, TX.

Boillot, G., E. Winterer, and A. Meyer (1987), Introduction, objectives, and principal results: Ocean Drilling Program Leg 103, west Galicia Margin, *Proc. Ocean Drill. Program, Initial Reports*, *103*, 3-17.

Borgmeyer, A. L. (2010), Three-dimensional geometries of rifting on a hyperextended margin-Interpretation of seismic reflection profiles from the Deep Galicia Basin, Iberia, MSc thesis, Rice University.

Boschi, C., G. L. Früh-Green, A. Delacour, J. A. Karson, and D. S. Kelley (2006), Mass transfer and fluid flow during detachment faulting and development of an oceanic core complex, Atlantis Massif (MAR 30 N), *Geochemistry, Geophysics, Geosystems*, *7*(1).

Bown, J. W., and R. S. White (1995), Effect of finite extension rate on melt generation at rifted continental margins, *Journal of Geophysical Research: Solid Earth*, *100*(B9), 18011-18029.

Brocher, T. M. (2005), Empirical relations between elastic wavespeeds and density in the Earth's crust, *Bulletin of the Seismological Society of America*, *95*(6), 2081-2092.

Bronner, A., D. Sauter, G. Manatschal, G. Péron-Pinvidic, and M. Munschy (2011), Magmatic breakup as an explanation for magnetic anomalies at magma-poor rifted margins, *Nature Geoscience*, *4*(8), 549-553.

Brossier, R., S. Operto, and J. Virieux (2009), Seismic imaging of complex onshore structures by 2D elastic frequency-domain full-waveform inversion, *Geophysics*, *74*(6), WCC105-WCC118.

Brun, J., and M. Beslier (1996), Mantle exhumation at passive margins, *Earth and Planetary Science Letters*, *142*(1-2), 161-173.

Buck, W. R. (1991), Modes of continental lithospheric extension, *Journal of Geophysical Research: Solid Earth*, *96*(B12), 20161-20178.

Bullock, A. D., and T. A. Minshull (2005), From continental extension to seafloor spreading: crustal structure of the Goban Spur rifted margin, southwest of the UK, *Geophysical Journal International*, *163*(2), 527-546.

Bunks, C., F. M. Saleck, S. Zaleski, and G. Chavent (1995), Multiscale seismic waveform inversion, *Geophysics*, *60*(5), 1457-1473.

Campillo, M., and A. Paul (2003), Long-range correlations in the diffuse seismic coda, *Science*, *299*(5606), 547-549.

Canales, J. P., R. A. Sohn, and B. J. Demartin (2007), Crustal structure of the Trans-Atlantic Geotraverse (TAG) segment (Mid-Atlantic Ridge, 26° 10′ N): Implications for the nature of hydrothermal circulation and detachment faulting at slow spreading ridges, *Geochemistry, Geophysics, Geosystems*, *8*(8), 1-18.

Cannat, M., D. Sauter, V. Mendel, E. Ruellan, K. Okino, J. Escartin, V. Combier, and M. Baala (2006), Modes of seafloor generation at a melt-poor ultraslow-spreading ridge, *Geology*, *34*(7), 605-608.

Carlson, R. L., and D. J. Miller (2003), Mantle wedge water contents estimated from seismic velocities in partially serpentinized peridotites, *Geophysical Research Letters*, *30*(5), 1250, doi:10.1029/2002GL016600.

Červený, V., I. A. e. Molotkov, and I. Pšenčík (1977), *Ray method in seismology*, 214 pp pp., University of Karlova, Prague.

Chazot, G., S. Charpentier, J. Kornprobst, R. Vannucci, and B. Luais (2005), Lithospheric mantle evolution during continental break-up: the West Iberia non-volcanic passive margin, *Journal of Petrology*, *46*(12), 2527-2568.

Chian, D., and K. E. Louden (1994), The continent-ocean crustal transition across the southwest Greenland margin, *Journal of Geophysical Research*, *99*(5), 9117-9135.

Chian, D., K. E. Louden, T. A. Minshull, and R. B. Whitmarsh (1999), Deep structure of the ocean-continent transition in the southern Iberia Abyssal Plain from seismic refraction profiles: Ocean Drilling Program (Legs 149 and 173) transect, *Journal of Geophysical Research: Solid Earth (1978–2012)*, *104*(B4), 7443-7462.

Christensen, N. I. (1996), Poisson's ratio and crustal seismology, *Journal of Geophysical Research: Solid Earth*, *101*(B2), 3139-3156.

Christensen, N. I. (2004), Serpentinites, peridotites, and seismology, *International Geology Review*, *46*(9), 795-816.

Conley, M. M., and R. A. Dunn (2011), Seismic shear wave structure of the uppermost mantle beneath the Mohns Ridge, *Geochemistry, Geophysics, Geosystems*, *12*(10), Q0AK01.

Corchete, V., and M. Chourak (2011), Shear-wave velocity structure of the south-eastern part of the Iberian Peninsula from Rayleigh wave analysis, *International Journal of Earth Sciences*, *100*(7), 1733-1747.

Corela, C., G. Silveira, L. Matias, M. Schimmel, and W. H. Geissler (2017), Ambient seismic noise tomography of SW Iberia integrating seafloor-and land-based data, *Tectonophysics*, *700-701*, 131-149.

Cox, H. (1973), Spatial correlation in arbitrary noise fields with application to ambient sea noise, *The Journal of the Acoustical Society of America*, *54*(5), 1289-1301.

D'Alessandro, A., G. Mangano, G. D'Anna, and S. Scudero (2016), Evidence for serpentinization of the Ionian upper mantle from simultaneous inversion of P-and S-wave arrival times, *Journal of Geodynamics*, *102*, 115-120.

Davis, M., and N. Kusznir (2004), Depth-dependent lithospheric stretching at rifted continental margins, *Proc. NSF Rifted Margins Theoretical Institute, Columbia University Press*, *1*, 92-136.

Davy, R., T. Minshull, G. Bayrakci, J. Bull, D. Klaeschen, C. Papenberg, T. J. Reston, D. Sawyer, and C. Zelt (2016), Continental hyperextension, mantle exhumation, and thin oceanic crust at the continent-ocean transition, West Iberia: New insights from wide-angle seismic, *Journal of Geophysical Research: Solid Earth*, *121*(5), 3177-3199.

De Charpal, O. (1978), Rifting, crustal attenuation and subsidence in the Bay of Biscay, *Nature*, *275*, 706-711.

De Nisco, G., and C. Nunziata (2011), VS profiles from noise cross correlation at local and small scale, *Pure and applied geophysics*, *168*(3-4), 509-520.

Dean, S., T. Minshull, R. Whitmarsh, and K. Louden (2000), Deep structure of the ocean-continent transition in the southern Iberia Abyssal Plain from seismic refraction profiles: The IAM-9 transect at 40 20' N, *Journal of Geophysical Research: Solid Earth*, *105*(B3), 5859-5885.

Dean, S., D. Sawyer, and J. Morgan (2015), Galicia Bank ocean–continent transition zone: New seismic reflection constraints, *Earth and Planetary Science Letters*, *413*, 197-207.

Dean, S. M. (1999), Structure of the Ocean-Continent Transition in the Southern Iberia Abyssal Plain, PhD thesis, Universtiy of Cambridge.

Dessa, J. X., S. Operto, S. Kodaira, A. Nakanishi, G. Pascal, J. Virieux, and Y. Kaneda (2004), Multiscale seismic imaging of the eastern Nankai trough by full waveform inversion, *Geophysical Research Letters*, *31*(18), L18606.

Dijkstra, E. W. (1959), A note on two problems in connexion with graphs, *Numerische mathematik*, *1*(1), 269-271.

Direen, N. G., H. M. Stagg, P. A. Symonds, and J. B. Colwell (2011), Dominant symmetry of a conjugate southern Australian and East Antarctic magma-poor rifted margin segment, *Geochemistry, Geophysics, Geosystems*, *12*(2).

Direen, N. G., H. M. Stagg, P. A. Symonds, and I. O. Norton (2013), Variations in rift symmetry: cautionary examples from the Southern Rift System (Australia–Antarctica), *Geological Society, London, Special Publications*, *369*(1), 453-475.

Dziewonski, A., S. Bloch, and M. Landisman (1969), A technique for the analysis of transient seismic signals, *Bulletin of the seismological Society of America*, *59*(1), 427-444.

Ebinger, C., and M. Casey (2001), Continental breakup in magmatic provinces: An Ethiopian example, *Geology*, *29*(6), 527-530.

Eddy, D. R., H. J. Van Avendonk, and D. J. Shillington (2013), Compressional and shear-wave velocity structure of the continent-ocean transition zone at the eastern Grand Banks, Newfoundland, *Geophysical Research Letters*, *40*(12), 3014-3020.

Egan, S., and D. Meredith (2007), A kinematic modelling approach to lithosphere deformation and basin formation: application to the Black Sea, *Geological Society, London, Special Publications*, *282*(1), 173-198.

Espurt, N., J. P. Callot, F. Roure, J. M. Totterdell, H. I. Struckmeyer, and R. Vially (2012), Transition from symmetry to asymmetry during continental rifting: an example from the Bight Basin–Terre Adélie (Australian and Antarctic conjugate margins), *Terra Nova*, *24*(3), 167-180.

Franke, D. (2013), Rifting, lithosphere breakup and volcanism: Comparison of magma-poor and volcanic rifted margins, *Marine and Petroleum Geology*, *43*, 63-87.

Funck, T., J. R. Hopper, H. C. Larsen, K. E. Louden, B. E. Tucholke, and W. S. Holbrook (2003), Crustal structure of the ocean-continent transition at Flemish Cap: Seismic refraction results, *Journal of Geophysical Research: Solid Earth*, *108*(B11), 2531, doi:10.1029/2003JB002434.

Gallo, G., and S. Pallottino (1986), Shortest path methods: A unifying approach, in *Netflow at Pisa*, edited, pp. 38-64, Springer.

Gardner, G., L. Gardner, and A. Gregory (1974), Formation velocity and density —The diagnostic basics for stratigraphic traps, *Geophysics*, *39*(6), 770-780.

Gerlings, J., K. E. Louden, and H. R. Jackson (2011), Crustal structure of the Flemish Cap Continental Margin (eastern Canada): an analysis of a seismic refraction profile, *Geophysical Journal International*, *185*(1), 30-48.

Gerlings, J., K. E. Louden, T. A. Minshull, and M. R. Nedimović (2012), Flemish Cap–Goban Spur conjugate margins: new evidence of asymmetry, *Geology*, *40*(12), 1107-1110.

Gerstoft, P., and T. Tanimoto (2007), A year of microseisms in southern California, *Geophysical Research Letters*, *34*(20), L20304.

Gillard, M., G. Manatschal, and J. Autin (2016), How can asymmetric detachment faults generate symmetric Ocean Continent Transitions?, *Terra nova*, *28*(1), 27-34.

Gradstein, F. M., J. G. Ogg, M. Schmitz, and G. Ogg (2012), *The Geologic Time Scale 2012 2-Volume Set*, Elsevier.

Granot, R., J. Dyment, and Y. Gallet (2012), Geomagnetic field variability during the Cretaceous Normal Superchron, *Nature Geoscience*, *5*(3), 220-223.

Hamilton, E. L. (1979), V p/V s and Poisson's ratios in marine sediments and rocks, *The Journal of the Acoustical Society of America*, *66*(4), 1093-1101.

Harmon, N., D. Forsyth, and S. Webb (2007), Using ambient seismic noise to determine short-period phase velocities and shallow shear velocities in young oceanic lithosphere, *Bulletin of the Seismological Society of America*, *97*(6), 2009-2023.

Harmon, N., P. Gerstoft, C. A. Rychert, G. A. Abers, M. Salas de La Cruz, and K. M. Fischer (2008), Phase velocities from seismic noise using beamforming and cross correlation in Costa Rica and Nicaragua, *Geophysical Research Letters*, *35*(19), L19303.

Harmon, N., C. Rychert, and P. Gerstoft (2010), Distribution of noise sources for seismic interferometry, *Geophysical Journal International*, *183*(3), 1470-1484.

Harmon, N., and C. A. Rychert (2016), Joint inversion of teleseismic and ambient noise Rayleigh waves for phase velocity maps, an application to Iceland, *Journal of Geophysical Research: Solid Earth*, *121*(8), 5966-5987.

Henning, A. T., D. S. Sawyer, and D. C. Templeton (2004), Exhumed upper mantle within the ocean-continent transition on the northern West Iberia margin: Evidence from prestack depth migration and total tectonic subsidence analyses, *Journal of Geophysical Research: Solid Earth*, *109*(B5), B05103.

Henrys, S., M. Reyners, I. Pecher, S. Bannister, Y. Nishimura, and G. Maslen (2006), Kinking of the subducting slab by escalator normal faulting beneath the North Island of New Zealand, *Geology*, *34*(9), 777-780.

Hinz, K. (1981), A Hypothesis on Terrestrial Catastrophes: Wedges of very thick oceanward dipping layers beneath passive continental margins, *Geologisches Jahrbuch*, *22*, 3-28.

Holbrook, W. S., H. Larsen, J. Korenaga, T. Dahl-Jensen, I. D. Reid, P. Kelemen, J. Hopper, G. Kent, D. Lizarralde, and S. Bernstein (2001), Mantle thermal structure and active upwelling during continental breakup in the North Atlantic, *Earth and Planetary Science Letters*, *190*(3), 251-266.

Hopper, J. R., T. Dahl-Jensen, W. S. Holbrook, H. C. Larsen, D. Lizarralde, J. Korenaga, G. M. Kent, and P. B. Kelemen (2003), Structure of the SE Greenland margin from seismic reflection and refraction data: Implications for nascent spreading center subsidence and asymmetric crustal accretion during North Atlantic opening, *Journal of Geophysical Research: Solid Earth*, *108*(B5), 2269.

Hopper, J. R., T. Funck, B. E. Tucholke, H. C. Larsen, W. S. Holbrook, K. E. Louden, D. Shillington, and H. Lau (2004), Continental breakup and the onset of ultraslow seafloor spreading off Flemish Cap on the Newfoundland rifted margin, *Geology*, *32*(1), 93-96.

Hopper, J. R., T. Funck, B. E. Tucholke, K. E. Louden, W. S. Holbrook, and H. C. Larsen (2006), A deep seismic investigation of the Flemish Cap margin: implications for the origin of deep reflectivity and evidence for asymmetric break-up between Newfoundland and Iberia, *Geophysical Journal International*, *164*(3), 501-515.

Jackson, J. (1987), Active normal faulting and crustal extension, *Geological Society, London, Special Publications*, *28*(1), 3-17.

Jagoutz, O., O. Müntener, G. Manatschal, D. Rubatto, G. Péron-Pinvidic, B. D. Turrin, and I. M. Villa (2007), The rift-to-drift transition in the North Atlantic: A stuttering start of the MORB machine?, *Geology*, *35*(12), 1087-1090.

Jaiswal, P., C. A. Zelt, A. W. Bally, and R. Dasgupta (2008), 2-D traveltime and waveform inversion for improved seismic imaging: Naga Thrust and Fold Belt, India, *Geophysical Journal International*, *173*(2), 642-658.

Jian, H., S. C. Singh, Y. J. Chen, and J. Li (2017), Evidence of an axial magma chamber beneath the ultraslow-spreading Southwest Indian Ridge, *Geology*, *45*(2), 143-146.

John, B. E., and M. J. Cheadle (2010), Deformation and alteration associated with oceanic and continental detachment fault systems: Are they similar?, *Diversity of Hydrothermal Systems on Slow Spreading Ocean Ridges*, 175-205.

Jokat, W., O. Ritzmann, M. C. Schmidt-Aursch, S. Drachev, S. Gauger, and J. Snow (2003), Geophysical evidence for reduced melt production on the Arctic ultraslow Gakkel mid-ocean ridge, *Nature*, *423*(6943), 962-965.

Jokat, W., and M. C. Schmidt-Aursch (2007), Geophysical characteristics of the ultraslow spreading Gakkel Ridge, Arctic Ocean, *Geophysical journal international*, *168*(3), 983-998.

Jones, C., M. Evans, A. Ratcliffe, G. Conroy, R. Jupp, J. Selvage, and L. Ramsey (2013), Full waveform inversion in a complex geological setting-a narrow azimuth towed streamer case study from the Barents Sea, in *Proceedings of the 75th EAGE Conference*, edited, Extended Abstracts, doi:10.3997/2214-4609.20130830.

Kamei, R., R. G. Pratt, and T. Tsuji (2012), Waveform tomography imaging of a megasplay fault system in the seismogenic Nankai subduction zone, *Earth and Planetary Science Letters*, *317*, 343-353.

Kapoor, S., D. Vigh, E. Wiarda, and S. Alwon (2013), Full waveform inversion around the world, paper presented at Proceedings of the 75th EAGE Conference, Extended Abstracts, doi: 10.3997/2214-4609.20130827.

Kern, H., C. Walther, E. Flüh, and M. Marker (1993), Seismic properties of rocks exposed in the POLAR profile region—constraints on the interpretation of the refraction data, *Precambrian Research*, *64*(1-4), 169-187.

Klingelhöfer, F., L. Geli, L. Matias, N. Steinsland, and J. Mohr (2000), Crustal structure of a super-slow spreading centre: a seismic refraction study of Mohns Ridge, 72 N, *Geophysical Journal International*, *141*(2), 509-526.

Klitgord, K., and H. Schouten (1986), Plate kinematics of the central Atlantic, *The Geology of North America*, *1000*, 351-378.

Kolb, P., F. Collino, and P. Lailly (1986), Pre-stack inversion of a 1-D medium, *Proceedings of the IEEE*, *74*(3), 498-508.

Korenaga, J., W. Holbrook, G. Kent, P. Kelemen, R. Detrick, H. C. Larsen, J. Hopper, and T. Dahl-Jensen (2000), Crustal structure of the southeast Greenland margin from joint refraction and reflection seismic tomography, *Journal of Geophysical Research: Solid Earth*, *105*(B9), 21591-21614.

Kusznir, N., and G. Karner (2007), Continental lithospheric thinning and breakup in response to upwelling divergent mantle flow: application to the Woodlark, Newfoundland and Iberia margins, *Geological Society, London, Special Publications*, *282*(1), 389-419.

Lailly, P. (1983), The seismic inverse problem as a sequence of before stack migrations, paper presented at Conference on Inverse Scattering: Theory and Application, Soc. Industr. Appl. Math., Philadelphia.

Lavier, L. L., and G. Manatschal (2006), A mechanism to thin the continental lithosphere at magma-poor margins, *Nature*, *440*(7082), 324-328.

Le Pichon, X., and J. C. Sibuet (1981), Passive margins: a model of formation, *Journal of Geophysical Research: Solid Earth (1978–2012)*, *86*(B5), 3708-3720.

Levshin, A., and M. Ritzwoller (2001), Automated detection, extraction, and measurement of regional surface waves, in *Monitoring the Comprehensive Nuclear-Test-Ban Treaty: Surface Waves*, edited, pp. 1531-1545, Springer.

Levshin, A., T. Yanovskaya, A. Lander, B. Bukchin, M. Barmin, L. Ratnikova, and E. Its (1989), Seismic surface waves in a laterally inhomogeneous Earth, *Modern Approaches in Geophysics*, *9*, 131-169.

Leythaeuser, T., T. J. Reston, and T. Minshull (2005), Waveform inversion of the S reflector west of Spain: Fine structure of a detachment fault, *Geophysical research letters*, *32*(22), L22304.

Lister, G., M. Etheridge, and P. Symonds (1986), Detachment faulting and the evolution of passive continental margins, *Geology*, *14*(3), 246-250.

Lister, G. S., and G. A. Davis (1989), The origin of metamorphic core complexes and detachment faults formed during Tertiary continental extension in the northern Colorado River region, USA, *Journal of Structural Geology*, *11*(1-2), 65-94.

Lobkis, O. I., and R. L. Weaver (2001), On the emergence of the Green's function in the correlations of a diffuse field, *The Journal of the Acoustical Society of America*, *110*(6), 3011-3017.

Loocke, M., J. E. Snow, and Y. Ohara (2013), Melt stagnation in peridotites from the Godzilla Megamullion oceanic core complex, Parece Vela Basin, Philippine Sea, *Lithos*, *182*, 1-10.

Ludwig, W. J., J. E. Nafe, and C. L. Drake (1970), Seismic refraction, *The sea*, *4*(Part 1), 53-84.

Lundin, E. R., and A. G. Doré (2011), Hyperextension, serpentinization, and weakening: A new paradigm for rifted margin compressional deformation, *Geology*, *39*(4), 347-350.

Manatschal, G., N. Froitzheim, M. Rubenach, and B. Turrin (2001), The role of detachment faulting in the formation of an ocean-continent transition: insights from the Iberia Abyssal Plain, *Geological Society, London, Special Publications*, *187*(1), 405-428.

Manatschal, G. (2004), New models for evolution of magma-poor rifted margins based on a review of data and concepts from West Iberia and the Alps, *International Journal of Earth Sciences*, *93*(3), 432-466.

Marrett, R., and R. W. Allmendinger (1992), Amount of extension on" small" faults: An example from the Viking graben, *Geology*, *20*(1), 47-50.

Masson, D., and P. Miles (1984), Mesozoic seafloor spreading between Iberia, Europe and North America, *Marine Geology*, *56*(1), 279-287.

Mauffret, A., and L. Montadert (1987), Rift tectonics on the passive continental margin off Galicia (Spain), *Marine and Petroleum Geology*, *4*(1), 49-70.

Maus, S., U. Barckhausen, H. Berkenbosch, N. Bournas, J. Brozena, V. Childers, F. Dostaler, J. Fairhead, C. Finn, and R. Von Frese (2009), EMAG2: A 2–arc min resolution Earth Magnetic Anomaly Grid compiled from satellite, airborne, and marine magnetic measurements, *Geochemistry, Geophysics, Geosystems*, *10*(8), Q08005.

McDermott, K., and T. Reston (2015), To see, or not to see? Rifted margin extension, *Geology*, *43*(11), 967-970.

McKenzie, D. (1978), Some remarks on the development of sedimentary basins, *Earth and planetary science letters*, *40*(1), 25-32.

Menzies, M. A., S. L. Klemperer, C. J. Ebinger, and J. Baker (2002), *Characteristics of volcanic rifted margins*, Special Paper, vol. 362. Geological Society of America, Boulder, CO.

Minshull, T., S. Dean, R. White, and R. Whitmarsh (2001), Anomalous melt production after continental break-up in the southern Iberia Abyssal Plain, *Geological Society, London, Special Publications*, *187*(1), 537-550.

Minshull, T., S. Dean, and R. Whitmarsh (2014), The peridotite ridge province in the southern Iberia Abyssal Plain: Seismic constraints revisited, *Journal of Geophysical Research: Solid Earth*, *119*(3), 1580-1598.

Minshull, T., S. Dean, R. Whitmarsh, S. Russell, K. Louden, and D. Chian (1998), Deep structure in the vicinity of the ocean-continent transition zone under the southern Iberia Abyssal Plain, *Geology*, *26*(8), 743-746.

Minshull, T., M. Muller, and R. White (2006), Crustal structure of the Southwest Indian Ridge at 66 E: Seismic constraints, *Geophysical Journal International*, *166*(1), 135-147.

Minshull, T. A. (2009), Geophysical characterisation of the ocean–continent transition at magma-poor rifted margins, *Comptes Rendus Geoscience*, *341*(5), 382-393.

Minshull, T. A., M. C. Sinha, and C. Peirce (2005), Multi-disciplinary, sub-seabed geophysical imaging, *Sea Technology*, *46*(10), 27-31.

Mispel, J., M. Houbiers, B. Knudsen, and L. Amundsen (2013), FWI with OBC Data From the Mariner Field, UK-The Impact on Mapping Sands at Reservoir Level, paper presented at Proceedings of the 75th EAGE Conference, Extended Abstracts, doi: 10.3997/2214-4609.20130829.

Mjelde, R., A. Breivik, T. Raum, E. Mittelstaedt, G. Ito, and J. Faleide (2008), Magmatic and tectonic evolution of the North Atlantic, *Journal of the Geological Society*, *165*(1), 31-42.

Mohn, G., G. D. Karner, G. Manatschal, and C. A. Johnson (2015), Structural and stratigraphic evolution of the Iberia–Newfoundland hyper-extended rifted margin: a quantitative modelling approach, *Geological Society, London, Special Publications*, *413*, 52-89.

Mohn, G., G. Manatschal, O. Müntener, M. Beltrando, and E. Masini (2010), Unravelling the interaction between tectonic and sedimentary processes during lithospheric thinning in the Alpine Tethys margins, *International Journal of Earth Sciences*, *99*(1), 75-101.

Morgan, J., M. Warner, G. Arnoux, E. Hooft, D. Toomey, B. VanderBeek, and W. Wilcock (2016), Next-generation seismic experiments–II: wide-angle, multi-azimuth, 3-D, full-waveform inversion of sparse field data, *Geophysical Journal International*, *204*(2), 1342-1363.

Morgan, J., M. Warner, R. Bell, J. Ashley, D. Barnes, R. Little, K. Roele, and C. Jones (2013), Next-generation seismic experiments: wide-angle, multi-azimuth, three-dimensional, full-waveform inversion, *Geophysical Journal International*, *195*(3), 1657-1678.

Moser, T. (1991), Shortest path calculation of seismic rays, *Geophysics*, *56*(1), 59-67.

Moser, T., G. Nolet, and R. Snieder (1992), Ray bending revisited, *Bulletin of the Seismological Society of America*, *82*(1), 259-288.

Mothi, S., K. Schwarz, and H. Zhu (2013), Impact of full-azimuth and long-offset acquisition on Full Waveform Inversion in deep water Gulf of Mexico, paper presented at Proceedings of the 75th EAGE Conference, Extended Abstracts, doi: 10.1190/segam2013-0102.1.

Muller, M., T. Minshull, and R. White (2000), Crustal structure of the Southwest Indian Ridge at the Atlantis II fracture zone, *Journal of Geophysical Research: Solid Earth*, *105*(B11), 25809-25828.

Murillas, J., D. Mougenot, G. Boulot, M. Comas, E. Banda, and A. Mauffret (1990), Structure and evolution of the Galicia Interior Basin (Atlantic western Iberian continental margin), *Tectonophysics*, *184*(3), 297-319.

Mutter, C. Z., and J. C. Mutter (1993), Variations in thickness of layer 3 dominate oceanic crustal structure, *Earth and Planetary Science Letters*, *117*(1), 295-317.

Mutter, J. C. (1985), Seaward dipping reflectors and the continent-ocean boundary at passive continental margins, *Tectonophysics*, *114*(1-4), 117-131.

Mutter, J. C. (1993), Margins declassified, *Nature*, *364*(6436), 393-394.

Mutter, J. C., M. Talwani, and P. L. Stoffa (1982), Origin of seaward-dipping reflectors in oceanic crust off the Norwegian margin by "subaerial sea-floor spreading", *Geology*, *10*(7), 353-357.

Nakanishi, I., and K. Yamaguchi (1986), A numerical experiment on nonlinear image reconstruction from first-arrival times for two-dimensional island arc structure, *Journal of Physics of the Earth*, *34*(2), 195-201.

Nirrengarten, M., G. Manatschal, J. Tugend, N. J. Kusznir, and D. Sauter (2017), Nature and origin of the J-magnetic anomaly offshore Iberia–Newfoundland: implications for plate reconstructions, *Terra Nova*, *29*(1), 20-28.

Nishimura, C. E., and D. W. Forsyth (1989), The anisotropic structure of the upper mantle in the Pacific, *Geophysical Journal International*, *96*(2), 203-229.

Ohara, Y., K. Okino, and J. Kasahara (2007), Seismic study on oceanic core complexes in the Parece Vela back-arc basin, *Island Arc*, *16*(3), 348-360.

Operto, S., J. Virieux, P. Amestoy, J.-Y. L'Excellent, L. Giraud, and H. B. H. Ali (2007), 3D finite-difference frequency-domain modeling of visco-acoustic wave propagation using a massively parallel direct solver: A feasibility study, *Geophysics*, *72*(5), SM195-SM211.

Operto, S., J. Virieux, J. X. Dessa, and G. Pascal (2006), Crustal seismic imaging from multifold ocean bottom seismometer data by frequency domain full waveform tomography: Application to the eastern Nankai trough, *Journal of Geophysical Research: Solid Earth*, *111*(B9), B09306.

Osmundsen, P., and J. Ebbing (2008), Styles of extension offshore mid-Norway and implications for mechanisms of crustal thinning at passive margins, *Tectonics*, *27*(6), TC6016

Paige, C. C., and M. A. Saunders (1982), LSQR: An algorithm for sparse linear equations and sparse least squares, *ACM transactions on Mathematical Software*, *8*(1), 43-71.

Pedersen, T., and H. E. Ro (1992), Finite duration extension and decompression melting, *Earth and planetary science letters*, *113*(1-2), 15-22.

Pérez-Gussinyé, M. (2013), A tectonic model for hyperextension at magma-poor rifted margins: an example from the West Iberia–Newfoundland conjugate margins, *Geological Society, London, Special Publications*, *369*(1), 403-427.

Pérez-Gussinyé, M., J. P. Morgan, T. J. Reston, and C. R. Ranero (2006), The rift to drift transition at non-volcanic margins: insights from numerical modelling, *Earth and Planetary Science Letters*, *244*(1), 458-473.

Pérez-Gussinyé, M., C. Ranero, T. J. Reston, and D. Sawyer (2003), Mechanisms of extension at nonvolcanic margins: Evidence from the Galicia interior basin, west of Iberia, *Journal of Geophysical Research: Solid Earth*, *108*(B5), 2245.

Pérez-Gussinyé, M., and T. J. Reston (2001), Rheological evolution during extension at nonvolcanic rifted margins: onset of serpentinization and development of detachments leading to continental breakup, *Journal of Geophysical Research: Solid Earth*, *106*(B3), 3961-3975.

Péron-Pinvidic, G., and G. Manatschal (2009), The final rifting evolution at deep magma-poor passive margins from Iberia-Newfoundland: a new point of view, *International Journal of Earth Sciences*, *98*(7), 1581-1597.

Peron-Pinvidic, G., G. Manatschal, and P. T. Osmundsen (2013), Structural comparison of archetypal Atlantic rifted margins: a review of observations and concepts, *Marine and Petroleum Geology*, *43*, 21-47.

Péron-Pinvidic, G., G. Manatschal, T. A. Minshull, and D. S. Sawyer (2007), Tectonosedimentary evolution of the deep Iberia-Newfoundland margins: Evidence for a complex breakup history, *Tectonics*, *26*(2), TC2011.

Pickup, S., R. Whitmarsh, C. Fowler, and T. Reston (1996), Insight into the nature of the ocean-continent transition off West Iberia from a deep multichannel seismic reflection profile, *Geology*, *24*(12), 1079-1082.

Pratt, R. G. (1999), Seismic waveform inversion in the frequency domain, Part 1: Theory and verification in a physical scale model, *Geophysics*, *64*(3), 888-901.

Pratt, R. G., C. Shin, and G. Hick (1998), Gauss–Newton and full Newton methods in frequency–space seismic waveform inversion, *Geophysical Journal International*, *133*(2), 341-362.

Prothero, W., W. J. Taylor, and J. Eickemeyer (1988), A fast, two-point, three-dimensional raytracing algorithm using a simple step search method, *Bulletin of the Seismological Society of America*, *78*(3), 1190-1198.

Radhakrishna, M., C. Subrahmanyam, and T. Damodharan (2010), Thin oceanic crust below Bay of Bengal inferred from 3-D gravity interpretation, *Tectonophysics*, *493*(1), 93-105.

Ranero, C. R., J. P. Morgan, K. McIntosh, and C. Reichert (2003), Bending-related faulting and mantle serpentinization at the Middle America trench, *Nature*, *425*(6956), 367.

Ranero, C. R., and M. Pérez-Gussinyé (2010), Sequential faulting explains the asymmetry and extension discrepancy of conjugate margins, *Nature*, *468*(7321), 294-299.

Ratcliffe, A., C. Win, V. Vinje, G. Conroy, M. Warner, A. Umpleby, I. Stekl, T. Nangoo, and A. Bertrand (2011), Full waveform inversion: A North Sea OBC case study, paper presented at 2011 SEG Annual Meeting, , Society of Exploration Geophysicists, Expanded Abstracts 30, pp. 2384–2388.

Reston, T. (2007a), Extension discrepancy at North Atlantic nonvolcanic rifted margins: Depth-dependent stretching or unrecognized faulting?, *Geology*, *35*(4), 367-370.

Reston, T., and K. McDermott (2014), An assessment of the cause of the 'extension discrepancy' with reference to the west Galicia margin, *Basin Research*, *26*(1), 135-153.

Reston, T. J. (2005), Polyphase faulting during the development of the west Galicia rifted margin, *Earth and Planetary Science Letters*, *237*(3), 561-576.

Reston, T. J. (2007b), The formation of non-volcanic rifted margins by the progressive extension of the lithosphere: the example of the West Iberian margin, *Geological Society, London, Special Publications*, *282*(1), 77-110.

Reston, T. J. (2009a), The extension discrepancy and syn-rift subsidence deficit at rifted margins, *Petroleum Geoscience*, *15*(3), 217-237.

Reston, T. J. (2009b), The structure, evolution and symmetry of the magma-poor rifted margins of the North and Central Atlantic: a synthesis, *Tectonophysics*, *468*(1), 6-27.

Reston, T. J. (2010), The opening of the central segment of the South Atlantic: symmetry and the extension discrepancy, *Petroleum Geoscience*, *16*(3), 199-206.

Reston, T. J., C. M. Krawczyk, and D. Klaeschen (1996), The S reflector west of Galicia (Spain): Evidence from prestack depth migration for detachment faulting during continental breakup, *Journal of Geophysical Research: Solid Earth (1978–2012)*, *101*(B4), 8075-8091.

Reston, T. J., T. Leythäuser, G. Booth-Rea, D. Sawyer, D. Klaeschen, and C. Long (2007), Movement along a low-angle normal fault: The S reflector west of Spain, *Geochemistry, Geophysics, Geosystems*, *8*(6), Q06002.

Rost, S., and C. Thomas (2002), Array seismology: Methods and applications, *Reviews of geophysics*, *40*(3), 1008.

Roux, P., K. G. Sabra, W. A. Kuperman, and A. Roux (2005), Ambient noise cross correlation in free space: Theoretical approach, *The Journal of the Acoustical Society of America*, *117*(1), 79-84.

Russell, S., and R. Whitmarsh (2003), Magmatism at the west Iberia non-volcanic rifted continental margin: evidence from analyses of magnetic anomalies, *Geophysical Journal International*, *154*(3), 706-730.

Sabra, K. G., P. Gerstoft, P. Roux, W. Kuperman, and M. C. Fehler (2005a), Extracting time-domain Green's function estimates from ambient seismic noise, *Geophysical Research Letters*, *32*(3), L03310.

Sabra, K. G., P. Gerstoft, P. Roux, W. Kuperman, and M. C. Fehler (2005b), Surface wave tomography from microseisms in Southern California, *Geophysical Research Letters*, *32*(14), L14311.

Saito, M. (1988), DISPER80: A subroutine package for the calculation of seismic normal-mode solutions, *Seismological algorithms*, 293-319.

Sallarès, V., A. Gailler, M.-A. Gutscher, D. Graindorge, R. Bartolomé, E. Gracia, J. Diaz, J. J. Dañobeitia, and N. Zitellini (2011), Seismic evidence for the presence of Jurassic oceanic crust in the central Gulf of Cadiz (SW Iberian margin), *Earth and Planetary Science Letters*, *311*(1), 112-123.

Sánchez-Sesma, F. J., and M. Campillo (2006), Retrieval of the Green's function from cross correlation: the canonical elastic problem, *Bulletin of the Seismological Society of America*, *96*(3), 1182-1191.

Sawyer, D., R. Whitmarsh, and A. Klaus (1994), Iberia Abyssal Plain Sites 897-901, *Proceedings of the Ocean Drilling Program Initial Reports*, *149*.

Sawyer, D. S., M. F. Coffin, T. J. Reston, J. M. Stock, and J. R. Hopper (2007), COBBOOM: the continental breakup and birth of oceans mission, *Scientific Drilling*, *5*, 13-25.

Sawyer, D. S., T. Reston, M. P. Gussinye, C. A. Zelt, J. A. Austin, Y. Nakamura, J. Danobeitia, and D. Cordoba (1997), The Iberia Seismic Experiment (ISE97): MCS reflection profiles, *EOS*, *78*(F468).

Schärer, U., J. Kornprobst, M.-O. Beslier, G. Boillot, and J. Girardeau (1995), Gabbro and related rock emplacement beneath rifting continental crust: U Pb geochronological and geochemical constraints for the Galicia passive margin (Spain), *Earth and Planetary Science Letters*, *130*(1), 187-200.

Scott, C. L. (2009), Formation and evolution of the eastern Black Sea basin: Constraints from wide-angle seismic data, PhD thesis, 190 pp, University of Southampton.

Seats, K. J., J. F. Lawrence, and G. A. Prieto (2012), Improved ambient noise correlation functions using Welch's method, *Geophysical Journal International*, *188*(2), 513-523.

Shapiro, N. M., and M. Campillo (2004), Emergence of broadband Rayleigh waves from correlations of the ambient seismic noise, *Geophysical Research Letters*, *31*(7), L07614.

Shapiro, N. M., M. Campillo, L. Stehly, and M. H. Ritzwoller (2005), High-resolution surface-wave tomography from ambient seismic noise, *Science*, *307*(5715), 1615-1618.

Shillington, D. J., W. S. Holbrook, H. J. Van Avendonk, B. E. Tucholke, J. R. Hopper, K. E. Louden, H. C. Larsen, and G. T. Nunes (2006), Evidence for asymmetric nonvolcanic rifting and slow incipient oceanic accretion from seismic reflection data on the Newfoundland margin, *Journal of Geophysical Research: Solid Earth*, *111*(B9), B09402.

Shipboard Scientific Party (1987), Introduction, objectives, and principal results: ocean drilling program Leg103, West Galicia margin, *Proc Ocean Drill Program Init Rep*, *103*, 3-17.

Shipboard Scientific Party ODP Leg 149 (1993), ODP drills the West Iberia rifted margin, *Eos*, *74*, 454-455.

Shipboard Scientific Party ODP Leg 173 (1998), Drilling reveals transition from continental breakup to early magmatic crust, *Eos*, *79*(173), 180-181.

Sibuet, J.-C. (1992), New constraints on the formation of the non-volcanic continental Galicia–Flemish Cap conjugate margins, *Journal of the Geological Society*, *149*(5), 829-840.

Sibuet, J.-C., V. Louvel, R. B. Whitmarsh, R. S. White, S. J. Horsefield, B. Sichler, P. Léon, and M. Recq (1995), Constraints on rifting processes from refraction and deep-tow magnetic data: the example of the Galicia continental margin (West Iberia), in *Rifted ocean-continent boundaries*, edited, pp. 197-217, Springer.

Sibuet, J.-C., J.-P. Maze, P. Amortila, and X. Le Pichon (1987), Physiography and structure of the western Iberian continental margin off Galicia from Sea-Beam and seismic data, *Initial Reports of the Ocean Drilling Program*, *103*, 77-97.

Sibuet, J. C., S. Srivastava, and G. Manatschal (2007), Exhumed mantle-forming transitional crust in the Newfoundland-Iberia rift and associated magnetic anomalies, *Journal of Geophysical Research: Solid Earth*, *112*(B6), B06105.

Singh, S. C., H. Carton, A. S. Chauhan, S. Androvandi, A. Davaille, J. Dyment, M. Cannat, and N. D. Hananto (2011), Extremely thin crust in the Indian Ocean possibly resulting from Plume —Ridge Interaction, *Geophysical Journal International*, *184*(1), 29-42.

Sirgue, L. (2006), The importance of low frequency and large offset in waveform inversion, paper presented at Proceedings of the 68th EAGE Conference, Extended Abstracts, doi: 10.3997/2214-4609.201402146.

Sirgue, L., O. Barkved, J. Dellinger, J. Etgen, U. Albertin, and J. Kommedal (2010), Thematic set: Full waveform inversion: The next leap forward in imaging at Valhall, *First Break*, *28*(4), 65-70.

Skogseid, J. (2001), Volcanic margins: geodynamic and exploration aspects, *Marine and Petroleum Geology*, *18*(4), 457-461.

Skogseid, J., S. Planke, J. I. Faleide, T. Pedersen, O. Eldholm, and F. Neverdal (2000), NE Atlantic continental rifting and volcanic margin formation, *Geological Society, London, Special Publications*, *167*(1), 295-326.

Sohn, R. A., J. P. Canales, and S. E. Humphris (2007), Kinematics and geometry of active detachment faulting beneath the Trans-Atlantic Geotraverse (TAG) hydrothermal field on the Mid-Atlantic Ridge, *Geology*, *35*(8), 711-714.

Srivastava, S., J.-C. Sibuet, S. Cande, W. Roest, and I. D. Reid (2000), Magnetic evidence for slow seafloor spreading during the formation of the Newfoundland and Iberian margins, *Earth and Planetary Science Letters*, *182*(1), 61-76.

Stroup, J. B., and P. J. Fox (1981), Geologic investigations in the Cayman Trough: Evidence for thin oceanic crust along the Mid-Cayman Rise, *The Journal of Geology*, *89*(4), 395-420.

Sutra, E., and G. Manatschal (2012), How does the continental crust thin in a hyperextended rifted margin? Insights from the Iberia margin, *Geology*, *40*(2), 139-142.

Tarantola, A. (1984), Inversion of seismic reflection data in the acoustic approximation, *Geophysics*, *49*(8), 1259-1266.

Tarantola, A. (1987), Inverse Problem Theory: Models for Data Fitting and Model Parameter Estimation, edited, Elsevier, Amsterdam.

Tucholke, B., D. Sawyer, and J.-C. Sibuet (2007), Breakup of the Newfoundland–Iberia rift, *Geological Society, London, Special Publications*, *282*(1), 9-46.

Tucholke, B., J. Sibuet, and A. Klaus (2004), Leg 210 Summary, *Proceedings of the Ocean Drilling Program, Initial Report*, *210*, 1-78.

Tucholke, B. E., and J.-C. Sibuet (2007), Leg 210 synthesis: tectonic, magmatic, and sedimentary evolution of the Newfoundland-Iberia rift, *Proceedings of the Ocean Drilling Program, Scientific Results*, *210*, 1-56.

Tucholke, B. E., and J.-C. Sibuet (2012), Problematic plate reconstruction, *Nature Geoscience*, *5*(10), 676-677.

Um, J., and C. Thurber (1987), A fast algorithm for two-point seismic ray tracing, *Bulletin of the Seismological Society of America*, *77*(3), 972-986.

Van Avendonk, H. J., W. S. Holbrook, G. T. Nunes, D. J. Shillington, B. E. Tucholke, K. E. Louden, H. C. Larsen, and J. R. Hopper (2006), Seismic velocity structure of the rifted margin of the eastern Grand Banks of Newfoundland, Canada, *Journal of Geophysical Research: Solid Earth*, *111*(B11), B11404.

Van Avendonk, H. J., L. L. Lavier, D. J. Shillington, and G. Manatschal (2009), Extension of continental crust at the margin of the eastern Grand Banks, Newfoundland, *Tectonophysics*, *468*(1), 131-148.

Virieux, J. (1986), P-SV wave propagation in heterogeneous media: Velocity-stress finite-difference method, *Geophysics*, *51*(4), 889-901.

Virieux, J., and S. Operto (2009), An overview of full-waveform inversion in exploration geophysics, *Geophysics*, *74*(6), WCC1-WCC26.

Walsh, J., and J. Watterson (1992), Populations of faults and fault displacements and their effects on estimates of fault-related regional extension, *Journal of Structural Geology*, *14*(6), 701-712.

Warner, M. (2012), Full-waveform inversion - internal notes: Imperial College London.

Warner, M., A. Ratcliffe, T. Nangoo, J. Morgan, A. Umpleby, N. Shah, V. Vinje, I. Štekl, L. Guasch, and C. Win (2013), Anisotropic 3D full-waveform inversion, *Geophysics*, *78*(2), R59-R80.

Warner, M., A. Umpleby, I. Stekl, and J. Morgan (2010), 3D full-wavefield tomography: imaging beneath heterogeneous overburden, paper presented at Proceedings of the 72nd EAGE Conference, Extended Abstracts, doi: 10.3997/2214-4609.20149944

Weinberg, R. F., K. Regenauer-Lieb, and G. Rosenbaum (2007), Mantle detachment faults and the breakup of cold continental lithosphere, *Geology*, *35*(11), 1035-1038.

Welch, P. (1967), The use of fast Fourier transform for the estimation of power spectra: a method based on time averaging over short, modified periodograms, *IEEE Transactions on audio and electroacoustics*, *15*(2), 70-73.

Wernicke, B. (1981), Low-angle normal faults in the Basin and Range Province: nappe tectonics in an extending orogen, *Nature*, *291*, 645-648.

Wernicke, B. (1985), Uniform-sense normal simple shear of the continental lithosphere, *Canadian Journal of Earth Sciences*, *22*(1), 108-125.

White, R., and D. McKenzie (1989), Magmatism at rift zones: the generation of volcanic continental margins and flood basalts, *Journal of Geophysical Research: Solid Earth*, *94*(B6), 7685-7729.

White, R., L. Smith, A. Roberts, P. Christie, N. Kusznir, A. Roberts, D. Healy, R. Spitzer, A. Chappell, and J. Eccles (2008), Lower-crustal intrusion on the North Atlantic continental margin, *Nature*, *452*(7186), 460-464.

White, R. S., D. McKenzie, and R. K. O'Nions (1992), Oceanic crustal thickness from seismic measurements and rare earth element inversions, *Journal of Geophysical Research: Solid Earth*, *97*(B13), 19683-19715.

White, R. S., and L. K. Smith (2009), Crustal structure of the Hatton and the conjugate east Greenland rifted volcanic continental margins, NE Atlantic, *Journal of Geophysical Research: Solid Earth*, *114*(B2), B02305

White, R. S., and R. A. Stephen (1980), Compressional to shear wave conversion in oceanic crust, *Geophysical Journal International*, *63*(2), 547-565.

Whitmarsh, R., M. Beslier, and P. Wallace (1998), Leg 173, *Proceedings of the Ocean Drilling Program, Initial Report*, *173*, 493.

Whitmarsh, R., G. Manatschal, and T. Minshull (2001a), Evolution of magma-poor continental margins from rifting to seafloor spreading, *Nature*, *413*(6852), 150-154.

Whitmarsh, R., T. Minshull, S. Russell, S. Dean, K. Louden, and D. Chian (2001b), The role of syn-rift magmatism in the rift-to-drift evolution of the West Iberia continental margin: geophysical observations, *Geological Society, London, Special Publications*, *187*(1), 107-124.

Whitmarsh, R. B., and P. R. Miles (1995), Models of the development of the West Iberia rifted continental margin at 40° 30′ N deduced from surface and deep-tow magnetic anomalies, *Journal of Geophysical Research: Solid Earth*, *100*(B3), 3789-3806.

Whitmarsh, R. B., P. J. Wallace, and M.-O. Beslier (2001c), The rift-to-drift development of the west Iberia nonvolcanic continental margin: a summary and review of the contribution of Ocean Drilling Program Leg 173, *Proceedings of the Ocean Drilling Program, Scientific Results, 173*, 36-36.

Whitmarsh, R. B., R. S. White, S. J. Horsefield, J. C. Sibuet, M. Recq, and V. Louvel (1996), The ocean-continent boundary off the western continental margin of Iberia: Crustal structure west of Galicia Bank, *Journal of Geophysical Research: Solid Earth*, *101*(B12), 28291-28314.

Williamson, P. (1991), A guide to the limits of resolution imposed by scattering in ray tomography, *Geophysics*, *56*(2), 202-207.

Wu, R.-S., and M. N. Toksöz (1987), Diffraction tomography and multisource holography applied to seismic imaging, *Geophysics*, *52*(1), 11-25.

Yao, H., R. D. van Der Hilst, and V. Maarten (2006), Surface-wave array tomography in SE Tibet from ambient seismic noise and two-station analysis—I. Phase velocity maps, *Geophysical Journal International*, *166*(2), 732-744.

Zelt, C., and R. Ellis (1988), Practical and efficient ray tracing in two-dimensional media for rapid traveltime and amplitude forward modeling, *Canadian Journal of Exploration Geophysics*, *24*(1), 16-31.

Zelt, C., and R. Smith (1992), Seismic traveltime inversion for 2-D crustal velocity structure, *Geophysical journal international*, *108*(1), 16-34.

Zelt, C. A., and P. J. Barton (1998), Three-dimensional seismic refraction tomography: A comparison of two methods applied to data from the Faeroe Basin, *Journal of Geophysical Research: Solid Earth*, *103*(B4), 7187-7210.

Zelt, C. A., K. Sain, J. V. Naumenko, and D. S. Sawyer (2003), Assessment of crustal velocity models using seismic refraction and reflection tomography, *Geophysical Journal International*, *153*(3), 609-626.

Zhang, J., and M. N. Toksöz (1998), Nonlinear refraction traveltime tomography, *Geophysics*, *63*(5), 1726-1737.